Transverse target-spin asymmetry in exclusive electroproduction of ρ^0 mesons

The work described in this thesis was carried out at the ‘National institute for subatomic physics’ (Nikhef) in Amsterdam, the Netherlands. The work is part of the research program of the ‘Stichting voor Fundamenteel Onderzoek der Materie’ (FOM), which is financially supported by the ‘Nederlandse Organisatie voor Wetenschappelijk Onderzoek’ (NWO).

VRIJE UNIVERSITEIT

Transverse target-spin asymmetry in exclusive electroproduction of ρ^0 mesons

ACADEMISCH PROEFSCHRIFT

ter verkrijging van de graad Doctor aan
de Vrije Universiteit Amsterdam,
op gezag van de rector magnificus
prof.dr. L.M. Bouter,
in het openbaar te verdedigen
ten overstaan van de promotiecommissie
van de faculteit der Exacte Wetenschappen
op dinsdag 7 oktober 2008 om 15.45 uur
in de aula van de universiteit,
De Boelelaan 1105

door

Jeroen Dreschler

geboren te Sentani, Indonesië

promotor: prof.dr. G. van der Steenhoven
copromotor: dr. H.P. Blok

Contents

Chapter 1

Introduction

The origin of the nucleon spin is an important subject in the study of the nucleon structure. Spin, also referred to as intrinsic angular momentum, is a fundamental quantum-mechanical property of particles. Particles are classified as bosons, which carry a spin of 0, $\hbar$, $2\,\hbar, \ldots$, or fermions, which carry a spin of $\hbar/2$, $\hbar\,3/2, \ldots$ (Note that in the following the reduced Plank constant $\hbar$ is omitted[1].) The nucleon, i.e., a proton or a neutron, carries a spin of 1/2. It is known that nucleons, the building blocks of the nuclei of all atoms observed in nature, are themselves composite systems consisting of more elementary constituents [1]. How the spin and the orbital angular momentum of each of these constituents contribute to the overall spin of the nucleon, is one of the central unresolved research questions in strong-interaction physics.

Investigations of the nucleon structure The first evidence for the nucleon to be a composite particle was the measurement of the magnetic moment of the proton already in 1932-33 by Estermann, Frisch and Stern in Hamburg [2]. It was found that the magnetic moment significantly deviates from the value calculated under the assumption that the proton is an elementary particle, which indicated that the proton has an internal structure.

In order to gain information about the internal structure of the nucleon many experiments have been performed in which leptons (electrons, positrons, muons or neutrinos) were scattered from proton or deuteron targets. For the elastic process $e\,p \to e\,p$, where e denotes the lepton and p the proton, it has been found that the scattering pattern differs from theoretical predictions for the scattering from a point-like particle, i.e., a particle without any substructure or spatial extension. This was discovered in 1955 by Hofstadter and collaborators [3], who investigated elastic electron scattering from the proton at Stanford. A good description of the elastic scattering data was obtained by models that assume the nucleon to have a spatial distribution of charge and magnetization densities, which are taken into

---

[1] Throughout this thesis natural units are used, for which the physics constants c and $\hbar$ are taken equal to unity.

account by quantities called the Dirac and Pauli electromagnetic form factors. From the obtained electromagnetic form factors the proton mean square charge radius was determined to be about 0.8 fm [1].

Investigation of the so-called deep-inelastic scattering (DIS) process offers the possibility to resolve the structure of the nucleon in terms of its constituents. In the DIS process an interaction takes place between the incoming lepton and an individual constituent of the nucleon. This interaction causes the nucleon to fragment into various hadronic states, which are collectively denoted by X. In case none of the final hadronic states in the process $e\,p \to e\,X$ is specifically identified, this process is referred to as inclusive DIS. The pioneering DIS measurements were performed at Stanford in the late 1960s [4]. These inclusive measurements led Feynman and Bjorken to the interpretation of the first DIS data in terms of scattering from point-like constituents of the nucleon, which were called partons.

Numerous DIS experiments have succeeded these measurements. From the interpretation of the inclusive DIS data the parton model emerged. Within the parton model the nucleon is pictured as a collection of partons, which are identified as electrically charged spin-1/2 particles called (anti)quarks and electrically neutral spin-1 partons called gluons. One can distinguish valence quarks and sea quarks. The valence quarks account for the main static properties of the nucleon, such as its charge, spin and isospin, which is the quantum number determining whether the nucleon is a proton or a neutron. Sea quarks appear in the nucleon as quark-antiquark pairs originating from gluon splitting. The quarks come in different types specified by a property called flavor. The flavor of the valence quarks of the nucleon is either up or down, whereas the sea quarks may also carry other flavors, such as strangeness.

The cross section of the DIS process for a given polarization state of the incident lepton and target nucleon is usually expressed in terms of quantities referred to as structure functions. At present, the structure functions cannot be calculated from first principles. In the parton model a phenomenological description of the DIS structure functions is given in terms of so-called parton distribution functions that relate the structure functions to distributions of partons inside the nucleon. The spin-dependent structure function g_1 can be measured in DIS with a longitudinally polarized lepton beam and a longitudinally polarized target with respect to the beam direction. This structure function can be interpreted in terms of quark-helicity distribution functions, from which one can determine the fractional quark-spin contribution $\Delta\Sigma$ to the nucleon spin. In 1988 the EMC experiment at CERN reported the first measurement of the structure function g_1^{p} for the proton [5]. This measurement led to the discovery that the spins of quarks are responsible for only a small fraction of the proton spin. The quark-spin contribution $\Delta\Sigma$ determined from the results on g_1 from various experiments at CERN, SLAC and DESY was found to be about 20-30%.

The investigation of the origin of the nucleon spin in terms of quark, sea quark, and gluon spin and orbital angular momentum contributions is the main focus of the HERMES experiment at DESY, which started taking data in 1995. The HERMES experiment has performed high precision measurements of g_1 for the proton, deuteron and the neutron by using various types of polarized targets [6]. These measurements provide some of the world's most precise data on g_1. Moreover, from measurements of semi-inclusive DIS, in which one of the produced hadrons is also detected, the quark-helicity distribution functions have been determined separately for different quark flavors [7]. From these measurements it has been concluded that within the uncertainty margins of the experiment the spins of sea quarks do not contribute to the nucleon spin.

Quark orbital-angular momentum, generalized parton distributions and exclusive processes As the world's measurements of g_1 and the semi-inclusive DIS measurements have demonstrated, the spin of the nucleon cannot be fully attributed to the spin of quarks. Therefore, the nucleon spin of 1/2 must arise also from other contributions, which are specified by the angular momentum sum rule [8]

$$\frac{1}{2} = \frac{1}{2}\Delta\Sigma + L_q + \Delta G + L_g, \tag{1.1}$$

where L_q represents the orbital angular momentum of quarks, and ΔG and L_g represent the contributions from the intrinsic spin and the orbital angular momentum of gluons, respectively. The total angular momentum J_q carried by all quarks in the nucleon can be written as

$$J_q = \frac{1}{2}\Delta\Sigma + L_q. \tag{1.2}$$

Therefore, by measuring the total angular momentum J_q one can obtain information on the unknown orbital angular momentum L_q of quarks in the nucleon making use of the available data on $\Delta\Sigma$.

Experimental information on the total angular momentum J_q can be obtained within the framework of generalized parton distributions (GPDs). At high enough momentum transfer GPDs provide a description of exclusive production processes, such as deeply virtual Compton scattering ($e\,p \rightarrow e\,p\,\gamma$) and exclusive meson leptoproduction ($e\,p \rightarrow e\,p\,M$), where γ and M represent a real photon and a meson, respectively. It should be noted that for exclusive meson production the GPD description applies only if both the produced meson and the virtual photon that is exchanged in the process are longitudinally polarized. GPDs are generalizations of the usual parton distribution functions and the form factors, describing the DIS process and the elastic scattering process, respectively. Hence, GPDs provide a unified description of exclusive production processes, as well as elastic scattering and (semi-)inclusive DIS processes.

As was shown for the first time in [9], specific GPDs are related to the total angular momentum of quarks in the nucleon. Since GPDs cannot be directly measured, models of GPDs have been developed, which are extrapolations of the data on parton distribution functions and form factors. From the investigation of exclusive processes additional constraints on GPD models can be obtained resulting in more detailed knowledge on the structure of the nucleon. In particular, as is described in [10], measurements of specific observables in exclusive meson production can be used to provide a model-dependent constraint on the total angular momentum J_q and, therefore, also on the orbital angular momentum L_q of the quarks in the nucleon. At present, no precise experimental information exists on the orbital angular momentum carried by the quarks and gluons in the nucleon.

Transverse target-spin asymmetry in exclusive ρ^0 leptoproduction GPD-model calculations are available for the transverse target-spin asymmetry A_{UT} in exclusive ρ^0 leptoproduction that can be measured with an unpolarized beam on a transversely polarized target. From these calculations it follows that the $\sin(\phi-\phi_s)$ moment of the asymmetry A_{UT} depends on J_q. Here ϕ and ϕ_s are the azimuthal angles of the produced ρ^0 meson and the transverse component of the nucleon spin vector, respectively, around the virtual-photon direction. Hence, one can obtain an estimate of J_q by comparing the measurements of this azimuthal moment of A_{UT} to the GPD-based calculations. However, since the calculations only apply to the case where both the exchanged virtual photon and the produced meson are longitudinally polarized, for such a comparison it is required that the asymmetry is measured for this case specifically.

The experimental separation of longitudinally and transversely polarized virtual photons is usually done by the Rosenbluth method. This method requires that measurements are performed at different beam energies, which is in general not done at the HERMES experiment. However, under the assumption of s-channel helicity conservation (SCHC) the helicity of the exchanged virtual photon is taken over by the produced ρ^0 meson. Therefore, in that case it is sufficient to measure the asymmetry A_{UT} for the different polarization states of the ρ^0 meson. One can perform such a separation experimentally by using the fact that the polarization of the ρ^0 meson is reflected by its decay angular distribution.

The contributions to the cross section and the asymmetry A_{UT} for exclusive ρ^0 production from the various polarization states of the virtual photon and the ρ^0 meson can be expressed in terms of so-called spin density-matrix elements (SDMEs). The (combinations of) SDMEs each corresponding to a specific polarization state of the produced ρ^0 meson can be extracted from the angular distributions of the ρ^0 meson and its decay products. Data are available on the SDMEs for the case of an unpolarized target. These results imply that SCHC holds reasonably well at HERMES kinematics. Recently, a new SDME formalism for vector-meson production on a polarized nucleon was developed [11]. Within this formalism a detailed investigation of exclusive ρ^0 production can be performed for the case of a polarized target. The SDME formalism can thus also be used to extract the asymmetry A_{UT} separately for longitudinally and transversely polarized ρ^0 mesons.

This thesis This thesis reports the first determination of the transverse target-spin asymmetry A_{UT} in exclusive ρ^0 production on a transversely polarized hydrogen target. The analysis is based on the data obtained at HERMES during the

2002-2005 data taking periods. In the analysis also the SDMEs for an unpolarized and a polarized target are extracted from this data set. This is done for the first time within the recently developed SDME formalism [11] for vector-meson production on a polarized nucleon. The asymmetry A_{UT} is extracted for longitudinally and transversely polarized ρ^0 mesons separately. Under the assumption of SCHC, the results for the $\sin(\phi - \phi_s)$ moment of the asymmetry for longitudinally polarized ρ^0 mesons are compared with GPD-model calculations. From this comparison a model-dependent constraint on the total and the orbital angular momentum of the quarks in the nucleon is obtained.

In chapter 2 a description of the theoretical framework used in the analysis, in particular for the asymmetry A_{UT}, the SDMEs, and the GPDs, is given. In chapter 3 the HERMES experiment is described. The selection of exclusive ρ^0 production events from the data collected at HERMES with a transversely polarized hydrogen target is the subject of chapter 4. The selected data set contains contributions from various sources of background. These contributions are evaluated in section 4.3. In chapter 5 the methods used for the determination of A_{UT} and the extraction of SDMEs are discussed. A Monte Carlo simulation is used to take the effect of the acceptance of the HERMES spectrometer into account in the various extraction methods. Monte Carlo simulations are used as well to verify the performance of these methods. A description of these Monte Carlo studies is given in chapter 6. In chapter 7 the results for the asymmetries and SDMEs extracted from the exclusive ρ^0 production data are presented. This chapter includes discussions of the systematic uncertainties and the interpretation of the measured asymmetry A_{UT} for longitudinally polarized ρ^0 mesons in terms of the total angular momentum J_q carried by the quarks in the nucleon. The conclusions of the analyses are presented in chapter 8.

Chapter 2

Theoretical framework

In this chapter a brief description is given of the theoretical framework used to determine the transverse target-spin asymmetry in exclusive ρ^0 electroproduction. In order to introduce the basic theoretical concepts first, the deep-inelastic scattering (DIS) process and its description in terms of parton distribution functions are presented in section 2.1 and 2.2, respectively. In section 2.3 generalized parton distributions (GPDs) are introduced, which provide a unified description of DIS, elastic lepton-nucleon scattering, and hard exclusive processes. However, it must be realized that hard exclusive meson production can only be described in terms of GPDs if both the produced meson and the virtual photon that is exchanged in the process are longitudinally polarized [12].

Before discussing specific GPD calculations for exclusive ρ^0 production, the general formalism relating the expression of the cross section to the polarization of the lepton, nucleon, virtual photon, and the produced ρ^0 meson is introduced. The relevant kinematic variables, angles, and polarizations are introduced in section 2.4. In section 2.5, a description of the electroproduction cross section is given in terms of the virtual-photon absorption cross section and interference terms within the Diehl-Sapeta formalism [13]. These terms describe the interference of amplitudes for a specific target-nucleon helicity and virtual-photon polarization. Each term is associated with a specific dependence of the cross section on the angles ϕ and ϕ_S, which are the azimuthal angles of the produced ρ^0 meson and the transverse component of the nucleon spin, respectively, with respect to the virtual-photon direction (see section 2.4).

The (ϕ, ϕ_S) dependence of the cross section is contained in the angular distribution function, which is decomposed into separate parts for different polarizations of the target nucleon, the beam lepton, and the produced ρ^0 meson in section 2.6. The polarization of the ρ^0 meson is associated with the additional dependence of the angular distribution function on the polar ρ^0 angle $\theta_{\pi\pi}$. In section 2.7 the transverse target-spin asymmetry is introduced in relation to the angular distribution function. The decomposition of the angular distribution into parts for longitudinal (ρ_L) and transverse ρ^0 polarization (ρ_T) is used to express the $\rho_L - \rho_T$

separated transverse target-spin asymmetries. Whereas in theory the transverse and longitudinal components of the target polarization are defined with respect to the virtual-photon direction, the experimental target polarization is defined with respect to the lepton-beam direction. For the latter case the transverse target-spin is defined differently, which is discussed in more detail in section 2.8.

A full description of the angular distribution function, including also the azimuthal ρ^0 angle $\phi_{\pi\pi}$, is given in terms of spin density-matrix elements (SDMEs) for vector-meson production in section 2.9. Each SDME is associated with specific polarization states of the produced ρ^0 meson and the exchanged virtual photon. For this reason the SDMEs can be used to verify how well the assumption of s-channel helicity conservation (SCHC) holds, which implies that the helicity of the virtual photon is taken over by the produced ρ^0 meson. Two SDME formalisms are presented, the Wolf-Schilling formalism [14] for an unpolarized target, and the Diehl formalism [11] for a polarized target. Within the latter formalism the $\rho_L - \rho_T$ separated transverse target-spin asymmetries are expressed in terms of SDMEs.

Available GPD-model calculations of the transverse target-spin asymmetry are discussed in section 2.10. These calculations apply to the $\sin(\phi - \phi_S)$ component of the asymmetry, provided that both the virtual photon and the ρ^0 meson are longitudinally polarized. Under the assumption of SCHC these calculations can be compared with the obtained $\sin(\phi - \phi_S)$ component of the asymmetry for longitudinally polarized ρ^0 mesons. Some of these calculations have been performed for the kinematic range accessible by the HERMES experiment. These calculations are presented for varying values of the total angular momentum of up-quarks inside the nucleon. In comparison with the experimentally extracted values these calculations can be used to constrain the total angular momentum of quarks in the proton. Since the quark-spin contribution to the nucleon spin is already measured by various experiments, such a comparison can also be used to constrain the orbital angular momentum of quarks inside the nucleon.

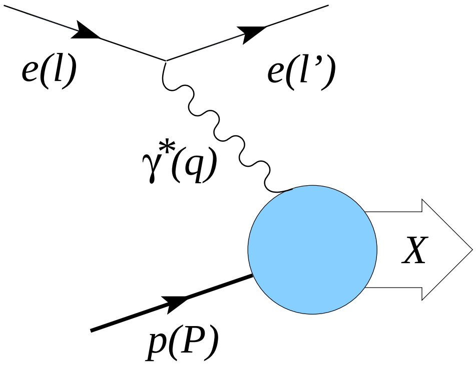

Figure 2.1: Leading-order Feynman diagram of the deep-inelastic scattering process. The energy-momentum four-vectors of the involved particles are specified between the brackets.

2.1 Deep-inelastic scattering

The inclusive DIS process $e\,p \rightarrow e\,X$ under the assumption of one-photon exchange is depicted in figure 2.1. Here, the energy-momentum four-vectors of the incoming lepton and nucleon, the scattered lepton, and the exchanged virtual photon are given by

- incoming lepton: $l = (E, \boldsymbol{l})$
- incoming nucleon: $P = (E_p, \boldsymbol{P})$
- scattered lepton: $l' = (E', \boldsymbol{l'})$.
- exchanged virtual photon: $q = (E_\gamma, \boldsymbol{q}) = l - l'$

The corresponding cross section can be expressed as the contraction

$$d\sigma \propto L^{\nu\mu}\, W^{DIS}_{\mu\nu}\, \frac{d^3 l'}{2E'}, \tag{2.1}$$

of a leptonic tensor $L^{\mu\nu}$ with a hadronic tensor $W^{DIS}_{\mu\nu}$. The leptonic tensor can be calculated within QED

$$L^{\nu\mu} = l'^{\nu} l^{\mu} + l^{\nu} l'^{\mu} - (l' \cdot l - m_e^2)\, g^{\nu\mu} + i m_e\, \epsilon^{\nu\mu\alpha\beta} q_\alpha s_\beta, \tag{2.2}$$

where m_e is the electron mass and s is the lepton-spin four-vector. Furthermore $g^{\nu\mu}$ is the metric tensor and the convention $\epsilon_{0123} = 1$ has been used. The leptonic tensor describes the transition of the lepton from the initial to the final state under the emission of a virtual photon. The hadronic tensor describes the absorption of the exchanged virtual photon by the nucleon and the transition of the nucleon to the final hadronic state X. The calculation of $W_{\mu\nu}^{DIS}$ for an incoming nucleon with mass M and spin S yields:

$$\begin{aligned} W_{\mu\nu}^{DIS}(q,P,S) &= \frac{1}{4\pi M}\sum_N \int \prod_{n=1}^{N} \frac{d^3 P'_n}{(2\pi)^3 2P'^0_n} \\ &\times (2\pi)^4\,\delta^4\left(P+q-\sum_n p'_n\right) H_{\mu\nu}(P,S,P_X), \end{aligned} \tag{2.3}$$

with

$$H_{\mu\nu}(P,S,P_X) = \langle P,S\,|J_\mu(0)|X\rangle\,\langle X|J_\nu(0)|\,P,S\rangle, \tag{2.4}$$

where J_μ represents the electromagnetic proton transition-current four-vector. Evaluation of equation 2.3 requires the integration over the phase space of all final hadronic states in X with total momentum P_X. The number N of final states in X varies, which is accounted for in the expression as it represents a sum over all possible values of N.

It is not possible to calculate the transition amplitudes in equation 2.4 from first principles, because this requires detailed knowledge about the nucleon structure and about the interactions taking place. However, it is possible to obtain a general parameterization of the hadronic tensor. As a result of the symmetry properties parity, time reversal and translation invariance, current conservation, and hermiticity, the number of terms in the parameterization is restricted. The resulting parameterization is given by

$$W_{\mu\nu}^{DIS} = W_{\mu\nu}^{DIS\,(U)} + W_{\mu\nu}^{DIS\,(A)}, \tag{2.5}$$

where $W_{\mu\nu}^{DIS\,(U)}$ parameterizes the symmetric part of the hadronic tensor, which is independent from the nucleon spin S:

$$\begin{aligned} W_{\mu\nu}^{DIS\,(U)}(q,P) &= \left(-g_{\mu\nu} - \frac{q_\mu q_\nu}{Q^2}\right) F_1 \\ &+ \left(P_\mu + \frac{P\cdot q}{Q^2}q_\mu\right)\left(P_\nu + \frac{P\cdot q}{Q^2}q_\nu\right)\frac{F_2}{P\cdot q} \end{aligned}$$

and $W_{\mu\nu}^{DIS\,(A)}$ parameterizes the asymmetric part associated with the nucleon spin:

$$W_{\mu\nu}^{DIS\,(A)}(q,P,S) = -i\epsilon_{\mu\nu\lambda\sigma}\frac{q^\lambda}{P\cdot q}\left[S^\sigma g_1 + \left(S^\sigma - \frac{S\cdot q}{P\cdot q}P^\sigma\right)g_2\right]. \tag{2.6}$$

The quantities F_1, F_2, g_1, g_2 are referred to as structure functions. The structure functions F_1 and F_2 should not be confused with the form factors for elastic scattering, which are often represented by the same notation.

For the description of the structure functions the relevant kinematic variables are the virtuality $Q^2 = -q^2$ of the exchanged photon and the Bjorken variable x, which is given by $x = Q^2/2P \cdot q$. The (x, Q^2)-dependencies of F_1 and F_2 have been determined by several fixed-target and collider experiments [15]. A striking property of the determined values of F_2 is that they depend mainly on the variable x and only relatively weakly on Q^2. This behavior of F_2 resembles the expectation for scattering from a point-like charged particle, which predicts that F_2 depends only on Bjorken x and not on Q^2. This property is called scaling. The observation of scaling has led to the development of the parton model, which was introduced by R. Feynman. Although scaling holds relatively well for intermediate values of x $(0.02 \lesssim x \lesssim 0.4)$, violations of scaling are observed mostly for relatively low values of x. The explanation for the observed scaling violations is that there are interactions between gluons and quarks leading to a logarithmic dependence of the structure functions on Q^2.

2.2 Parton distribution functions

Within the parton model the DIS structure functions introduced in the previous section can be expressed in terms of quark-distribution functions q_f and quark helicity distribution functions Δq_f by

$$\begin{aligned} F_1(x) &= \frac{1}{2}\sum_f e_f^2 q_f(x), && (2.7) \\ F_2(x) &= \sum_f e_f^2 x q_f(x), && (2.8) \\ g_1(x) &= \frac{1}{2}\sum_f e_f^2 \Delta q_f(x), && (2.9) \\ g_2(x) &= 0, && (2.10) \end{aligned}$$

where e_f represents the fractional electric charge for quarks of flavor f. The distribution functions are given by

$$q_f(x) = q_f^+(x) + q_f^-(x) \quad \text{and} \quad \Delta q_f(x) = q_f^+(x) - q_f^-(x), \tag{2.11}$$

where $q_f^{+(-)}$ represent the distribution functions describing the probability of finding a quark in the nucleon with its spin parallel (q_f^+) or anti-parallel (q_f^-) to the longitudinal spin of the nucleon. In the frame where the nucleon momentum approaches infinity (infinite-momentum frame), the variable x describes the momentum fraction of the interacting quark relative to the nucleon momentum. The experimental verification at high Q^2 of the relation between equations 2.7 and 2.8

$$2xF_1(x) = F_2(x), \tag{2.12}$$

which is known as the Callan-Gross relation, confirmed the assumption that quarks are spin-1/2 particles.

In the parton-model description of DIS quarks are moving independently from each other. In reality this is only true in the limit $Q^2 \rightarrow \infty$, a property known as asymptotic freedom. In contrast, at low Q^2 quarks occur only in bound states, a property referred to as confinement. From this observation it is concluded that quarks interact very strongly with each other, in particular at low Q^2, i.e. at large distance scales. The force responsible for both asymptotic freedom and confinement is called the strong force. The theory describing the corresponding interactions is called quantum chromodynamics (QCD). Within QCD the strong interaction is described as the coupling between color charges carried by quarks. The color coupling is mediated by the gluons. In total three different kinds of color charges are needed to describe the strong force. Gluons carry a color charge themselves as well. In contrast, the mediating particles of the electromagnetic force, photons, do not carry any electric charge. The fact that gluons carry color charges affects the dynamics of QCD such that it results in an increase of the color-coupling constant α_s, describing the strength of the interaction between partons, when the distance between these partons increases. Similarly, the value of α_s decreases for increasing values of Q^2, which accounts for the property of asymptotic freedom.

If Q^2 is relatively large, so that α_s is small, perturbative techniques can be used to perform QCD calculations. In this regime the interaction amplitude for several processes can be divided into two parts. The first part can be described by perturbative QCD and is referred to as the hard part, and the second part for which perturbative techniques cannot be used, is called the soft part. In perturbative QCD strong interactions are treated as perturbations of freely moving partons, and the corresponding interaction amplitudes are expanded in terms of α_s.

One can determine the importance of the various contributions to the DIS process in the limit of $Q^2 \rightarrow \infty$ by expanding the hadronic tensor in terms of $1/Q$. The order of the terms in this expansion is specified by the quantity twist. According to [16], terms with a $(1/Q)^{\tau-2}$ dependence are referred to as twist-τ terms. Leading twist is thus equal to twist-two.

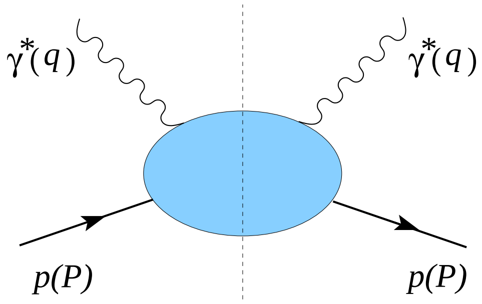

Figure 2.2: Diagram representing the hadronic tensor. The dashed line indicates that the square is taken of the corresponding amplitudes.

In order to go beyond the parton-model description represented by equations 2.7-2.10 it is convenient to ignore the leptonic part of the cross section and to focus on the virtual photon absorption cross section of the nucleon, which can be expressed in terms of the hadronic tensor $W_{\mu\nu}^{DIS}$ as

$$\sigma^{\gamma^* p \to X} = \frac{4\pi^2\alpha}{K} \epsilon^{\mu *} W_{\mu\nu}^{DIS} \epsilon^{\nu}, \tag{2.13}$$

where K is the virtual-photon flux factor [1] and ϵ^{ν} is the virtual-photon polarization vector. As can be seen from figure 2.2, the corresponding diagram is similar to the diagram representing the forward Compton scattering amplitude $T_{\mu\nu}$, describing the absorption and emission of a virtual photon by the nucleon, where "forward" refers to the property that the initial and the final states are equal. In fact, the optical theorem gives a relation between $W_{\mu\nu}$ and $T_{\mu\nu}$,

$$W_{\mu\nu} = \frac{1}{2\pi} \mathrm{Im} T_{\mu\nu}, \tag{2.14}$$

from which it follows that one can obtain a description of the hadronic tensor by applying perturbative QCD techniques to the forward Compton scattering amplitude. The resulting amplitude, at leading order in α_s is shown in figure 2.3.

The soft part of the interaction, represented by the blob in figure 2.3, is described by the quark-quark correlation function, also called the quark density matrix

$$\Phi_{ij}(k, P, S) = \int \frac{d^4 z}{(2\pi)^4} \, e^{ik\cdot z} \, \langle P, S | \, \bar{\psi}_j(-\frac{z}{2}) \, \psi_i(\frac{z}{2}) \, | P, S \rangle, \tag{2.15}$$

where i, j are the Dirac indices, $\psi_{i(j)}$ is the quark field, and k is the quark momentum. In high-energy processes, only the quark-momentum component collinear to the nucleon momentum, i.e., the light-cone component[1] $k^+ = xP^+$, is important, where x represents the momentum fraction of the quark relative to the nucleon momentum[2]. In this case, the quark-quark correlation function involves quark fields at different space-time points in the direction conjugate to P^+. Although perturbative techniques cannot be used to calculate the quark-quark correlation function, it can be parameterized by making use of its symmetry properties. This parameterization is usually done in terms of parton distribution functions [17].

At leading twist there are three parton distribution functions for each quark flavor, two of which are equal to the quark distribution function $q_f(x)$ and the quark helicity distribution function $\Delta q_f(x)$. The other leading twist parton distribution function is the transversity distribution function $\delta q_f(x)$, which describes the probability of finding a transversely polarized quarks in a transversely polarized nucleon. The transversity distribution function cannot be measured in inclusive DIS, but it is possible to measure $\delta q_f(x)$ in semi-inclusive DIS [18, 19].

---

[1] The light-cone components of a four-vector a are defined as $a^{\pm} = (a^0 \pm a^3)/\sqrt{2}$. The scalar product of two four-vectors, a and b, is then given by $a \cdot b = a^+ b^- + a^- b^+ - a^1 b^1 - a^2 b^2$.

[2] As was mentioned earlier in this section, in DIS the quark-momentum fraction is identified with the Bjorken variable $x = Q^2/2P \cdot q$.

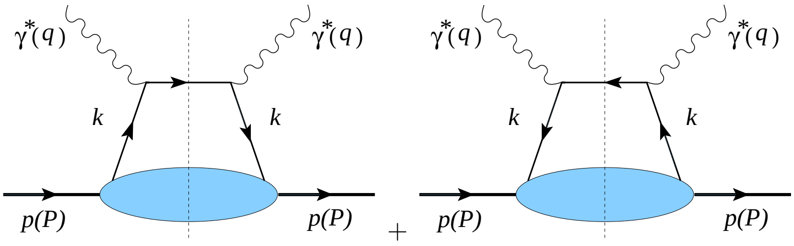

Figure 2.3: Leading order diagrams of the hadronic tensor in perturbative QCD. The blob represents the quark-quark correlation function, also called the quark density matrix, which represents the soft part of the interaction. The quark-quark correlation function is parameterized by parton distribution functions.

2.3 Generalized parton distributions

The formalism of generalized parton distributions (GPDs) is used in the description of exclusive processes in the Bjorken limit, where the exchanged photon has a high energy and a large virtuality Q^2 at a fixed value of Bjorken x. A GPD description can be given for a wide range of exclusive processes, such as deeply virtual Compton scattering (DVCS: $e\,p\, \rightarrow\, e\,p\,\gamma$) and hard exclusive meson production ($e\,p\, \rightarrow\, e\,p\,M$, with $M = \pi,\, \rho,\, \omega, \ldots$). The amplitude for such exclusive processes is depicted in figure 2.4. Within the GPD descriptions the amplitudes of these processes are factorized, i.e., separated into perturbative and non-perturbative parts. At leading order the factorized amplitude for DVCS is represented by the so-called 'handbag' diagram as represented in the left-hand side of figure 2.5.

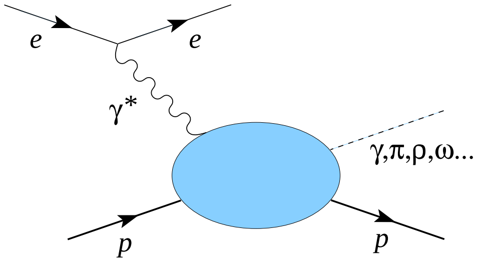

Figure 2.4: Diagram representing the amplitude for exclusive electroproduction of a meson or a real photon. The produced meson or photon is represented by the dashed line.

In [12] it was proven that a QCD factorization theorem applies to hard exclusive electroproduction of mesons in case the virtual photon that induces the process is longitudinally polarized. The factorization theorem expresses the corresponding amplitude in terms of a hard-scattering function, which can be calculated in perturbative QCD, and two soft parts, representing the wave function of the meson and a density matrix for partons in the nucleon. The factorized amplitude is represented by the diagram displayed in the right-hand side of figure 2.5. The hard-scattering function describes the interaction of the virtual photon with a quark, which leads to the formation of a quark pair changing into a meson. The last step of this process is described by the wave function of the meson.

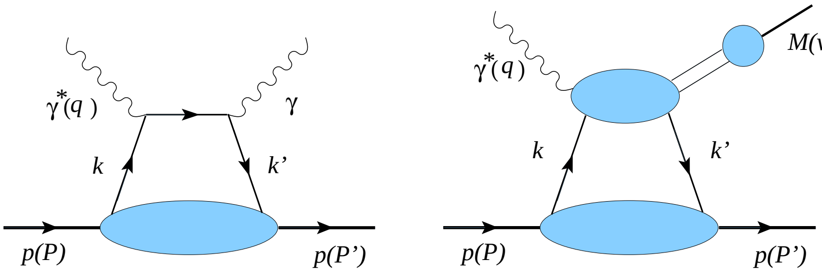

Figure 2.5: Feynman diagrams representing the leading order DVCS amplitude (left) and the factorized amplitude of exclusive meson production (right).

The lower soft part in the diagram of the factorized amplitude represents the density matrix (see figure 2.6)

$$\Phi'_{ij}(k,P,\Delta) = \int \frac{d^4z}{(2\pi)^4} e^{i\bar{k}\cdot z} \, \langle P',S'|\, \bar{\psi}_j(-\frac{z}{2})\, \psi_i(\frac{z}{2})\, |P,S\rangle, \tag{2.16}$$

where $\bar{k} = (k'+k)/2$ and $\Delta = P' - P = k' - k$ (see figure 2.5 for a specification of the energy-momentum four-vectors k, k', P and P'). The density matrix also represents the non-perturbative part of the leading-order amplitude of the DVCS process. It describes how a parton, represented by the field ψ, is taken from the nucleon in the initial state with a momentum k and put back with a momentum k' to form the nucleon in the final state. This density matrix is a generalization of the density matrix of equation 2.15. Because it appears in the description on the amplitude level, it corresponds to the non-forward case, where the nucleon in the final state has in general a different momentum and spin compared to the initial state. In contrast, the forward density matrix of equation 2.15 appears on the cross section level in the description of DIS.

The non-forward density matrix given by equation 2.16 can be parameterized in terms of generalized parton distributions (GPDs). At leading twist level there are for each quark flavor f four quark chirality conserving GPDs: H^f, E^f, $\tilde{H}^f$ and $\tilde{E}^f$ [10]. Whereas the GPDs H^f and $\tilde{H}^f$ are associated with conservation of the nucleon helicity, the GPDs E^f and $\tilde{E}^f$ are associated with a helicity flip of the

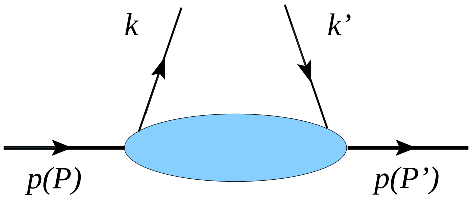

Figure 2.6: Diagram of the non-forward quark density matrix, which is parameterized at leading twist by the generalized parton distributions H^f, E^f, $\tilde{H}^f$ and $\tilde{E}^f$.

nucleon. The GPDs depend on the variables $\bar{x}, \xi$ and t. Here the variable $t = \Delta^2$ is the squared four-momentum transfer to the nucleon. The average longitudinal momentum fraction $\bar{x}$ is given by $\bar{k}^+ = \bar{x}\bar{P}^+$, where $\bar{k}^+$ and $\bar{P}^+$ are the longitudinal light-cone components of, respectively, $\bar{k}$ and $\bar{P} = (P' + P)/2$. The skewedness parameter ξ, given by $\Delta^+ = -2\xi\bar{P}^+$, represents the fractional momentum transfer to the active quark[3]. It follows from these definitions that the momenta of the active quarks are given by $k^+ = (\bar{x}+\xi)\bar{P}^+$ and $k^{+\prime} = (\bar{x}-\xi)\bar{P}^+$, with $\bar{x}$ running from -1 to +1. In case the momentum fraction $\bar{x} \pm \xi$ is positive, it corresponds to quarks and in case the momentum fraction is negative it corresponds to antiquarks.

GPDs are generalizations of the usual parton distribution functions introduced in the description of the DIS cross section and the form factors of elastic scattering. In the forward limit $\Delta \to 0$ with $\bar{x} > 0$ the GPDs H and $\tilde{H}$ are equal to the quark density distribution q and the quark helicity distribution Δq:

$$H^f(\bar{x}, 0, 0) = q_f(\bar{x}), \qquad \tilde{H^f}(\bar{x}, 0, 0) = \Delta q_f(\bar{x}). \tag{2.17}$$

In case $\bar{x} < 0$ one obtains the anti-quark distributions:

$$H^f(\bar{x}, 0, 0) = -\bar{q_f}(-\bar{x}), \qquad \tilde{H^f}(\bar{x}, 0, 0) = \Delta\bar{q_f}(-\bar{x}). \tag{2.18}$$

The GPDs E and $\tilde{E}$ do not contribute to the amplitudes of exclusive processes in the forward limit, which implies that these GPDs cannot be measured in DIS. The elastic form factors for quarks with flavor f in the nucleon are obtained by

---

[3] In the Bjorken limit the variable ξ is related to Bjorken x by $\xi \to x/(2-x)$.

integrating the GPDs over the variable $\bar{x}$:

$$\begin{aligned}\int_{-1}^{+1} d\bar{x}\, H^f(\bar{x},\xi,t) &= F_1^f(t),\\ \int_{-1}^{+1} d\bar{x}\, E^f(\bar{x},\xi,t) &= F_2^f(t),\\ \int_{-1}^{+1} d\bar{x}\, \tilde{H}^f(\bar{x},\xi,t) &= g_A^f(t),\\ \int_{-1}^{+1} d\bar{x}\, \tilde{E}^f(\bar{x},\xi,t) &= h_A^f(t).\end{aligned} \tag{2.19}$$

Here F_1 and F_2 are the Dirac and Pauli form factors, and g_A and h_A are the axial form factor and the pseudoscalar form factor, respectively.

GPDs provide new information about nucleon structure, for instance about the contribution J^f of the total angular momentum of quarks to the nucleon spin. It has been shown in [9] that J^f is related to the second moment of the sum of the GPDs H^f and E^f:

$$J^f = \frac{1}{2}\lim_{t\to 0}\int_{-1}^{1} \bar{x}\left(H^f(\bar{x},\xi,t) + E^f(\bar{x},\xi,t)\right) d\bar{x}. \tag{2.20}$$

Because the contribution of the longitudinal quark spin to the longitudinal nucleon spin has been measured through polarized semi-inclusive DIS by several experiments (see e.g. [7]), measurements of J^f would provide a way to determine the unknown contribution of the orbital angular momentum of quarks to the nucleon spin.

The description of exclusive meson production in terms of GPDs only applies if both the exchanged virtual photon and the produced meson are longitudinally polarized. It has been shown that only in that case transitions are allowed at leading twist, whereas all other transitions are suppressed by at least one power of $1/Q$ [13].

The sensitivity of exclusive meson production to GPDs is determined by the quantum numbers of the produced meson. In case of vector-meson production the process is only sensitive to the GPDs H and E. Note that the observables that can be measured for this process, such as cross sections or asymmetries, can be expressed in terms of convolutions of GPDs over the variable $\bar{x}$. A description of the transverse target-spin asymmetry in exclusive ρ^0 production in terms of convolutions of the GPDs H and E is given in section 2.10.

2.4 Exclusive electroproduction of ρ^0 mesons

In the process of exclusive ρ^0 electroproduction the scattering of a lepton e on a nucleon p is followed by the production of a ρ^0 meson

$$e(l) + p(p) \rightarrow e(l') + p(p') + \rho^0(v). \tag{2.21}$$

A characteristic property of this process is that the nucleon remains intact. The produced ρ^0 meson decays into a pair of pions with opposite charges

$$\rho^0(v) \rightarrow \pi^+(k_\pi) + \pi^-(k'_\pi). \tag{2.22}$$

The energy-momentum four-vectors of the various particles involved in the production and the decay processes are denoted by (see figure 2.7)

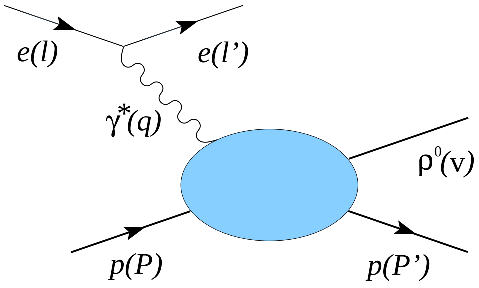

Figure 2.7: Diagram representing exclusive electroproduction of ρ^0 mesons.

- incoming lepton: $l = (E, \boldsymbol{l})$
- incoming nucleon: $P = (E_p, \boldsymbol{P})$
- scattered lepton: $l' = (E', \boldsymbol{l'})$
- recoiling nucleon: $P' = (E'_p, \boldsymbol{P'})$
- produced ρ^0 meson: $v = (E_V, \boldsymbol{v})$
- exchanged virtual photon: $q = (E_\gamma, \boldsymbol{q}) = l - l'$
- decay pion π^+: $k = (E_{\pi^+}, \boldsymbol{k}_\pi)$
- decay pion π^-: $k' = (E'_\pi, \boldsymbol{k}'_\pi)$.

Similarly to equation 2.1, the differential cross section for exclusive ρ^0 production can be expressed in terms of a hadronic and a leptonic tensor

$$d\sigma^{ep \rightarrow ep\rho^0} \propto L^{\nu\mu} W_{\mu\nu} \frac{d^3 l'}{2E'} \frac{d^3 v}{2E_V}. \tag{2.23}$$

The leptonic tensor $L^{\nu\mu}$ is given by equation 2.2. The hadronic tensor $W_{\mu\nu}$ describes the subprocess $\gamma^* p \rightarrow p\rho^0$ of the absorption of a virtual photon by the nucleon and the production of the ρ^0 meson. The definitions and descriptions of the relevant kinematic variables are listed in table 2.1.

2.4.1 Azimuthal angles ϕ and ϕ_S

The direction of the produced ρ^0 meson (see figure 2.8) is specified by the azimuthal angle ϕ, which is defined according to the Trento convention [20] as the angle of the hadron production plane with respect to the lepton scattering plane in the

Variable	Description
$Q^2 \equiv -q^2 \overset{lab}{\approx} 4EE' \sin^2 \frac{\theta}{2}$	γ^* virtuality
$\nu \equiv P \cdot q/M \overset{lab}{=} E - E'$	γ^* energy in the laboratory frame
$x \equiv Q^2/(2P \cdot q) = Q^2/2M\nu$	Bjorken variable x
$y \equiv (P \cdot q)/(P \cdot l) \overset{lab}{=} \nu/E$	Bjorken variable y
$W^2 \equiv (q+P)^2 = M^2 + 2M\nu - Q^2$	center-of-mass energy squared of the $\gamma^* p$ system
$t \equiv (q-v)^2 = (P-P')^2$	four-momentum transfer from γ^* to ρ^0 squared
$t_0 \overset{CM}{=} (E_\gamma - E_V)^2 - (\lvert\boldsymbol{q}\rvert - \lvert\boldsymbol{v}\rvert)^2$	maximal value of t kinematically allowed at given Q^2 and x
$t' = t - t_0$	measure of the transverse momentum transfer
$\varepsilon \equiv \frac{1-y-\frac{1}{4}y^2Q^2/\nu^2}{1-y+\frac{1}{2}y^2+\frac{1}{4}y^2Q^2/\nu^2} \overset{lab}{=} \left(1 + 2(1+\frac{\nu^2}{Q^2}) \tan^2 \frac{\theta}{2}\right)^{-1}$	γ^* polarization parameter
$M_{\pi\pi} \equiv \sqrt{(k_\pi + k'_\pi)^2}$	invariant mass of the $\pi^+\pi^-$ system
$\Delta E \equiv (M_X^2 - M^2)/2M \overset{lab}{=} \nu - E_V + \frac{t}{2M}$	missing energy, exclusivity of the process (see section 4.2)

Table 2.1: The definitions and descriptions of the relevant kinematic variables characterizing exclusive ρ^0 production. Included are the expressions that can be used in the HERMES laboratory (*lab*) frame, where θ is the angle between the incoming and the scattered lepton and M is the nucleon rest mass. The expression for t_0 applies in the $\gamma^* p$ center of mass frame (CM).

center-of-mass frame of the $\gamma^* p$ system

$$\begin{aligned}\cos\phi &= \frac{(\hat{\boldsymbol{q}}\times\boldsymbol{l})}{|\hat{\boldsymbol{q}}\times\boldsymbol{l}|}\cdot\frac{(\hat{\boldsymbol{q}}\times\boldsymbol{v})}{|\hat{\boldsymbol{q}}\times\boldsymbol{v}|},\\ \sin\phi &= \frac{(\boldsymbol{l}\times\boldsymbol{v})\cdot\hat{\boldsymbol{q}}}{|\hat{\boldsymbol{q}}\times\boldsymbol{l}||\hat{\boldsymbol{q}}\times\boldsymbol{v}|},\end{aligned}\tag{2.24}$$

with $\hat{\boldsymbol{q}} = \boldsymbol{q}/|\boldsymbol{q}|$. This is illustrated in figure 2.8.

For a polarized nucleon the corresponding polarization vector $\boldsymbol{S}$ can be decomposed into a transverse component $\boldsymbol{S_T}$ and a longitudinal component $\boldsymbol{S_L}$ relative to the virtual-photon direction. The azimuthal angle of $\boldsymbol{S_T}$ with respect to the lepton scattering plane is represented by ϕ_S (see figure 2.8). One can obtain the definition of ϕ_S from equation 2.24 by replacing $\boldsymbol{v}$ with $\boldsymbol{S}$ [20].

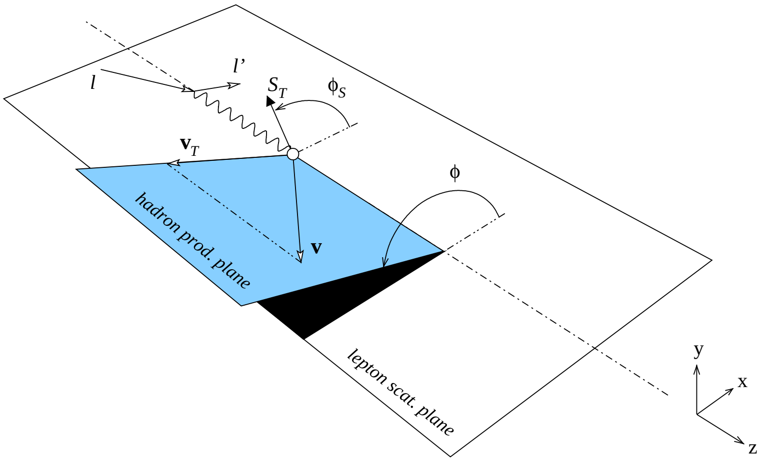

Figure 2.8: The azimuthal angles ϕ and ϕ_S of, respectively, the hadron production plane and the transverse component $\boldsymbol{S_T}$ of the target spin, with respect to the lepton scattering plane [20].

Alternatively, the polarization vector $\boldsymbol{S}$ can be decomposed into components $\boldsymbol{P_T}$ and $\boldsymbol{P_L}$, transverse and parallel to the lepton-beam direction. These components are related to the transverse and longitudinal components $\boldsymbol{S_T}$ and $\boldsymbol{S_L}$ relative to the virtual-photon direction by

$$\begin{aligned}S_T\cos\phi_S &= \cos\theta_\gamma\, P_T\cos\psi - \sin\theta_\gamma\, P_L,\\ S_T\sin\phi_S &= P_T\sin\psi,\\ S_L &= \sin\theta_\gamma\, P_T\cos\psi + \cos\theta_\gamma\, P_L,\end{aligned}\tag{2.25}$$

where θ_γ is the angle between the vectors $\boldsymbol{q}$ and $\boldsymbol{l}$ and ψ is the azimuthal angle of $\boldsymbol{P_T}$ around the lepton-beam direction [13]. In case $P_L = 0$ and thus $\boldsymbol{S} = \boldsymbol{P_T}$, the relation becomes

$$\begin{aligned} S_T(\theta_\gamma,\phi_S) &= \frac{\cos\theta_\gamma}{\sqrt{1-\sin^2\!\theta_\gamma\,\sin^2\!\phi_S}}\,P_T, \\ S_L(\theta_\gamma,\phi_S) &= \frac{\sin\theta_\gamma\,\cos\phi_S}{\sqrt{1-\sin^2\!\theta_\gamma\,\sin^2\!\phi_S}}\,P_T. \end{aligned} \tag{2.26}$$

2.4.2 The ρ^0 decay angles

The decay of the ρ^0 meson, which is illustrated in figure 2.9, is specified by the angles $\theta_{\pi\pi}$ and $\phi_{\pi\pi}$, which represent the polar and the azimuthal angle, respectively, of the π^+ momentum in the $\pi^+\pi^-$ center-of-mass frame (i.e. the ρ^0 rest frame). In this frame the decay angles can be expressed with respect to the rectangular coordinate system $(\boldsymbol{x}_{\pi\pi},\boldsymbol{y}_{\pi\pi},\boldsymbol{z}_{\pi\pi})$ with [14, 21]

$$\boldsymbol{z}_{\pi\pi} = -\frac{\boldsymbol{p'}}{|\boldsymbol{p'}|}, \qquad \boldsymbol{y}_{\pi\pi} = \frac{\hat{\boldsymbol{q}}\times\boldsymbol{z}_{\pi\pi}}{|\hat{\boldsymbol{q}}\times\boldsymbol{z}_{\pi\pi}|}, \qquad \boldsymbol{x}_{\pi\pi} = \boldsymbol{y}_{\pi\pi}\times\boldsymbol{z}_{\pi\pi}, \tag{2.27}$$

where $\boldsymbol{z}_{\pi\pi}$ is the unit vector opposite to the momentum of the recoiling target nucleon in the ρ^0 rest frame, $\boldsymbol{y}_{\pi\pi}$ is the unit vector normal to the hadron production plane and the unit vector $\boldsymbol{x}_{\pi\pi}$ lies in the hadron production plane. The expressions for $\theta_{\pi\pi}$ and $\phi_{\pi\pi}$ are then given by

$$\begin{aligned} \cos\theta_{\pi\pi} &= \frac{\boldsymbol{k_\pi}\cdot\boldsymbol{z}_{\pi\pi}}{|\boldsymbol{k_\pi}|}, \\ \cos\phi_{\pi\pi} &= \frac{\boldsymbol{y}_{\pi\pi}\cdot(\boldsymbol{z}_{\pi\pi}\times\boldsymbol{k_\pi})}{|\boldsymbol{z}_{\pi\pi}\times\boldsymbol{k_\pi}|}, \\ \sin\phi_{\pi\pi} &= -\frac{\boldsymbol{x}_{\pi\pi}\cdot(\boldsymbol{z}_{\pi\pi}\times\boldsymbol{k_\pi})}{|\boldsymbol{z}_{\pi\pi}\times\boldsymbol{k_\pi}|}. \end{aligned} \tag{2.28}$$

2.4.3 The virtual-photon polarization

In order to describe exclusive ρ^0 production for a specific virtual-photon polarization, first the corresponding polarization vectors are introduced. Following [13] and [11] the polarization vectors for virtual photons are described in a right-handed coordinate system with the z-axis opposite to the virtual-photon direction, the x-axis in the ρ^0 production plane, such that the ρ^0 momentum has a positive x-component and the y-axis perpendicular to the hadron production plane. The polarization vector for virtual photons with zero (i.e. longitudinal) helicity is given by

$$\epsilon_0^\mu = \frac{1}{Q\sqrt{1+\gamma^2}}\Big(q^\mu + \frac{Q^2}{P\cdot q}\,P^\mu\Big), \tag{2.29}$$

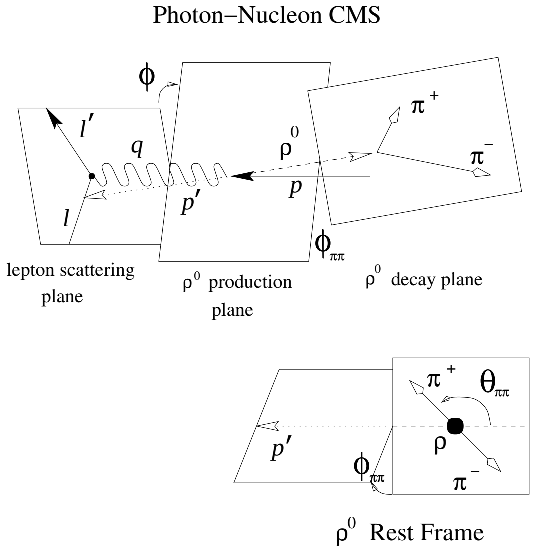

Figure 2.9: The ρ^0 decay angles illustrated for the γ^* center-of-mass frame (top) and the ρ^0 rest frame (bottom).

with $\gamma^2 = Q^2/\nu^2$. The polarization vectors ϵ_{+1} and ϵ_{-1} for virtual photons with positive and negative helicity are obtained as combinations of the polarization vectors $\epsilon_{\perp 1} = (0,1,0,0)$ and $\epsilon_{\perp 2} = (0,0,1,0)$ describing transversely polarized virtual photons

$$\epsilon_{+1} = -\tfrac{1}{\sqrt{2}}\left(\epsilon_{\perp 1} + i\epsilon_{\perp 2}\right) = \frac{1}{\sqrt{2}}(0,-1,i,0), \qquad (2.30)$$

$$\epsilon_{-1} = \tfrac{1}{\sqrt{2}}\left(\epsilon_{\perp 1} - i\epsilon_{\perp 2}\right) = \frac{1}{\sqrt{2}}(0,1,i,0). \qquad (2.31)$$

The polarization of the exchanged virtual photon is fully described by the leptonic tensor. In fact, the spin density matrix of the virtual photon can be obtained by expressing the leptonic tensor $L^{\nu\mu}$ in terms of combinations of $\epsilon_n^{\nu}\epsilon_m^{\mu *}$ [13].

2.5 The leptoproduction cross section

In [13] a general formalism is presented for the cross section of lepton scattering on a polarized proton. This formalism is referred to as the Diehl-Sapeta formalism. Within this formalism the polarizations of the virtual photon and the proton in the initial state are explicitly taken into account in the expression of the leptoproduction cross section in terms of so-called polarized photoabsorption cross sections and interference terms denoted by σ_{mn}^{ij}. The indices $i, j = \pm\frac{1}{2}$ specify the proton spin with respect to the axis pointing opposite to the virtual-photon direction in the target rest frame. Equivalently these indices specify the proton helicity in the $\gamma^* p$ center-of-mass frame. The indices $m, n = -1, 0, 1$ specify the helicities of the virtual photon. For the process of exclusive ρ^0 production these terms are directly related to the amplitudes T_{mi} for the process $\gamma^* p \rightarrow p\rho^0$ by

$$\frac{d\sigma_{mn}^{ij}}{dt} \propto \sum_{\text{spins}} (T_{mi})^* T_{nj}, \tag{2.32}$$

where $\sum_{\text{spins}}$ denotes the sum over all helicities that contribute to the final state $p\rho^0$, which are not specified any further in [13].

The relation of these terms with the hadronic tensor can be obtained from a contraction of σ_{mn}^{ij} with the spin density matrix τ_{ji} of the proton. Density matrices [22] are convenient quantities to describe processes involving many (spin) degrees of freedom. In appendix A (spin) density matrices are introduced and defined. From equation A.8 it follows that the relation between the density matrix τ_{ji}, and the proton polarization vector $\boldsymbol{S}$ and the polarization operator $\boldsymbol{\sigma}_{ji}$ is given by

$$\tau_{ji} = \frac{1}{2}\Big[\delta_{ji} + \boldsymbol{S} \cdot \boldsymbol{\sigma}_{ji}\Big] = \frac{1}{2}\begin{pmatrix} 1 + S_L & S_T e^{-i(\phi-\phi_S)} \\ S_T e^{i(\phi-\phi_S)} & 1 - S_L \end{pmatrix}. \tag{2.33}$$

By using the spin density matrix τ_{ji} one can obtain the following relation between the hadronic tensor $W_{\mu\nu}$ and σ_{mn}^{ij}

$$\epsilon_m^{\mu *}\, W_{\mu\nu}\, \epsilon_n^{\nu} \propto \sum_{ij} \tau_{ji} \frac{d\sigma_{mn}^{ij}}{dt} = \frac{d\sigma_{mn}}{dt}. \tag{2.34}$$

The contraction $L^{\nu\mu} W_{\mu\nu}$ in equation 2.23 is obtained from a contraction of σ_{mn} with the spin density matrix of the virtual photon. By using equation 2.34 and by expressing the leptonic tensor in terms of combinations of $\epsilon_n^{\nu}\epsilon_m^{\mu *}$ one can write the contraction $L^{\nu\mu} W_{\mu\nu}$ in terms of σ_{mn}^{ij}. The resulting expression for the leptoproduction cross section is then given by [13]

$$
\begin{aligned}
&\left[\frac{\alpha_{\mathrm{em}}}{8\pi^3}\,\frac{y^2}{1-\varepsilon}\,\frac{1-x}{x}\,\frac{1}{Q^2}\right]^{-1}\frac{d\sigma}{dx\,dQ^2\,d\phi\,d\psi} \\
&= \frac{1}{2}\Big(\sigma_{++}^{++}+\sigma_{++}^{--}\Big)+\varepsilon\sigma_{00}^{++} \\
&\quad -\varepsilon\cos(2\phi)\,\mathrm{Re}\,\sigma_{+-}^{++}-\sqrt{\varepsilon(1+\varepsilon)}\,\cos\phi\,\mathrm{Re}\,(\sigma_{+0}^{++}+\sigma_{+0}^{--}) \\
&\quad -P_\ell\sqrt{\varepsilon(1-\varepsilon)}\,\sin\phi\,\mathrm{Im}\,(\sigma_{+0}^{++}+\sigma_{+0}^{--}) \\
&\quad -S_L\left[\varepsilon\sin(2\phi)\,\mathrm{Im}\,\sigma_{+-}^{++}+\sqrt{\varepsilon(1+\varepsilon)}\,\sin\phi\,\mathrm{Im}\,(\sigma_{+0}^{++}-\sigma_{+0}^{--})\right] \\
&\quad +S_LP_\ell\left[\sqrt{1-\varepsilon^2}\,\frac{1}{2}\Big(\sigma_{++}^{++}-\sigma_{++}^{--}\Big)-\sqrt{\varepsilon(1-\varepsilon)}\,\cos\phi\,\mathrm{Re}\,(\sigma_{+0}^{++}-\sigma_{+0}^{--})\right] \\
&\quad -S_T\Bigg[\sin(\phi-\phi_S)\,\mathrm{Im}\,(\sigma_{++}^{+-}+\varepsilon\sigma_{00}^{+-})+\frac{\varepsilon}{2}\sin(\phi+\phi_S)\,\mathrm{Im}\,\sigma_{+-}^{+-} \\
&\qquad +\frac{\varepsilon}{2}\sin(3\phi-\phi_S)\,\mathrm{Im}\,\sigma_{+-}^{-+}+\sqrt{\varepsilon(1+\varepsilon)}\,\sin\phi_S\,\mathrm{Im}\,\sigma_{+0}^{+-} \\
&\qquad +\sqrt{\varepsilon(1+\varepsilon)}\,\sin(2\phi-\phi_S)\,\mathrm{Im}\,\sigma_{+0}^{-+}\Bigg] \\
&\quad +S_TP_\ell\Bigg[\sqrt{1-\varepsilon^2}\,\cos(\phi-\phi_S)\,\mathrm{Re}\,\sigma_{++}^{+-}-\sqrt{\varepsilon(1-\varepsilon)}\,\cos\phi_S\,\mathrm{Re}\,\sigma_{+0}^{+-} \\
&\qquad -\sqrt{\varepsilon(1-\varepsilon)}\,\cos(2\phi-\phi_S)\,\mathrm{Re}\,\sigma_{+0}^{-+}\Bigg]. \qquad (2.35)
\end{aligned}
$$

Here α_{em} is the electromagnetic coupling constant, P_ℓ is the longitudinal beam polarization, and S_L and S_T are the target polarizations parallel and transverse to the virtual-photon direction, respectively. The Hand convention is used for the virtual-photon flux factor and the virtual-photon polarization parameter ε is given in table 2.1. It is noted that equation 2.35 can be rewritten differential in t without changing its structure.

2.6 The angular distribution function

It is convenient to express the differential leptoproduction cross section, which is given in the Diehl-Sapeta formalism by equation 2.35, as the product

$$\frac{d\sigma}{d\psi\, d\phi\, dx\, dQ^2\, dt} = \frac{1}{(2\pi)^2}\, \frac{d\sigma}{dx\, dQ^2\, dt}\, W(x, Q^2, t, \phi, \phi_S) \tag{2.36}$$

with [11, 13]

$$\frac{d\sigma}{dx\, dQ^2\, dt} = \frac{\alpha_{\text{em}}}{2\pi}\, \frac{y^2}{1-\epsilon}\, \frac{1-x}{x}\, \frac{1}{Q^2} \left(\frac{d\sigma_T}{dt} + \epsilon\, \frac{d\sigma_L}{dt} \right), \tag{2.37}$$

where

$$\sigma_T = \frac{1}{2}\Big(\sigma_{++}^{++} + \sigma_{++}^{--}\Big) \qquad \text{and} \qquad \sigma_L = \sigma_{00}^{++} \tag{2.38}$$

represent the $\gamma^* p$ cross sections for an unpolarized proton, and a transversely and longitudinally polarized photon, respectively.

In equation 2.36 the (ϕ, ϕ_S) dependence is completely described by the angular distribution function[4] $W(x, Q^2, t, \phi, \phi_S)$. In the following the x, Q^2, t dependence of W will be suppressed. The normalization of the angular distribution function is given by

$$\int \frac{d\phi}{2\pi} \int \frac{d\phi_S}{2\pi}\, W(\phi, \phi_S) \;=\; 1. \tag{2.39}$$

The angular distribution function consists of several contributions corresponding to different polarization states of the incoming lepton and the target nucleon

$$\begin{aligned} W(\phi, \phi_S) \quad &= \quad W_{UU}(\phi) + P_\ell W_{LU}(\phi) + S_L W_{UL}(\phi) + P_\ell S_L W_{LL}(\phi) + \\ &\qquad S_T W_{UT}(\phi, \phi_S) + P_\ell S_T W_{LT}(\phi, \phi_S), \end{aligned} \tag{2.40}$$

where the left subscript specifies the beam polarization states: unpolarized (U) or longitudinally polarized (L), and the right subscript specifies the target polarization states: unpolarized (U), longitudinally polarized (L), or transversely polarized (T).

2.6.1 $\rho_L - \rho_T$ Separation

The angular distribution function given by equation 2.40 has been integrated over the ρ^0 decay angles. One can decompose the angular distribution function into parts for longitudinally and transversely polarized ρ^0 mesons (denoted by ρ_L and ρ_T, respectively) by using the fact that each ρ^0 polarization state results into a characteristic dependence on the decay angle $\theta_{\pi\pi}$ (see [13]). For the photoabsorption terms σ_{mn}^{ij} the $\theta_{\pi\pi}$ dependence is given by

---

[4] The angular distribution function is written in terms of the angle ϕ_S whereas it is more simple to express the phase space element, on the left-hand side of equation 2.36, in terms of the angle ψ [13].

$$
\begin{aligned}
&\frac{d\sigma^{ij}_{mn}(\gamma^* p \to \pi^+\pi^- p)}{d(\cos\theta_{\pi\pi})} \\
&= \frac{3\cos^2\theta_{\pi\pi}}{2}\,\sigma^{ij}_{mn}(\gamma^* p \to \rho_L\, p) \\
&+ \frac{3\sin^2\theta_{\pi\pi}}{4}\,\sigma^{ij}_{mn}(\gamma^* p \to \rho_T\, p). \qquad (2.41)
\end{aligned}
$$

One obtains the $\rho_L - \rho_T$ separated leptoproduction cross section by combining this equation with equation 2.35. One can include the $\theta_{\pi\pi}$ dependence of the cross section in the angular distribution function by decomposing each term of equation 2.40 as

$$
\begin{aligned}
W_{XY}(\phi_S, \phi, \theta_{\pi\pi}) = \frac{3}{2} \Big[& W^{LL}_{XY}(\phi_S, \phi)\cos^2\theta_{\pi\pi} + \\
& W^{TT}_{XY}(\phi_S, \phi)\sin^2\theta_{\pi\pi} \Big]. \qquad (2.42)
\end{aligned}
$$

The $\rho_L - \rho_T$ separated angular distributions are given by W^{LL}_{XY} and W^{TT}_{XY}, respectively. Here the subscripts X and Y specify the beam and target polarization states, respectively, as in equation 2.40. The superscripts LL specify purely longitudinal and the superscripts TT specify purely transverse ρ^0 polarization. It is noted that the angular distribution function in equation 2.42 effectively has been integrated over the decay angle $\phi_{\pi\pi}$. As a result, terms coming from the interference between different ρ^0 polarizations cancel.

2.7 Transverse target-spin asymmetry

In this section the transverse target-spin asymmetry is introduced in relation with the angular distribution function of the cross section, which is given for the general case by equation 2.40. For an unpolarized beam and a transversely polarized target the angular distribution is given by

$$W(\phi, \phi_S) = W_{UU}(\phi) + S_T W_{UT}(\phi, \phi_S). \qquad (2.43)$$

The transverse target-spin asymmetry $A_{UT}(\phi, \phi_S)$ is defined here in relation with the angular distributions W_{UT} and W_{UU} as

$$A_{UT}(\phi, \phi_S) = \frac{W_{UT}(\phi, \phi_S)}{\widehat{W}_{UU}}, \qquad (2.44)$$

where $\widehat{W}_{UU}$ is $W_{UU}(\phi)$ averaged over the angle ϕ. The ϕ dependence of W_{UU} can be expressed in terms of the unpolarized azimuthal asymmetry $A_{UU}(\phi)$ as

$$W_{UU}(\phi) = \widehat{W}_{UU}\left(1 + A_{UU}(\phi)\right). \qquad (2.45)$$

The angular distribution function is then given in terms of the asymmetries A_{UU} and A_{UT} by

$$W(\phi,\phi_S) = \widehat{W}_{UU}\left(1 + A_{UU}(\phi) + S_T A_{UT}(\phi,\phi_S)\right). \tag{2.46}$$

It is noted that the transverse target-spin asymmetry given by equation 2.44 is slightly redefined in comparison to the usual definition of the asymmetry given within the Trento convention [20] by

$$A_{UT}^{\text{Trento}}(\phi,\phi_S) = \frac{1}{S_T}\frac{d\sigma(\phi,\phi_S) - d\sigma(\phi,\phi_S+\pi)}{d\sigma(\phi,\phi_S) + d\sigma(\phi,\phi_S+\pi)}, \tag{2.47}$$

which can be expressed as

$$A_{UT}^{\text{Trento}}(\phi,\phi_S) = \frac{W_{UT}(\phi,\phi_S)}{W_{UU}(\phi)}, \tag{2.48}$$

as follows from the property $W_{UT}(\phi,\phi_S) = -W_{UT}(\phi,\phi_S+\pi)$. One can see in equation 2.48 that this asymmetry contains the ϕ dependence of the unpolarized cross section in its denominator. This dependence is caused by the interference between different photon polarizations. As GPD-model calculations of the asymmetry in general do not consider this dependence, it is preferred to use the definition of the asymmetry given by equation 2.44.

Azimuthal-moment expansion of asymmetries The azimuthal angular dependencies of the asymmetries A_{UU} and A_{UT} can be expanded into independent trigonometric functions of the angles ϕ and ϕ_S. It follows from equation 2.46 in combination with equations 2.35 and 2.36 that these expansions can be written as

$$\begin{aligned}
A_{UU}(\phi) &= A_{UU}^{\cos(\phi)}\cos(\phi) + A_{UU}^{\cos(2\phi)}\cos(2\phi), && (2.49)\\
A_{UT}(\phi,\phi_S) &= A_{UT}^{\sin(\phi-\phi_S)}\sin(\phi-\phi_S) + A_{UT}^{\sin(\phi+\phi_S)}\sin(\phi+\phi_S) + \\
&\quad A_{UT}^{\sin(3\phi-\phi_S)}\sin(3\phi-\phi_S) + A_{UT}^{\sin(\phi_S)}\sin(\phi_S) + \\
&\quad A_{UT}^{\sin(2\phi-\phi_S)}\sin(2\phi-\phi_S). && (2.50)
\end{aligned}$$

The coefficients appearing in these expansions are referred to as the azimuthal moments of the asymmetries [13, 20], as they are equal to

$$A_{UU}^{\omega(\phi)} = \frac{2\int d\phi\,\omega(\phi)\,[W(\phi) - W(\phi+\pi)]}{\int d\phi\,[W(\phi) + W(\phi+\pi)]}\Big|_{S_T=0,\,S_L=0}, \tag{2.51}$$

$$A_{UT}^{\omega(\phi,\phi_S)} = \frac{2\int d\phi\,d\phi_S\,\omega(\phi,\phi_S)\,[W(\phi,\phi_S) - W(\phi,\phi_S+\pi)]}{\int d\phi\,d\phi_S\,[W(\phi,\phi_S) + W(\phi,\phi_S+\pi)]}\Big|_{S_T=1,\,S_L=0}. \tag{2.52}$$

$\rho_L - \rho_T$ Separation of asymmetries The transverse target-spin asymmetries A_{UT,ρ_L} and A_{UT,ρ_T} for longitudinally and transversely polarized ρ^0 mesons, respectively, can be defined in relation to the $\rho_L - \rho_T$ separated parts of the angular distribution by (see equation 2.42)

$$A_{UT,\rho_L}(\phi,\phi_S) = \frac{W_{UT}^{LL}(\phi,\phi_S)}{\widehat{W}_{UU}^{LL}}, \qquad A_{UT,\rho_T}(\phi,\phi_S) = \frac{W_{UT}^{TT}(\phi,\phi_S)}{\widehat{W}_{UU}^{TT}}. \tag{2.53}$$

By using equation 2.42 one can express the angular distribution in terms of the $\rho_L - \rho_T$ separated asymmetries as

$$\begin{aligned} &W(\phi,\phi_S,\theta_{\pi\pi}) = \\ &\tfrac{3}{2}\big[\ \widehat{W}_{UU}^{LL}\cos^2\theta_{\pi\pi} \quad \big(1 + A_{UU,\rho_L}(\phi) + P_T A_{UT,\rho_L}(\phi,\phi_S)\big)\ + \\ &\quad\ \widehat{W}_{UU}^{TT}\sin^2\theta_{\pi\pi} \quad \big(1 + A_{UU,\rho_T}(\phi) + P_T A_{UT,\rho_T}(\phi,\phi_S)\big) \qquad \big]. \end{aligned} \tag{2.54}$$

As follows from this decomposition one can determine the $\rho_L - \rho_T$ separated asymmetries $A_{UT,\rho_L}(\phi,\phi_S)$ and $A_{UT,\rho_T}(\phi,\phi_S)$ by extracting the angular distribution for transverse target polarization as a function of $\theta_{\pi\pi}$. The averaged contributions $\widehat{W}_{UU}^{LL}$ and $\widehat{W}_{UU}^{TT}$, as well as the unpolarized asymmetries $A_{UU,\rho_L}(\phi)$ and $A_{UU,\rho_T}(\phi)$, can be determined from the spin density-matrix elements for ρ^0 production from an unpolarized target, which are discussed in section 2.9.

2.8 Transverse target polarization with respect to the beam direction

For an experimental setup the target polarization is defined with respect to the lepton-beam direction rather than to the virtual-photon direction. Due to the non-zero angle θ_γ between the directions of the incoming lepton and the virtual photon, a transverse target polarization P_T with respect to the lepton-beam direction comes along with a transverse, as well as a longitudinal component with respect to the virtual-photon direction (see section 2.4.1). Hence, the angular distribution function W^ℓ for the case of a transversely polarized target with respect to the lepton-beam direction can be written as

$$W^\ell(\theta_\gamma,\phi,\phi_S) = W_{UU}(\phi)\ +\ P_T\, W_{UT}^\ell(\theta_\gamma,\phi,\phi_S), \tag{2.55}$$

where the term W_{UT}^ℓ is the mixture of the terms W_{UT} and W_{UL} given by [13]

$$P_T\, W_{UT}^\ell(\theta_\gamma,\phi,\phi_S)\ =\ S_T(\theta_\gamma,\phi_S)\, W_{UT}(\phi,\phi_S)\ +\ S_L(\theta_\gamma,\phi_S)\, W_{UL}(\phi). \tag{2.56}$$

One obtains the explicit expression for W_{UT}^ℓ by inserting equation 2.26 into equation 2.56:

$$W_{UT}^\ell(\theta_\gamma,\phi,\phi_S) = \frac{\cos\theta_\gamma\, W_{UT}(\phi,\phi_S) + \sin\theta_\gamma\cos\phi_S\, W_{UL}(\phi)}{\sqrt{1-\sin^2\theta_\gamma\ \sin^2\phi_S}}. \tag{2.57}$$

The transverse target-spin asymmetry A^{ℓ}_{UT} with respect to the beam direction is now defined relative to W^{ℓ}_{UT} as

$$\begin{aligned} A^{\ell}_{UT}(\theta_\gamma,\phi,\phi_S) &= \frac{W^{\ell}_{UT}(\theta_\gamma,\phi,\phi_S)}{\widehat{W}_{UU}} \\ &= \frac{\cos\theta_\gamma\, A_{UT}(\phi,\phi_S)+\sin\theta_\gamma\,\cos\phi_S\, A_{UL}(\phi)}{\sqrt{1-\sin^2\theta_\gamma\,\sin^2\phi_S}}, \end{aligned} \tag{2.58}$$

where A_{UL} is the longitudinal target-spin asymmetry with respect to the virtual-photon direction. The angular distribution function W^{ℓ} in equation 2.55 can be expressed, analogous to equation 2.46, in terms of asymmetries as

$$W^{\ell}(\theta_\gamma,\phi,\phi_S) = \widehat{W}_{UU}\left(1+A_{UU}(\phi)+P_T A^{\ell}_{UT}(\theta_\gamma,\phi,\phi_S)\right). \tag{2.59}$$

It is noted that one can decompose equation 2.59 into ρ_L-ρ_T separated asymmetries analogous to equation 2.54 by using equation 2.42.

2.9 SDMEs for vector-meson production

The angular distribution function for exclusive ρ^0 production can be expressed in terms of spin density-matrix elements (SDMEs). Compared to the description given by equations 2.40 and 2.42, the description in terms of SDMEs is more complete, since it includes the $\phi_{\pi\pi}$ dependence (instead of integrating over it), which is caused by the interference of different ρ^0 polarization states. Moreover, the SDMEs give a description of the spin transfer from the virtual photon to the ρ^0 meson.

A general introduction of the spin density matrix formalism can be found in appendix A. The SDMEs for vector-meson production on an unpolarized target are given within the Wolf-Schilling formalism [14]. Several experiments, including HERMES, have already measured the SDMEs for an unpolarized target in this formalism (see e.g. [23, 24, 25, 26]). Recently, an SDME formalism was developed for vector-meson production on a polarized target [11], in which the angular distribution function is decomposed in separate terms for specific vector-meson polarization states by using

$$\begin{aligned} W_{XY}(\phi_S,\phi,\phi_{\pi\pi},\theta_{\pi\pi}) = \frac{3}{4\pi}\Big[\; & W^{LL}_{XY}(\phi_S,\phi)\cos^2\theta_{\pi\pi} + \\ & W^{LT}_{XY}(\phi_S,\phi,\phi_{\pi\pi})\sqrt{2}\cos\theta_{\pi\pi}\sin\theta_{\pi\pi} + \\ & W^{TT}_{XY}(\phi_S,\phi,\phi_{\pi\pi})\sin^2\theta_{\pi\pi}\;\Big]. \end{aligned} \tag{2.60}$$

Here, the superscript LT specifies the interference between transverse and longitudinal vector-meson polarization states, whereas the subscript XY labels the beam and target polarization as usual. The formalism of [11], which is referred to as the Diehl formalism, is a generalization of the Diehl-Sapeta [13] and the Wolf-Schilling

[14] formalisms, a key difference being the inclusion of the explicit dependence on $\phi_{\pi\pi}$ for a polarized target.

The Wolf-Schilling formalism is described briefly in section 2.9.1. In section 2.9.2 the Diehl formalism is introduced. Since the present analysis mainly uses this formalism, its structure is presented in more detail. Some of the existing HERMES results for the SDMEs for an unpolarized target are presented in section 2.9.3. The implications of these results for the validity of s-channel helicity conservation (SCHC), which implies that the helicity of the virtual photon is taken over by the ρ^0 meson, are discussed. Existing results for the ratio $R = \sigma_L/\sigma_T$ of the cross-sections for longitudinally polarized over transversely polarized virtual photons determined under the assumption of SCHC are presented as well in this section.

2.9.1 Vector-meson production from an unpolarized target

In the Wolf-Schilling formalism [14], the angular distribution function for an unpolarized target and a polarized lepton beam is expressed in terms of 23 SDMEs as

$$
\begin{aligned}
W(\Phi,\phi_{\pi\pi},\theta_{\pi\pi}) &= W_{UU}(\Phi,\phi_{\pi\pi},\theta_{\pi\pi}) + P_\ell W_{UL}(\Phi,\phi_{\pi\pi},\theta_{\pi\pi}) \\
&= \frac{3}{4\pi}\Bigl\{ \quad \frac{1}{2}(1-r^{04}_{00}) + \frac{1}{2}(3r^{04}_{00}-1)\cos^2\theta_{\pi\pi} \\
&\quad -\sqrt{2}\,\mathrm{Re}\,(r^{04}_{10})\sin 2\theta_{\pi\pi}\cos\phi_{\pi\pi} - r^{04}_{1-1}\sin^2\theta_{\pi\pi}\cos 2\phi_{\pi\pi} \\
&\quad -\varepsilon\cos 2\Phi\Bigl(r^1_{11}\sin^2\theta_{\pi\pi} + r^1_{00}\cos^2\theta_{\pi\pi} \\
&\qquad -\sqrt{2}\,\mathrm{Re}\,(r^1_{10})\sin 2\theta_{\pi\pi}\cos\phi_{\pi\pi} - r^1_{1-1}\sin^2\theta_{\pi\pi}\cos 2\phi_{\pi\pi}\Bigr) \\
&\quad -\varepsilon\sin 2\Phi\Bigl(\sqrt{2}\,\mathrm{Im}\,(r^2_{10})\sin 2\theta_{\pi\pi}\sin\phi_{\pi\pi} + \mathrm{Im}\,(r^2_{1-1})\sin^2\theta_{\pi\pi}\sin 2\phi_{\pi\pi}\Bigr) \\
&\quad +\sqrt{2\varepsilon(1+\varepsilon)}\cos\Phi\Bigl(r^5_{11}\sin^2\theta_{\pi\pi} + r^5_{00}\cos^2\theta_{\pi\pi} \\
&\qquad -\sqrt{2}\,\mathrm{Re}\,(r^5_{10})\sin 2\theta_{\pi\pi}\cos\phi_{\pi\pi} - r^5_{1-1}\sin^2\theta_{\pi\pi}\cos 2\phi_{\pi\pi}\Bigr) \\
&\quad +\sqrt{2\varepsilon(1+\varepsilon)}\sin\Phi\Bigl(\sqrt{2}\,\mathrm{Im}\,(r^6_{10})\sin 2\theta_{\pi\pi}\sin\phi_{\pi\pi} + \mathrm{Im}\,(r^6_{1-1})\sin^2\theta_{\pi\pi}\sin 2\phi_{\pi\pi}\Bigr) \\
&\quad + P_\ell\Bigl[\ \sqrt{1-\varepsilon^2}\ \Bigl(\sqrt{2}\,\mathrm{Im}\,(r^3_{10})\sin 2\theta_{\pi\pi}\sin\phi_{\pi\pi} + \mathrm{Im}\,(r^3_{1-1})\sin^2\theta_{\pi\pi}\sin 2\phi_{\pi\pi}\Bigr) \\
&\quad +\sqrt{2\varepsilon(1-\varepsilon)}\cos\Phi\Bigl(\sqrt{2}\,\mathrm{Im}\,(r^7_{10})\sin 2\theta_{\pi\pi}\sin\phi_{\pi\pi} + \mathrm{Im}\,(r^7_{1-1})\sin^2\theta_{\pi\pi}\sin 2\phi_{\pi\pi}\Bigr) \\
&\quad +\sqrt{2\varepsilon(1-\varepsilon)}\sin\Phi\Bigl(r^8_{11}\sin^2\theta_{\pi\pi} + r^8_{00}\cos^2\theta_{\pi\pi} - \sqrt{2}\,\mathrm{Re}\,(r^8_{10})\sin 2\theta_{\pi\pi}\cos\phi_{\pi\pi} \\
&\qquad -r^8_{1-1}\sin^2\theta_{\pi\pi}\cos 2\phi_{\pi\pi}\Bigr)\ \Bigr]\ \Bigr\},
\end{aligned}
\tag{2.61}
$$

where P_ℓ represents the lepton-beam polarization and the SDMEs are denoted by $r^{04}_{\alpha\beta}$ or $r^a_{\alpha\beta}$. The subscripts $\alpha, \beta = -1, 0, 1$ indicate the polarization states of the vector meson and the superscript a indicates the polarization states of the virtual photon[5]. The matrix elements in the Wolf-Schilling formalism are discussed in more detail in appendix B. The angle Φ represents the azimuthal production angle of the vector meson defined according to [14, 21], which is given by $\Phi = -\phi$, with ϕ being defined according to the Trento convention [20] (see section 2.4.1).

2.9.2 Vector-meson production from a polarized target

The Diehl formalism provides a general description of vector-meson production from a polarized target in terms of spin density-matrix elements. The SDMEs for ρ^0 production are related to the transition amplitudes $T^{\alpha\sigma}_{mi}$ of the process $\gamma^*(m)\ p(i) \to p(\sigma)\ \rho^0(\alpha)$, where $i, \sigma = \pm\frac{1}{2}$ represent the spins and $m, \alpha = -1, 0, 1$ the helicities of the involved particles specified between the brackets. Within the Diehl formalism this relation is given by[6]

$$\rho^{\alpha\beta}_{mn,ij} = (N_T + \varepsilon N_L)^{-1} \sum_{\sigma} T^{\alpha\sigma}_{mi} \left(T^{\beta\sigma}_{nj}\right)^* , \tag{2.62}$$

where the SDMEs are represented by $\rho^{\alpha\beta}_{mn,ij}$, and N_T and N_L are normalization factors given by

$$N_T = \tfrac{1}{2} \sum_{i,\alpha,\sigma} \left|T^{\alpha\sigma}_{+i}\right|^2 , \qquad N_L = \tfrac{1}{2} \sum_{i,\alpha,\sigma} \left|T^{\alpha\sigma}_{0i}\right|^2 . \tag{2.63}$$

The structure of equation 2.62 resembles the structure of the terms σ^{ji}_{nm} of the Diehl-Sapeta formalism [13] given by equation 2.32. In fact, the SDMEs $\rho^{\alpha\beta}_{mn,ij}$ and the terms σ^{ji}_{nm} are related by

$$\sum_{\alpha} \rho^{\alpha\alpha}_{mn,ij} \propto \frac{d\sigma^{ji}_{nm}}{dt} . \tag{2.64}$$

In order to obtain the angular distribution function, the spin density-matrix $\rho^{\alpha\beta}_{mn,ij}$ is contracted with the spin density-matrix τ_{ij} of the proton, analogous to equation 2.34. The spherical harmonics $Y_{1\alpha}(\theta_{\pi\pi}, \phi_{\pi\pi})$, corresponding to a ρ^0 polarization α, are included in this contraction in order to take into account the decay of the ρ^0 meson. The contraction results in the matrix

$$\rho_{mn} = \sum_{\alpha,\beta} \sum_{ij} \tau_{ij}\, \rho^{\alpha\beta}_{mn,ij}\, Y_{1\alpha}(\theta_{\pi\pi}, \phi_{\pi\pi})\, Y^*_{1\beta}(\theta_{\pi\pi}, \phi_{\pi\pi}) , \tag{2.65}$$

---

[5] It is noted that within the Wolf-Schilling formalism [14] the convention used for the notation of the virtual-photon polarization differs from the convention introduced in section 2.4.3 that is used within the Diehl-Sapeta [13] and the Diehl [11] formalisms.

[6] For the SDMEs of the Wolf-Schilling formalism the relation with the transition amplitudes is given in appendix B.

where the spherical harmonics are given by

$$\begin{aligned} Y_{1+1} &= -\sqrt{\frac{3}{8\pi}}\,\sin\theta_{\pi\pi}\,e^{i\phi_{\pi\pi}}\,, \\ Y_{10} &= \sqrt{\frac{3}{4\pi}}\,\cos\theta_{\pi\pi}\,, \\ Y_{1-1} &= \sqrt{\frac{3}{8\pi}}\,\sin\theta_{\pi\pi}\,e^{-i\phi_{\pi\pi}}\,. \end{aligned} \tag{2.66}$$

Following the steps discussed in section 2.5 and [11, 13], the expression for the leptoproduction cross section can then be obtained by a contraction of the matrix ρ_{mn} with the spin density-matrix of the virtual photon.

The result is conveniently expressed in terms of the combinations

$$u^{\alpha\beta}_{mn} = \tfrac{1}{2}\big(\rho^{\alpha\beta}_{mn,++} + \rho^{\alpha\beta}_{mn,--}\big)\,, \qquad l^{\alpha\beta}_{mn} = \tfrac{1}{2}\big(\rho^{\alpha\beta}_{mn,++} - \rho^{\alpha\beta}_{mn,--}\big)\,, \tag{2.67}$$

respectively, for an unpolarized and a longitudinally polarized target and the combinations

$$s^{\alpha\beta}_{mn} = \tfrac{1}{2}\big(\rho^{\alpha\beta}_{mn,+-} + \rho^{\alpha\beta}_{mn,-+}\big)\,, \qquad n^{\alpha\beta}_{mn} = \tfrac{1}{2}\big(\rho^{\alpha\beta}_{mn,+-} - \rho^{\alpha\beta}_{mn,-+}\big)\,, \tag{2.68}$$

for a transversely polarized target. The use of these combinations simplifies the expression for the contraction of the matrices ρ and τ:

$$\sum_{ij} \tau_{ij}\,\rho^{\alpha\beta}_{mn,ij} = u^{\alpha\beta}_{mn} + S_L\,l^{\alpha\beta}_{mn} + S_T\cos(\phi-\phi_S)\,s^{\alpha\beta}_{mn} - S_T\sin(\phi-\phi_S)\,in^{\alpha\beta}_{mn}, \tag{2.69}$$

where S_L and S_T are, respectively, the longitudinal and the transverse components of the target polarization with respect to the virtual-photon direction.

The full expressions of the various contributions to the angular distribution function in terms of SDMEs can be found in [11]. The angular distribution function for an unpolarized target and an unpolarized lepton beam is given by

$$
\begin{aligned}
W_{UU}^{LL}(\phi) &= \left(u_{++}^{0\,0} + \varepsilon u_{0\,0}^{0\,0}\right) - 2\cos\phi\,\sqrt{\varepsilon(1+\varepsilon)}\,\mathrm{Re}\,u_{0+}^{0\,0} \\
&\quad - \cos(2\phi)\,\varepsilon u_{-+}^{0\,0}\,, \\
W_{UU}^{LT}(\phi,\phi_{\pi\pi}) &= \cos(\phi+\phi_{\pi\pi})\,\sqrt{\varepsilon(1+\varepsilon)}\,\mathrm{Re}\left(u_{0+}^{0+} - u_{0+}^{-0}\right) \\
&\quad - \cos\phi_{\pi\pi}\,\mathrm{Re}\left(u_{++}^{0+} - u_{++}^{-0} + 2\varepsilon u_{0\,0}^{0+}\right) \\
&\quad + \cos(2\phi+\phi_{\pi\pi})\,\varepsilon\mathrm{Re}\,u_{-+}^{0+} \\
&\quad - \cos(\phi-\phi_{\pi\pi})\,\sqrt{\varepsilon(1+\varepsilon)}\,\mathrm{Re}\left(u_{0+}^{0-} - u_{0+}^{+0}\right) \\
&\quad + \cos(2\phi-\phi_{\pi\pi})\,\varepsilon\mathrm{Re}\,u_{-+}^{+0}\,, \\
W_{UU}^{TT}(\phi,\phi_{\pi\pi}) &= \tfrac{1}{2}\left(u_{++}^{++} + u_{++}^{--} + 2\varepsilon u_{0\,0}^{++}\right) + \tfrac{1}{2}\cos(2\phi+2\phi_{\pi\pi})\,\varepsilon u_{-+}^{-+} \\
&\quad - \cos\phi\,\sqrt{\varepsilon(1+\varepsilon)}\,\mathrm{Re}\left(u_{0+}^{++} + u_{0+}^{--}\right) \\
&\quad + \cos(\phi+2\phi_{\pi\pi})\,\sqrt{\varepsilon(1+\varepsilon)}\,\mathrm{Re}\,u_{0+}^{-+} \\
&\quad - \cos(2\phi_{\pi\pi})\,\mathrm{Re}\left(u_{++}^{-+} + \varepsilon u_{0\,0}^{-+}\right) - \cos(2\phi)\,\varepsilon\mathrm{Re}\,u_{-+}^{++} \\
&\quad + \cos(\phi-2\phi_{\pi\pi})\,\sqrt{\varepsilon(1+\varepsilon)}\,\mathrm{Re}\,u_{0+}^{+-} \\
&\quad + \tfrac{1}{2}\cos(2\phi-2\phi_{\pi\pi})\,\varepsilon u_{-+}^{+-}\,,
\end{aligned}
\tag{2.70}
$$

where the superscripts represent the three vector-meson polarization states. The normalization of the angular distribution W_{UU} is ensured by the relation

$$
(u_{++}^{++} + u_{++}^{--} + 2\varepsilon u_{0\,0}^{++}) = 1 - (u_{++}^{0\,0} + \varepsilon u_{0\,0}^{0\,0}). \tag{2.71}
$$

The terms appearing in W_{UU}^{LL}, W_{UU}^{LT} and W_{UU}^{TT} are ordered according to the corresponding SDMEs. First, the terms including at least one SDME corresponding to only s-channel helicity-conserving amplitudes are listed. Then, the terms corresponding to the interference of helicity-conserving and helicity-changing amplitudes, and after that the terms corresponding to only helicity-changing amplitudes are listed.

The angular distribution corresponding to transverse target polarization with respect to the virtual-photon direction and an unpolarized beam is given by

$$
\begin{aligned}
&W_{UT}^{LL}(\phi_S,\phi) = \\
&\qquad \sin(\phi-\phi_S)\Big[\mathrm{Im}\left(n_{++}^{00}+\varepsilon n_{00}^{00}\right) \\
&\qquad\quad -2\cos\phi\,\sqrt{\varepsilon(1+\varepsilon)}\,\mathrm{Im}\,n_{0+}^{00}-\cos(2\phi)\,\varepsilon\mathrm{Im}\,n_{-+}^{00}\Big] \\
&\qquad +\cos(\phi-\phi_S)\Big[-2\sin\phi\,\sqrt{\varepsilon(1+\varepsilon)}\,\mathrm{Im}\,s_{0+}^{00}-\sin(2\phi)\,\varepsilon\mathrm{Im}\,s_{-+}^{00}\Big], \\
&W_{UT}^{LT}(\phi_S,\phi,\phi_{\pi\pi}) = \\
&\qquad \sin(\phi-\phi_S)\Big[\cos(\phi+\phi_{\pi\pi})\,\sqrt{\varepsilon(1+\varepsilon)}\,\mathrm{Im}\left(n_{0+}^{0+}-n_{0+}^{-0}\right) \\
&\qquad\quad -\cos\phi_{\pi\pi}\,\mathrm{Im}\left(n_{++}^{0+}-n_{++}^{-0}+2\varepsilon n_{00}^{0+}\right)+\cos(2\phi+\phi_{\pi\pi})\,\varepsilon\mathrm{Im}\,n_{-+}^{0+} \\
&\qquad\quad -\cos(\phi-\phi_{\pi\pi})\,\sqrt{\varepsilon(1+\varepsilon)}\,\mathrm{Im}\left(n_{0+}^{0-}-n_{0+}^{+0}\right)+\cos(2\phi-\phi_{\pi\pi})\,\varepsilon\mathrm{Im}\,n_{-+}^{+0}\Big] \\
&\qquad +\cos(\phi-\phi_S)\Big[\sin(\phi+\phi_{\pi\pi})\,\sqrt{\varepsilon(1+\varepsilon)}\,\mathrm{Im}\left(s_{0+}^{0+}-s_{0+}^{-0}\right) \\
&\qquad\quad -\sin\phi_{\pi\pi}\,\mathrm{Im}\left(s_{++}^{0+}-s_{++}^{-0}+2\varepsilon s_{00}^{0+}\right)+\sin(2\phi+\phi_{\pi\pi})\,\varepsilon\mathrm{Im}\,s_{-+}^{0+} \\
&\qquad\quad -\sin(\phi-\phi_{\pi\pi})\,\sqrt{\varepsilon(1+\varepsilon)}\,\mathrm{Im}\left(s_{0+}^{0-}-s_{0+}^{+0}\right)+\sin(2\phi-\phi_{\pi\pi})\,\varepsilon\mathrm{Im}\,s_{-+}^{+0}\Big], \\
&W_{UT}^{TT}(\phi_S,\phi,\phi_{\pi\pi}) = \\
&\qquad \sin(\phi-\phi_S)\Big[\tfrac{1}{2}\mathrm{Im}\left(n_{++}^{++}+n_{++}^{--}+2\varepsilon n_{00}^{++}\right)+\tfrac{1}{2}\cos(2\phi+2\phi_{\pi\pi})\,\varepsilon\mathrm{Im}\,n_{-+}^{-+} \\
&\qquad\quad -\cos\phi\,\sqrt{\varepsilon(1+\varepsilon)}\,\mathrm{Im}\left(n_{0+}^{++}+n_{0+}^{--}\right)+\cos(\phi+2\phi_{\pi\pi})\,\sqrt{\varepsilon(1+\varepsilon)}\,\mathrm{Im}\,n_{0+}^{-+} \\
&\qquad\quad -\cos(2\phi_{\pi\pi})\,\mathrm{Im}\left(n_{++}^{-+}+\varepsilon n_{00}^{-+}\right)-\cos(2\phi)\,\varepsilon\mathrm{Im}\,n_{-+}^{++} \\
&\qquad\quad +\cos(\phi-2\phi_{\pi\pi})\,\sqrt{\varepsilon(1+\varepsilon)}\,\mathrm{Im}\,n_{0+}^{+-}+\tfrac{1}{2}\cos(2\phi-2\phi_{\pi\pi})\,\varepsilon\mathrm{Im}\,n_{-+}^{+-}\Big] \\
&\qquad +\cos(\phi-\phi_S)\Big[\tfrac{1}{2}\sin(2\phi+2\phi_{\pi\pi})\,\varepsilon\mathrm{Im}\,s_{-+}^{-+} \\
&\qquad\quad -\sin\phi\,\sqrt{\varepsilon(1+\varepsilon)}\,\mathrm{Im}\left(s_{0+}^{++}+s_{0+}^{--}\right)+\sin(\phi+2\phi_{\pi\pi})\,\sqrt{\varepsilon(1+\varepsilon)}\,\mathrm{Im}\,s_{0+}^{-+} \\
&\qquad\quad -\sin(2\phi_{\pi\pi})\,\mathrm{Im}\left(s_{++}^{-+}+\varepsilon s_{00}^{-+}\right)-\sin(2\phi)\,\varepsilon\mathrm{Im}\,s_{-+}^{++} \\
&\qquad\quad +\sin(\phi-2\phi_{\pi\pi})\,\sqrt{\varepsilon(1+\varepsilon)}\,\mathrm{Im}\,s_{0+}^{+-}+\tfrac{1}{2}\sin(2\phi-2\phi_{\pi\pi})\,\varepsilon\mathrm{Im}\,s_{-+}^{+-}\Big].
\end{aligned}
\tag{2.72}
$$

The terms appearing in W_{UT}^{LL}, W_{UT}^{LT} and W_{UT}^{TT} are ordered similar to the terms appearing in equation 2.70. However, the terms corresponding to the SDMEs $n_{mn}^{\alpha\beta}$ containing a $\sin(\phi-\phi_S)$ dependence are ordered separately from the terms corresponding to the SDMEs $s_{mn}^{\alpha\beta}$ containing a $\cos(\phi - \phi_S)$ dependence.

It has been shown in [12] that at leading twist only transitions from a longitudinally polarized virtual photon to a longitudinally polarized ρ^0 meson are allowed. As a result the only leading-twist SDMEs are n_{00}^{00} and u_{00}^{00} [11]. As follows from equation 2.44, in combination with equations 2.70 and 2.72, the corresponding $\sin(\phi - \phi_S)$ moment of the transverse target-spin asymmetry can be conveniently expressed as

$$A_{UT}^{\sin(\phi-\phi_S)}(\gamma_L^* \, p \;\rightarrow\; \rho_L \, p) \;=\; \frac{\operatorname{Im} n_{00}^{00}}{u_{00}^{00}}. \tag{2.73}$$

GPD-based calculations of this asymmetry are available, which are briefly discussed in section 2.10.

2.9.3 Existing results for an unpolarized target

Experimental results are available for the SDMEs for an unpolarized target obtained from measurements performed at HERMES during the 1996-2000 periods with unpolarized hydrogen and deuterium targets [26]. The extracted SDME values, which are represented in the Wolf-Schilling formalism, are displayed in figure 2.10. Various SDME values are multiplied with a factor 2, $2\sqrt{2}$, $1/\sqrt{2}$, or $\sqrt{2}$, in order to obtain a fair comparison of the combination of amplitudes contributing to the SDMEs. The SDMEs are ordered into different categories A, B, C, D, and E, according to the corresponding virtual-photon and vector-meson helicities. Under the assumption of SCHC, the SDMEs in the categories A and B are allowed to be non-zero, whereas the SDMEs in the categories C, D and E are predicted to be equal to zero. The measured values in categories A and B are significantly larger than the values in the other categories. In the categories D and E, the values are not significantly different from zero, whereas most of the values in the category C differ significantly from zero and therefore violate SCHC. However, since the values in category C are relatively small in comparison to the values in categories A and B, helicity-conserving amplitudes are clearly favored over helicity-changing amplitudes. Thus the results support the use of the assumption of SCHC as an approximation.

The SDME r_{00}^{04} represents the fractional contribution from longitudinally polarized ρ^0 mesons to the cross section. Under the assumption of s-channel helicity conservation (SCHC) r_{00}^{04} can be used to separate the cross sections for longitudinally and transversely polarized virtual photons. Such an $L - T$ separation is necessary when GPD-based calculations are compared with measured observables, since these calculations are valid only if the exchanged virtual photon is longitudinally polarized. One can obtain σ_L from the total cross section σ_{total} by using

$$\sigma_L = \frac{R}{1 + \epsilon R} \sigma_{total}, \tag{2.74}$$

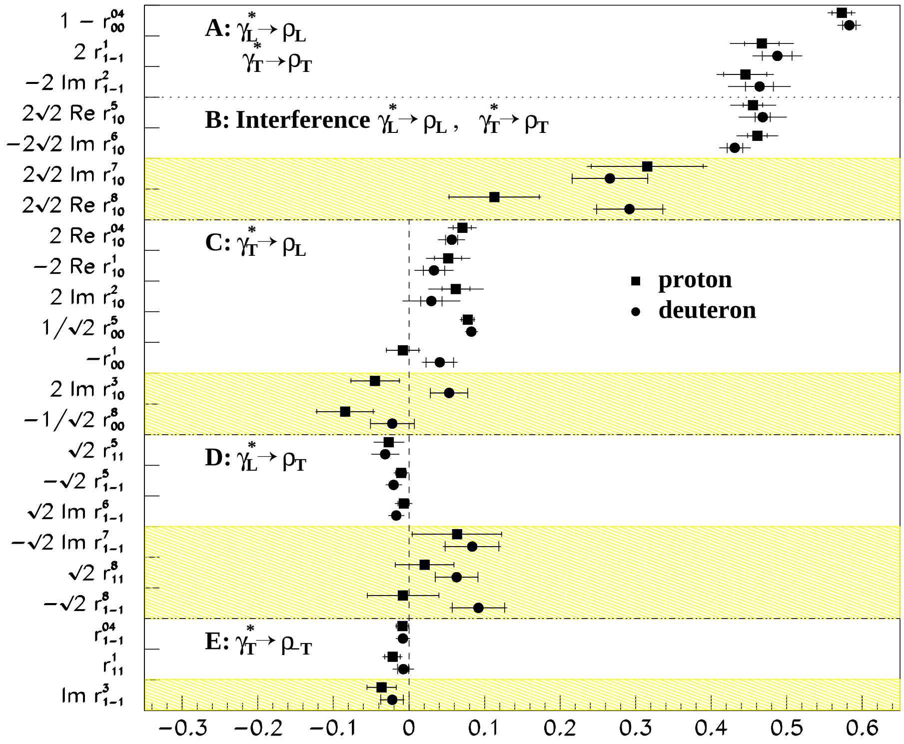

Figure 2.10: SDMEs obtained from the HERMES data for exclusive ρ^0 production on a hydrogen (filled squares) and a deuterium target (filled circles) [26]. The dotted, horizontal lines separate the different categories explained in the text. The shaded areas indicate beam-polarization dependent SDMEs.

where, under the assumption of SCHC, the cross section ratio $R = \sigma_L/\sigma_T$ is given by

$$R \overset{SCHC}{=} \frac{r^{04}_{00}}{\epsilon(1 - r^{04}_{00})}. \tag{2.75}$$

As SCHC was shown to be a reasonable approximation at HERMES kinematics, equation 2.75 has been used to determine the ratio R from the HERMES results for r^{04}_{00} [26]. The results for R as a function of Q^2 are shown in figure 2.11 together with the data from other experiments [27]. The majority of the data are in mutual agreement despite considerable differences in the center-of-mass energy W. The results for R obtained at HERMES kinematics are typically of order unity or less and increase with increasing Q^2. This implies that at HERMES the cross sections σ_L and σ_T are comparable in size, with σ_T being typically larger than σ_L, but with the relative contribution from σ_T decreasing with Q^2. Since the contribution to the cross section from transversely polarized virtual photons cannot be ignored, observables should be extracted separately for longitudinally and transversely polarized photons in order to justify a comparison of data with GPD-based calculations.

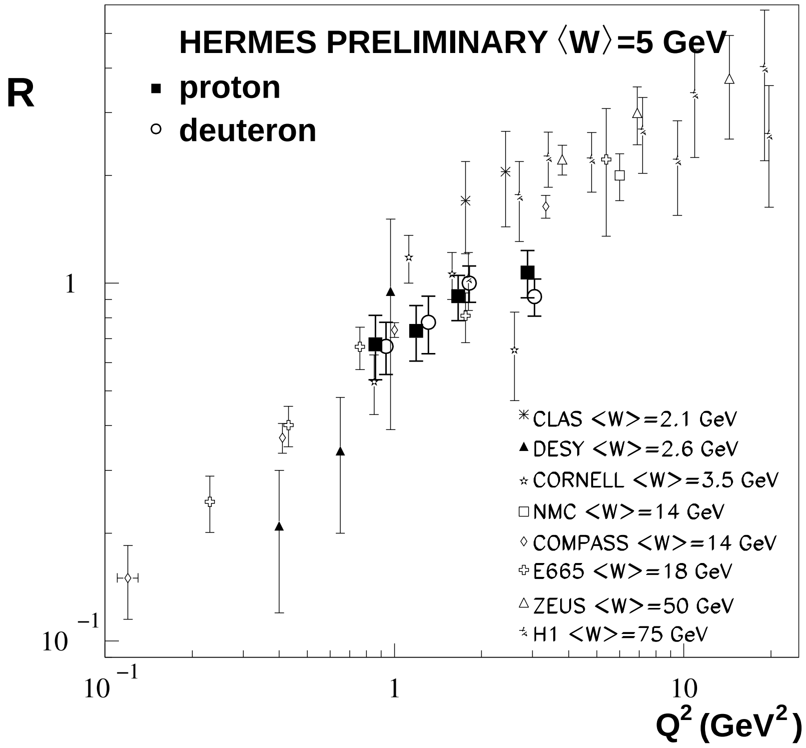

Figure 2.11: The ratio $R = \sigma_L/\sigma_T$ of the longitudinal over the transverse cross section obtained under the assumption of SCHC from the HERMES data for exclusive ρ^0 production from a hydrogen (filled squares) and a deuterium target (open circles) [26]. The results are compared to data from other experiments [27].

2.10 GPD-model calculations for A_{UT}

As noted in section 2.3, observables for hard exclusive processes can be calculated in terms of convolutions of GPDs over the variable $\bar{x}$. These convolutions are given for the GPDs H^f and E^f by, respectively,

$$\begin{aligned} A &= \frac{1}{\sqrt{2}} \int_{-1}^{1} d\bar{x} \left[\frac{1}{\xi - \bar{x} - i\varepsilon} - \frac{1}{\xi + \bar{x} - i\varepsilon} \right] \\ &\quad \times \left[\frac{2}{3} H^u(\bar{x}, \xi, t) + \frac{1}{3} H^d(\bar{x}, \xi, t) + \frac{3}{8} \frac{H^g(\bar{x}, \xi, t)}{\bar{x}} \right], \qquad (2.76) \\ B &= \frac{1}{\sqrt{2}} \int_{-1}^{1} d\bar{x} \left[\frac{1}{\xi - \bar{x} - i\varepsilon} - \frac{1}{\xi + \bar{x} - i\varepsilon} \right] \\ &\quad \times \left[\frac{2}{3} E^u(\bar{x}, \xi, t) + \frac{1}{3} E^d(\bar{x}, \xi, t) + \frac{3}{8} \frac{E^g(\bar{x}, \xi, t)}{\bar{x}} \right], \qquad (2.77) \end{aligned}$$

where the superscript $f = u, d, g$ labels up-quarks, down-quarks or gluons [13]. It has been shown [10, 11, 13, 28] that at leading twist, i.e., with both the virtual photon and the produced meson longitudinally polarized, the $\sin(\phi - \phi_S)$ moment of the transverse target-spin asymmetry A_{UT} in exclusive ρ^0 production is given in terms of the convolutions A and B by

$$\begin{aligned} & A_{UT}^{\sin(\phi-\phi_S)}(\gamma_L^* \, p \to \rho_L \, p) = \\ & \quad \frac{\sqrt{t_0 - t}}{M} \, \frac{\sqrt{1-\xi^2}\, \mathrm{Im}\left(B^* A\right)}{(1-\xi^2)\,|A|^2 - \left(\xi^2 + t/(4M^2)\right)|B|^2 - 2\xi^2 \mathrm{Re}\left(B^* A\right)}, \qquad (2.78) \end{aligned}$$

where $-4M^2\xi^2/(1-\xi^2) = t_0$ [29]. Since the denominator of equation 2.78 is in practice dominated by the $|A|^2$ term, the asymmetry is by approximation linearly dependent on the term B that contains the GPDs E^f. As can be seen from equation 2.20 the GPD E^f directly contributes to J^f, the total angular momentum of quarks or gluons inside the proton. Hence, from equation 2.78 it can be concluded that the corresponding azimuthal moment of the asymmetry is sensitive to J^f as well.

Experimental information on the $\sin(\phi - \phi_S)$ moment of the asymmetry can be obtained by extracting the angular distribution function of the cross section (see section 2.7). One can distinguish the asymmetries for longitudinally and transversely polarized ρ^0 mesons by evaluating the angular distribution as a function of the ρ^0 angle $\theta_{\pi\pi}$ (see equation 2.54). Such a $\rho_L - \rho_T$ separation is also possible by determining spin density-matrix elements, which are presented in section 2.9. Under the assumption of SCHC the $\sin(\phi - \phi_S)$ component of A_{UT} for longitudinally ρ^0 mesons can be compared with GPD model calculations, since this assumption implies that longitudinally polarized ρ^0 mesons are produced by longitudinally polarized virtual photons. Note that available data of SDMEs for an unpolarized target (see section 2.9.1) suggest that SCHC is a reasonable but not exact approximation.

Various GPD-model calculations are available for the asymmetry A_{UT} [10, 28, 29, 30]. Within the used models the GPDs H^u, H^d, and H^g have been extrapolated from the available information on the parton distribution functions and elastic form factors. These extrapolations make use of equations 2.17-2.19. The nucleon spin-flip GPDs E^u, E^d, and E^g cannot be extrapolated from the inclusive deep-inelastic scattering data. Different approaches have been used for modelling these GPDs.

In [10, 28] the total angular momenta J^u and J^d of up-quarks and down-quarks enter directly as free parameters in the parameterization of the GPDs E^u and E^d. Figure 2.12 shows the result of model-dependent calculations [10] for the x dependence of the transverse target-spin asymmetry at different values of J^u. Possible contributions to J^u coming from gluons have not been taken into account in these calculations. It is noted that the convention used for the asymmetry $\mathcal{A}$ in [10] differs from the convention used here. The asymmetry $\mathcal{A}$ displayed in figure 2.12 is given by

$$\mathcal{A} \quad = \quad -\frac{2}{\pi} A_{UT}^{\sin(\phi-\phi_S)}. \tag{2.79}$$

The calculations in [28] do take into account the GPD H^g for gluons. Evidence for a non-zero gluon contribution originates from data on the ratio of ϕ and ρ^0 electroproduction cross sections, which indicate that there is a substantial contribution from gluons to the cross section for the ρ^0 production at HERMES kinematics [31, 32]. The contribution from H^g results into an increase of the denominator of 2.78 and therefore causes the magnitude of the $\sin(\phi-\phi_S)$ component of A_{UT} to be smaller. The corresponding results for the x dependence and the t dependence of the asymmetry at different values of J^u are shown in figure 2.13. Note that, as expected from equation 2.79, the sign in figure 2.13 is mostly opposite to that in figure 2.12. It is concluded that according to the model calculations shown in figures 2.12 and 2.13 transverse target-spin asymmetries up to $10-15\,\%$ can be expected in the kinematic range of the HERMES experiment.

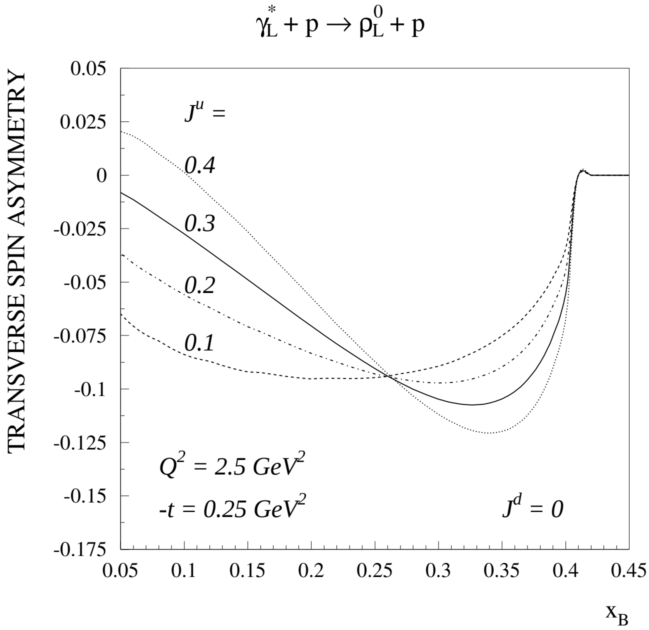

Figure 2.12: GPD-model calculations [10] of the transverse target-spin asymmetry versus x for $J^d = 0$ and different values of J^u ($J^u = 0.1$, 0.2, 0.3, 0.4). The quantity shown on the vertical axis is equal to $\mathcal{A} = -\frac{2}{\pi} A_{UT}^{\sin(\phi-\phi_S)}$. The calculations do not account for possible gluon contributions.

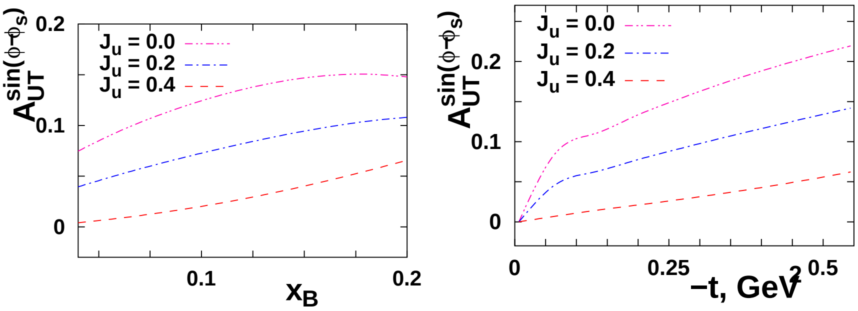

Figure 2.13: GPD-model calculations [28] for $Q^2 = 2$ GeV^2 of $A_{UT}^{\sin(\phi-\phi_S)}$ versus x and t for $J^d = 0$ and different values of J^u ($J^u = 0$, 0.2, 0.4). The calculations have been performed for $-t = 0.14$ GeV^2 (left plot) and $x = 0.085$ (right plot).

Chapter 3

The HERMES experiment

The HERMES (HERA MEasurement of Spin) experiment is located at the HERA (Hadron Electron Ring Anlage) accelerator at the DESY (Deutsches Electronen SYnchrotron) institute in Hamburg, Germany. The HERMES experiment investigates the spin structure of the nucleon by measuring the scattering of longitudinally polarized leptons from a polarized fixed internal gas target. In section 3.1 the HERA storage ring, which is used to accelerate the leptons, is described. The HERMES internal gas target is described in section 3.2. Scattered leptons and particles produced in the scattering process are detected by the HERMES forward spectrometer [33, 34], which is the subject of section 3.3. The main components of the spectrometer are detectors used for tracking, which are described in section 3.4, a magnet, and detectors used for particle identification, which are descibed in section 3.5. A brief description of the readout system of the detectors and the so-called data production chain can be found in section 3.6 and section 3.7, respectively.

3.1 The HERA electron or positron storage ring

The HERA facility accommodates storage rings for a lepton (electron or positron) beam and a proton beam, both with a circumference of 6.3 km. The lepton and proton beams are accelerated up to an energy of about 27.6 and 920 GeV, respectively. Both beams are used by the lepton-proton collider experiments H1 and ZEUS, whereas the HERMES experiment only uses the lepton beam. The initial current of the lepton beam injected into the storage ring is typically about 30 to 40 mA. After injection the current gradually decreases with a lifetime of typically 12 hours. The beam is dumped at a beam current of about 10 mA.

For the lepton beam a transverse polarization is built up spontaneously through the Sokolov-Ternov mechanism [35]. The maximum transverse polarization that can be obtained through this mechanism is about 60%. Spin rotators upstream and downstream of the HERMES experiment change the orientation of the beam polarization from transverse to longitudinal and from longitudinal to transverse, respectively, so that the HERMES experimental set-up is located in the section with a longitudinally polarized beam. The longitudinal polarization is either parallel or anti-parallel to the lepton beam. Measurements of the lepton-beam polarization are performed with a longitudinal polarimeter (LPOL) [36], in the section with a longitudinally polarized beam, and with a transverse polarimeter (TPOL) [37] in the section with a transversely polarized beam. These devices determine the polarization by measuring the Compton scattering of polarized laser light from the lepton beam. The polarization measured by the LPOL has an absolute statistical precision of 0.01 for a time interval of typically one minute and a systematic uncertainty of 1.6%.

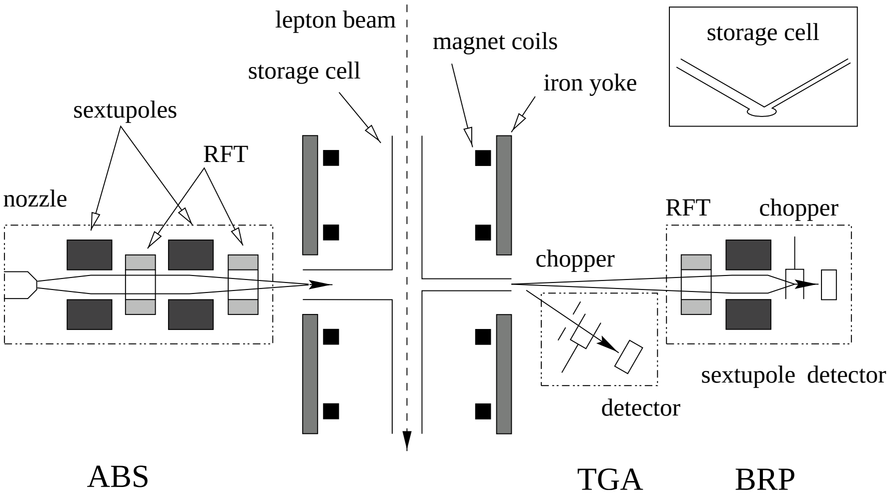

Figure 3.1: Schematic overview of the setup of the polarized internal gas target, including a side view of the storage cell in the inlay figure.

3.2 The HERMES internal gas target

The target gas used at HERMES can either be polarized atomic hydrogen, deuterium or ^{3}He, or unpolarized hydrogen, deuterium, H_2, D_2, ^{3}He, ^{4}He, N_2, Ne, Kr, or Xe. The setup for the polarized target is illustrated in figure 3.1. An atomic beam source (ABS) [38] provides nuclear polarized atoms by using a system of sextupole magnets and radio frequency transmitters (RFT). Based on the Stern-Gerlach principle the sextupole magnets focus specific hyperfine states of atoms and deflect other hyperfine states. Nuclear polarization is obtained by an interchange of atomic and nuclear polarization, where the former is achieved by populating certain hyperfine states selected by a combination of radio-frequency transitions.

The target gas is injected into a storage cell, which is located within the vacuum of the HERA electron beam pipe. The cell is made of 75 μm thick pure aluminum and has the shape of an open ended tube with a length of 400 mm and an elliptical cross section of 21×8.9 mm^2. It is mounted so that the tube surrounds the passing electron beam. In case of a polarized target, densities of about 10^{14} nucl/cm^2 are reached inside the storage cell. The target gas diffuses from the storage cell into the beam pipe, from where it is removed by a high-capacity pumping system, so that the beam vacuum is maintained.

The direction of the spin of the target nucleons is defined relative to a homogeneous magnetic holding field provided by a superconducting solenoid magnet. For the longitudinally polarized target the magnetic field has a strength of about 350 mT and is directed parallel to the HERA beam direction. For the transversely polarized target the magnetic field has a strength of about 300 mT and is directed parallel to the negative y direction of the HERMES coordinate system (see section 3.3). The direction of the target polarization changes about once every 90 seconds between parallel and anti-parallel with respect to the magnetic field, such that about equal luminosities are obtained for both polarization states.

Attached to the storage cell is a tube through which a sample of the target gas is probed by the Target Gas Analyzer (TGA) and the Breit-Rabi Polarimeter (BRP). The TGA determines the relative molecular and atomic content of the gas. The BRP [39] determines the polarization of the target by measuring the relative population of the hyperfine states of the target atoms. In order to select different combinations of hyperfine states radio frequency transmitters are used in combination with a sextupole magnet. In the period 2002-2005 an average luminosity-weighted magnitude of the transverse polarization was measured of 0.72 ± 0.06 (syst.).

3.3 The HERMES spectrometer

A schematic overview of the HERMES spectrometer is presented in figure 3.2. All components of the spectrometer appear in two halves, an upper and a lower half, which are installed mirror symmetrically with respect to a horizontal mid-plane. The gap in between the two spectrometer halves contains the storage rings of both the lepton beam and the unused proton beam. Because the upper and lower half are identical, in the following sections the description of the components of the spectrometer will be given for one half only.

The spectrometer magnet provides a magnetic field causing a predominantly horizontal deflection of charged particles. It has a deflecting power of 1.3 Tm. An iron plate, referred to as the septum plate, installed between the two spectrometer halves shields the lepton and the proton beam from this magnetic field. Field clamps reduce the fringe fields in the detectors in front of and behind the magnet. The magnet divides the spectrometer into three regions: the front region, the magnet region, and the back region. The front region is upstream and the back region is downstream with respect to the position of the magnet, and the magnet region is the region in between. As is described in section 3.4, the HERMES tracking system determines the momenta of charged particles by determining the difference between the direction of its trajectory in the front and the back region.

The HERMES coordinate system is a right handed orthogonal coordinate system with axes x, y, z and its origin in the center of the target. The z-axis lies along the direction of the lepton beam, the x-axis points horizontally towards the outside of the HERA storage rings and the y-axis points upwards. The directions of particle trajectories are described in the HERMES laboratory frame by the polar angle θ and the azimuthal angle ϕ defined with respect to the z-direction. Alternatively, the angles θ_x and θ_y can be used. These angles are also defined with respect to the z-direction, but specify the directions of the trajectories projected on the zx-plane and the yz-plane, respectively. The angular acceptance of the HERMES spectrometer is given in the horizontal direction by $|\theta_x| \leq 170$ mrad and in the vertical direction by $40 \leq |\theta_y| \leq 140$ mrad.

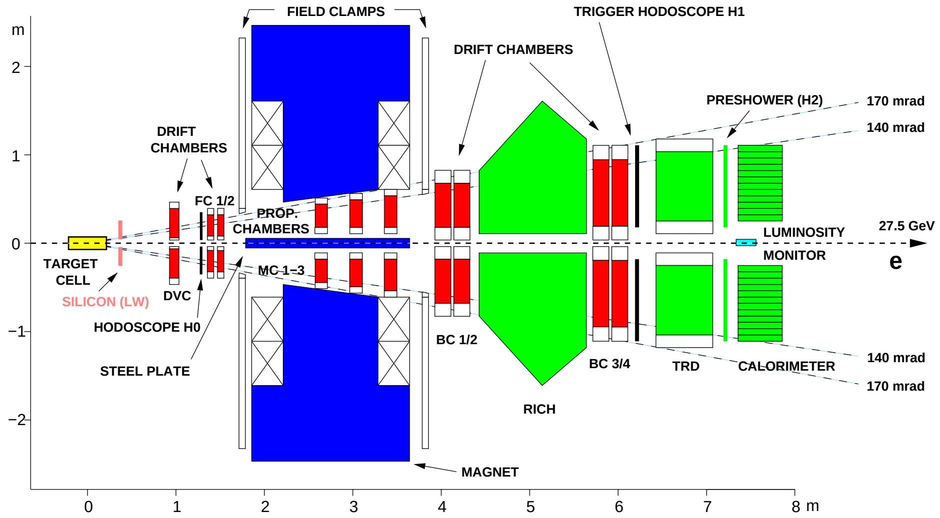

Figure 3.2: Schematic overview of the HERMES spectrometer (side view).

3.4 The tracking system

The trajectories (tracks) of particles passing through the spectrometer are reconstructed by the tracking system [34, 40]. The main purpose of the tracking system is the determination of the angles under which charged particles are scattered or produced and the determination of the corresponding charges, momenta, and the vertex positions. In addition, the track information is used by the particle identification (PID) system to identify hits in the PID detectors associated with each track.

Tracking detectors are installed in the front region, the magnet region and the back region of the spectrometer. In the front region horizontal-drift chambers are installed, which are known as the Drift Vertex Chambers (DVC) and the Front Chambers FC1 and FC2. In the back region two sets of drift chambers are installed, which are referred to as the Back Chambers BC1, BC2, BC3, and BC4. In the gap of the spectrometer magnet three proportional wire chambers are installed, which are called the Magnet Chambers MC1, MC2, and MC3.

The raw information of the hit wire positions and drift times measured by the drift chambers is converted offline by the HERMES reconstruction code (HRC) into information about tracks. First, straight partial tracks are reconstructed independently for the front and the back regions. Front tracks are reconstructed from the information obtained with FC1 and FC2. Optionally the information from the DVC can be used in addition. HRC reconstructs the complete track by matching associated front and back partial tracks inside the spectrometer magnet with an algorithm called ‘forced bridging’ [40]. The charge and momentum corresponding to the track are determined from the degree of bending of the track inside the magnetic field of the spectrometer magnet with momentum look-up tables. In case of data taking with a transversely polarized target the track information is corrected for bending caused by the transversely directed magnetic field in the target area by the TMC program.

The magnet chambers are used for the reconstruction and momentum determination of short tracks, which are tracks that are detected by the front chambers and the magnet chambers, but not by all back chambers. These tracks correspond to particles having a relatively low momentum, for which the deflection inside the spectrometer magnetic field is so large that the trajectory escapes the full acceptance of the back chambers.

In addition to the standard tracking detectors a detector, called the Lambda Wheels (LW) [41, 42], was installed in 2002 in the front region of the spectrometer. It consists of two wheels of silicon strip detectors situated at $z=$ 45 cm and z=50 cm inside the vacuum of the lepton storage ring of HERA. The LW can be used to determine the directions and vertices of tracks. It increases the acceptance in the front region, for instance, for the decay products of Λ^0, Λ_c^+ and J/Ψ particles. This is particularly important for the determination of the polarization of Λ^0 hyperons [43]. The track reconstruction for the LW is performed by a program called the extended tracking code (XTC), which is used in addition to the HRC software.

3.5 The particle identification system

Various components of the HERMES spectrometer are used for particle identification (PID): the ring imaging Čerenkov detector (RICH) [44, 45], a transition radiation detector (TRD), a preshower hodoscope, and an electromagnetic calorimeter

(CALO) [46].

3.5.1 The ring imaging Čerenkov detector

The RICH was installed in 1998. It replaced a threshold Čerenkov detector that was used during the 1996-1997 data taking periods. Both detectors make use of the Čerenkov radiation that charged particles emit if they pass through a radiator material with a velocity higher than the velocity of light in this material. The RICH contains an array of spherical mirrors, which reflect the produced Čerenkov radiation onto an array of photomultiplier tubes, which are used to detect the radiation. By analyzing the observed pattern of photons corresponding to a specific track, one can reconstruct the Čerenkov angle, which is the angle of the emitted photon with respect to the direction of the particle's momentum. For a specific radiator material and a given momentum, the Čerenkov angle is characteristic for the particle that emitted the Čerenkov photon. This property is used by the RICH to identify different types of hadrons. The RICH uses two radiator materials with a different index of refraction: silica aerogel and C_4F_{10} gas. By using this combination of these two radiator materials, the RICH provides a clean separation of pions, kaons, and protons over a large part of the kinematic range of the HERMES experiment.

3.5.2 The transition radiation detector

The TRD consists of six modules each containing a 6.35 mm thick radiator consisting of polypropylene / polyethylene fibers, followed by a 2.54 cm thick multi-wire proportional chamber [34]. A relativistic charged particle passing through the radiator emits transition radiation. The transition radiation results from the fact that the charged particle crosses many subsequent boundaries between media of different dielectric constants. Since the energy of the emitted photons depends on the Lorentz factor $\gamma = E/m$ of the particle, only leptons produce transition radiation with high enough energy to be detected by the proportional chamber. Due to the transition radiation, leptons deposit on average approximately two times more energy in the detector than hadrons. The detection of transition radiation in coincidence with the lepton can be used to discriminate between leptons and hadrons.

3.5.3 The preshower hodoscope

The preshower hodoscope consists of a 1.1 cm thick wall of lead positioned directly in front of a row of vertical plastic scintillator paddles. The thickness of the lead wall corresponds to roughly 2 radiation lengths. Leptons passing through the lead initiate electromagnetic showers, which deposit their energy in the scintillator, whereas hadrons typically produce only a minimum ionizing signal in the scintillator.

3.5.4 The electromagnetic calorimeter

Each half of the electromagnetic calorimeter consists of a 42 × 10 array of lead-glass blocks, which are viewed from the rear by photomultipliers. Each block covers an area of 9×9 cm^2 and is 50 cm long, which corresponds to about 18 radiation lengths for leptons. The associated electromagnetic showers typically deposit more than 99% of their energy within a cluster of 3 × 3 blocks. The detector provides a measurement of the energy of the scattered leptons, and of photons produced in, e.g., the decay of π^0 and η particles. By comparing the deposited energies of the charged particles with the corresponding momenta determined by the tracking system one can use the calorimeter to select leptons.

3.5.5 Lepton-hadron separation

The combined outputs of the RICH, the TRD, the preshower hodoscope, and the CALO can be used to obtain the best possible separation between leptons and hadrons. For each of these detectors the likelihoods $\mathcal{L}^e$ and $\mathcal{L}^h$ for a particle being a lepton (e) or a hadron (h), respectively, are determined. From these likelihoods the PID value is obtained, which is defined as [47]

$$PID = \log_{10}\frac{\mathcal{L}^e}{\mathcal{L}^h} - \log_{10}\Phi, \tag{3.1}$$

where Φ is the ratio of the hadron flux over the lepton flux. This ratio can be estimated in an iterative procedure as is explained in [47]. The summation of PID values for different detectors results into the combined PID values:

$$\begin{aligned}
PID2 &= PID_{CALO} + PID_{pre}, && (3.2)\\
PID3 &= PID_{CALO} + PID_{pre} + PID_{RICH}, && (3.3)\\
PID5 &= PID_{TRD}. && (3.4)
\end{aligned}$$

Requirements on the sum $PID3 + PID5$ or $PID2 + PID5$ are typically used to identify leptons or hadrons.

3.6 Trigger and data acquisition

The readout of detector signals is initiated by the trigger system. The aim of this system is to distinguish events that are interesting for physics research from background events. The trigger corresponding to deep-inelastic electron or positron scattering requires hits in the three scintillator hodoscopes H0, H1 and H2 (see figure 3.2) and a calorimeter response above threshold in two adjacent columns in coincidence with the bunch crossing signal of the HERA beam. For the calorimeter signal it is required that the corresponding energy exceeds an adjustable threshold set above the minimum ionizing energy deposition of 0.8 GeV. In this way charged background events can be suppressed. For normal data taking this threshold is 1.4 GeV and for data taking with a high-density target the threshold is increased to 3.5 GeV. In addition to the DIS trigger various other triggers are used, such as triggers sensitive to produced hadrons and triggers for detector monitoring and calibration.

The actual readout procedure is performed by the data acquisition system (DAQ). The DAQ digitizes the information recorded by all detector components via a system of TDCs and ADCs. This raw information is sorted by the DAQ into a standard data structure for each event and stored in the EPIO (Experimental Physics Input Output) format. The information is organized into runs, with each run corresponding to one EPIO file containing about 450 MB of data. Due to the time needed for readout and event collection not all triggers can be accepted. This results into a certain dead-time fraction, which is defined as the ratio of rejected triggers to generated triggers. A double buffering structure is implemented so that event collection is done in parallel with the readout of the next event, which reduces the dead time. Under normal data-taking conditions a trigger rate up to 500 triggers per second can be achieved with a dead time below 10%.

3.7 The data production chain

A chain of software packages converts the raw data stored in EPIO files into data suitable for physics analysis. The HERMES decoder (HDC) program converts the raw detector signals into basic information, such as hit positions and deposited energies by using information about the geometry, alignment, and calibration of detector components. The HDC output for the tracking detectors is converted into information about tracks by the HERMES reconstruction code (see section 3.4).

The obtained track information is synchronized and merged with the so-called slow-control data. The slow-control data represent information about the status and the readings of the polarimeters, the luminosity monitors, and about the status of the various tracking and PID components. The merged data are organized in terms of bursts each containing the data that are read out during the time interval between subsequent read outs of the slow control, which covers about 10 s. These data are stored in so-called μDST (micro Data Summary Tape) files, which are made available for physics analysis.

Chapter 4

Data selection

In this chapter it is described how the data set used in the analysis was obtained. The data-quality criteria applied at the level of runs and bursts are described in section 4.1. In section 4.2 further selection requirements are described that have been imposed on the data at the level of tracks and events in order to obtain exclusive ρ^0 production data. The imposed requirements do not exclude all background events. Estimates of the remaining contributions of background events to the selected data set are given in section 4.3.

4.1 Data quality selection

Data taken with a transversely-polarized hydrogen target were selected from all data collected by the HERMES experiment in the years 2002-2005. Information from the logbook of the data taking was used to exclude runs with a suspicious data quality or runs taken for the purpose of detector or target studies from the selection. On the burst level, data-quality criteria were applied by using burst lists. These lists are based on the information stored in the μDST productions and are made available for each data production by the HERMES data-quality group [48]. Burst lists contain information about the status of the HERA beam, the target, the DAQ, the data reconstruction, and the spectrometer components for each individual burst. This information is represented by patterns of 32 bits. Each entry in a burst list contains a bit pattern for the top halve and an independent bit pattern for the bottom half of the spectrometer. Each bit specifies whether a specific data quality criterion is fulfilled or not for the corresponding burst. Which of these criteria should be used in the data selection can be specified by the analyzer. The criteria used for the present analysis are discussed below.

Data taking and data reconstruction The dead time of the data acquisition was required to be smaller than 50 %. The first burst of each run was discarded and only bursts were selected that cover a reasonable time period t_{burst} ($0 < t_{\text{burst}} < 11$

s). Bursts were discarded for which problems appeared during data taking or data reconstruction, e.g., problems with synchronization of slow control and event data, jumps of the burst or event numbers, or table overflows.

Performance of the target Bursts during which the target polarization changed its direction are divided into different records corresponding to either a period with stable target polarization or a period with changing target polarization. The data quality information is provided by the burst lists for each record separately. Only records were selected for which the registered polarization direction is either parallel or anti-parallel to the transverse magnet holding field of the target. It was verified that the measured direction of the target polarization was consistent with the expected direction. In order to ensure that the proper transverse target polarization was used in the analysis various requirements were imposed. It was required that the target was in the same transverse polarization mode as listed in the logbook. In addition the registered target valve settings were verified to be correct. Information about the performance and the status of the various target components was used to select only those records for which the components of the target were in the correct operational mode.

Performance of the PID detectors, luminosity monitor, and the tracking detectors The responses of the calorimeter blocks, the scintillator paddles of the preshower hodoscope and the calorimeter blocks of the luminosity monitor were continuously observed by the HERMES gain monitoring system [49]. Records for which at least one dead block, i.e., a block with an incorrect response, was found in at least one of these detector systems, were discarded. If PID information was not available for a record, because of initialization problems, or because the calorimeter threshold was not known, this record was discarded as well. Records for which high voltage trips appeared in the FCs, BCs or the TRD were also discarded.

In addition to the data quality criteria listed above, a reasonable luminosity rate ($1 \leq L \leq 100$ Hz) and a reasonable beam current ($2 \leq I_{\text{beam}} \leq 50$ mA) was required. For all selected data the same data quality requirements were used. In table 4.1 the number of selected bursts for the four years of data taking with a transversely polarized target are listed.

period	bursts	DIS	exclusive ρ^0
2002	177952	708817	536
2003	136174	427200	301
2004	437788	2791326	1942
2005	848276	5382373	4347

Table 4.1: Number of selected bursts, DIS events and exclusive ρ^0 candidates, obtained for each data taking period

4.2 Event Selection

Requirements were imposed at the event level in order to obtain a data set containing an optimized number of exclusive ρ^0 production events and a minimized number of background events. The tracks contained in each event were required to fulfill geometric requirements, which are described in section 4.2.1. In addition to these geometric requirements further requirements were imposed on the kinematic variables of each event, which are discussed in section 4.2.2. A separate data set for inclusive deep-inelastic scattering events was selected in order to have a measure of the luminosity. The selection criteria for that data set are described in section 4.2.3. The number of events in the selected exclusive ρ^0 data set and the inclusive DIS data set are listed in table 4.1.

4.2.1 Geometry of tracks

All tracks were required to consist of both a front and a back partial track. Requirements were imposed on the x and y coordinates of both partial tracks at the z positions of several specific detectors of the spectrometer. These requirements select tracks that pass through the active areas of the tracking and PID detectors and exclude tracks that pass through the septum plate or through one of the field clamps of the spectrometer (see section 3.3). Furthermore it was required that the z-component of the vertex position was within the dimensions of the target cell for each track. An overview of the applied geometric requirements is given in table 4.2.

front partial track		
equipment	position	requirement
target cell	vertex	$\|z\| < 18$ cm
front field clamp	$z = 172$ cm	$\|x\| < 31$ cm
septum plate	$z = 181$ cm	$\|y\| > 7$ cm
rear field clamp	$z = 383$ cm	$\|y\| < 54$ cm

back partial track			
equipment	position	requirement	
rear field clamp	$z = 383$ cm	$\|x\| < 100$ cm,	$\|y\| < 54$ cm
calorimeter	$z = 738$ cm	$\|x\| < 175$ cm,	30 cm $< \|y\| < 108$ cm

Table 4.2: Geometric requirements for front and back partial tracks at different z positions and for the vertex position for the front track. The first column specifies the relevant equipment at each of these positions.

4.2.2 Selection of exclusive ρ^0 events

Because of their short lifetime the produced ρ^0 mesons can only be identified by measuring their decay products. In the event selection the decay channel $\rho^0 \rightarrow$

$\pi^+\pi^-$ was used, which has a branching ratio very close to 100% [15]. Because the momentum of the recoiling nucleon is too low to be detected by the HERMES spectrometer, events were selected with only three tracks: one from the scattered lepton and two from hadrons with opposite charges. The scattered leptons were identified by requiring PID3 + PID5 > 1 and by requiring that the charge is equal to the beam charge. Hadrons were identified by requiring PID3 + PID5 < 1 (see section 3.5.5). Kinematic requirements were imposed on these events in order to select exclusive ρ^0 production events and to exclude events coming from other processes. These requirements are listed in table 4.3.

incl. DIS and exclusive ρ^0 production				
		W^2	$>$	4 GeV^2
		Q^2	$>$	1 GeV^2
		y	$<$	0.85
exclusive ρ^0 production				
0.6	$<$	$M_{2\pi}$	$<$	1.0 GeV
		M_{2K}	$>$	1.04 GeV
		ΔE	$<$	0.6 GeV
		$-t'$	$<$	0.4 GeV^2

Table 4.3: Kinematic requirements for the selection of inclusive DIS events and exclusive ρ^0 production events.

For the selection of scattered DIS leptons requirements were imposed on the kinematic variables Q^2, W and y. The photon virtuality Q^2 was required to be in the deep-inelastic region, i.e., larger than 1 GeV^2. Resonances were excluded by selecting only events for which the invariant mass W of the $\gamma^* p$ system is larger than 2 GeV. The variable y, which is the fractional energy loss of the lepton, was required to be smaller than 0.85 in order to minimize radiative effects.

The invariant mass $M_{2\pi}$ of the two-hadron system was determined under the assumption that both hadrons are pions. The value of $M_{2\pi}$ for resonant $\pi^+\pi^-$ pairs, i.e., pairs produced in the decay $\rho^0 \to \pi^+\pi^-$, is expected to be distributed around the ρ^0 mass. For the $\rho^0(770)$ meson the documented value of the mass is equal to 775.5 ± 0.4 MeV and the value of the width of its decay is equal to 149.4 ± 1.0 MeV [15]. The $M_{2\pi}$ distribution shown in figure 4.1 shows a clear peak around the ρ^0 mass. For the selection of resonant $\pi^+\pi^-$ pairs the requirement $0.6 < M_{2\pi} < 1.0$ GeV has been used. However, without additional requirements the selected sample would be dominated by hadron pairs that cannot be associated with ρ^0 decay, but instead belong to the large slope of background events below the ρ^0 peak. In order to select exclusively produced ρ^0 mesons, the missing mass M_X, which is the rest mass of the recoiling hadronic system, was reconstructed from the kinematics of the detected particles as

$$M_X = \sqrt{(P + q - v)^2}, \tag{4.1}$$

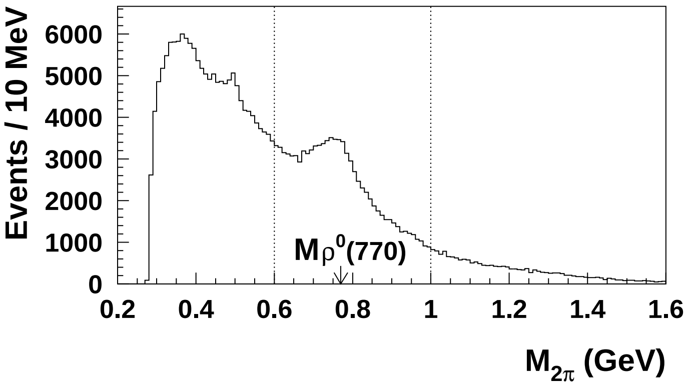

Figure 4.1: The distribution of the reconstructed invariant 2-hadron mass $M_{2\pi}$, assuming that both both hadrons are pions, after imposing requirements to the kinematic variables W^2, Q^2 and y of the scattered lepton. The vertical lines indicate the $M_{2\pi}$ range from which potential ρ^0 decay events are selected.

where P, q, and v are the energy-momentum four-vectors of the incoming proton, the exchanged virtual photon, and the produced ρ^0 meson, respectively. In case of exclusive production M_X is equal to the mass M of the recoil proton. Exclusive events were selected by using the variable (see section 2.4)

$$\Delta E = \frac{M_X^2 - M^2}{2M} \overset{lab}{=} \nu - E_V + \frac{t}{2M}, \tag{4.2}$$

which is the missing energy of the reaction. The measured value of ΔE is peaked around zero for exclusive reactions. This peak is clearly visible in the measured ΔE distribution shown in figure 4.2. In the same figure also the ΔE distribution of a Monte-Carlo simulation of the non-exclusive background obtained with PYTHIA [62] is shown. More details on the Monte Carlo simulation are given in section 6.1. The lower tail of this distribution reaches down to the ΔE region around 0 GeV. Up to $\Delta E \approx 4.0$ GeV the simulated background yield is seen to increase with increasing ΔE. The requirement $\Delta E < 0.6$ GeV was used to select events from the exclusive peak and to suppress non-exclusive background events.

The $-t'$ dependencies of the yield of the selected data and the non-exclusive background data given by the PYTHIA Monte Carlo are shown in figure 4.3. The yield for exclusive ρ^0 production decreases exponentially for an increasing value of the variable $-t'$. According to the Monte Carlo simulation, the fraction of events due to the non-exclusive background fraction increases with $-t'$. In order to restrict the non-exclusive background fraction the requirement $-t' < 0.4$ GeV^2 was applied.

In order to exclude kaon pairs coming from the decay of a ϕ meson the invariant

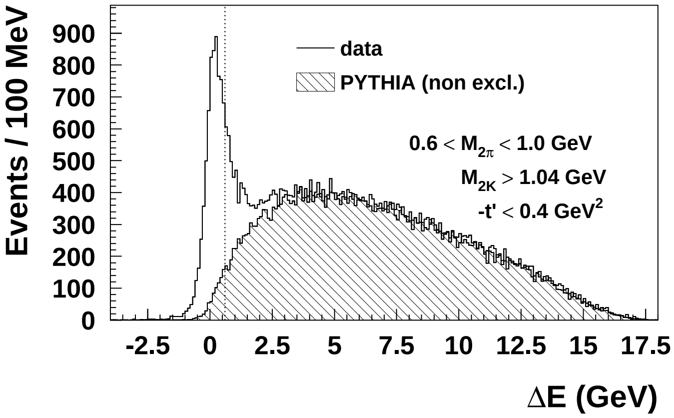

Figure 4.2: The ΔE distributions of the measured data (histogram) and a Monte-Carlo simulation of the non-exclusive background obtained with PYTHIA (hatched area). The kinematic requirements listed in table 4.3 are applied, except for the upper limit on ΔE, which is indicated in the plot by the dotted vertical line.

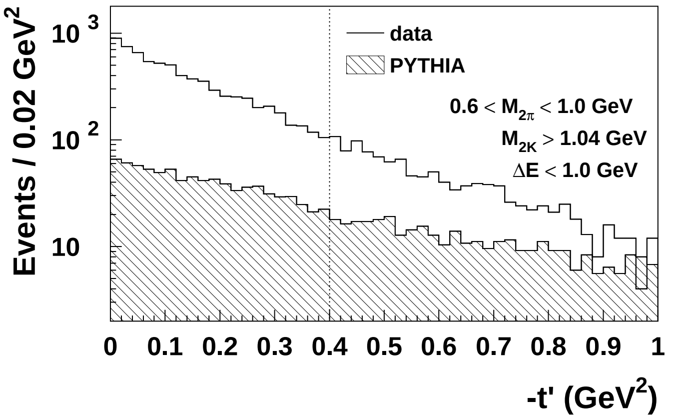

Figure 4.3: The $-t'$ distributions of the measured data (histogram) and a Monte-Carlo simulation of the non-exclusive background obtained with PYTHIA (hatched area). The kinematic requirements listed in table 4.3 are applied, except for the upper limit on $-t'$, which is indicated by the dotted vertical line.

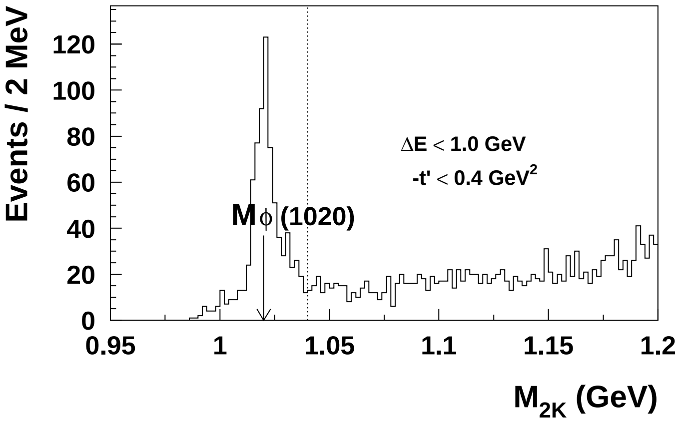

Figure 4.4: The distribution of the reconstructed invariant 2-hadron mass M_{2K}, assuming that both hadrons are kaons, after imposing the kinematic requirements listed in table 4.3, except for the lower and upper limit on $M_{2\pi}$, and the lower limit on M_{2K}, which is indicated by the dotted vertical line.

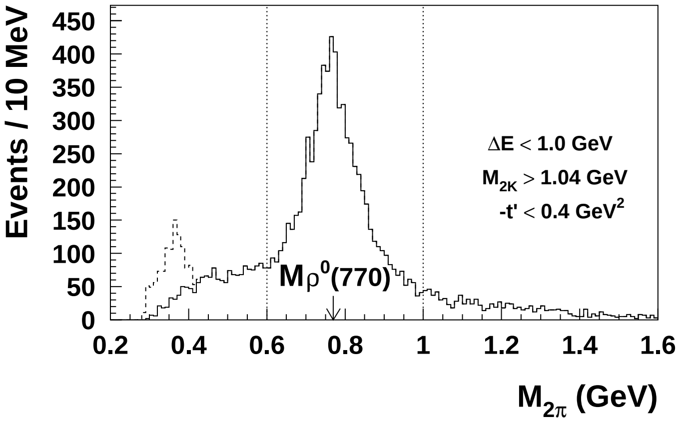

Figure 4.5: The distribution of the reconstructed invariant 2-hadron mass $M_{2\pi}$, assuming that both both hadrons are pions, after imposing the kinematic requirements listed in table 4.3, except for the lower and upper limit on $M_{2\pi}$, which are indicated by the dotted vertical lines. The dashed histogram represents the same distribution without the requirement on M_{2K}.

2-hadron mass M_{2K} was determined under the assumption that both hadrons are kaons. The M_{2K} distribution is shown in figure 4.4. A clear peak is visible around the $\phi(1020)$ mass, which has a documented value of 1019.460 ± 0.019 MeV [15]. This peak was excluded by the requirement $M_{2K} > 1.04$ GeV. The effect of this requirement is illustrated in figure 4.5, which shows the $M_{2\pi}$ distributions after applying the afore-mentioned requirements on ΔE and $-t'$ with (solid histogram) and without the requirement for M_{2K} (dashed histogram). In both cases the $M_{2\pi}$ distribution is dominated by the peak around the ρ^0 mass. However, in the latter case an additional peak appears at lower values of $M_{2\pi}$, which is associated with the decay of the ϕ meson into two kaons. This additional peak had disappeared after the requirement for M_{2K} was imposed.

bin	$\langle Q^2 \rangle$ (GeV^2)	$\langle -t' \rangle$ (GeV^2)	$\langle x \rangle$
$1.0 < Q^2 < 7.0$ GeV^2	1.96	0.133	0.085
$0.5 < Q^2 < 1.0$ GeV^2	0.83	0.121	0.033
$1.0 < Q^2 < 1.4$ GeV^2	1.19	0.130	0.056
$1.4 < Q^2 < 2.0$ GeV^2	1.67	0.132	0.076
$2.0 < Q^2 < 7.0$ GeV^2	3.08	0.137	0.124
$0.00 < -t' < 0.05$ GeV^2	1.91	0.023	0.082
$0.05 < -t' < 0.10$ GeV^2	1.97	0.074	0.084
$0.10 < -t' < 0.20$ GeV^2	1.96	0.145	0.086
$0.20 < -t' < 0.40$ GeV^2	1.99	0.283	0.087
$0.02 < x < 0.07$	1.34	0.128	0.053
$0.07 < x < 0.10$	1.83	0.132	0.083
$0.10 < x < 0.35$	3.14	0.141	0.140

Table 4.4: Average values of Q^2, t' and x for all selected data and for the data binned in Q^2, t' and x.

The number of selected exclusive ρ^0 events for each year of data taking is shown in table 4.1. The selected data from the combined 2002-2005 periods have been binned in the kinematical variables Q^2, t' and x. The binnings that were used and the average values of the kinematic variables for the data binned in these kinematic variables and for all selected data are listed in table 4.4. In addition, events were selected for the lower Q^2 range $0.5 < Q^2 < 1.0$ GeV^2 with the same requirements on all other kinematic variables as those listed in table 4.3. However, as the requirement $Q^2 > 1.0$ GeV^2 was used for the total data set and for the t' and x bins, the information for the lowest Q^2 bin is separated from the information for the other bins by the horizonthal line in table 4.4.

4.2.3 Selection of inclusive DIS events

At the level of runs, bursts, and tracks the same selection criteria were used for inclusive DIS events as for the exclusive ρ^0 production events. Inclusive DIS events were selected by requiring exactly one lepton track with a charge equal to the beam charge. The used kinematic requirements are listed in table 4.3. The number of selected DIS events for each year of data taking are listed in table 4.1.

4.3 Background contributions

In this section it is described how the background contribution to the selected exclusive ρ^0 electroproduction data is determined. Background events can be categorized as non-exclusive and/or non-resonant events. The non-exclusive events can be further subdivided into non-resonant events of the type

$$e + p \to e + h^+ + h^- + X, \tag{4.3}$$

where h^+ and h^- are positively and negatively charged hadrons and X is the undetected hadronic system, and resonant events

$$e + p \to e + \rho^0 + X, \quad \text{followed by} \quad \rho^0 \to \pi^+ + \pi^-. \tag{4.4}$$

The contribution from non-exclusive events of both types has been estimated by means of a PYTHIA Monte Carlo simulation. This is described in more detail in section 4.3.1.

Exclusive non-resonant events contain a detected hadron pair not originating from ρ^0 decay. These events can be represented by

$$e + p \to e + h^+ + h^- + p. \tag{4.5}$$

The background due to these non-resonant hadron pairs can be distinguished from the resonant pion pairs produced in ρ^0 decay, which have a characteristic $M_{2\pi}$ distribution around the ρ^0 mass. The background contribution from the exclusive non-resonant events was estimated by fitting the invariant-mass distribution for exclusive events (see section 4.3.2).

The results of the background studies presented in this chapter are used for the correction for background in the extraction of asymmetries and spin density-matrix elements as described in chapter 5.

4.3.1 Non-exclusive background contribution

The contribution from non-exclusive events was estimated by using a PYTHIA Monte Carlo simulation, in which exclusive processes (PYTHIA process number 91) were excluded. The simulated events were fully tracked through the HERMES spectrometer (see section 6.2) and subject to the same requirements on the level of reconstructed tracks and events as were applied for the exclusive ρ^0 selection (see section 4.2). The main contribution to the thus obtained background events is coming from semi-inclusive DIS events.

The simulated background was normalized to the data by comparing the yields of the Monte Carlo and the data in the region $6 < \Delta E < 10$ GeV, where ΔE represents the missing energy given by equation 4.2. The measured yields are compared to the normalized Monte Carlo yields binned in ΔE in figure 4.6 for all selected data and in figure 4.7 for the data binned in Q^2, x and $-t'$. The Monte Carlo yields were normalized for each kinematic bin separately. The fraction $F_{\rm nex}$ of non-exclusive background events in the exclusive ρ^0 data sample was obtained by comparing the normalized yields in the range $\Delta E < 0.6$ GeV:

$$F_{\rm nex} = \mathcal{N}_{\rm MC} \left. \frac{N_{\rm MC}}{N_{\rm dat}} \right|_{\Delta E < 0.6\,{\rm GeV}}, \quad \text{with} \quad \mathcal{N}_{\rm MC} = \left. \frac{N_{\rm dat}}{N_{\rm MC}} \right|_{6 < \Delta E < 10\,{\rm GeV}}, \tag{4.6}$$

where $N_{\rm dat}$ and $N_{\rm MC}$ represent the number of selected events from, respectively, the data and the Monte Carlo for the indicated ΔE ranges.

In table 4.5 the obtained background fractions are listed for the various kinematic bins. The background fractions vary from 7 to 18%. The listed systematic uncertainties represent the uncertainties due to a possible shift in the measured value of ΔE by 0.1 GeV (see section 7.4).

4.3.2 Exclusive non-resonant background contribution

The contribution from exclusive non-resonant background events has been determined by fitting the measured $M_{2\pi}$ distribution of exclusive events with a theoretical shape, while allowing for a free background contribution. In order to determine the experimental yields of exclusive events, the normalized yield of the non-exclusive Monte Carlo sample was subtracted from the data (see figure 4.8). Next, the experimental yield of exclusive events was corrected for acceptance effects by using a Monte Carlo simulation generated by PYTHIA. In order to perform the acceptance correction, an estimate of the acceptance efficiency $\epsilon_{\rm est}$ was obtained by comparing for each bin in $M_{2\pi}$ the yield $N^{\rm gen}$ at the generated level with the yield $N^{\rm tracked}$ at the tracked level of the simulation,

$$\epsilon_{\rm est} = \frac{N^{\rm tracked}}{N^{\rm gen}}. \tag{4.7}$$

For $M_{2\pi} \gtrsim 0.7$ GeV the acceptance efficiency versus $M_{2\pi}$ was found to be relatively flat, whereas for $M_{2\pi} \lesssim 0.7$ GeV it was found to increase with decreasing $M_{2\pi}$. The acceptance corrected yield binned in $M_{2\pi}$ is shown in figure 4.9 in comparison

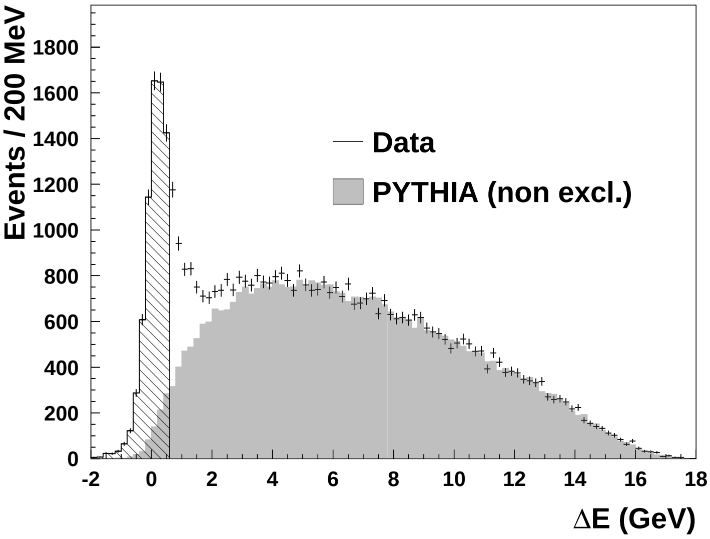

Figure 4.6: The ΔE distribution of the measured data and a Monte Carlo simulation of the non-exclusive background obtained with PYTHIA normalized to the data in the region $6 < \Delta E < 10$ GeV. The hatched region corresponds to the selected data sample.

bin	F_{nex} (%)				
$1.0 < Q^2 < 7.0$ GeV^2	11.2	±	0.3	±	2.2
$0.5 < Q^2 < 1.0$ GeV^2	8.0	±	0.5	±	1.4
$1.0 < Q^2 < 1.4$ GeV^2	9.7	±	0.5	±	1.7
$1.4 < Q^2 < 2.0$ GeV^2	9.7	±	0.5	±	1.9
$2.0 < Q^2 < 7.0$ GeV^2	14.3	±	0.6	±	3.0
$0.02 < x < 0.07$	7.7	±	0.4	±	1.4
$0.07 < x < 0.10$	9.3	±	0.5	±	1.9
$0.10 < x < 0.35$	17.9	±	0.9	±	3.6
$0.00 < -t' < 0.05$ GeV^2	7.1	±	0.4	±	1.6
$0.05 < -t' < 0.10$ GeV^2	9.3	±	0.6	±	1.8
$0.10 < -t' < 0.20$ GeV^2	11.3	±	0.6	±	2.0
$0.20 < -t' < 0.40$ GeV^2	16.8	±	0.8	±	3.2

Table 4.5: The fractions F_{nex} of non-exclusive background contributions to the selected data sample in various kinematic bins. The listed uncertainties are statistical and systematic, respectively.

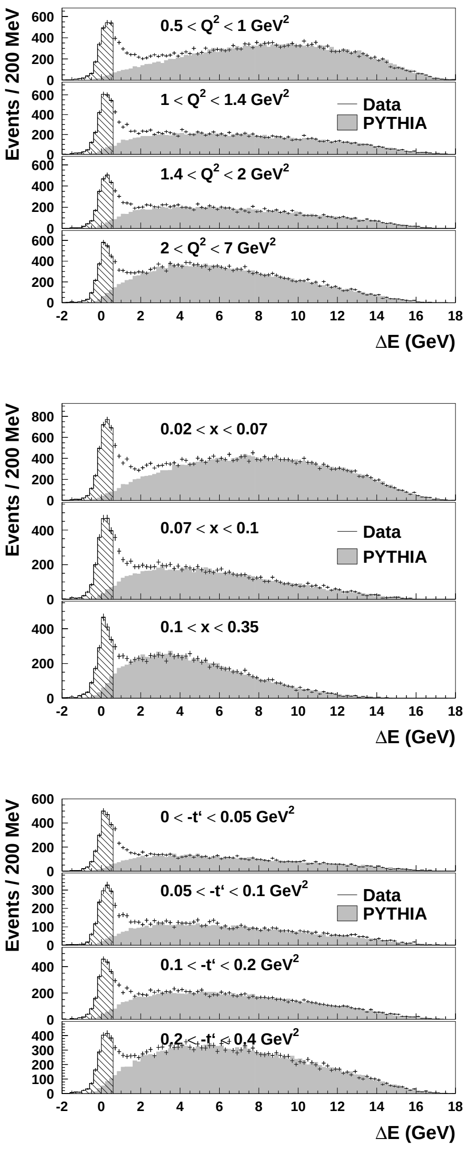

Figure 4.7: The ΔE distributions of the measured data in various kinematic domains compared to the Monte Carlo simulations of the non-exclusive background obtained with PYTHIA normalized to the data in the region $6 < \Delta E < 10$ GeV. The distributions are shown for various kinematic bins in Q^2 (top), x (middle) and $-t'$ (bottom). The hatched regions correspond to the selected data samples.

with the yield before acceptance correction. The effects of the acceptance efficiency on the shape of the distribution are clearly visible in the region $M_{2\pi} \lesssim 0.7$ GeV.

The acceptance-corrected distribution can now be fit with a function describing the shape of the $M_{2\pi}$-distribution for the exclusive resonant events and the non-resonant background events. Various parameterizations describing the $M_{2\pi}$-distribution are available. In the present analysis the commonly used Söding parameterization [25, 50, 51, 52] and Ross-Stodolsky parameterization are used [53]. Both parameterizations make use of the relativistic Breit-Wigner function [54, 55], which is discussed first, as a starting point.

The relativistic Breit-Wigner function Originally the shape of the ρ^0 resonance was described by a relativistic p-wave Breit-Wigner function for a spin-1 particle decaying into two spin-0 particles:

$$\frac{d\sigma}{dM_{2\pi}} \propto f_{\mathrm{BW}}(M_{2\pi}) = \frac{2}{\pi} \frac{M_{2\pi}\, M_\rho\, \Gamma(M_{2\pi})}{\left(M_\rho^2 - M_{2\pi}^2\right)^2 + \left(\, M_\rho \Gamma(M_{2\pi})\,\right)^2}, \tag{4.8}$$

where Γ is given by

$$\Gamma(M_{2\pi}) = \Gamma_\rho \left(\frac{M_{2\pi}^2 - 4M_\pi^2}{M_\rho^2 - 4M_\pi^2} \right)^{3/2} \frac{M_\rho}{M_{2\pi}} \tag{4.9}$$

with M_ρ being the ρ^0 mass, M_π the π mass, and Γ_ρ the intrinsic width of the resonance. As the description of the data was not always satisfactory, alternative parameterizations were introduced.

The Söding parameterization In this parameterization a skewing of the $M_{2\pi}$ distribution is introduced, which possibly arises from the interference of exclusive ρ^0 production,

$$e + p \rightarrow e + \rho^0 + p \quad \text{followed by} \quad \rho^0 \rightarrow \pi^+ + \pi^- \tag{4.10}$$

with the exclusive production of two oppositely charged pions,

$$e + p \rightarrow e + \pi^+ + \pi^- + p. \tag{4.11}$$

The skewed distribution is described by the parameterization

$$\frac{d\sigma}{dM_{2\pi}} \propto c_{\mathrm{BW}}\, f_{\mathrm{BW}}(M_{2\pi}) + f_{\mathrm{I}}(M_{2\pi}) + f_{\mathrm{nr}}(M_{2\pi}), \tag{4.12}$$

where $f_{\mathrm{nr}}(M_{2\pi})$ represents the contribution from exclusive non-resonant two-pion production, which is parameterized as a first order polynomial. The interference term is described by the function

$$f_{\mathrm{I}}(M_{2\pi}) = c_{\mathrm{I}} \frac{M_\rho^2 - M_{2\pi}^2}{\left(M_\rho^2 - M_{2\pi}^2\right)^2 + \left(\, M_\rho \Gamma(M_{2\pi})\,\right)^2}, \tag{4.13}$$

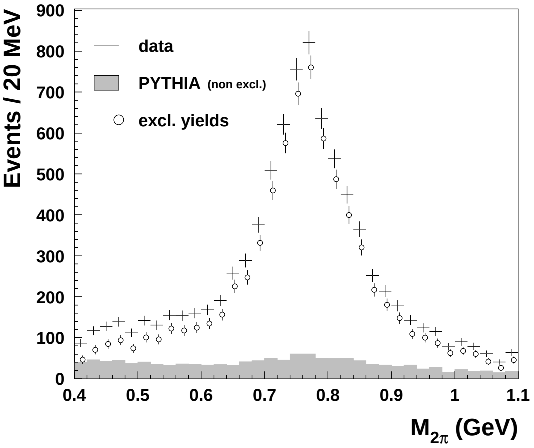

Figure 4.8: Distribution of the invariant mass $M_{2\pi}$ for the data in the region $\Delta E < 0.6$ GeV (crosses). Also shown is a distribution representing a Monte Carlo simulation of non-exclusive background events (histogram), and the distribution for exclusive events (open symbols) obtained after subtracting the simulated background from the data.

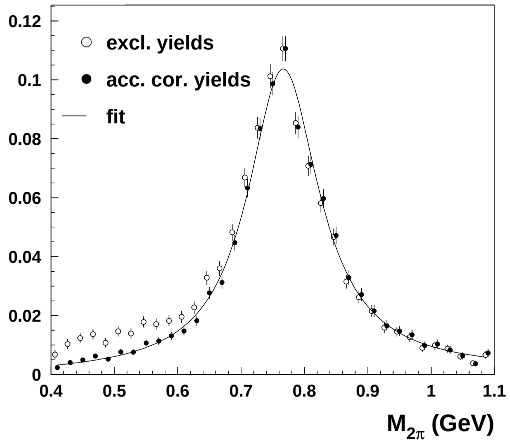

Figure 4.9: Distributions of the invariant mass $M_{2\pi}$ for the data in the region $\Delta E < 0.6$ GeV after subtracting the non-exclusive background simulation. The distributions are shown before (open circles) and after (filled circles) applying the acceptance correction. The curve represents a fit using equation 4.14 to the acceptance corrected data.

which is based on a phenomenological description by Söding [25, 50, 51, 52]. In the fit performed with the Söding parameterization given by equation 4.12, the parameters M_ρ, Γ_ρ, c_{BW}, c_{I}, and the two coefficients of the polynomial $f_{\mathrm{nr}}(M_{2\pi})$ were free parameters.

The Ross-Stodolsky parameterization An alternative description of skewing, without using an interference term, was introduced within a phenomenological model by Ross and Stodolsky [53]. Within this model the skewing of the $M_{2\pi}$ distribution is described by the parameterization

$$\frac{d\sigma}{dM_{2\pi}} \propto c_{\mathrm{BW}}\, f_{\mathrm{BW}}(M_{2\pi}) \left(\frac{M_\rho}{M_{2\pi}}\right)^{n_{\mathrm{skew}}} + f_{\mathrm{nr}}(M_{2\pi}), \tag{4.14}$$

where n_{skew} is referred to as the skewing parameter. In the fit performed with this parameterization M_ρ, Γ_ρ, n_{skew}, c_{BW}, and the two coefficients of the first-order polynomial $f_{\mathrm{nr}}(M_{2\pi})$ were free parameters.

Fit results The acceptance-corrected yields for exclusive events, binned in $M_{2\pi}$, were described by using either the Söding parameterization given by equation 4.12 or the Ross-Stodolsky parameterization given by equation 4.14 (see figures 4.10 and 4.11, respectively). The results for M_ρ and Γ_ρ from both fits, which are listed in table 4.6, are sufficiently close to the documented values of, respectively, 775.5 ± 0.4 MeV and 149.4 ± 1.0 MeV [15]. On basis of these fits the fractions of exclusive non-resonant background events in the exclusive ρ^0 selection (i.e., in the range $0.6 < M_{2\pi} < 1.0$ GeV) were determined to be, respectively -0.01 ± 0.044% and 0.02 ± 0.027%. The negative fraction of -0.01 ± 0.044% is statistically consistent with zero and therefore not considered to be non-physical.

parameterization	M_ρ (GeV)	Γ_ρ (GeV)	χ^2/n.d.f.
Söding (4.12)	0.771 ± 0.0036	0.139 ± 0.0065	0.972
Ross-Stodolsky (4.14)	0.771 ± 0.0038	0.140 ± 0.0065	0.972

Table 4.6: The results for M_ρ and Γ_ρ obtained from fits to the data with the Söding and Ross-Stodolsky parameterizations.

Background from exclusive production of other mesons The exclusive production of mesons other than ρ^0 mesons could result into contributions to the $M_{2\pi}$ distribution, for which corrections need to be applied. At HERMES kinematics the main contributions of this type are the exclusive production of ϕ

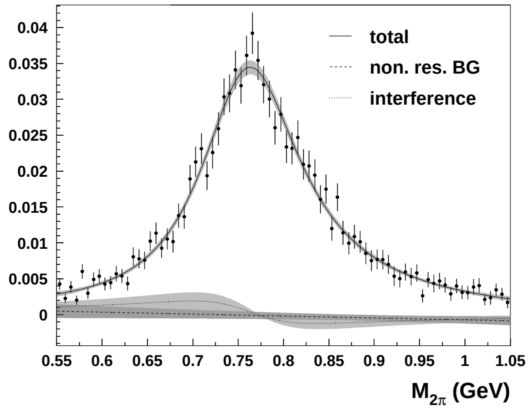

Figure 4.10: Distribution of the invariant mass $M_{2\pi}$ for the data ($\Delta E < 0.6$ GeV) after subtracting the simulated non-exclusive background contribution and correcting for acceptance effects (filled circles). The solid line represents the description of these data using the Söding parameterization (equation 4.12). The dashed line represents the non-resonant contribution and the dotted line the interference term (eq. 4.13).

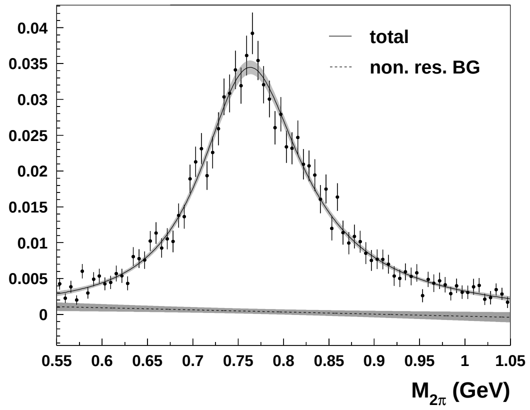

Figure 4.11: Distribution of the invariant mass $M_{2\pi}$ for the data ($\Delta E < 0.6$ GeV) after subtracting the simulated non-exclusive background contribution and correcting for acceptance effects (filled circles). The solid line represents the description of these data using the Ross-Stodolsky parameterization (equation 4.14) and the dashed line represents the non-resonant contribution.

and ω mesons, followed by the decays

$$\phi \rightarrow \quad K^+ + K^- \qquad (\text{B.R.} = 49\%), \tag{4.15}$$

$$\begin{aligned} \omega \rightarrow \quad & \pi^+ + \pi^- + \pi^0 && (\text{B.R.} = 89\%) \\ & \pi^+ + \pi^- && (\text{B.R.} = 2\%), \end{aligned} \tag{4.16}$$

where B.R. denotes the branching ratio of the decay channel. The contribution of the channel $\phi \rightarrow K^+ + K^-$ is almost entirely excluded by the requirement $M_{2K} >$ 1.04 GeV, which has been applied in the data analysis (see section 4.2). The decay channel $\omega \rightarrow \pi^+ + \pi^- + \pi^0$ results in an $M_{2\pi}$ distribution centered around $M_{2\pi} = 0.45$ GeV, for which only a small fraction satisfies the selection requirement $M_{2\pi} > 0.6$ GeV. Since the π^0 remains undetected, only a negligibly small fraction of these events passes the requirement $\Delta E < 0.6$ GeV. The contribution from the decay channel $\omega \rightarrow \pi^+\pi^-$ was found to be very small at HERMES kinematics [25]. For this reason it is neglected here in the determination of the background contributions.

Chapter 5

Extraction methods

In this chapter a description is given of the procedures used to extract the $\sin(\phi-\phi_S)$ moments of the transverse target-spin asymmetry for longitudinal and transverse ρ^0 polarization. The procedures used to extract the corresponding spin density-matrix elements (SDMEs) for an unpolarized and a transversely polarized target are presented as well. The extraction procedures make use of an unbinned maximum likelihood fit method. Other methods considered are the moments method and the binned least-χ^2 fit, which are briefly described in appendix C. The unbinned maximum likelihood fit is preferred, because it features a good performance at low statistics, the possibility to take into account the acceptance of the HERMES spectrometer in the extraction procedure, and the possibility to account for the contribution from background processes.

The unbinned maximum likelihood fit method is described in section 5.1. The used parameterizations of the fit function are described in section 5.2. As the fit function depends on whether the $\sin(\phi-\phi_S)$ moments of A_{UT} are extracted or the SDMEs for an unpolarized or a transversely polarized target, this section contains a discussion of several parameterizations. The method used to account for the spectrometer acceptance in the fits is described in section 5.3. The method used to take the contribution from background processes into account in the extraction procedure is the subject of section 5.4.

5.1 The unbinned maximum likelihood fit

In the unbinned maximum likelihood method the fit function is a parameterization of the probability density function (PDF) describing the distribution of the events of interest. One performs the fit by tuning the fit parameters such that one maximizes the likelihood that the distribution of events originates from the corresponding PDF. For a PDF $f(\boldsymbol{x};\boldsymbol{\theta})$, described in terms of n parameters $\boldsymbol{\theta}=(\theta_1,\ldots,\theta_n)$ as a function of a set of variables $\boldsymbol{x}$, the likelihood is calculated as the product

$$L(\boldsymbol{\theta}) = \prod_{i=1}^{N} f(\boldsymbol{x}_i;\boldsymbol{\theta}), \tag{5.1}$$

where $i = 1, 2, \ldots N$ labels the included events. In practice, when performing the fit, one maximizes $\ln L(\boldsymbol{\theta})$, which is given by the sum

$$\ln L(\boldsymbol{\theta}) = \sum_{i=1}^{N} \ln f(\boldsymbol{x}_i;\boldsymbol{\theta}). \tag{5.2}$$

The fit result is the set of parameter values $\widehat{\boldsymbol{\theta}} = (\widehat{\theta_1}, \ldots, \widehat{\theta_n})$, for which $\ln L$ is at its maximum. One determines the corresponding covariance matrix V from the matrix of second derivatives of $\ln L$ by using

$$(\widehat{V}^{-1})_{km} = \left.\frac{\partial^2 \ln L}{\partial\theta_k \partial\theta_m}\right|_{\widehat{\boldsymbol{\theta}}}. \tag{5.3}$$

The statistical uncertainties of the fit parameters are then obtained from the diagonal elements of the covariance matrix as $\Delta\widehat{\theta}_m = (V_{mm})^{1/2}$.

5.2 Parameterizations of the used PDFs

In each of the used extraction procedures the measured yields are described by a PDF that is expressed as the normalized product of a function representing the cross section and a function ϵ representing the acceptance efficiency of the spectrometer. More explicitly, the PDFs are expressed as

$$N(\phi, \phi_S) \;=\; \mathcal{N}^{-1}\, \epsilon(\phi, \phi_S)\, \sigma_0\, \frac{d\psi}{d\phi_S}\, W^{\ell}(\phi, \phi_S). \tag{5.4}$$

The actually used expressions also include the dependencies on the ρ^0 decay angles, which are suppressed here for simplicity reasons. The factor $\mathcal{N}$ represents the normalization integral of the considered PDF, which is defined in section 5.3. The factor σ_0 represents the cross section integrated over the angles ϕ, ϕ_S, and the ρ^0 decay angles. In the used parameterizations the dependence of the angular distribution W^{ℓ} on the kinematic variables x, Q^2, t is ignored. For this reason, the kinematic dependence of σ_0 is not taken into account either. As a result, the factor σ_0 cancels due to the normalization. Therefore, no free parameter is assigned for this factor. The factor $d\psi/d\phi_S$ is given by [13]

$$\frac{d\psi}{d\phi_S} = \frac{\cos\theta_\gamma}{1 - \sin^2\theta_\gamma\, \sin^2\phi_S}. \tag{5.5}$$

This factor takes into account the fact that the yields are evaluated differentially in the azimuthal angle ϕ_S, rather than the angle ψ. The difference between the angles ϕ_S and ψ is that the former is defined with respect to the virtual-photon direction and the latter with respect to the lepton-beam direction (see section 2.4.1).

The last term in equation 5.4 is the angular distribution function W^ℓ given by

$$W^\ell(\phi, \phi_S) = W_{UU}(\phi) \,+\, P_T\, W^\ell_{UT}(\phi, \phi_S). \tag{5.6}$$

Here beam-polarization dependent terms are ignored. The functions W_{UU} and W^ℓ_{UT} represent, respectively, the angular distribution for an unpolarized target and the angular distribution corresponding to the transverse target polarization P_T defined with respect to the beam direction. One can parameterize the distribution W_{UU} either using the Wolf-Schilling [14] or the Diehl [11] formalism. One can parameterize the distribution W^ℓ_{UT} by using either a combination of the Wolf-Schilling [14] and the Diehl-Sapeta formalisms or the more recent Diehl [11] formalism.

In the present analysis the transverse target polarization P_T is defined to have a positive or negative sign if the orientation of the target polarization was directed parallel or anti-parallel to the negative y-axis of the HERMES coordinate system, respectively. However, in the theoretical framework of [11, 13] the transverse target polarization is defined to be positive. In the convention used in the present analysis a sign change of P_T at a fixed value of ϕ_S is equivalent to a transformation $\phi_S \rightarrow \phi_S + \pi$ in the theoretical framework. Since the spectrometer acceptance is independent from the orientation of the target polarization, the use of the data for both orientations of the polarization allows us to distinguish the transverse target-spin asymmetry A_{UT} from possible asymmetries of the acceptance under this transformation (to the extent that this has not been accounted for in the description of the acceptance efficiency ϵ).

As mentioned in section 2.8 the angular distribution W^ℓ_{UT} receives an admixture from the longitudinal component S_L of the target polarization with respect to the virtual-photon direction. In section 5.2.1 it is described in more detail how this admixture affects W^ℓ_{UT}. Different parameterizations of the angular distribution function are used in the extraction of the $\sin(\phi - \phi_S)$ moments of the transverse target-spin asymmetry A_{UT}. The parameterization described in section 5.2.2 uses a combination of the Diehl-Sapeta [13] and the Wolf-Schilling [14] formalisms. The alternative parameterization described in section 5.2.3 uses only the Diehl formalism [11]. The parameterizations used in the extraction of the SDMEs for an unpolarized and a transversely polarized target are presented in section 5.2.4.

5.2.1 The admixture from longitudinal target polarization

The angular distribution W^ℓ_{UT} for the case of an experimental setup with a transversely polarized target is a mixture of the angular distributions W_{UT} and W_{UL} (see section 2.8). This mixture is given by

$$P_T\, W^\ell_{UT}(\theta_\gamma, \phi, \phi_S) \;=\; S_T(\theta_\gamma, \phi_S)\, W_{UT}\,(\phi, \phi_S) \,+\, S_L(\theta_\gamma, \phi_S)\, W_{UL}(\phi). \tag{5.7}$$

The mixing of these distributions is a result of the fact that the angle θ_γ between the lepton-beam direction and the virtual-photon direction is non-zero. Hence, for a definite transverse target polarization P_T with respect to the lepton-beam direction there is a transverse component S_T, but also a longitudinal component S_L of the polarization with respect to the virtual-photon direction. These components are given by (see equation 2.26 in section 2.4.1)

$$S_T(\theta_\gamma, \phi_S) = \frac{\cos\theta_\gamma}{\sqrt{1 - \sin^2\theta_\gamma \, \sin^2\phi_S}} \, P_T, \tag{5.8}$$

$$S_L(\theta_\gamma, \phi_S) = \frac{\sin\theta_\gamma \, \cos\phi_S}{\sqrt{1 - \sin^2\theta_\gamma \, \sin^2\phi_S}} \, P_T. \tag{5.9}$$

For the selected exclusive ρ^0 data the distribution of the angle θ_γ and the corresponding distributions of S_L/P_T and S_T/P_T are shown in figure 5.1 and figure 5.2, respectively. The deviation of S_T from P_T is on average only 0.3 % with a variance of 0.2 %, whereas $|S_L/P_T|$ is on average 7.2 % with a variance of 2.7 %. Since the magnitude of S_L is relatively small, the contribution from W_{UT} dominates over the contribution from W_{UL}.

One obtains the explicit expression for the angular distribution W^ℓ_{UT} by inserting equations 5.8 and 5.9 into equation 5.7. The resulting expression can be simplified by dividing it by the overall factor $(1 - \sin^2\theta_\gamma \, \sin^2\phi_S)^{-1/2}$, which is close to unity. The remaining angular distribution W'_{UT} can be expressed as (see equation 2.57)

$$\begin{aligned} W'_{UT}(\theta_\gamma, \phi, \phi_S) &= (1 - \sin^2\theta_\gamma \, \sin^2\phi_S)^{1/2} \, W^\ell_{UT}(\theta_\gamma, \phi, \phi_S) \\ &= \cos\theta_\gamma \, W_{UT}(\phi, \phi_S) \, + \, \sin\theta_\gamma \cos\phi_S \, W_{UL}(\phi). \end{aligned} \tag{5.10}$$

Equivalently, one can express the asymmetry A'_{UT} as (see equation 2.58)

$$\begin{aligned} A'_{UT}(\theta_\gamma, \phi, \phi_S) &= (1 - \sin^2\theta_\gamma \, \sin^2\phi_S)^{1/2} \, A^\ell_{UT}(\theta_\gamma, \phi, \phi_S) \\ &= \cos\theta_\gamma \, A_{UT}(\phi, \phi_S) \, + \, \sin\theta_\gamma \cos\phi_S \, A_{UL}(\phi). \end{aligned} \tag{5.11}$$

In the present analysis the angular distribution W'_{UT} is effectively evaluated integrated over the angle θ_γ. Thus, the contributions to the angular distribution from W_{UT} and W_{UL} are not disentangled. The admixture from W_{UL} possibly affects the results for the transverse target-spin asymmetries or the SDMEs for a transversely polarized target. However, because of the relatively small magnitude of S_L and the relatively small differences between S_T and P_T, such effects are expected to be limited. As described in section 7.4, systematic uncertainties have been assigned to the results for the SDMEs for a transversely polarized target and the transverse target-spin asymmetries in order to account for the admixture from longitudinal target polarization.

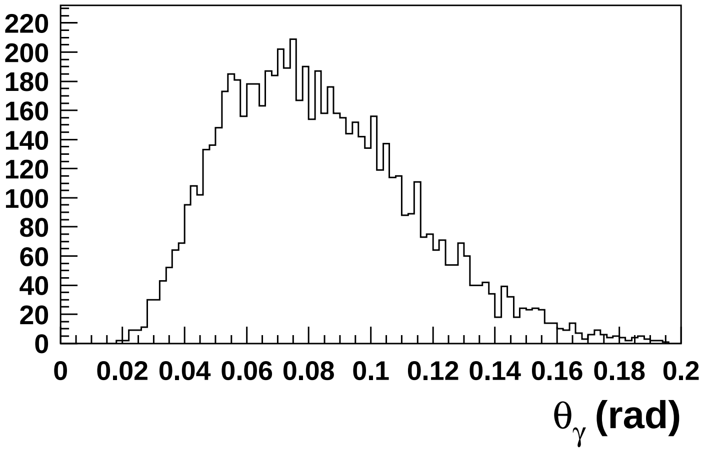

Figure 5.1: The distribution of the angle θ_γ between the directions of the incoming lepton and the virtual photon in the target rest frame for the selected exclusive ρ^0 production data.

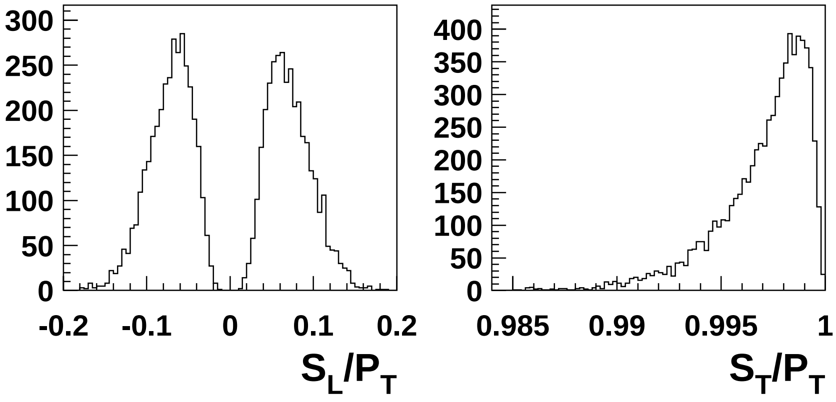

Figure 5.2: The distributions of the ratios S_L/P_T and S_T/P_T for the selected exclusive ρ^0 production data.

	$W_{UT}(\phi,\phi_S)$	$W_{UL}(\phi,\phi_S)$	$W'_{UT}(\phi,\phi_S)$
All	5	2	6

Table 5.1: Number of independent terms for the angular distributions W_{UT}, W_{UL} and W'_{UT} when evaluated differentially in the angles ϕ, ϕ_S and integrated over the ρ^0 angles $\phi_{\pi\pi}, \theta_{\pi\pi}$.

	$W_{UT}(\phi,\phi_S,\theta_{\pi\pi})$	$W_{UL}(\phi,\phi_S,\theta_{\pi\pi})$	$W'_{UT}(\phi,\phi_S,\theta_{\pi\pi})$
LL	5	2	6
TT	5	2	6
All	10	4	12

Table 5.2: Number of independent terms for the angular distributions W_{UT}, W_{UL} and W'_{UT} when evaluated differentially in the angles $\phi, \phi_S, \theta_{\pi\pi}$ and integrated over the angle $\phi_{\pi\pi}$. These numbers are given for all terms (All) and for the terms corresponding to longitudinal (LL) and transverse (TT) ρ^0 polarization.

	$W_{UT}(\phi,\phi_S,\phi_{\pi\pi},\theta_{\pi\pi})$	$W_{UL}(\phi,\phi_S,\phi_{\pi\pi},\theta_{\pi\pi})$	$W'_{UT}(\phi,\phi_S,\phi_{\pi\pi},\theta_{\pi\pi})$
LL	5	2	6
LT	10	5	12
TT	15	7	18
All	30	14	36

Table 5.3: Number of independent terms for the angular distributions W_{UT}, W_{UL} and W'_{UT} when evaluated differentially in the angles $\phi, \phi_S, \phi_{\pi\pi}, \theta_{\pi\pi}$. These numbers are given for all terms (All) and for the terms corresponding to the ρ^0 polarizations: longitudinal (LL), interference (LT), and transverse (TT).

5.2.2 Extraction of $A_{UT,\rho_L}^{\sin(\phi-\phi_S)}$ using the Diehl-Sapeta and the Wolf-Schilling formalisms

The extraction procedure initially applied to determine the $\sin(\phi-\phi_S)$ moment of A_{UT} uses a combination of the Diehl-Sapeta and the Wolf-Schilling formalisms. The description of the PDF in this procedure is given by

$$\begin{aligned} N(\phi,\phi_S) \;&=\; \mathcal{N}^{-1}\,\epsilon(\phi,\phi_S)\,\frac{d\psi}{d\phi_S}\,\sigma_0\,\times \\ &\qquad \widehat{W}_{UU}\,\left(1+A_{UU}(\phi)+P_T A_{UT}^{\ell}(\phi,\phi_S)\right), \end{aligned} \tag{5.12}$$

where for the sake of simplicity the dependencies on the ρ^0 angles are omitted. The angular distribution function W^{ℓ} is expressed in terms of the asymmetries A_{UU} and A_{UT}^{ℓ} according to equation 2.59, where $\widehat{W}_{UU}$ is the angular distribution W_{UU} integrated over ϕ. The dependence of A_{UT}^{ℓ} on the angles ϕ and ϕ_S is expanded in terms of the six azimuthal moments of A'_{UT} (see table 5.1). This expansion, which is done within the Diehl-Sapeta formalism, is given by[1]

$$\begin{aligned} A'_{UT}(\phi,\phi_S) \;&=\; (1-\sin^2\theta_\gamma\,\sin^2\phi_S)^{1/2}\;A_{UT}^{\ell}(\phi,\phi_S) \\ &=\; A_{UT}^{\prime\,\sin(\phi-\phi_S)}\sin(\phi-\phi_S)\;+\;A_{UT}^{\prime\,\sin(\phi+\phi_S)}\sin(\phi+\phi_S)\;+ \\ &\qquad A_{UT}^{\prime\,\sin(3\phi-\phi_S)}\sin(3\phi-\phi_S)\;+\;A_{UT}^{\prime\,\sin(\phi_S)}\sin(\phi_S)\;+ \\ &\qquad A_{UT}^{\prime\,\sin(2\phi-\phi_S)}\sin(2\phi-\phi_S)\;+\;A_{UT}^{\prime\,\sin(2\phi+\phi_S)}\sin(2\phi+\phi_S)\,. \end{aligned} \tag{5.14}$$

In order to extract the moments of A'_{UT} for longitudinally and transversely polarized ρ^0 mesons separately, the dependencies of the yields on the ρ^0 angle $\theta_{\pi\pi}$ are included in the description of the PDF. As follows from equation 2.54 this description is given by

$$\begin{aligned} N(\phi,\phi_S,\theta_{\pi\pi}) \;&=\; \mathcal{N}^{-1}\,\epsilon(\phi,\phi_S,\theta_{\pi\pi})\,\frac{d\psi}{d\phi_S}\,\sigma_0\,\times \\ &\frac{3}{2}\Big[\;\widehat{W}_{UU}^{LL}\,\cos^2\theta_{\pi\pi}\left(1+A_{UU,\rho_L}(\phi)+P_T A_{UT,\rho_L}^{\ell}(\phi,\phi_S)\right)\;+ \\ &\qquad \widehat{W}_{UU}^{TT}\,\sin^2\theta_{\pi\pi}\left(1+A_{UU,\rho_T}(\phi)+P_T A_{UT,\rho_T}^{\ell}(\phi,\phi_S)\right)\Big], \end{aligned} \tag{5.15}$$

---

[1] As is explained in section 5.2.1 the asymmetry A'_{UT} contains a small admixture from the asymmetry A_{UL}, which is not distinguished in the parameterization given by equation 5.14. Therefore, the azimuthal moments of A'_{UT} appearing in equation 5.14 are defined slightly differently as compared to those in equation 2.52 as

$$A_{UT}^{\prime\,\omega(\phi,\phi_S)} = \tag{5.13}$$

$$\left.\frac{2\int d\phi\,d\phi_S\,\omega(\phi,\phi_S)\,\sqrt{1-\sin^2\theta_\gamma\,\sin^2\phi_S}\;\left[W^{\ell}(\phi,\phi_S)\;-\;W^{\ell}(\phi,\phi_S+\pi)\right]}{\int d\phi\,d\phi_S\;\left[W^{\ell}(\phi,\phi_S)\;+\;W^{\ell}(\phi,\phi_S+\pi)\right]}\right|_{P_T=1,\,P_L=0}.$$

In the following the azimuthal moments of A'_{UT} are also referred to as the azimuthal moments of A_{UT}^{ℓ}. In that case one should bear in mind the presence of the additional factor $(1-\sin^2\theta_\gamma\,\sin^2\phi_S)^{-1/2}$ in A_{UT}^{ℓ}, which is close to unity.

where the asymmetries for longitudinal and transverse ρ^0 polarization are labelled by ρ_L and ρ_T, respectively. The terms $\widehat{W}_{UU}^{LL}$ and $\widehat{W}_{UU}^{TT}$ are given in the Wolf-Schilling formalism by

$$\widehat{W}_{UU}^{LL} = r_{00}^{04}, \qquad \widehat{W}_{UU}^{TT} = 1 - r_{00}^{04}. \tag{5.16}$$

The unpolarized asymmetries A_{UU,ρ_L} and A_{UU,ρ_T} are each parameterized in terms of their azimuthal moments, analogous to equation 2.49. These moments are given in terms of SDMEs in the Wolf-Schilling formalism by

$$A_{UU,\rho_L}^{\cos(\phi)} = \frac{\sqrt{2\,\varepsilon\,(1+\varepsilon)}\,r_{00}^{5}}{r_{00}^{04}}, \qquad A_{UU,\rho_L}^{\cos(2\phi)} = \frac{-\varepsilon r_{00}^{1}}{r_{00}^{04}}, \tag{5.17}$$

$$A_{UU,\rho_T}^{\cos(\phi)} = \frac{2\sqrt{2\,\varepsilon\,(1+\varepsilon)}\,r_{11}^{5}}{(1-r_{00}^{04})}, \qquad A_{UU,\rho_T}^{\cos(2\phi)} = \frac{-2\varepsilon r_{11}^{1}}{(1-r_{00}^{04})}. \tag{5.18}$$

The SDMEs are determined from a separate fit described in section 5.2.4. The thus obtained values for r_{00}^{04} and the SDMEs appearing in equations 5.17 and 5.18 are inserted in the description of the PDF as fixed parameters. The $\rho_L - \rho_T$ separated asymmetries A_{UT,ρ_L}^{ℓ} and A_{UT,ρ_T}^{ℓ} are each parameterized in terms of 6 azimuthal moments analogous to equation 5.14. These, in total, 12 moments (see table 5.2) are the free parameters of the fit.

5.2.3 Extraction of $A_{UT,\rho_L}^{\sin(\phi-\phi_S)}$ using the Diehl formalism

When the more recent Diehl formalism [11] for vector-meson production from a polarized target became available, it was decided to use this formalism in the extraction of the $\sin(\phi-\phi_S)$ moment of A_{UT} for longitudinally polarized ρ^0 mesons. In comparison to the Diehl-Sapeta and the Wolf-Schilling formalisms the Diehl formalism provides a more complete description of the angular distribution function, since it includes the dependencies on the angle $\phi_{\pi\pi}$ for a polarized target as well. By including the dependencies on this angle in the fit function one accounts for the coupling between the $\phi_{\pi\pi}$ dependencies of the cross section and the acceptance. In this way possible cross contaminations are avoided (see section 5.3).

In this approach the used PDF is thus a function of all the angles $\phi, \phi_s, \phi_{\pi\pi}, \theta_{\pi\pi}$, which reads

$$\begin{aligned} N(\phi, \phi_S, \phi_{\pi\pi}, \theta_{\pi\pi}) &= \mathcal{N}^{-1}\,\epsilon(\phi, \phi_s, \phi_{\pi\pi}, \theta_{\pi\pi})\,\frac{d\psi}{d\phi_S}\,\sigma_0\,\times \\ &\quad \Big(W_{UU}(\phi, \phi_{\pi\pi}, \theta_{\pi\pi}) + P_T\,W_{UT}^{\ell}(\phi, \phi_S, \phi_{\pi\pi}, \theta_{\pi\pi})\Big). \end{aligned} \tag{5.19}$$

The unpolarized angular distribution W_{UU} is parameterized in terms of 15 (combinations of) SDMEs, which are kept fixed in the fit. The parameterization of W_{UU} and the determination of the corresponding SDMEs is described in section 5.2.4. The angular distribution W_{UT}^{ℓ} is decomposed in terms of distributions for different polarizations of the ρ^0 meson. This decomposition is given by

$$\begin{aligned} W'_{UT}(\phi_S,\phi,\phi_{\pi\pi},\theta_{\pi\pi}) &= (1-\sin^2\theta_\gamma\ \sin^2\phi_S)^{1/2}\ W^{\ell}_{UT}(\phi_S,\phi,\phi_{\pi\pi},\theta_{\pi\pi}) \\ &= \frac{3}{4\pi}\Big[\ W'^{LL}_{UT}(\phi_S,\phi)\cos^2\theta_{\pi\pi} + \\ &\qquad W'^{LT}_{UT}(\phi_S,\phi,\phi_{\pi\pi})\sqrt{2}\cos\theta_{\pi\pi}\sin\theta_{\pi\pi} + \\ &\qquad W'^{TT}_{UT}(\phi_S,\phi,\phi_{\pi\pi})\sin^2\theta_{\pi\pi}\ \Big], \end{aligned} \tag{5.20}$$

where the superscripts LL, LT, and TT specify the ρ^0 polarization states (see equations 2.42 and 2.60). In the parameterization of the angular distribution the contributing distributions W'^{LL}_{UT}, W'^{LT}_{UT}, W'^{TT}_{UT} are expanded as

$$\begin{aligned} & W'^{AB}_{UT}(\phi,\phi_S,\phi_{\pi\pi}) = \\ &\quad \sum_{m,n} W'^{AB,\sin(\phi-\phi_S)\cos(m\phi+n\phi_{\pi\pi})}_{UT}\sin(\phi-\phi_S)\cos(m\phi+n\phi_{\pi\pi}) + \\ &\quad \sum_{m,n} W'^{AB,\cos(\phi-\phi_S)\sin(m\phi+n\phi_{\pi\pi})}_{UT}\cos(\phi-\phi_S)\sin(m\phi+n\phi_{\pi\pi}), \end{aligned} \tag{5.21}$$

whit $A = L,T$ and $B = L,T$. One can identify the coefficients

$$W'^{AB,\sin(\phi-\phi_S)\cos(m\phi+n\phi_{\pi\pi})}_{UT}, \qquad W'^{AB,\cos(\phi-\phi_S)\sin(m\phi+n\phi_{\pi\pi})}_{UT} \tag{5.22}$$

by comparing equation 5.21 with the explicit expressions for the distributions W'^{AB}_{UT} given in [11]. Note that these distributions receive small admixtures from the distributions W^{AB}_{UL}, which are not made explicit in the used parameterization of the fit function (see section 5.2.1). As follows from table 5.3 the number of independent terms needed to describe W^{ℓ}_{UT} is 36. The corresponding 36 parameters are the free parameters of the fit.

From the extracted fit parameters one obtains the $\sin(\phi-\phi_S)$ moments of A'_{UT} for longitudinally and transversely polarized ρ^0 mesons using (see equation 2.53)

$$A'^{\sin(\phi-\phi_S)}_{UT,\rho_L} = \frac{W'^{LL,\sin(\phi-\phi_S)}_{UT}}{\widehat{W}^{LL}_{UU}}, \qquad A'^{\sin(\phi-\phi_S)}_{UT,\rho_T} = \frac{W'^{TT,\sin(\phi-\phi_S)}_{UT}}{\widehat{W}^{TT}_{UU}}. \tag{5.23}$$

The denominators of these expressions can be expressed in terms of the SDMEs in the Diehl formalism as

$$\widehat{W}^{LL}_{UU} = u^{0\,0}_{++} + \varepsilon u^{0\,0}_{0\,0}, \qquad \widehat{W}^{TT}_{UU} = 1-(u^{0\,0}_{++} + \varepsilon u^{0\,0}_{0\,0}). \tag{5.24}$$

The combination $(u^{0\,0}_{++} + \varepsilon u^{0\,0}_{0\,0})$ is determined from the fit to the unpolarized data described in the next section 5.2.4.

5.2.4 Extraction of SDMEs

The SDMEs for an unpolarized target The SDMEs corresponding to an unpolarized target and an unpolarized beam are extracted from the data taken with a transversely polarized target. Since the luminosities for the opposite orientations of the target polarization are to good approximation equal, the net target polarization for these data can be taken equal to zero. The PDF used in the extraction of the unpolarized SDMEs reads

$$N(\phi, \phi_{\pi\pi}, \theta_{\pi\pi}) \;=\; \mathcal{N}^{-1}\, \epsilon(\phi, \phi_{\pi\pi}, \theta_{\pi\pi})\, \sigma_0\, W_{UU}(\phi, \phi_{\pi\pi}, \theta_{\pi\pi}). \tag{5.25}$$

As is explained in section 5.3, the inclusion of the normalization factor $\mathcal{N}$ is relevant particularly for a fit with this PDF, since $\mathcal{N}$ depends on the parameters describing the angular distribution W_{UU}.

The distribution W_{UU} is decomposed according to equation 2.60 as

$$\begin{aligned} W_{UU}(\phi, \phi_{\pi\pi}, \theta_{\pi\pi}) \;&=\; \frac{3}{4\pi}\Big[\, W_{UU}^{LL}(\phi)\cos^2\theta_{\pi\pi} + \\ &\qquad W_{UU}^{LT}(\phi, \phi_{\pi\pi})\sqrt{2}\cos\theta_{\pi\pi}\sin\theta_{\pi\pi} + \\ &\qquad W_{UU}^{TT}(\phi, \phi_{\pi\pi})\sin^2\theta_{\pi\pi} \quad \Big]. \end{aligned} \tag{5.26}$$

Here the angular distributions W_{UU}^{LL}, W_{UU}^{LT}, W_{UU}^{TT} for the different ρ^0 polarization states are parameterized in terms of (combinations of) the SDMEs $u_{mn}^{\alpha\beta}$. The expression used for this parameterization follows directly from equations 2.70 and 2.71. It is noted that SDMEs corresponding to the same ρ^0 polarization, but to different virtual-photon polarizations cannot be separated in the fit procedure. Therefore, the number of independent parameters describing W_{UU} is 15.

Alternatively, by using equation 2.61, one can parameterize the distribution W_{UU} in terms of the SDMEs in the Wolf-Schilling formalism [14]. However, in the present analysis we obtained the SDMEs in the Wolf-Schilling formalism by converting the fit results for the SDMEs obtained in the Diehl formalism using equations D.1-D.15. In this conversion the statistical uncertainties were propagated by using the covariance matrix of the fit.

The SDMEs for a transversely polarized target The PDF used in the extraction of the SDMEs corresponding to a transversely polarized target and an unpolarized beam is given by

$$\begin{aligned} N(\phi, \phi_S, \phi_{\pi\pi}, \theta_{\pi\pi}) \;&=\; \mathcal{N}^{-1}\, \epsilon(\phi, \phi_s, \phi_{\pi\pi}, \theta_{\pi\pi})\, \frac{d\psi}{d\phi_S}\, \sigma_0 \;\times \\ &\Big(W_{UU}(\phi, \phi_{\pi\pi}, \theta_{\pi\pi}) \;+\; S_T\, W_{UT}(\phi, \phi_S, \phi_{\pi\pi}, \theta_{\pi\pi})\Big). \end{aligned} \tag{5.27}$$

Here the angular distribution W_{UU} is described in terms of the SDMEs extracted for an unpolarized target, which are fixed input parameters of the fit. As described in section 5.2.1, the actual yields also receive a relatively small contribution from the term $S_L\, W_{UL}$. Because the magnitude of S_L is too small to extract the SDMEs representing W_{UL}, this contribution is neglected in the used fit function[2]. A systematic uncertainty is assigned to account for this contribution (see section 7.4).

The angular distribution W_{UT} is decomposed similarly to equation 5.26 into terms of distributions for the different ρ^0 polarization states:

$$\begin{aligned} W_{UT}(\phi_S, \phi, \phi_{\pi\pi}, \theta_{\pi\pi}) &= \frac{3}{4\pi}\Big[W_{UT}^{LL}(\phi_S, \phi)\cos^2\theta_{\pi\pi} + \\ &\quad W_{UT}^{LT}(\phi, \phi_S, \phi_{\pi\pi})\sqrt{2}\cos\theta_{\pi\pi}\sin\theta_{\pi\pi} + \\ &\quad W_{UT}^{TT}(\phi, \phi_S, \phi_{\pi\pi})\sin^2\theta_{\pi\pi} \Big]. \end{aligned} \tag{5.28}$$

The angular distributions W_{UT}^{LL}, W_{UT}^{LT}, W_{UT}^{TT} are parameterized in terms of the SDMEs $n_{mn}^{\alpha\beta}$ and $s_{mn}^{\alpha\beta}$ for a transversely polarized target. The full expressions used for this parameterization are given by equation 2.72. The number of independent terms of W_{UT} is 30 (see table 5.3). The corresponding 30 (combinations of) SDMEs are the free parameters of the fit.

The $\sin(\phi - \phi_S)$ moments of A_{UT} From the extracted SDMEs for an unpolarized target and a transversely polarized target, one can also obtain the $\sin(\phi-\phi_S)$ moment of A_{UT} for longitudinally and transversely polarized ρ^0 mesons by using

$$A_{UT,\rho_L^0}^{\sin(\phi-\phi_S)} = \frac{\mathrm{Im}\left(n_{++}^{0\,0} + \varepsilon n_{0\,0}^{0\,0}\right)}{u_{++}^{0\,0} + \varepsilon u_{0\,0}^{0\,0}}, \tag{5.29}$$

$$A_{UT,\rho_T^0}^{\sin(\phi-\phi_S)} = \frac{\mathrm{Im}\left(n_{++}^{++} + n_{++}^{--} + 2\varepsilon n_{0\,0}^{++}\right)}{1 - (u_{++}^{0\,0} + \varepsilon u_{0\,0}^{0\,0})}. \tag{5.30}$$

The resulting azimuthal moments can be compared to the azimuthal moments obtained from the fit described in section 5.2.3 by using equation 5.23. The main difference between the two methods is the parameterization of the PDFs. The used parameterization of the PDF given by equation 5.19 implicitly accounts for the small admixture from the longitudinal component S_L of the target polarization and includes the corresponding additional 6 terms. Apart from this small difference, both parameterizations describe the same angular distribution function.

---

[2] The SDMEs corresponding to W_{UL} can be extracted from data taken with a longitudinally polarized target. At present, results on these SDMEs are not available.

5.3 The role of the acceptance efficiency

Not only the cross section σ, but also the acceptance efficiency ϵ depends on the variables x, Q^2, t', ϕ, ϕ_S, $\phi_{\pi\pi}$, $\theta_{\pi\pi}$. If the distribution of measured events is evaluated differentially in all of these variables, the corresponding probability distribution function can be expressed as the product

$$f(\boldsymbol{v}, P_T; \boldsymbol{\theta}) \ = \mathcal{N}^{-1}(\boldsymbol{\theta}) \ \epsilon(\boldsymbol{v}) \ \sigma^{\mathrm{fit}}(\boldsymbol{v}, P_T; \boldsymbol{\theta}), \tag{5.31}$$

where $\boldsymbol{v}$ denotes the set of variables, P_T is the transverse target polarization, and $\boldsymbol{\theta}$ denotes a set of parameters that are used to parameterize the cross section $\sigma^{\mathrm{fit}}(\boldsymbol{v}, P_T; \boldsymbol{\theta})$. The normalization integral $\mathcal{N}$ is given by

$$\mathcal{N}(\boldsymbol{\theta}) = \int \big(\epsilon(\boldsymbol{v}) \ \sigma^{\mathrm{fit}}(\boldsymbol{v}, P_T; \boldsymbol{\theta})\big) \ d\boldsymbol{v} \, dP_T. \tag{5.32}$$

Ignoring the dependence on the variables x, Q^2, t', equation 5.31 describes the general structure of the fit functions used in the maximum likelihood method to describe the yields. From combining equation 5.31 with equation 5.2 it follows that the logarithm of the likelihood $\mathcal{L}$ as a function of the fit parameters is given by

$$\ln \mathcal{L}(\boldsymbol{\theta}) = \sum_{i=1}^{N} \ln \epsilon(\boldsymbol{v}_i) \ + \sum_{i=1}^{N} \ln \sigma^{\mathrm{fit}}(\boldsymbol{v}_i, P_{T,i}; \boldsymbol{\theta}) \ - \ N \ln \mathcal{N}(\boldsymbol{\theta}) \tag{5.33}$$

with the index $i = 1, \ldots, N$ labelling the events. Since the first term, $\sum_i \ln \epsilon(\boldsymbol{v}_i)$, in equation 5.33 does not depend on the free parameters of the fit, it does not affect the position of the maximum of $\mathcal{L}$ in the parameter space. Therefore, in the performance of the fit this term can be discarded, which greatly simplifies the computation of $\ln \mathcal{L}(\boldsymbol{\theta})$.

In case the normalization integral of the PDF does not depend on the free parameters of the fit either, the term $N \ln \mathcal{N}$ can also be discarded in the computation of the likelihood. This is the case if the fit includes only free parameters for the P_T-dependent part of the PDF and in addition the used data set has no net target polarization [56], which is usually true as the data are taken with equal luminosity for positive and negative target polarization. Furthermore, it should be noted that the P_T-dependent part of the cross section and the acceptance efficiency behave differently under the transformation $(\phi, \phi_S) \rightarrow (-\phi, -\phi_S)$. Whereas the HERMES geometric acceptance is by approximation even, the P_T-dependent part of the cross section is odd under this transformation. From these symmetry properties it follows that the normalization integral, by approximation, does not depend on the parameters describing A_{UT}^{ℓ} or equivalently W_{UT}^{ℓ}.

For a fit of the polarization-independent part of the cross section, i.e. W_{UU}, the normalization integral depends on the free parameters describing W_{UU} and should therefore not be discarded. The normalization integral in equation 5.32 can be numerically computed by using Monte Carlo integration. Neglecting the dependence on the variables x, Q^2, t' this computation is performed by calculating the sum

$$\mathcal{N}(\boldsymbol{\theta}) \propto \sum_{j=1}^{N_{MC}} W_{UU}(\phi_j, \phi_{\pi\pi,j}, \theta_{\pi\pi,j}; \boldsymbol{\theta}). \tag{5.34}$$

Here, one sums over Monte Carlo events, labelled by $j = 1, \ldots, N_{MC}$, that are within the simulated acceptance of the spectrometer. The simulated Monte Carlo events are generated isotropically in the angles $\phi, \phi_S, \phi_{\pi\pi}, \theta_{\pi\pi}$.

In practice, equation 5.31 is used in such a way that only the dependence of the yields on the most sensitive variables is taken into account in the parameterization of the fit function. The most relevant dependencies have to be chosen, since more fit parameters are needed to give a complete parameterization of the full dependence than is practically possible. It was decided to include only the dependence of the yields on the angles $\phi, \phi_S, \phi_{\pi\pi}, \theta_{\pi\pi}$ and the target polarization P_T. As the dependence on the remaining set of variables x, Q^2, t' is not accounted for in such a parameterization, one has effectively integrated the fit function over these variables. Therefore, the used fit function can be expressed as

$$\begin{aligned} f(\phi, \phi_S, \phi_{\pi\pi}, \theta_{\pi\pi}, P_T; \boldsymbol{\theta}) \; &= \\ \mathcal{N}^{-1}(\boldsymbol{\theta}) \, \epsilon^{\text{int}}(\phi, \phi_S, \phi_{\pi\pi}, \theta_{\pi\pi}) & \, \sigma^{\text{fit}}(\phi, \phi_S, \phi_{\pi\pi}, \theta_{\pi\pi}, P_T; \boldsymbol{\theta}), \end{aligned} \tag{5.35}$$

where ϵ^{int} is the acceptance efficiency integrated over the variables x, Q^2, t'. In this case the used fit function does not give an exact description of the actual distribution of events, which is given instead by the integral

$$\begin{aligned} N(\phi, \phi_S, \phi_{\pi\pi}, \theta_{\pi\pi}) \; &= \\ \int \epsilon(\phi, \phi_S, \phi_{\pi\pi}, \theta_{\pi\pi}, x, Q^2, t') & \, \sigma(\phi, \phi_S, \phi_{\pi\pi}, \theta_{\pi\pi}, x, Q^2, t', P_T) \, dx \, dQ^2 \, dt'. \end{aligned} \tag{5.36}$$

In principle, it is possible to include some of the dependencies of the cross section on the kinematic variables x, Q^2, t' explicitly in the fit fuction by using for the shape of these dependencies a theoretically motivated parameterization or a general parameterization, such as a Taylor expansion in terms of the kinematic variables [56]. It was decided not to include such theoretical dependencies, but instead to perform fits with equation 5.35 for separate bins in x, Q^2, t'. If the dependencies of the angular distributions on x, Q^2, t' are flat enough in each bin, it is justified to ignore these dependencies in the parameterization of the fit function. Monte Carlo studies have been performed to estimate the effect of integrating the yields over these kinematic variables (see section 6.7).

Since the measured yields are fit rather than the cross section, one has to take into account that the angular dependencies of the acceptance efficiency may cause correlations between terms that are orthogonal in the cross section. In case the correlated terms are left out of the fit, i.e., implicitly assumed to be zero, the fit result is possibly affected by the coupling between the ignored terms and the acceptance efficiency. This effect is referred to as "cross contamination". In order to avoid cross contamination the correlated terms are also included in the fit.

In order to illustrate the effect of cross contamination a simplified case is considered here, with the yields given by

$$N^{\text{data}}(P_T,\phi,\phi_S) = \epsilon(\phi,\phi_S)\,\sigma(P_T,\phi,\phi_S), \tag{5.37}$$

and the acceptance efficiency and cross section given by, respectively,

$$\begin{aligned}\epsilon(\phi,\phi_S) &\propto 1 + a\,\cos(2\phi_S) + b\,\cos(\phi), &(5.38)\\ \sigma(P_T,\phi,\phi_S) &\propto 1 + P_T\big[\,A\,\sin(\phi-\phi_S)\\ &\qquad\qquad + B\,\sin(\phi+\phi_S) + C\,\sin(\phi_S)\,\big]. &(5.39)\end{aligned}$$

If the used fit function only includes a description of the $\sin(\phi-\phi_S)$ component of the cross section:

$$\sigma^{\text{fit}}(P_T,\alpha) \propto 1 + P_T\big(\,A^{\text{fit}}\,\sin\alpha\,\big) \tag{5.40}$$

with $\alpha = \phi - \phi_S$, one finds that the normalization integral (see equation 5.32) does not play a role in the fit, since it does not depend on the fit parameter A^{fit}. This implies that also the acceptance efficiency can be discarded in the expression used for the fit function, which is therefore effectively given by $f^{\text{fit}} = \sigma^{\text{fit}}$. Since the dependencies of the yields on the angle $\beta = \phi + \phi_S$ are not included in this function, the yields can be described as an integral over β

$$\begin{aligned}N^{\text{data}}(P_T,\alpha) &= \int \epsilon(\alpha,\beta)\,\sigma(P_T,\alpha,\beta)\,d\beta\\ &\propto 1 + P_T\big(\,A + \frac{aB}{2} - \frac{bC}{2}\,\big)\,\sin\alpha, \end{aligned}\tag{5.41}$$

which is obtained from the trigonometric relations

$$\begin{aligned}\cos(2\phi_S)\,\sin(\phi+\phi_S) &= \frac{1}{2}\,(\,\sin(\phi+3\phi_S) + \sin(\phi-\phi_S)\,)\,, &(5.42)\\ \cos(\phi)\,\sin(\phi_S) &= \frac{1}{2}\,(\,\sin(\phi+\phi_S) - \sin(\phi-\phi_S)\,)\,. &(5.43)\end{aligned}$$

The $\sin(\phi-\phi_S)$ moment of the integrated yields in equation 5.41 contains the contributions $aB/2$ and $-bC/2$ coming from the coupling of, respectively, the $\sin(\phi+\phi_S)$ moment and the $\sin(\phi_S)$ moment of the cross section with the acceptance efficiency (as follows from equations 5.42 and 5.43).

The actual acceptance efficiency may contain more terms that can cause correlations between terms of the angular distribution of the cross section. Cross contaminations are prevented by including all the terms of the angular distribution of the cross section in the fit function. In this way, the correlations between these terms are explicitly taken into account in the extraction procedure. Monte Carlo studies confirm that if all correlated terms are included in the fit function as free parameters the extracted values are not affected by such cross contamination effects (see section 6.4).

5.4 Background contribution

The selected data set for exclusive ρ^0 production contains contributions from background events such as non-exclusive and non-resonant events. Estimates of the relative contributions from background events are given in chapter 4.3. Since the studies discussed in that chapter have shown that the background is dominated by the contribution from non-exclusive events only this contribution is accounted for in the extraction of the asymmetries and SDMEs from the data.

The probability density function describing the data is thus given by

$$N_{\mathrm{tot}}\; f_{\mathrm{tot}}(\boldsymbol{v}) \;=\; N_\rho\; f_\rho(\boldsymbol{v}) \;+\; N_{\mathrm{bg}}\; f_{\mathrm{bg}}(\boldsymbol{v}), \tag{5.44}$$

where $\boldsymbol{v}$ represents the set of variables x, Q^2, t', ϕ, ϕ_S, $\phi_{\pi\pi}$, $\theta_{\pi\pi}$, P_T, the numbers N represent the expected number of events, and the functions f represent probability density functions normalized to unity. The subscripts "tot", "ρ" and "bg" denote the total data set, the contribution from exclusive ρ^0 production data, and the non-exclusive background contribution, respectively.

Equation 5.44 is used to take into account the background contribution in the evaluation of the asymmetries and SDMEs. First the PDF describing the background contribution is constructed. As both the cross section and the acceptance efficiency differ for the various non-exclusive background processes, several assumptions are made in order to obtain the parameterization of the PDF. For the PDF describing the background the same parameterization is chosen as the parameterization of the PDF describing exclusive ρ^0 production[3]. Moreover, the acceptance efficiency is taken to be identical to the acceptance efficiency for exclusive ρ^0 production. Then, the parameters describing the target-polarization independent part of the background are determined from a fit of the background PDF to a Monte Carlo sample representing the background. A flat distribution is assumed for the target-polarization dependent part of the cross section for background processes. For this reason the parameters describing the target-polarization dependent part are taken to be equal to zero.

In order to extract the parameters for exclusive ρ^0 production from the measured distribution of events, one can then construct a fit function in the form of equation 5.44,

$$f_{\mathrm{tot}}^{\mathrm{fit}}(\boldsymbol{v}) \;=\; (1 - F_{\mathrm{bg}})\; f_\rho^{\mathrm{fit}}(\boldsymbol{v}) \;+\; F_{\mathrm{bg}}\; f_{\mathrm{bg}}^{\mathrm{inp}}(\boldsymbol{v}), \tag{5.45}$$

where F_{bg} is the non-exclusive background fraction, which is listed for the various kinematic bins in table 4.5 in section 4.3. The function $f_{\mathrm{bg}}^{\mathrm{inp}}$ represents the PDF of the background contribution, which is determined by the fixed background parameters. As the term $F_{\mathrm{bg}}\, f_{\mathrm{bg}}^{\mathrm{inp}}$ accounts for the background contribution to $f_{\mathrm{tot}}^{\mathrm{fit}}$, the free parameters of the fit parameterizing the function f_ρ^{fit} are effectively fitted to the remaining contribution from exclusive ρ^0 production.

---

[3] It is noted that, although the parameters for exclusive ρ^0 production can be interpreted in terms of physics observables, this is in general not the case for the parameters describing the background.

Chapter 6

Monte Carlo simulations

The performance of the various methods used to extract azimuthal moments and spin density-matrix elements (SDMEs) from the experimental data was studied by means of Monte Carlo simulations. In this chapter the performed Monte Carlo studies are presented.

The Monte Carlo simulations were performed with the PYTHIA 6.2 event generator. The basic sets of simulated events were produced and made available by the HERMES Monte Carlo group. A brief description of the PYTHIA 6.2 generator is presented in section 6.1. In the simulations the limited acceptance of the HERMES spectrometer is taken into account. The simulation of the spectrometer acceptance and other instrumental effects is the subject of section 6.2. In section 6.3 it is described how the available sets of simulated events were post-processed so as to implement SDMEs or target-spin asymmetries into the simulation.

It has been verified whether the implemented asymmetries and SDMEs were correctly reconstructed. In section 6.4 the cross contaminations between different azimuthal moments of the asymmetry, which are induced by the limited acceptance of the spectrometer, are discussed. It is shown that these cross contaminations disappear when the various correlated azimuthal moments of the asymmetry are accounted for in the extraction procedure. The performances of the unbinned maximum likelihood fit and the binned χ^2 fit methods were studied for the case where the azimuthal moments of the asymmetry are extracted from data sets with relatively low statistics. The results of these studies are described in section 6.5. For low statistics event sets the unbinned maximum likelihood method was found to be more reliable, which is one of the reasons to use this method in the analyses of the actual data. The performance of this fit method, when it is applied to extract the separate azimuthal moments for longitudinally and transversely polarized ρ^0 mesons, is presented in section 6.6. In section 6.7 studies are discussed of the extraction of an asymmetry that varies as a function of kinematic variables. The studies of the methods used to extract the SDMEs for an unpolarized and for a transversely polarized target are discussed in section 6.8.

6.1 The PYTHIA 6.2 Monte Carlo generator

The PYTHIA 6.2 Monte Carlo generator [61, 62] was used for the simulation of high-energy lepton-nucleon scattering events. PYTHIA 6.2 simulates each of the various subprocesses that may contribute to the interaction of the exchanged virtual photon with the nucleon. By multiplying the corresponding cross section with the virtual-photon flux factor one obtains the lepton-nucleon cross section. The simulation includes leading-order descriptions of the DIS process in combination with phenomenological descriptions of several other possible subprocesses, which have been obtained by extrapolating descriptions of photoproduction processes to non-zero values of Q^2 [63]. The various descriptions used are each dominant in a specific region of phase space. In PYTHIA it is ensured that the transitions between these regions are smooth.

Simulation of virtual-photon nucleon interactions Apart from the leading order DIS interactions, the remaining photon-nucleon interactions included in PYTHIA can be classified as direct or resolved photon interactions. In direct interactions the bare, i.e. point-like, photon interacts with a parton inside the proton. The simulated direct processes are the QCD Compton process $\gamma^* q \rightarrow qg$, and the boson-gluon fusion process $\gamma^* g \rightarrow q\overline{q}$. These direct processes can be considered as next-to-leading-order corrections to the leading-order DIS processes.

In resolved interactions the photon fluctuates into hadronic states that interact with the nucleon [64]. The fluctuations $\gamma^* \rightarrow q\overline{q}$ of a virtual photon into a quark-antiquark pair can be characterized by the transverse momentum $k_\perp$ of the quarks with respect to the virtual-photon direction. If $k_\perp$ is relatively small, the fluctuations cannot be calculated within perturbative QCD and a vector-meson dominance (VMD) approach is used. In that case, the virtual photon turns into a vector meson (ρ^0, ω, ϕ or J/ψ) that scatters either diffractively or non-diffractively from the nucleon. For larger values of $k_\perp$ the virtual-photon nucleon interaction is calculated as a so-called anomalous (resolved) interaction, which is the interaction of a parton from the proton with a parton originating from a fluctuation of the photon into a $q\overline{q}$ pair.

The leading-order DIS processes in combination with the direct virtual-photon interactions are dominant over the resolved virtual-photon interactions for relatively large values of $k_\perp$, i.e. for $k_\perp$ larger than typically 2-4 GeV (depending on the center-of-mass energy of the interaction between the virtual photon and the nucleon) and $k_\perp > p_\perp$, where $p_\perp$ is the transverse momentum of the interacting parton inside the nucleon.

Fragmentation According to the principle of color confinement the creation of quarks or gluons is followed by the formation of hadrons. This process is called hadronization or fragmentation. In PYTHIA 6.2 various descriptions of the fragmentation process are available. Usually, and also in the simulations used in this work, the Lund model is used to describe fragmentation processes. Within the Lund model the QCD interactions between partons are represented by field lines called strings. If the invariant mass of the string is large enough, quark-antiquark pairs can be created and the string breaks up into various parts, of which the newly created (anti)quarks are the new end points. The break-up of Lund strings reproduces many of the observed properties of the fragmentation process.

Description of hadronic decays Many of the particles produced in the interactions are unstable and decay. For hadronic decays the branching ratios in general cannot be calculated from first principles. Instead, PYTHIA describes hadronic decays by making use of the experimentally observed hadronic decay modes, branching ratios, and resonance widths. The invariant mass distributions of the hadrons produced in the decay processes are described by relativistic or non-relativistic Breit-Wigner shapes (see section 4.3.2).

The use of PYTHIA at HERMES kinematics The default PYTHIA settings are such that an optimal description is given of scattering processes at energies that are substantially larger than the energy used at HERMES. For the simulation of scattering processes at HERMES kinematics various PYTHIA parameters were tuned, including for instance the parameters that specify the description of fragmentation and the relative contributions of the various scattering processes considered [65, 66]. This tuning process was performed in order to obtain an optimal description of measured observables such as inclusive and semi-inclusive differential cross sections, hadron (i.e. pion, kaon and proton) multiplicities [66], and the relative contributions of exclusive ρ and ϕ production to the production of pions and kaons. Moreover, the parameterization of the virtual-photon flux factor was adjusted so as to include its dependence on the target mass. In the original parameterization this dependence was not included as it is negligible at high values of W^2 [65]. In addition, the parameters used in the VMD model simulation were adjusted in order to give an improved description of the HERMES data for exclusive vector-meson production [25].

6.2 Simulation of the spectrometer acceptance

In order to enable a proper interpretation of the measured data it is crucial to take into account effects coming from the limited geometric acceptance of the HERMES spectrometer. The GEANT program [67], which is part of the CERN Program Library, was used for the simulation of acceptance effects. With the GEANT program geometrical volumes of the spectrometer components were assigned and their specific material properties were modelled. Moreover, the responses of the detectors to tracks passing through them were simulated. These simulated responses were used as input of the HRC track reconstruction program, which was introduced in section 3.4. In this way the full procedure applied to the measured data to reconstruct tracks was simulated. Here, the set of reconstructed Monte Carlo events is referred to as a 'tracked' Monte Carlo simulation. The tracked Monte

Carlo simulation includes smearing effects due to the limited resolution of the subdetectors. The GEANT program also simulates the interactions of particles inside the spectrometer material, which are responsible for additional smearing effects.

The simulation of partial tracks in the back part of the spectrometer makes use of the front-track information in combination with momentum look-up tables, which take into account the bending of tracks in the magnetic field of the spectrometer magnet. For each reconstructed track the geometric requirements discussed in section 4.2.1 are imposed in order to determine whether tracks are generated within the geometric acceptance of the spectrometer.

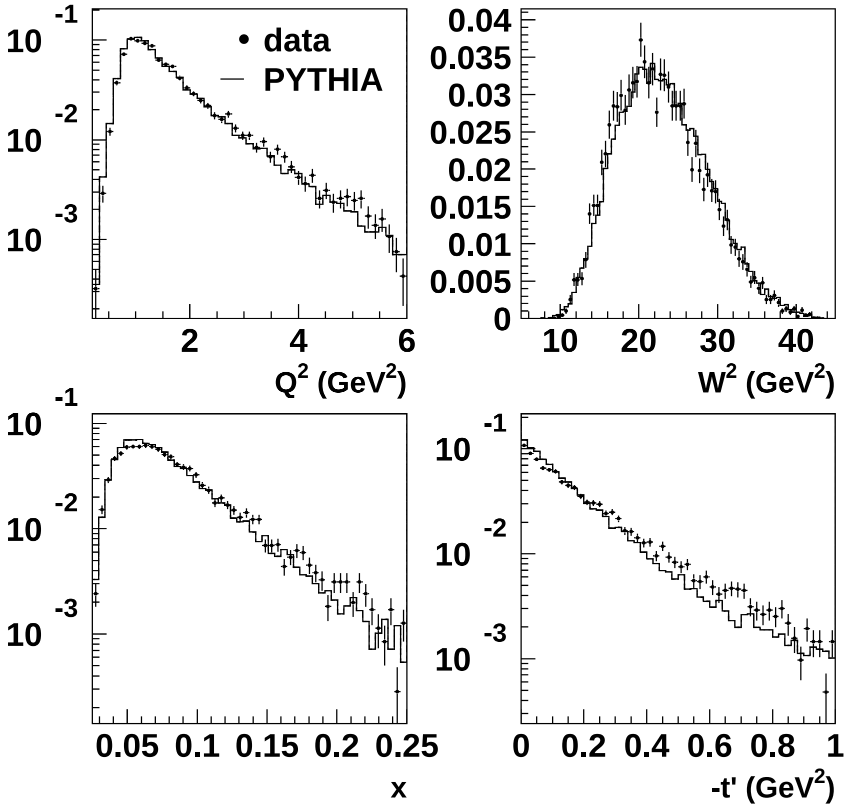

Figure 6.1: Normalized event distributions for exclusive ρ^0 production as a function of four kinematic variables. The solid circles represent the measured data, whereas the histograms represent a fully tracked Monte Carlo simulation obtained by using PYTHIA.

Figure 6.1 shows the normalized event distributions as a function of the kinematic variables Q^2, W^2, x, and $-t'$ for both the measured exclusive ρ^0 production data and the corresponding tracked Monte Carlo events. In both cases the same geometric requirements and kinematic selection requirements (see section 4.2) were imposed. Note that for each panel in figure 6.1 no requirements were imposed on the running variable. The distributions of Monte Carlo distributions are in general in good agreement with the measured distributions. The relatively good agreement between the kinematic dependencies of the data and the Monte Carlo validates the use of the Monte Carlo simulation for studies of effects such as those due to the limited geometric acceptance of the HERMES spectrometer.

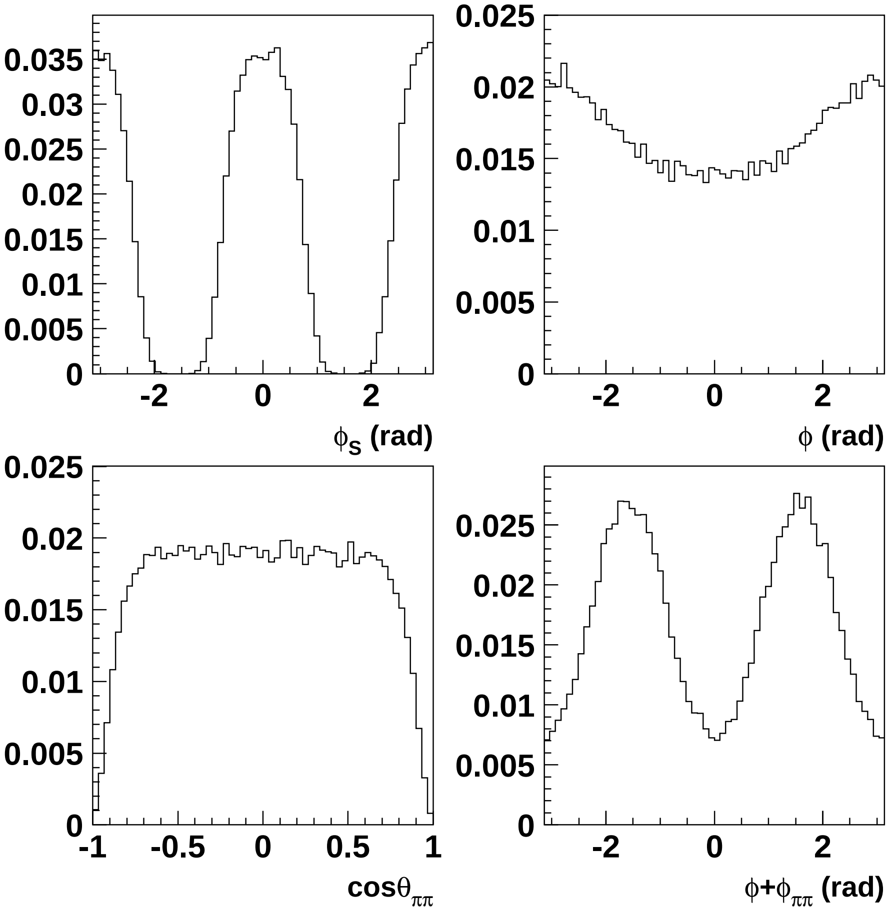

Figure 6.2: Normalized angular distributions of tracked Monte Carlo events generated with PYTHIA. At the generation level the events are distributed isotropically in the angles ϕ_S, ϕ, $\theta_{\pi\pi}$ and $\phi_{\pi\pi}$.

In order to study the effect of the limited acceptance of the HERMES spectrometer on the measured angular distributions, a set of Monte Carlo events was generated isotropically in the angles ϕ_S, ϕ, $\theta_{\pi\pi}$, and $\phi_{\pi\pi}$ (see section 2.4). It should be noted that the angle ϕ_S is defined here with respect to the negative y-axis of the HERMES coordinate system. The yields of the corresponding tracked events provide an estimate of the acceptance efficiency. The angular distributions of the tracked events are shown in figure 6.2. the distributions of tracked events were found to have strongly varying angular dependencies as a result of the geometric dependence of the spectrometer acceptance.

One can conveniently describe the acceptance of the spectrometer for single tracks by using the azimuthal and polar angles of the HERMES coordinate system (see section 3.3). The angle ϕ_S is, for instance, directly related to the azimuthal angle ϕ_e of the scattered lepton in the HERMES coordinate system[1] by $\phi_e \approx -(\phi_S - \pi)$. From this relation it follows directly that the gaps in the ϕ_S distribution around $\phi_S = \pm\pi/2$, illustrated in the upper left panel of figure 6.2, are a consequence of the gaps in the geometric acceptance for the scattered lepton due to the inactive volume in between the upper and lower halves of the spectrometer.

The ρ^0 production angle ϕ and the decay angles $\theta_{\pi\pi}$ and $\phi_{\pi\pi}$ depend on the directions and the momenta of the tracks of the scattered lepton and the two pions resulting from the ρ^0 decay. Hence, the dependence of the acceptance on these angles is related to the configuration of these three tracks. The acceptance efficiency as a function of ϕ, shown in figure 6.2, has its maxima around $\phi = \pm\pi$ and its minimum around $\phi = 0$. This behavior of the acceptance is due to a 3-track configuration, in which both decay pions appear together in the spectrometer half opposite to the one, in which the scattered lepton is observed. For such a configuration the overall efficiency is higher than for a configuration, in which one of the decay pions appears in the same halve as the scattered lepton and one decay pion in the opposite halve. For the latter configuration the acceptance efficiency is relatively flat as a function of ϕ. Note that configurations with all three tracks in the same spectrometer half are kinematically strongly suppressed.

The lower-left plot in figure 6.2 shows the dependence of the acceptance on $\cos\theta_{\pi\pi}$. The acceptance strongly decreases between $|\cos\theta_{\pi\pi}| \approx 0.8$ and $|\cos\theta_{\pi\pi}| = 1.0$, where in the ρ^0-rest frame the directions of the decay pions are parallel and anti-parallel to the direction of the recoiling nucleon. In the region $0.8 \lesssim |\cos\theta_{\pi\pi}| \leq 1$ the 'anti-parallel' pion has a relatively high momentum (typically between 5 and 22 GeV), whereas the 'parallel' pion has a relatively low momentum (typically below 3 GeV) in the laboratory frame. As the track of the higher-momentum pion in the HERMES coordinate system has on average a smaller polar angle with respect to the z-axis, the chance is larger that this track passes through the gap in between the two spectrometer halves, and thus outside the geometrical acceptance.

The lower-right plot in figure 6.2 shows the dependence of the acceptance on

---

[1] The angle ϕ_e slightly deviates from the angle $-(\phi_S - \pi)$ due to the non-zero angle θ_γ between the virtual-photon momentum and the z-direction.

the angle $\phi + \phi_{\pi\pi}$. The acceptance efficiency is observed to have its maxima around $\phi + \phi_{\pi\pi} = \pm\pi/2$, where the ρ^0 decay plane is on average perpendicular to the lepton scattering plane, and its minima around $\phi + \phi_{\pi\pi} = 0, \pm\pi$, where the angle between the decay plane and the lepton scattering plane is on average equal to zero.

For the evaluation of the acceptance dependence on the angle $\phi - \phi_S$ also the values of other angles, such as $\phi + \phi_S$ and $\phi_{\pi\pi}$ have to be taken into account. The reason for this is the fact that the acceptance induces strong correlations between these angles. The two-dimensional distributions of the Monte Carlo events inside the acceptance of the spectrometer, shown in figure 6.3, illustrate the simultaneous dependence of the acceptance on the angles $\phi - \phi_S$, $\phi + \phi_S$ and $\phi_{\pi\pi}$. In the upper plot of figure 6.3 the gaps in the acceptance are once more visible around the diagonals described by $(\phi - \phi_S) = (\phi + \phi_S) \pm \pi$, which correspond to the previously discussed gaps around $\phi_S = \pm\pi/2$, shown in the upper left panel of figure 6.2.

The lower plot of figure 6.3 shows a strong increase of the acceptance in the regions around the diagonals described by $(\phi - \phi_S) = n\pi/2 - \phi_{\pi\pi}$, with $n = -1, 1, 3, 5$. In these regions the detected events predominantly have the configuration with both decay pions in the other half of the spectrometer as the scattered lepton. In the $\gamma^* p$ center-of-mass frame the angles $\phi - \phi_S$ and $\phi_{\pi\pi}$ can be interpreted as, respectively, the azimuthal angle between the hadron production plane and the negative y-axis of the HERMES coordinate system around the virtual-photon direction, and the azimuthal angle between the decay plane and the hadron production plane around the ρ^0-meson direction (see section 2.4). Although these angles are defined around different axes, the dominant correlations between these angles indicate that on average an optimal geometric acceptance is obtained if the decay plane is perpendicular to the y-axis of the HERMES coordinate system. This situation corresponds to a preferred orientation of the decay plane perpendicular to the yz plane in the HERMES laboratory frame.

6.3 Implementation of SDMEs and asymmetries

The method used to implement SDMEs for an unpolarized target in Monte Carlo simulations is the so-called accept-reject method. As a starting point of the method, a set of events generated isotropically in the angles ϕ_S, ϕ, $\theta_{\pi\pi}$, and $\phi_{\pi\pi}$, but reconstructed within the simulated HERMES acceptance is used. In the method, for each individual event a random number r_i between 0 and $3/2\pi$ is generated, where i labels the events. The random number is used to decide whether the event is included in the final selection of events or not. An event is included if the condition

$$W_{UU}^{\text{imp}} \left(\phi_i, \phi_{\pi\pi,i}, \theta_{\pi\pi,i}\right) > r_i \tag{6.1}$$

is satisfied or excluded otherwise. In equation 6.1, W_{UU}^{imp} represents the angular distribution function corresponding to the values of the SDMEs for an unpolarized target to be implemented. Here W_{UU}^{imp} satisfies the same lower and upper bound

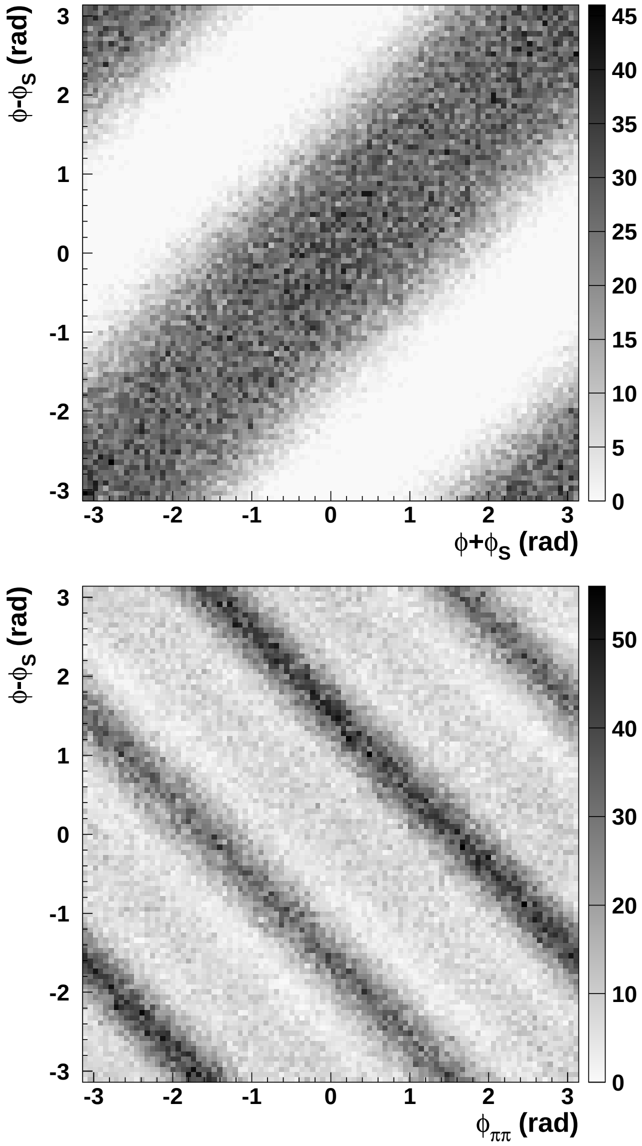

Figure 6.3: Two-dimensional angular distributions of tracked Monte Carlo events for exclusive ρ^0 production simulated with PYTHIA. At the generation level the events are distributed isotropically in the angles ϕ_S, ϕ, $\theta_{\pi\pi}$ and $\phi_{\pi\pi}$.

as the random number r_i. The set of events satisfying the condition in equation 6.1 are distributed according to the distribution function W_{UU}^{imp}. As only events in the HERMES acceptance are used, the additional acceptance effects are included in this selected set as well.

The method used to implement the SDMEs for a transversely polarized target in Monte Carlo simulations is similar to the accept-reject method. However, in this implementation method events are not accepted or rejected, i.e., included or excluded, but positive or negative target polarizations are assigned to all events instead. The simulated events used correspond to a known unpolarized angular distribution W_{UU}, and are reconstructed within the simulated HERMES acceptance. For each event, a random number r_j between 0 and 1 is generated, where j labels the events. The random number is used to attribute a sign to the transverse target polarization S_T. To each event a positive target polarization is assigned if the condition

$$\frac{1}{2}\left(1+|S_T|\frac{W_{UT}^{\mathrm{imp}}(\phi_j,\phi_{S,j},\cos\theta_{\pi\pi,j},\phi_{\pi\pi,j})}{W_{UU}(\phi_j,\phi_{\pi\pi,j},\theta_{\pi\pi,j})}\right) > r_j \tag{6.2}$$

is satisfied and a negative target polarization is assigned otherwise. The angular distribution function W_{UT}^{imp} in equation 6.2 corresponds to the implemented values of SDMEs for a polarized target.

The method used to implement a transverse target-spin asymmetry $A_{UT}^{\ell,\mathrm{imp}}$ in Monte Carlo simulations is similar. In this method, a set of events generated isotropically in the angles ϕ and ϕ_S, but reconstructed within the acceptance is used. Again, for each event a random number r_k between 0 and 1 is generated, where k labels the events. A positive target polarization P_T is assigned in case

$$\frac{1}{2}\left(1+|P_T|\,A_{UT}^{\ell,\mathrm{imp}}(\phi_k,\phi_{S,k})\right) > r_k, \tag{6.3}$$

and a negative target polarization is assigned otherwise.

6.4 Cross contamination of azimuthal moments

A Fourier analysis of the simulated acceptance shows that it contains a large $\cos(2\phi_S)$ component, which is directly visible in the upper-left plot of figure 6.2. From the relation

$$\sin(\phi+\phi_S)\cos(2\phi_S) = \frac{1}{2}\left(\sin(\phi+3\phi_S)+\sin(\phi-\phi_S)\right) \tag{6.4}$$

it follows that due to the $\cos(2\phi_S)$ component of the acceptance a $\sin(\phi+\phi_S)$ component of the cross section contributes to the $\sin(\phi+3\phi_S)$ and $\sin(\phi-\phi_S)$ components of the yields. As a result, the extracted $\sin(\phi-\phi_S)$ moment of the asymmetry A_{UT}^{ℓ} is correlated to the value of the $\sin(\phi+\phi_S)$ moment of the asymmetry. It is concluded that due to the geometric acceptance of the spectrometer

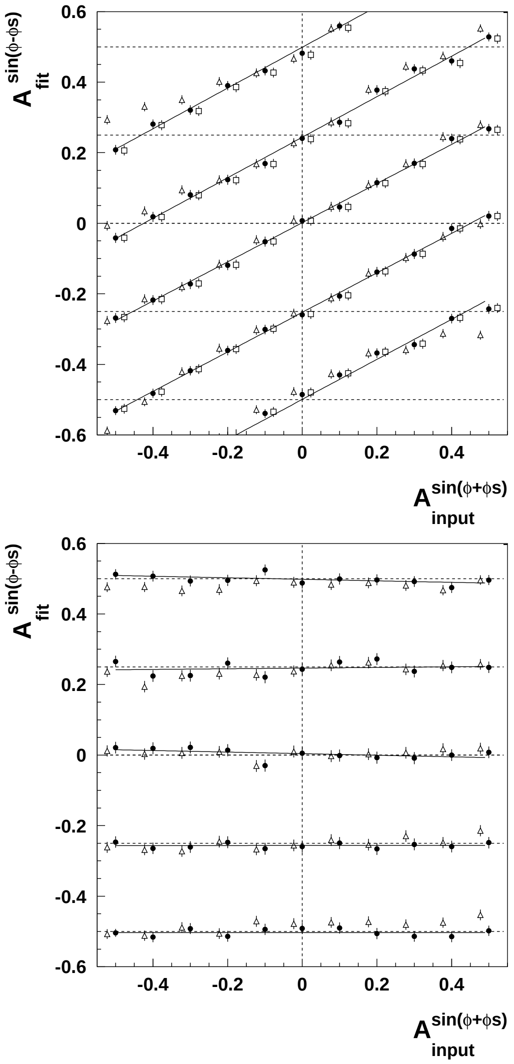

Figure 6.4: The values of the $\sin(\phi - \phi_S)$ moment of A_{UT}^{ℓ} extracted from Monte Carlo simulations for various input values of the $\sin(\phi - \phi_S)$ and $\sin(\phi + \phi_S)$ moments of the asymmetry. The input values of the $\sin(\phi + \phi_S)$ moment can be read from the horizontal axis, whereas the input values for the $\sin(\phi - \phi_S)$ moment are given by the horizontal dashed lines. The used extraction methods are explained in the text. The upper panel shows the values obtained with one-dimensional extraction methods. The lower panel shows the values obtained with two-dimensional fits that contain both the $\sin(\phi - \phi_S)$ moment and the $\sin(\phi + \phi_S)$ moment as free parameters.

each Fourier component of the cross section may contribute to various Fourier components of the observed yields. If the used extraction method does not account for such correlations between the different azimuthal moments of the asymmetry, the extracted azimuthal moments may be affected by cross contaminations, as was discussed in section 5.3.

A Monte Carlo simulation was used to study to what extent the extracted $\sin(\phi-\phi_S)$ moment of A_{UT} is affected by possible cross contaminations from other azimuthal moments. In figure 6.4 the extracted values of the $\sin(\phi-\phi_S)$ moment are plotted for varying input values of the $\sin(\phi-\phi_S)$ and the $\sin(\phi+\phi_S)$ moments of the asymmetry. The input values of the $\sin(\phi-\phi_S)$ moment are indicated by the horizontal dashed lines, whereas the input values of the $\sin(\phi+\phi_S)$ moment can be read from the horizontal axis. Three different methods are used to extract the azimuthal moment: the least-χ^2 fit (open triangles), the unbinned maximum likelihood fit (filled circles) and the moments method (open squares).

The upper panel of figure 6.4 shows the values obtained if only the $\sin(\phi-\phi_S)$ dependence of the asymmetry is evaluated in the extraction procedures. For each of the one-dimensional extraction procedures the obtained value of the $\sin(\phi-\phi_S)$ moment was found to deviate substantially from its input value unless the input value of the $\sin(\phi+\phi_S)$ moment was close to zero. For all methods a linear dependence was observed between the extracted $\sin(\phi-\phi_S)$ moment and the input value of the $\sin(\phi+\phi_S)$ moment. The observed dependencies correspond to a cross contamination from the $\sin(\phi+\phi_S)$ moment of about 60% of the latter. This cross contamination was not observed in similar studies performed with the least-χ^2 and unbinned maximum likelihood fit methods applied in two dimensions. In this case the fit procedures included both the $\sin(\phi-\phi_S)$ and $\sin(\phi+\phi_S)$ moments of the asymmetry as free parameters. The $\sin(\phi-\phi_S)$ moments obtained in these studies are shown in the lower panel of figure 6.4.

In all studies performed the $\sin(\phi-\phi_S)$ moment was found to be more strongly correlated with the $\sin(\phi+\phi_S)$ moment than with any other azimuthal moments of A_{UT}. The cross contaminations originating from the other moments of A^{ℓ}_{UT} were found to be at most around 10% of the latter. Cross contaminations associated with the $\cos(\phi-\phi_S)$, $\cos\phi_S$, and $\cos(2\phi-\phi_S)$ moments of A_{LT}, which could arise from of a non-zero net beam polarization, were not observed within the precision of the present studies.

6.5 Performance at low statistics

In section 6.4 it has been shown that in order to extract the $\sin(\phi-\phi_S)$ moment of the asymmetry A_{UT} from experimental data, the correlated moments of the asymmetry need to be accounted for the extraction procedure. One can account for the correlated azimuthal moments by using a multi-dimensional fit method that includes these additional moments as free fit parameters.

The performances of the multi-dimensional binned least-χ^2 fit and unbinned maximum likelihood fit methods were compared on Monte Carlo simulations containing a varying number of events [68]. In these studies it was found that the unbinned maximum likelihood fit reproduces the value of the asymmetry implemented into the Monte Carlo with the correct statistical uncertainty, whereas it was found that the results obtained with a conventional least-χ^2 fit method can be significantly biased for data sets with relatively low statistics.

A possible reason for the observed bias is that in the binned least-χ^2 fit method the expected value of the asymmetry in each bin is assumed to be given by a Gaussian probability-distribution function. This is an approximation that is reliable only if the number of events per bin is large enough. Another reason is that for low-statistics data sets the uncertainties on the yields in each bin, estimated by $\Delta N = \sqrt{N}$, are biased. In [69] it is shown that this bias affects the extracted azimuthal moments of the asymmetry. Hence, it was decided to proceed with the unbinned maximum likelihood fit method

6.6 $\rho_L - \rho_T$ Separation of azimuthal moments

The main goal of the present data analysis is the extraction of the transverse target-spin asymmetry for longitudinally polarized ρ^0 mesons. Hence, for each azimuthal moment of the asymmetry a distinction needs to be made between longitudinally and transversely polarized ρ^0 mesons. In order to study the extraction of the separated azimuthal moments for both ρ^0 polarization states, two Monte Carlo simulations were used. One simulation was performed for longitudinally polarized ρ^0 mesons, whereas the other was performed for transversely polarized ρ^0 mesons. The 6 azimuthal moments of the asymmetry A^{ℓ}_{UT} in equation 5.14 were randomly assigned to the simulated sets for both ρ^0 polarization states in such a way that the value of the asymmetries remained within the range $[-1, 1]$. Next, the events from both simulated sets were merged.

Since the number of generated ρ^0 mesons is equal for both ρ^0 polarization states the value of the SDME r^{04}_{00} for the merged set of events is equal to 0.5. Here r^{04}_{00} represents the relative contribution to the cross section from longitudinally polarized ρ^0 mesons. As discussed in section 2.6.1, the cross section for longitudinally polarized ρ^0 mesons is proportional to $\cos^2\theta_{\pi\pi}$, whereas the cross section for transversely polarized ρ^0 mesons is proportional to $\sin^2\theta_{\pi\pi}$. Since the acceptance of the spectrometer is lower at larger values of $|\cos\theta_{\pi\pi}|$, the number of selected events is lower for longitudinally polarized ρ^0 mesons than for transversely polarized ρ^0 mesons.

The azimuthal moments of the asymmetries for longitudinally and transversely polarized ρ^0 mesons were simultaneously extracted from the simulated events with the 12 parameter fit described in section 5.2.2. In order to verify whether the input values were correctly reproduced with a correct estimate of the statistical uncertainty, the procedure of creating event sets and extracting the azimuthal moments was repeated with randomly varying input values. A good agreement was observed between the input values and the extracted values for all 12 extracted azimuthal moments. In order to study to what extent the input values were correctly repro-

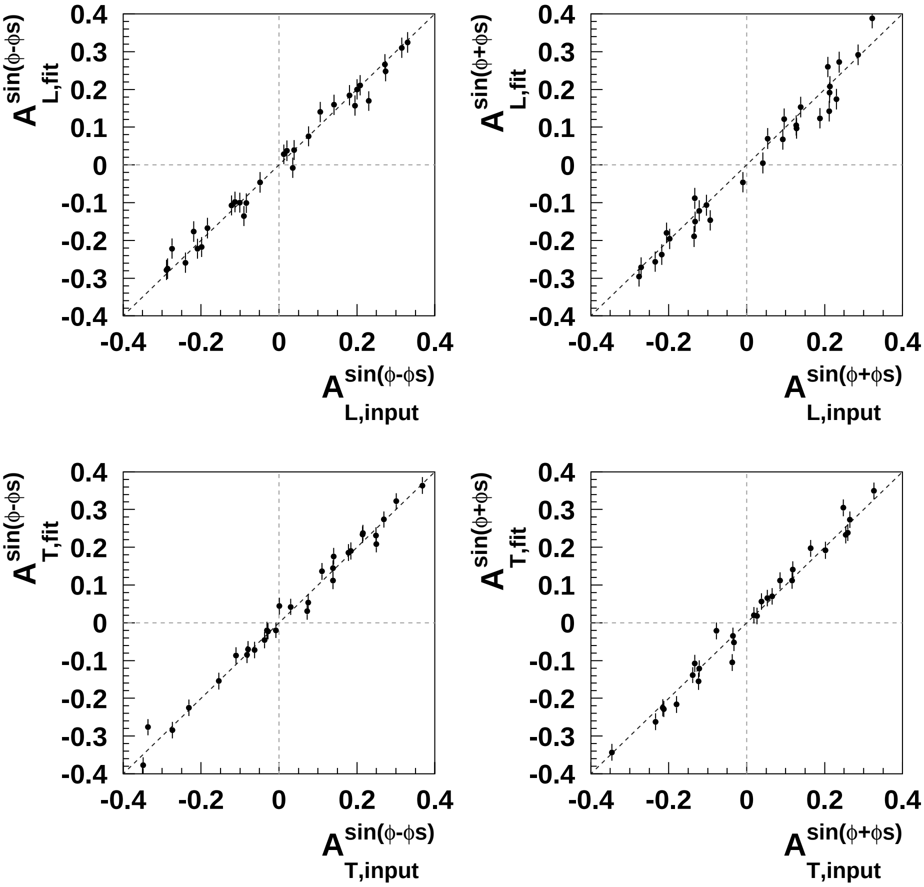

Figure 6.5: Reconstructed values of the $\sin(\phi - \phi_S)$ and the $\sin(\phi + \phi_S)$ moments of the asymmetry A^{ℓ}_{UT} versus the corresponding input values of these azimuthal moments for longitudinally and for transversely polarized ρ^0 mesons for various Monte Carlo simulations. In the simulations the values of the 12 expected azimuthal moments were randomly assigned. Each used Monte Carlo simulation is a combination of a simulation for longitudinally polarized ρ^0 mesons and one for transversely polarized ρ^0 mesons.

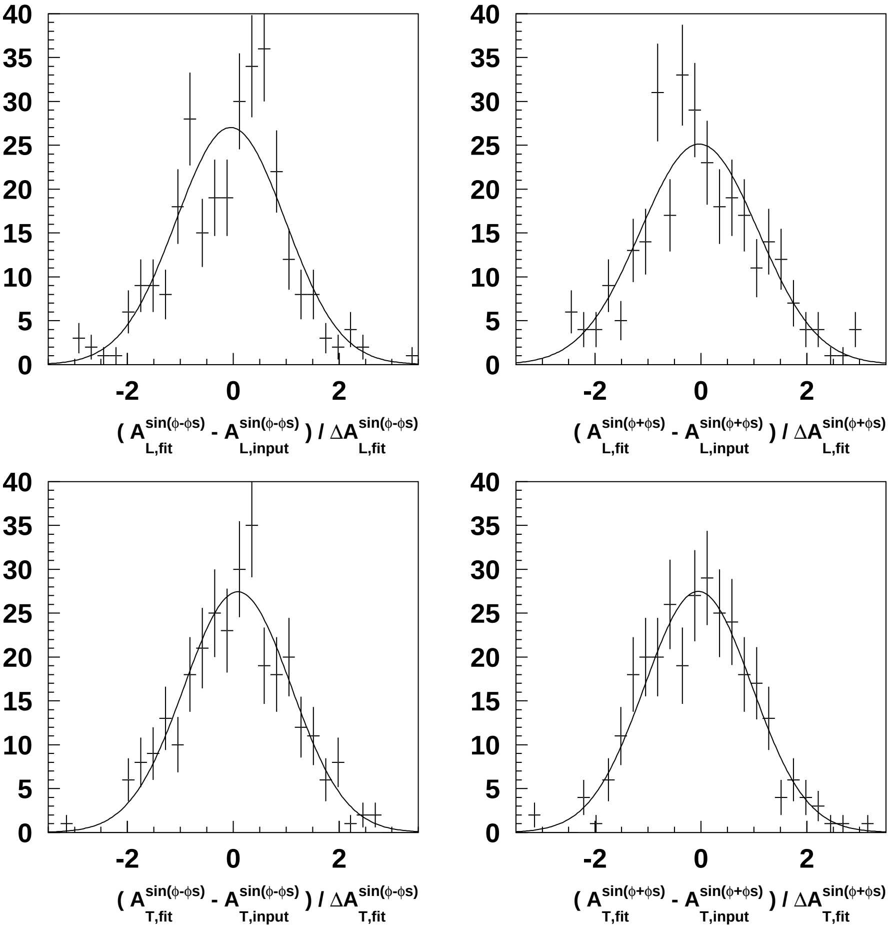

Figure 6.6: Pull distributions for the $\sin(\phi - \phi_S)$ and $\sin(\phi + \phi_S)$ moments of the asymmetry A^{ℓ}_{UT} for longitudinally and for transversely polarized ρ^0 mesons reconstructed from 300 Monte Carlo simulations, in which the values of the in total 12 expected azimuthal moments were randomly assigned. Each used Monte Carlo simulation is a combination of a simulation for longitudinally polarized ρ^0 mesons and transversely polarized ρ^0 mesons.

duced, the pull distributions were determined for the azimuthal moments extracted from 300 different sets of simulated events. These are the distributions of the difference between the determined and the input value of the moments normalized to the corresponding statistical uncertainty. The obtained distributions were found to have a mean value consistent with zero and a variance consistent with unity, which indicates that the input values were correctly determined, with a reliable estimate of the statistical uncertainty. Figure 6.5 shows the values of the extracted $\sin(\phi - \phi_S)$ and $\sin(\phi + \phi_S)$ moments of the asymmetries for longitudinally and transversely polarized ρ^0 mesons versus the corresponding input values. The pull distributions for these azimuthal moments are shown in figures 6.6.

6.7 Kinematic dependencies of the asymmetry

The measured asymmetries typically depend on several kinematic variables. As a result the asymmetry averaged over a certain kinematic domain may not be equal to the value of the asymmetry at the average values of the kinematic variables. This effect may be enhanced due to the fact that the acceptance depends on the same kinematic variables as well [56]. In the procedure used to determine the azimuthal moments of the asymmetry the acceptance efficiency is assumed to be described by a multiplicative function. However, since the dependencies on kinematic variables are not explicitly taken into account in the fit function, the evaluated yields are the product of the acceptance efficiency and the cross section integrated over the kinematic variables, as was discussed in section 5.3. As a result acceptance effects may not fully cancel in the extraction of the azimuthal moments.

The effect of possible kinematic dependencies of the azimuthal moments on the corresponding extracted values was studied by means of Monte Carlo simulation. For this purpose kinematic dependent azimuthal moments were assigned to the simulation. The model used to describe the $-t'$ and the x dependence of the $\sin(\phi - \phi_S)$ moment for longitudinally polarized ρ^0 mesons is based on predictions presented in [28], which describe the $\sin(\phi - \phi_S)$ for the process $\gamma_L^* \to \rho_L$. By using the same model, kinematic dependencies were inserted as well for the $\sin(\phi - \phi_S)$ moment for transversely polarized ρ^0 mesons and for the $\sin(\phi + \phi_S)$ moments for both ρ^0 polarization states in order to take into account possible cross contaminations.

Figure 6.7 compares the input values to the extracted values of the azimuthal moments for various Q^2, x, and $-t'$ and bins. The simulated set of events contains 60000 events in total. The extracted values of the azimuthal moments are in statistical agreement with the input values averaged over the corresponding bins. Also shown in figure 6.7 are the input values of the azimuthal moments at the average values of the kinematic variables in each bin. The observed differences between these values and the values of the azimuthal moments averaged over the kinematic variables are only small fractions of the values of the original azimuthal moments.

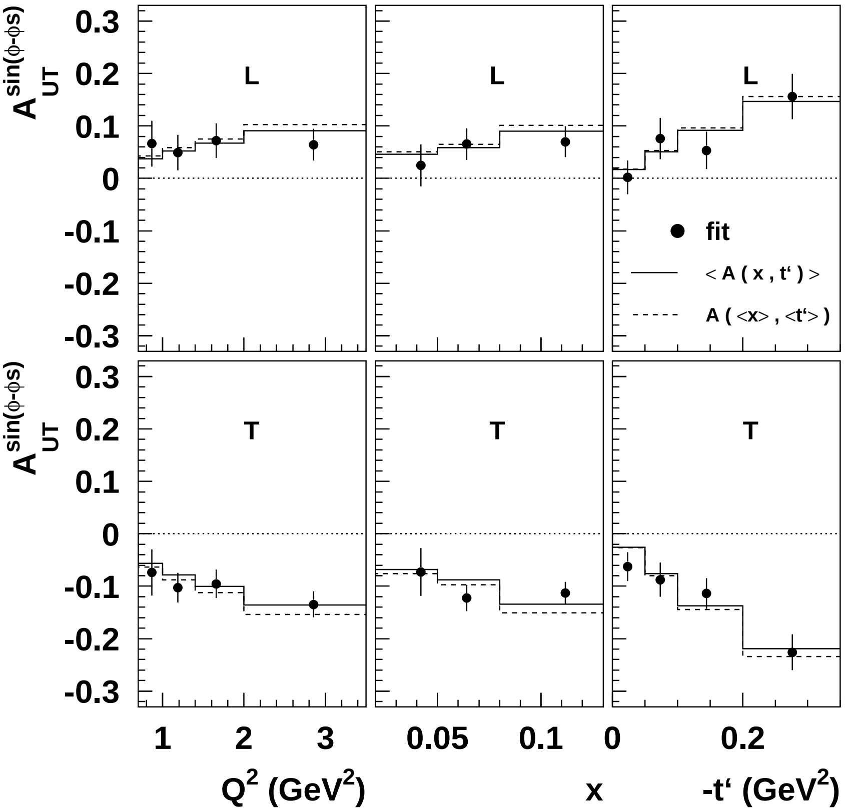

Figure 6.7: Kinematic dependencies of the $\sin(\phi - \phi_S)$ moments of A_{UT}^{ℓ} for longitudinally and transversely polarized ρ^0 mesons. The filled circles represent the results of a Monte Carlo simulation and a subsequent fit. The dashed lines indicate the input values at the average values of the kinematic variables in each kinematic bin. The solid lines indicate the input values averaged over each kinematic bin.

6.8 SDME extraction

In order to study the performance of the methods used to extract the SDMEs for an unpolarized or a transversely polarized target from the experimental data, these SDMEs were implemented in Monte Carlo simulations. The procedures used to implement these SDMEs are described in section 6.3. The values implemented for the SDMEs for an unpolarized target were similar to those extracted from the data. For this case, non-zero values were implemented only for the *s*-channel helicity conserving SDMEs and the SDMEs associated with the interference of a helicity-conserving amplitude and an amplitude for the transition $\gamma_T^* \to \rho_L$. The values assigned to the SDMEs for a transversely polarized target were only non-zero for the *s*-channel helicity conserving SDMEs.

The SDMEs were implemented at the generation level, i.e., in the implementation procedure the generated events were used to evaluate equations 6.1 or 6.2. The SDME were separately implemented in different sets of simulated events, each corresponding to a specific bin in Q^2, x, or $-t'$. The used binnings are the same as those used for the experimental data. For each binning the number of simulated events summed over all bins was about 7000 (for the binning in Q^2, the number of events in the additional lowest Q^2 bin was not included in this sum). This number is comparable to the number of selected experimental events.

The SDMEs for an unpolarized and a transversely polarized target were extracted from the simulated events with, respectively, the 15-parameter and the 30-parameter fits, both described in section 5.2.4. These fits were performed at the tracked level, i.e., the simulated tracked events were used. The procedure of SDME implementation and reconstruction was repeated 25 times each time with a different set of simulated events, but with the same SDME values on input. For each bin the averaged values of the extracted SDMEs and the averaged values of the corresponding statistical uncertainties were determined. In figures 6.8 and 6.9 the implemented values, the averaged extracted values, and the corresponding averaged uncertainties for the SDMEs for an unpolarized and a transversely polarized target are shown, respectively, for the various $-t'$ bins. These values are only shown for those SDMEs, for which the input value was non-zero. As expected, the uncertainties of the averaged values (dark-grey band) are about a factor 5 smaller than the averaged values of the uncertainties (light-grey bands).

The deviations of the averaged reconstructed values of the SDMEs from their input values were found to be smaller than, or comparable to, the corresponding statistical uncertainties. This is also the case for the bins in Q^2 and x, which are not shown. The averaged uncertainties were found to be consistent with the variances of the extracted values with respect to the corresponding input values. It is concluded that the used SDME-extraction methods obtained reliable values of the SDMEs for an unpolarized and for a transversely polarized target.

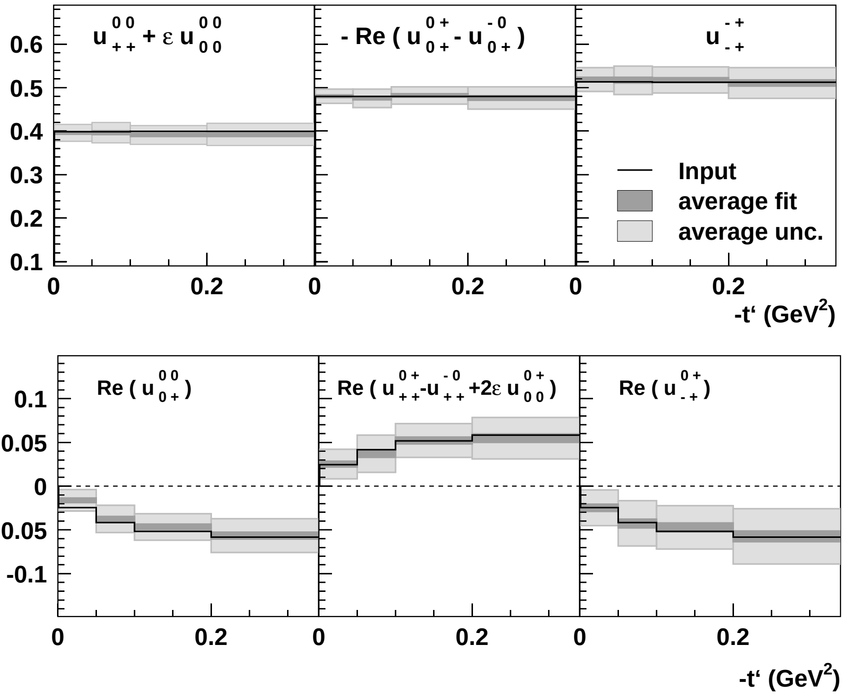

Figure 6.8: The average values of SDMEs for an unpolarized target that were extracted from 25 different simulated sets of events for each bin in $-t'$ (dark grey bands). The dark-grey bands represent the 1σ-uncertainty intervals for the average values. The light-grey bands represent the average 1σ-uncertainties on the individual fit results. The input values of the SDMEs are given by the solid black lines.

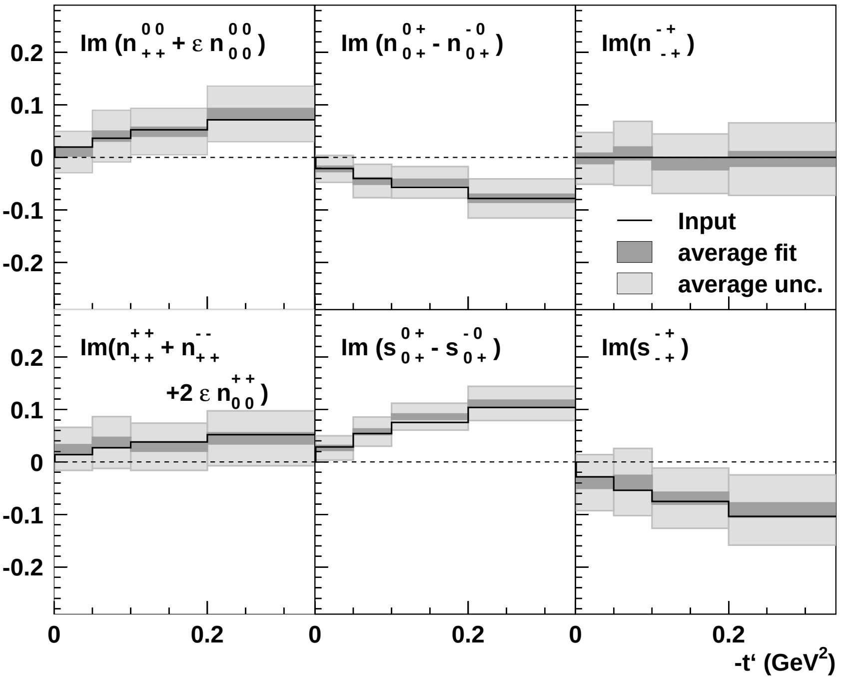

Figure 6.9: The average values of SDMEs for a polarized target that were extracted from 25 different simulated sets of events for each bin in $-t'$ (dark grey bands). The dark-grey bands represent the 1σ-uncertainty intervals for the average values. The light-grey bands represent the average 1σ-uncertainties on the individual fit results. The input values of the SDMEs are given by the solid black lines.

Chapter 7

Results

In this chapter the determined $\sin(\phi - \phi_s)$ moments of the transverse target-spin asymmetry A_{UT}^{ℓ} for longitudinally and transversely polarized ρ^0 mesons are presented. Furthermore, the results obtained for the corresponding spin density-matrix elements (SDMEs) for an unpolarized and a transversely polarized target are discussed. The measurements presented in this chapter have been obtained from fits to data on exclusive ρ^0 electroproduction from a transversely polarized proton target taken from the HERMES 2002-2005 data productions with the selection requirements described in chapter 4. The results have been obtained for various bins in the kinematic variables Q^2, x and $-t'$. The binnings used and the average values of the kinematic variables in each bin were specified in table 4.4. The fit procedures used to extract the asymmetries and SDMEs were introduced in chapter 5. Parameterizations of the contribution from non-exclusive background processes were included in the fit procedure according to the method that was described in section 5.4.

In section 7.1 the experimentally determined SDMEs for an unpolarized target are presented. These results are used in the analysis of the asymmetry A_{UT}^{ℓ}. The data on the $\sin(\phi - \phi_s)$ moments of A_{UT}^{ℓ} for longitudinally and transversely polarized ρ^0 mesons are presented in section 7.2. The results for SDMEs corresponding to transverse target polarization are the subject of section 7.3. The determination of various systematic uncertainties for the asymmetries and the SDMEs is discussed in section 7.4. Finally, a comparison of GPD-model calculations with the results obtained for the $\sin(\phi - \phi_s)$ moment of A_{UT}^{ℓ} for longitudinally polarized ρ^0 mesons is presented in section 7.5. The results are used to obtain a model-dependent estimate of the quark orbital momentum L_q.

7.1 SDMEs for an unpolarized target

As discussed in chapter 5, the SDMEs for an unpolarized target play an important role in the analysis of the transverse target-spin asymmetry when results on this asymmetry need to be obtained separately for longitudinally and transversely polarized ρ^0 mesons. The unpolarized SDMEs were determined from the data for a transversely polarized target[1]. Since the net target polarization of the data set used is approximately equal to zero, it is justified to ignore the target polarization in such an analysis. The matrix elements were determined within the Diehl formalism by a fit to the measured yields. The used fit function is given by equation 5.25 in combination with equations 5.26, 2.70, and 2.71, which parameterize the yields for an unpolarized target in terms of 15 independent (combinations of) SDMEs. The normalization integral of the fit function was computed for each iteration of the fit according to equation 5.34, so as to account for the acceptance of the HERMES spectrometer (see section 5.3).

The SDMEs extracted from the full data set integrated over all kinematic variables are shown in figure 7.1. (The results binned in the kinematic variables Q^2, x and t' are shown in figures E.1-E.9 in appendix E.) The results are presented in three categories, each corresponding to a set of SDMEs with a different degree of s-channel helicity conservation. The results for these categories are plotted in different panels in figure 7.1, which are separated from each other by the solid, horizontal lines.

In the upper panel three (combinations containing) s-channel helicity conserving SDMEs are shown[2]. These SDMEs differ significantly from zero and are larger than the SDMEs from the other categories. In the middle panel the eight (combinations of) SDMEs are shown, which are associated with the interference between s-channel helicity conserving and s-channel helicity changing amplitudes. Within this category the combinations are sorted into three groups that can be associated with different virtual photon and ρ^0 polarizations. The results for the different groups are separated from each other by the dotted horizontal lines. The (combinations containing) SDMEs associated with the interference between helicity-conserving amplitudes and amplitudes for the transition $\gamma^*_T \to \rho_L$, deviate significantly from zero, but are almost an order of magnitude smaller than the combinations containing s-channel helicity conserving SDMEs. The (combinations containing) SDMEs associated with the interference between s-channel helicity conserving amplitudes and amplitudes for the transition $\gamma^*_L \to \rho_T$ or $\gamma^*_T \to \rho_{-T}$, are not significantly different from zero. The lower panel shows the values for the four SDMEs associated with the interference of helicity-changing amplitudes only. These results are consistent with zero within the statistical accuracy.

The obtained results are consistent with the picture that s-channel helicity conserving transitions are favored over s-channel helicity changing transitions at

---

[1] In the preliminary version of the analysis of the transverse target-spin asymmetry [58], unpolarized SDMEs extracted from the HERMES 1996-2000 data for an unpolarized target were used [26]. These SDMEs were obtained within the Wolf-Schilling formalism [14]. Currently, efforts are underway to extract unpolarized SDMEs within the Diehl formalism from the combined 1996-2005 data.

[2] Note that also the combination $u^{++}_{++} + u^{--}_{++} + 2\epsilon u^{++}_{0\,0}$ belongs to this category. The result for this combination of matrix elements can be directly obtained from the relation $u^{++}_{++} + u^{--}_{++} + 2\epsilon u^{++}_{0\,0} = 1 - \left(u^{0\,0}_{++} + \epsilon u^{0\,0}_{0\,0}\right)$ (see equation 2.71).

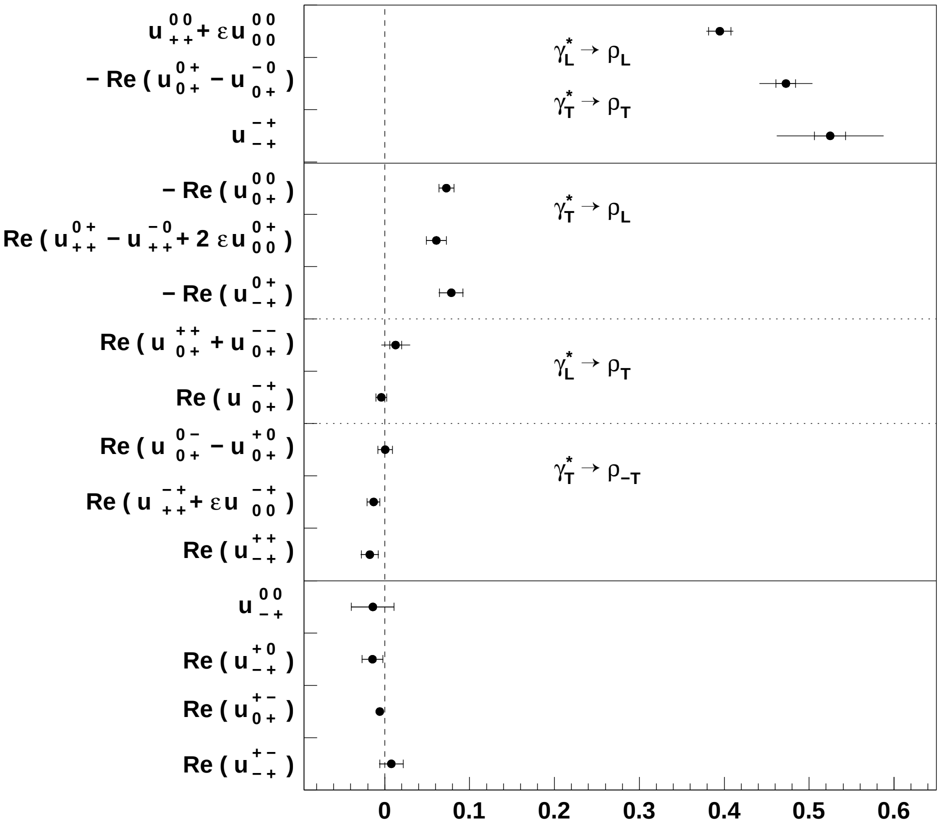

Figure 7.1: The SDMEs for an unpolarized target and an unpolarized beam extracted from 2002-2005 HERMES ρ^0-electroproduction data on a transversely polarized hydrogen target. The horizontal lines separate the different categories explained in the text. The full error bars represent the statistical and systematic uncertainties summed in quadrature, whereas the inner error bars represent the statistical uncertainties.

HERMES kinematics. The results indicate that the s-channel helicity changing amplitudes for $\gamma^*_T \to \rho_L$ transitions deviate from zero, but are small in comparison to the helicity-conserving transitions. Within the statistical accuracy, the results do not indicate deviations from zero for the amplitudes for $\gamma^*_L \to \rho_T$ and $\gamma^*_T \to \rho_{-T}$ transitions.

matrix elements	$p_{\min}$
$u^{0\,0}_{++} + \epsilon u^{0\,0}_{0\,0}$	0
$u^{0+}_{0+} - u^{-0}_{0+}$	0
$u^{++}_{++} + u^{--}_{++} + 2\epsilon u^{++}_{0\,0}$	0
u^{-+}_{-+}	0
$u^{0\,0}_{0+}$	1
$u^{0+}_{++} - u^{-0}_{++} + 2\mathrm{Re}\,\epsilon u^{0+}_{0\,0}$	1
u^{0+}_{-+}	1
$u^{++}_{0+} + u^{--}_{0+}$	1
u^{-+}_{0+}	1
$u^{0-}_{0+} - u^{+0}_{0+}$	2
$u^{-+}_{++} + \epsilon u^{-+}_{0\,0}$	2
u^{++}_{-+}	2
$u^{0\,0}_{-+}$	2
u^{+0}_{-+}	3
u^{+-}_{0+}	3
u^{+-}_{-+}	4

Table 7.1: Minimum values $p_{\min}$ of the power that controls the $(-t')^{1/2}$ dependence of the various combinations of spin density-matrix elements in the the limit $-t' \to 0$ [11].

When discussing the $-t'$ dependence of SDMEs it is of interest to study the limit of forward scattering, where the scattering angle Θ between the produced ρ^0 meson and the incoming virtual photon goes to zero. By using the property $\Theta \propto (-t')^{1/2}$ for small Θ, one can derive [11] from a partial wave decomposition of the transition amplitudes that

$$u^{\alpha\beta}_{mn} \sim (-t')^{p/2}, \tag{7.1}$$

where $p \in 0, 1, \ldots$ and $p \geq p_{\min}$. Here the value of $p_{\min}$ depends on the transferred helicity in the transitions $\gamma^*_m \to \rho_\alpha$ and $\gamma^*_n \to \rho_\beta$. The values of $p_{\min}$ for the various combinations of matrix elements u are listed in table 7.1. In order to compare the forward-limit behavior predicted by equation 7.1 with the data, the $-t'$ dependencies of the various non-zero SDME combinations were fitted with the function

$$f[(-t')^{1/2},\, p_{\min}] \;=\; a\,(-t')^{p_{\min}/2}, \tag{7.2}$$

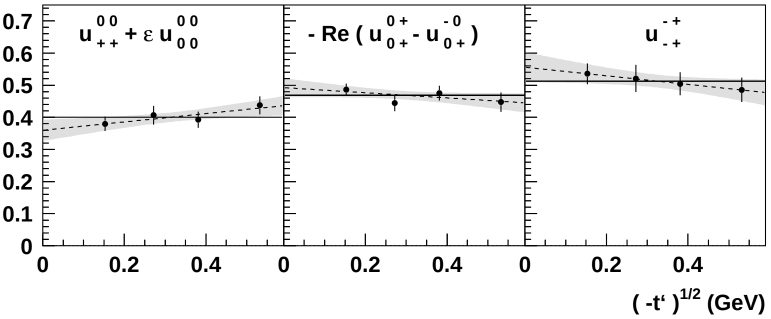

Figure 7.2: Combinations of SDMEs for an unpolarized target and an unpolarized beam binned in $(-t')^{1/2}$. Each combination contains an s-channel helicity conserving SDME. The error bars of the data represent the statistical uncertainties. The solid line represents the result of a fit to the data with a constant function, i.e., $p_{\min} = 0$. The dashed line and the shaded 1σ uncertainty band represent the result of a fit with a first-order polynomial in $(-t')^{1/2}$.

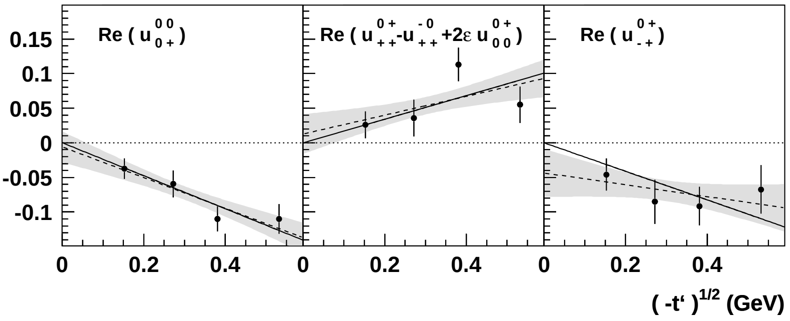

Figure 7.3: Combinations of SDMEs for an unpolarized target and an unpolarized beam binned in $(-t')^{1/2}$. Each combination contains an SDME associated with the interference between a helicity-conserving and a helicity-changing amplitude for the transition $\gamma^*_T \rightarrow \rho_L$. The error bars represent the statistical uncertainties. The solid line represents the result of a fit to the data points with the function $f(-t') = a\,(-t')^{1/2}$, i.e., $p_{\min} = 0$. The dashed line and the shaded 1σ uncertainty band represent the result of a fit with a first-order polynomial in $(-t')^{1/2}$.

with a being a free parameter and $p_{\min}$ taken from table 7.1. It can thus be studied whether the predicted dependencies in the limit of forward scattering give a good description of the data in the selected kinematic range.

This study has only been performed for (the combinations of) SDMEs for which the observed deviation from zero is statistically significant. The data and the results of the fits are shown in figures 7.2 and 7.3. The results of the fits with $p_{\min} = 0$ shown in figure 7.2 are consistent with the data for the combinations that contain an s-channel conserving SDME. In figure 7.3, the results of the fits with $p_{\min} = 1$ are shown, which are consistent with the data for the combinations each containing an SDME associated with the interference between helicity-conserving amplitudes and helicity-changing amplitudes for the transition $\gamma^*_T \rightarrow \rho_L$.

Alternative fits have been performed with a first-order polynomial in $(-t')^{1/2}$ given by $g[(-t')^{1/2}, b, c] = b + c\,(-t')^{1/2}$, where b and c are free parameters. The results of these fits are represented by the dashed lines and the shaded 1σ uncertainty bands in figures 7.2 and 7.3. The results of the fits to the data shown in figure 7.2 indicate that for the presently available precision an additional $(-t')^{1/2}$ term is not required in the description of the data. For the fits to the data shown in figure 7.3 the results for the constant term b were found to be consistent with zero as expected. The results for the $(-t')^{1/2}$ term, which is predicted to be the leading-order term for these matrix elements, deviate significantly from zero (although for the fit to the $\mathrm{Re}\, u^{0+}_{-+}$ data this deviation is only slightly more than 1σ). It is noted that also higher-order terms may contribute to the data. However, equation 7.2 with $p_{\min}$ taken from table 7.1 is already sufficient to describe these data. It is concluded that the predictions contained in table 7.1 and expressed by equation 7.1 are in agreement with the data.

The results of the present analysis have also been compared with results obtained from an earlier analysis of the HERMES 1996-2000 data [26] in order to investigate whether the results are consistent. The presently obtained SDMEs were converted from the Diehl formalism to the Wolf-Schilling formalism (see [11] and equations D.1-D.15 in appendix D). The covariance matrix was used in the propagation of the statistical uncertainties. Figure 7.4 shows a comparison of the 15 unpolarized SDMEs extracted from the 2002-2005 data set as obtained by the present analysis (filled circles), and the SDMEs obtained previously from the 1996-2000 data set (open circles). In general, the differences between the results for the SDMEs for the two analyses are smaller than or comparable to the corresponding total uncertainties, despite the fact that the extraction methods used and the experimental setup involved in the two data sets are somewhat different. Hence, it is concluded that the agreement between the previous and the present results is satisfactory. Comparisons of the results from both analyses binned in the kinematic variables Q^2, x, and t' can be found in figures E.10-E.12 in appendix E.

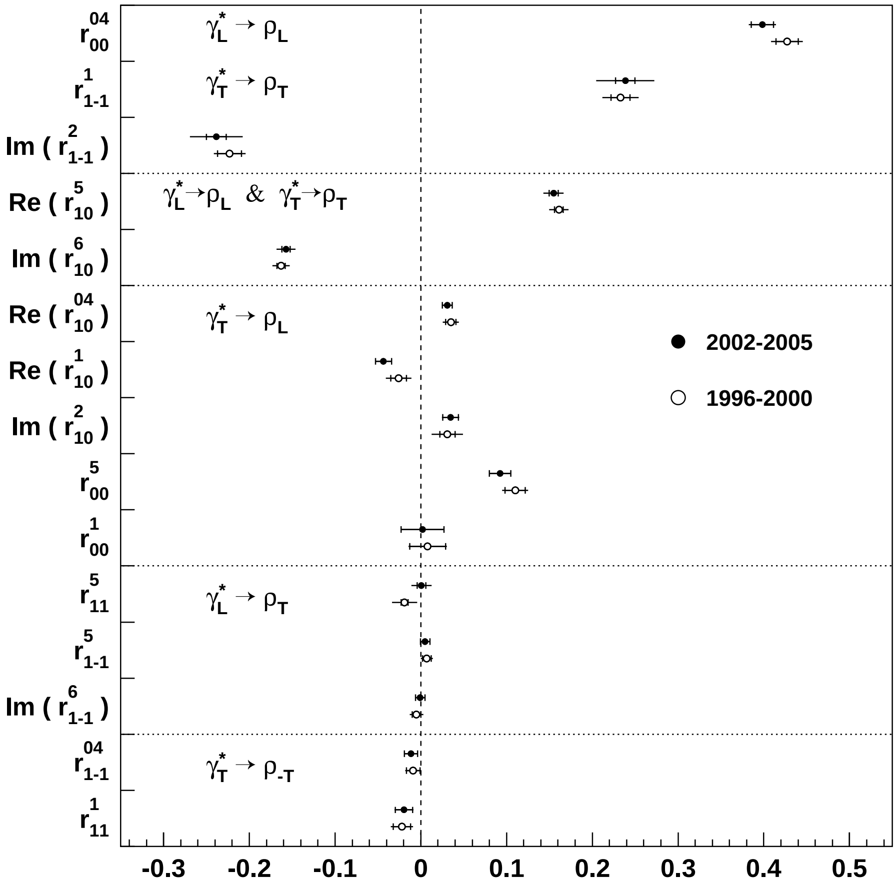

Figure 7.4: The extracted SDMEs for an unpolarized target and an unpolarized beam represented within the Wolf-Schilling formalism [14]. The results from the present analysis obtained from the HERMES 2002-2005 data for a transversely polarized hydrogen target (solid circles) are compared with the results from another analysis [26] based on the HERMES 1996-2000 data for an unpolarized hydrogen target (open circles). The full error bars represent the total uncertainties obtained by summing the statistical and systematic uncertainties in quadrature, whereas the inner error bars represent the statistical uncertainties.

7.2 The $\sin(\phi - \phi_s)$ moments of A^{ℓ}_{UT,ρ_L} and A^{ℓ}_{UT,ρ_T}

As discussed in section 5.2, the fit functions used to extract the $\sin(\phi{-}\phi_s)$ moments of the asymmetry A^{ℓ}_{UT} contain a parameterization of the angular distribution function for the cross section for a transversely polarized target. We have developed several parameterizations of the angular distribution function by using various theoretical formalisms. One of these parameterizations has been obtained by using a combination of the Diehl-Sapeta [13] and the Wolf-Schilling [14] formalisms. The results obtained from the fits performed with this parameterization are presented in section 7.2.1. It is noted that this parameterization was also used in the extraction of the first preliminary results for the $\rho_L - \rho_T$ separated $\sin(\phi - \phi_s)$ moments, which are presented in [58, 59, 60]. When the Diehl-SDME formalism [11] for vector-meson production from a polarized target became available in 2007, it was decided to also use this formalism in the parameterization of the fit function. The results obtained from the fits performed with this parameterization are presented in section 7.2.2.

7.2.1 Extraction within the Diehl-Sapeta and Wolf-Schilling formalisms

The parameterization of the fit function that we obtained by using a combination of the Diehl-Sapeta and the Wolf-Schilling formalisms is described in detail in section 5.2.2. In this parameterization the Diehl-Sapeta formalism has been used to obtain a description of the asymmetries A^{ℓ}_{UT,ρ_L} and A^{ℓ}_{UT,ρ_T} for, respectively, longitudinally and transversely polarized ρ^0 mesons. The asymmetries are each described by 6 parameters. All these parameters are left free in the fit procedure, so that the number of free parameters of the fit is 12. The relative contribution from longitudinally and transversely ρ^0 mesons is given by the separately determined value of the SDME r^{04}_{00}, which was included in the fit function as a fixed parameter. In addition, the values of several other SDMEs for an unpolarized target, which determine the part of the fit function that does not depend on the target polarization, were included as well. The values used for these SDMEs were determined from a separate fit to the 2002-2005 data. The results obtained for these SDMEs were presented in section 7.1.

The results for the $\sin(\phi - \phi_s)$ moments of A^{ℓ}_{UT} for longitudinally and transversely polarized ρ^0 mesons are shown in figure 7.5 (open squares). In each panel of figure 7.5 the results are shown for a specific kinematic binning. The left-most panels represent the asymmetries averaged over all kinematic variables, whereas in the remaining panels the asymmetries are plotted binned in the kinematic variables Q^2, x, and $-t'$, respectively. In general, the extracted values of the asymmetries are statistically consistent with zero.

7.2.2 Extraction within the Diehl-SDME formalism

The parameterization of the fit function that we obtained by using the the Diehl-SDME formalism is described in detail in section 5.2.3. The parameterization consists of a description of the angular distributions W_{UU} and W_{UT}^{ℓ}. The angular distribution W_{UU} is described in terms of the 15 independent (combinations of) SDMEs for an unpolarized beam and an unpolarized target. These parameters were fixed to the separately determined SDME values presented in section 7.1. The free parameters of the fit procedure were the 36 coefficients introduced in section 5.2.3 describing the angular distribution W_{UT}^{ℓ}.

We determined the $\sin(\phi - \phi_s)$ moments of A_{UT}^{ℓ} for longitudinally and transversely polarized ρ^0 mesons with the 36-parameter fit by using equation 5.23. The obtained results are shown for the various kinematic binnings in figure 7.5 (solid circles). Within the statistical accuracy the results are consistent with zero. It is noted that the observed deviations of about 2σ from zero in two of the panels are consistent with our expectation for statistical fluctuations in a set of 3 or 4 data points.

The major difference between the 36-parameter fit used for these results and the 12-parameter used for the results from section 7.2.1 is that the 36-parameter fit also takes into account the $\phi_{\pi\pi}$ dependence of the angular distribution. It has been verified that if all the $\phi_{\pi\pi}$-dependent terms are ignored the results obtained from both fits are identical.

The results from the 36-parameter fit and the 12-parameter fit are compared in figure 7.5. One can see that the inclusion of the $\phi_{\pi\pi}$-dependent terms leads to an increase of the statistical uncertainty of up to about 50%. The differences between the results of the 36-parameter fit and the results of the 12-parameter fit are in general smaller than, or comparable to the statistical uncertainty of the former results. On average the results of the 36-parameter fit are slightly more positive for both longitudinally and transversely polarized ρ^0 mesons. Because the $\phi_{\pi\pi}$-dependent terms are included in the fit, cross contamination effects are avoided, which would be present otherwise due to the coupling of these terms with the acceptance efficiency (see section 5.3). For this reason the results of the 36-parameter fit are considered to be more complete.

7.3 SDMEs for a transversely polarized target

The present analysis focuses on the determination of the $\sin(\phi - \phi_s)$ moment of the transverse target-spin asymmetry A_{UT} for longitudinal virtual-photon and longitudinal ρ^0 polarization. This azimuthal moment of the asymmetry is directly related to the ratio of the leading-twist SDMEs $\mathrm{Im}\, n_{0\,0}^{0\,0}$ corresponding to transverse target polarization, and $u_{0\,0}^{0\,0}$ for an unpolarized target (see equation 2.73).

In this section the results of the SDMEs corresponding to transverse target polarization with respect to the virtual-photon direction are presented. These SDMEs are associated with the interference between nucleon-helicity changing and conserving amplitudes. In combination with the SDMEs for an unpolarized target

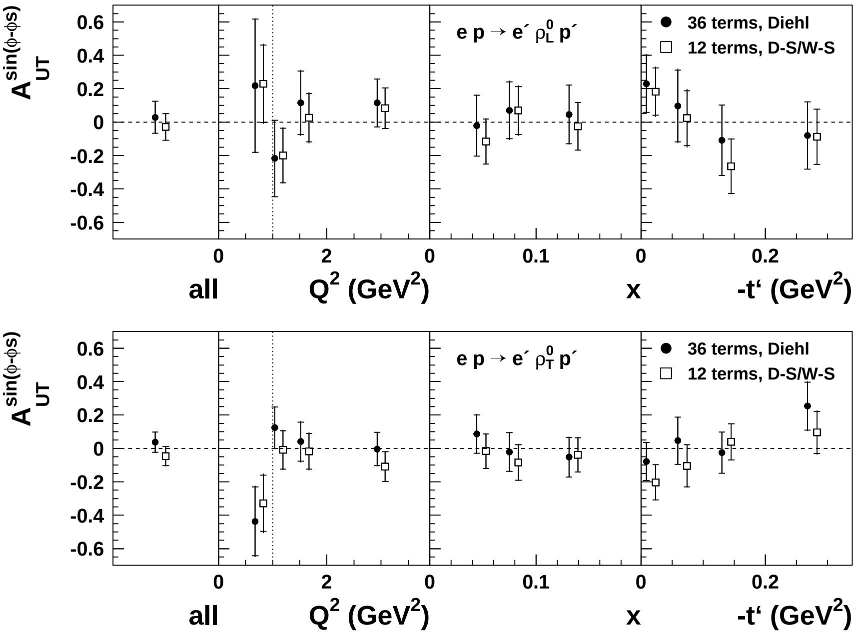

Figure 7.5: The extracted $\sin(\phi - \phi_s)$ component of A^{ℓ}_{UT} for longitudinally polarized ρ^0 mesons (top panel) and transversely polarized ρ^0 mesons (bottom panel). The results are displayed for both the 12-parameter fit using a combination of the Diehl-Sapeta [13] and the Wolf-Schilling [14] formalisms (open squares) and the 36-parameter fit using the Diehl formalism [11] (filled circles). The full error bars represent the statistical and systematic uncertainties summed in quadrature. The inner error bars represent the statistical uncertainties. The overall systematic scale uncertainty of 8.1% is not shown.

(see section 7.1), which provide information on the dominant nucleon-helicity conserving amplitudes, the SDMEs corresponding to transverse target polarization provide additional information on the nucleon-helicity changing amplitudes

The fit function used to extract the (combinations of) SDMEs corresponding to transverse target polarization is described in section 5.2.4. The fit function contains decompositions of the angular distributions W_{UU} and W_{UT}, which are parameterized in terms of (combinations of) SDMEs as given by the Diehl formalism. In the fit procedure the 15 (combinations of) unpolarized SDMEs are kept fixed at the values presented in section 7.1. The free parameters of the fit procedure are the 30 (combinations of) SDMEs corresponding to transverse target polarization.

The results for these 30 (combinations of) SDMEs are shown in figure 7.6. In figures F.1-F.9 of appendix F the results for these SDMES obtained for various bins in Q^2, x, and t' are shown. The (combinations of) SDMEs are sorted into the three categories introduced in relation to figure 7.1 in section 7.1. Each category represents a different degree of s-channel helicity conservation. Statistically, the overall results are consistent with the hypothesis that all SDMEs are equal to zero. However, for some of the (combinations of) SDMEs deviations larger than 1σ are observed. For $\mathrm{Im}\,(s^{0+}_{0+} - s^{-0}_{0+})$ and $\mathrm{Im}\,s^{-+}_{-+}$ deviations of 3.0σ and 1.7σ are observed, respectively[3]. A significant deviation from zero (3.3σ) is observed for the SCHC-violating SDME $\mathrm{Im}\,n^{00}_{0+}$, which contains the interference between s-channel helicity conserving amplitudes and helicity-changing amplitudes for the transition $\gamma^*_T \to \rho_L$. It is noted that, whereas the SDMEs for an unpolarized target in this category are predicted to be kinematically suppressed with a factor $(-t')^{1/2}$ at small values of $-t'$ (see section 7.1), this is not the case for the SDMEs corresponding to transverse target polarization [11].

The $\sin(\phi - \phi_s)$ moments of the asymmetry A_{UT} for longitudinally and transversely polarized ρ^0 mesons can be expressed in terms of combinations of SDMEs as (see equations 5.29 and 5.30)

$$A^{\sin(\phi-\phi_s)}_{UT,\rho_L} = \frac{\mathrm{Im}\left(n^{00}_{++} + \varepsilon n^{00}_{00}\right)}{u^{00}_{++} + \varepsilon u^{00}_{00}}, \tag{7.3}$$

$$A^{\sin(\phi-\phi_s)}_{UT,\rho_T} = \frac{\mathrm{Im}\left(n^{++}_{++} + n^{--}_{++} + 2\varepsilon n^{++}_{00}\right)}{1 - (u^{00}_{++} + \varepsilon u^{00}_{00})}. \tag{7.4}$$

The contribution from transversely polarized virtual photons to the azimuthal moment for longitudinally polarized ρ^0 mesons is represented by the (non leading-twist) SDMEs $\mathrm{Im}\,n^{00}_{++}$ and u^{00}_{++}. Under the assumption of SCHC these SDMEs are equal to zero. Although the SDMEs $\mathrm{Im}\,n^{00}_{++}$ and u^{00}_{++} have not been determined

---

[3] It is noted that non-zero values are anticipated for these (combinations of) SDMEs as the unnatural parity-exchange contribution to nucleon-helicity changing amplitudes for the transition $\gamma^*_T \to \rho_T$ are predicted to be non-zero at HERMES kinematics [70]. These predictions are supported by the earlier obtained results for SDMEs for an unpolarized target [26]. The SDMEs $\mathrm{Im}\,s^{0+}_{0+}$ and $\mathrm{Im}\,s^{-+}_{-+}$ are sensitive to these amplitudes since the SDMEs $s^{\alpha\beta}_{mn}$ involve the interference between natural and unnatural parity exchange amplitudes [11]. As a result these SDMEs are related to the GPDs $\tilde{H}$ and $\tilde{E}$.

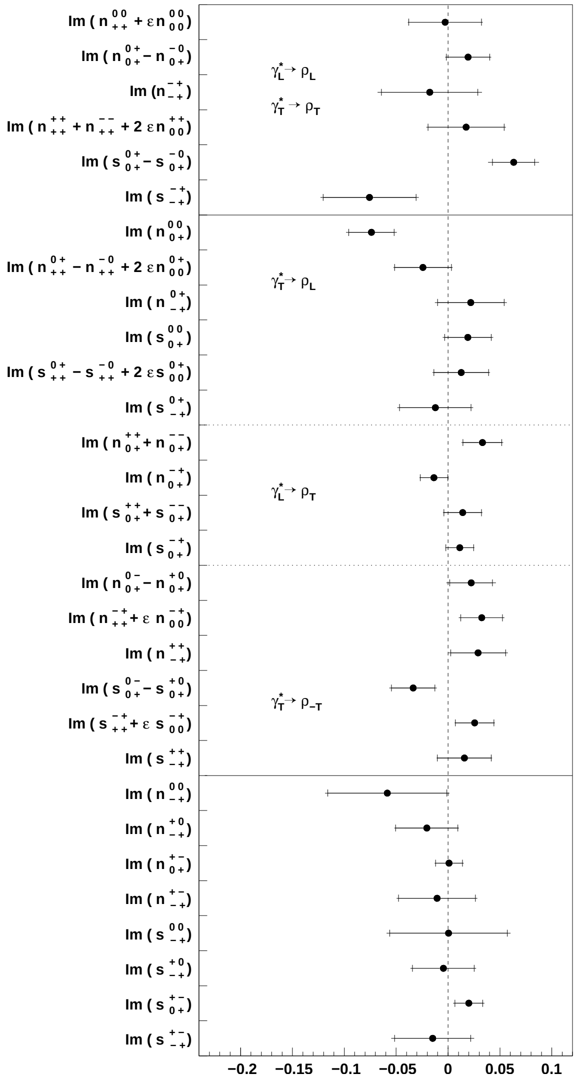

Figure 7.6: The combinations of SDMEs for a transversely polarized target and an unpolarized beam extracted from 2002-2005 HERMES electroproduction data on a transversely polarized hydrogen target. The horizontal lines divide the data into different categories explained in the text. The full error bars represent the statistical and systematic uncertainties summed in quadrature. The inner error bars represent the statistical uncertainties. In addition an overall systematic scale uncertainty is present of 8.1%.

separately, one can estimate to what extent the assumption of SCHC is valid for equation 7.3 by using the results obtained for the other SDMEs in combination with theoretically based assumptions. It is shown in [11] that one can use the approximations $\mathrm{Im}\, n_{++}^{0\,0} \approx -\mathrm{Im}\, n_{-+}^{0\,0}$ and $u_{++}^{0\,0} \approx -u_{-+}^{0\,0}$ if unnatural parity exchange is strongly suppressed (it is discussed in [70] that this is a reasonable assumption for the amplitudes contributing to these matrix elements). Since the results for the matrix elements $\mathrm{Im}\, n_{-+}^{0\,0}$ and $u_{-+}^{0\,0}$ are found to be consistent with zero given their present uncertainties (see figures 7.6 and 7.1), these results are consistent with the approximation of SCHC for equation 7.3. A more precise estimate of possible violations of SCHC could be obtained from an analysis of the amplitudes contributing to all determined SDMEs. Such an amplitude analysis is presented in [70] for the SDMEs for an unpolarized target, but has not yet been performed for the SDMEs for a transversely polarized target.

In order to check the consistency between the results obtained for the SDMEs and the azimuthal moments of the asymmetry A_{UT}^{ℓ} presented in section 7.2.2, we determined the azimuthal moments given by equations 7.3 and 7.4. The obtained results (open squares) are compared to the results from section 7.2.2 (filled circles) in figure 7.7. The main difference between the two approaches is that the admixture from longitudinal target polarization (see section 5.2.1) is taken into account in the parameterization of the 36 terms of W_{UT}^{ℓ} used for the results from section 7.2.2, whereas this admixture is neglected in the 30-parameter SDME fit used for the present results. The differences between the results of the general 36-parameter fit and the 30-parameter SDME fit are in magnitude smaller than the statistical uncertainties of both results. In order to verify whether the differences observed can be attributed to the additional 6 terms in the 36-parameter fit that correspond to only the admixture from longitudinal target polarization, we repeated this fit leaving out these terms. The differences between the results of that fit (open circles in figure 7.5) and the results of the SDME fit are negligible, from which one can conclude that the differences between the results of the SDME fit and the results from section 7.2.2 are indeed mainly caused by the inclusion of these 6 additional terms.

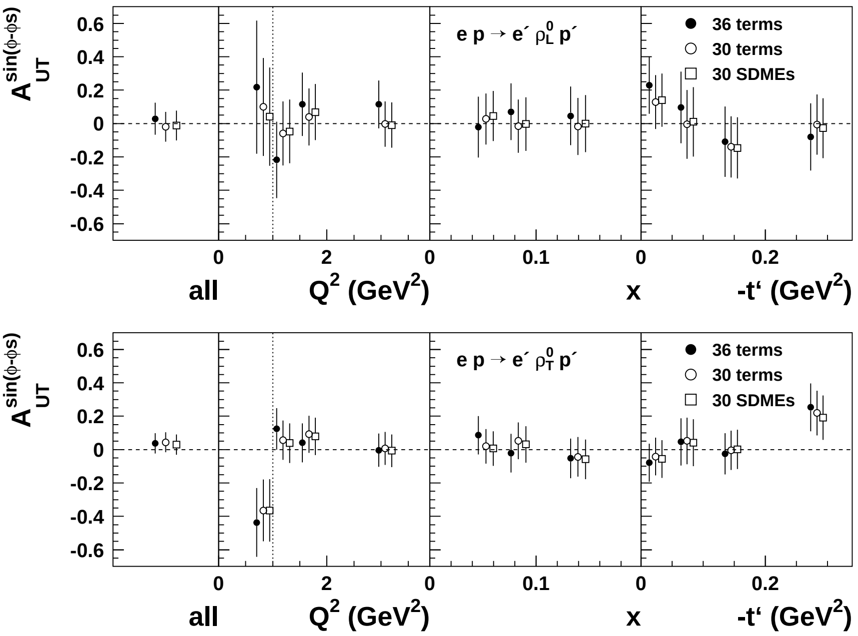

Figure 7.7: The determined $\sin(\phi - \phi_s)$ moment of A_{UT}^{ℓ} for longitudinally polarized ρ^0 mesons (top panel) and transversely polarized ρ^0 mesons (bottom panel). The results from fits using a general parameterization of all 36 expected terms of W_{UT}^{ℓ} (filled circles) are compared to those from fits using a general parameterization of only the 30 terms of W_{UT} (open circles) and a parameterization in terms of the 30 associated combinations of SDMEs (open squares). The error bars represent the statistical uncertainties.

7.4 Systematic uncertainties

In the determination of the systematic uncertainties of the extracted asymmetries and spin density-matrix elements the following contributions are considered: the uncertainty of the target polarization, the uncertainty of the background fractions, the angular distributions of background processes, contributions associated with the non-zero beam polarization P_b, smearing, the admixture of the longitudinal target polarization S_L, and radiative effects. These contributions are discussed in more detail in the following paragraphs. We obtained the total systematic uncertainty by adding the various contributions in quadrature. Some of the contributions were found to be negligible and were therefore not included in the determination of the total systematic uncertainty. The most important contributions to the systematic uncertainty on the determined asymmetry and the SDMEs are listed, for the results obtained from the full data set, at the end of this section in tables 7.3-7.5.

The uncertainty of the target polarization The target polarization P_T and its uncertainty were determined by the HERMES target group. The uncertainty is predominantly systematic. The data taking periods 2002-2005 were sub-divided into smaller periods during which the absolute value of P_T was reasonably constant. The values of $|P_T|$ and their uncertainty were made available for these specific periods separately. In table 7.2 the weighted averages of $|P_T|$ for each data taking period and for the combined 2002-2005 period are shown. The used weight for each period is the corresponding number of DIS events. The uncertainty on the average of $|P_T|$ has been determined by taking the weighted averages of the uncertainties for each sub period.

Since the determined values of the transverse target-spin asymmetry and the SDMEs corresponding to transverse target polarization are inversely proportional to the value taken for $|P_T|$, the uncertainty in $|P_T|$ corresponds to a scale uncertainty of these quantities. This scale uncertainty is equal to the fractional uncertainty of $|P_T|$, which is 8.1% for the combined 2002-2005 period.

period	average target polarization
2002	0.783 ± 0.041
2003	0.795 ± 0.033
2004	0.737 ± 0.055
2005	0.706 ± 0.065
2002-2005	0.724 ± 0.059

Table 7.2: Average absolute values of the target polarization and their uncertainties for each data taking period and for the combined periods.

The uncertainty of the non-exclusive background fraction The fractional contribution from non-exclusive background processes depends strongly on the upper limit of the missing energy ΔE used to select exclusive events (see section 4.2.2). The positions of the exclusive peaks for the 2004 and the 2005 periods were found to be shifted with respect to each other in ΔE with a shift of about 0.05-0.1 GeV. The observed shift in ΔE is related to the uncertainty in the determined beam energy E and the uncertainty in the reconstructed momenta of the detected particles as ΔE is given by $\Delta E = E - E' + E_V + t/2M$, with E' the energy of the scattered lepton, E_V the energy of the produced ρ^0 meson, and M the nucleon mass (see equation 4.2).

In order to estimate the systematic uncertainty of the background fraction due to the uncertainty in ΔE, we determined the background fraction by using the requirement $\Delta E < 0.5$ GeV for the Monte Carlo simulation of the background, instead of the requirement $\Delta E < 0.6$ GeV. The normalization range for the Monte Carlo was also shifted downwards in ΔE by 0.1 GeV. The difference between the results obtained with this shifted ΔE requirement and the nominal result was taken as the systematic uncertainty of the background fraction. This systematic uncertainty was determined separately for the various kinematic bins (see table 4.5).

In the determination of the SDMEs and the asymmetries the background fraction was varied within its total uncertainty. The maximal value of the resulting deviation is taken as the systematic uncertainty of the extracted quantities associated with the determination of the background fractions. Numerical values of the corresponding contributions to the systematic uncertainty on A^{ℓ}_{UT} and the SDMEs can be found in tables 7.3-7.5.

The angular dependencies of background processes The available knowledge about the angular dependencies of background processes is limited. For this reason the asymmetries and SDMEs were determined under the assumption that the background events were produced isotropically in the angles $\phi, \phi_s, \phi_{\pi\pi}, \theta_{\pi\pi}$. In order to estimate the corresponding systematic uncertainty we also determined these quantities without correcting for background, i.e., under the assumption that the angular distributions of the background events are equal to those of events for exclusive ρ^0 production. The difference between the background corrected results and the background-uncorrected results is taken to be the systematic uncertainty due to a possible angular dependence of the background processes. Numerical values of the corresponding contributions to the systematic uncertainty on A^{ℓ}_{UT} and the SDMEs are listed in table 7.3-7.5. In general, the systematic uncertainty related to the angular dependence of background processes was found to be larger than that associated with the background fraction itself.

Contributions due to a non-zero beam polarization Although the used data set corresponds to a non-zero net beam polarization P_b, the beam-polarization dependent angular distributions W_{LU} and W_{LT} were ignored in the determination of asymmetries and SDMEs. It has been studied how much the extracted values are affected by ignoring these angular distributions.

For some of the selected bursts there is no reliable information available about the beam polarization. These bursts contribute to 8% of the luminosity corresponding to all selected bursts. For the study of P_b-related effects these bursts were excluded from the selection. The number of the remaining bursts weighted by the corresponding number of DIS events (which is a measure of the luminosity) is shown versus P_b in figure 7.8. The weighted average of P_b over these bursts is around 9.5%.

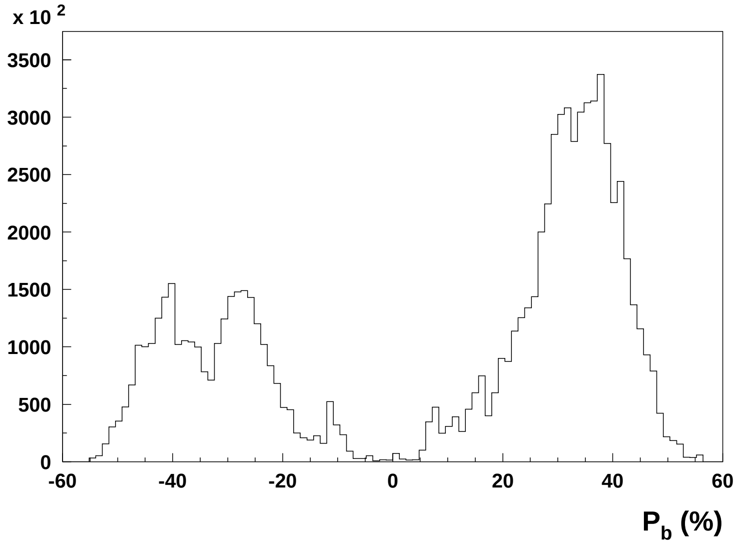

Figure 7.8: The number of selected DIS events versus the beam polarization for those selected bursts for which reliable information is available about the beam polarization.

Possible beam-polarization dependent effects on the extraction of the SDMEs for an unpolarized target and an unpolarized beam (i.e., corresponding to W_{UU}) were studied by comparing the results from two fits of the angular distributions

$$W^{\text{fit1}} = W_{UU}, \tag{7.5}$$

$$W^{\text{fit2}} = W_{UU} + P_b W_{LU}, \tag{7.6}$$

where W_{LU} is parameterized in terms of 8 additional combinations of SDMEs [11]. When applying equation 7.6, the individual value of P_b was evaluated for each event. In figure 7.9 the results from both fits to the full data set are shown.

The differences between the results from both fits for the SDMEs contributing to W_{UU} are negligibly small fractions of the statistical uncertainties.

We also studied effects from the beam polarization on the extraction of SDMEs corresponding to W_{UT} by comparing the results from two fits of the angular distributions

$$W^{\text{fit3}} = W_{UU} + S_T W_{UT}, \tag{7.7}$$

$$W^{\text{fit4}} = W_{UU} + P_b W_{LU} + S_T W_{UT} + P_l S_T W_{LT}, \tag{7.8}$$

where the approximation $S_T = P_T$ was used and W_{UU} and W_{LU} were included as fixed terms by using the results of the fits obtained with equations 7.5 and 7.6. The term W_{LT} in equation 7.8 is parameterized by 18 independent combinations of SDMEs [11], which were the free parameters of the fit in addition to the 30 combinations of SDMEs corresponding to W_{UT}. The results from both fits are shown in figure 7.10. The differences between the results from both fits for the SDMEs associated with W_{UT} are small compared to the statistical uncertainties.

The fact that the differences between the results of the fits including and not including the P_b dependence were found to be negligibly small can be explained by the fact that the net value of P_b was only about 10%, and by the fact that the correlations between the P_b-dependent terms and the P_b-independent terms were apparently relatively small.

From the studies described above we conclude that the beam polarization that was present can be safely ignored in the extraction of the SDMEs contributing to the angular distributions W_{UU} and W_{UT} from the 2002-2005 data. For this reason no systematic uncertainty for having a non-zero beam polarization was assigned to the extracted SDMEs or the transverse target-spin asymmetry.

Contributions from smearing The measured kinematic variables and angles are affected by smearing due to the limited detector resolution and interactions inside the spectrometer material. In order to study the effects from smearing on the extraction of SDMEs, 25 different sets of Monte Carlo events were generated with each the same set of input SDMEs (see section 6.8). A simulation was performed of the reconstruction of these events by the HERMES spectrometer including the effects from smearing. The SDME extraction procedure was applied to each set of reconstructed events.

Each of the simulated sets contains about 7000 reconstructed events, which is comparable to the number of real events selected from the combined 2002-2005 data taking periods. The average values of the SDMEs extracted from the various Monte Carlo sets are, given the statistical uncertainty, consistent with the inserted values. Note that the statistical uncertainties of the average values are considered, which are a factor 5 smaller compared to the uncertainties for each individual fit. The differences between the extracted values and the inserted value are for each SDME distributed according to their statistical uncertainty. Significant systematic differences between extracted and inserted values were not observed. For this reason no systematic uncertainty was assigned for smearing effects.

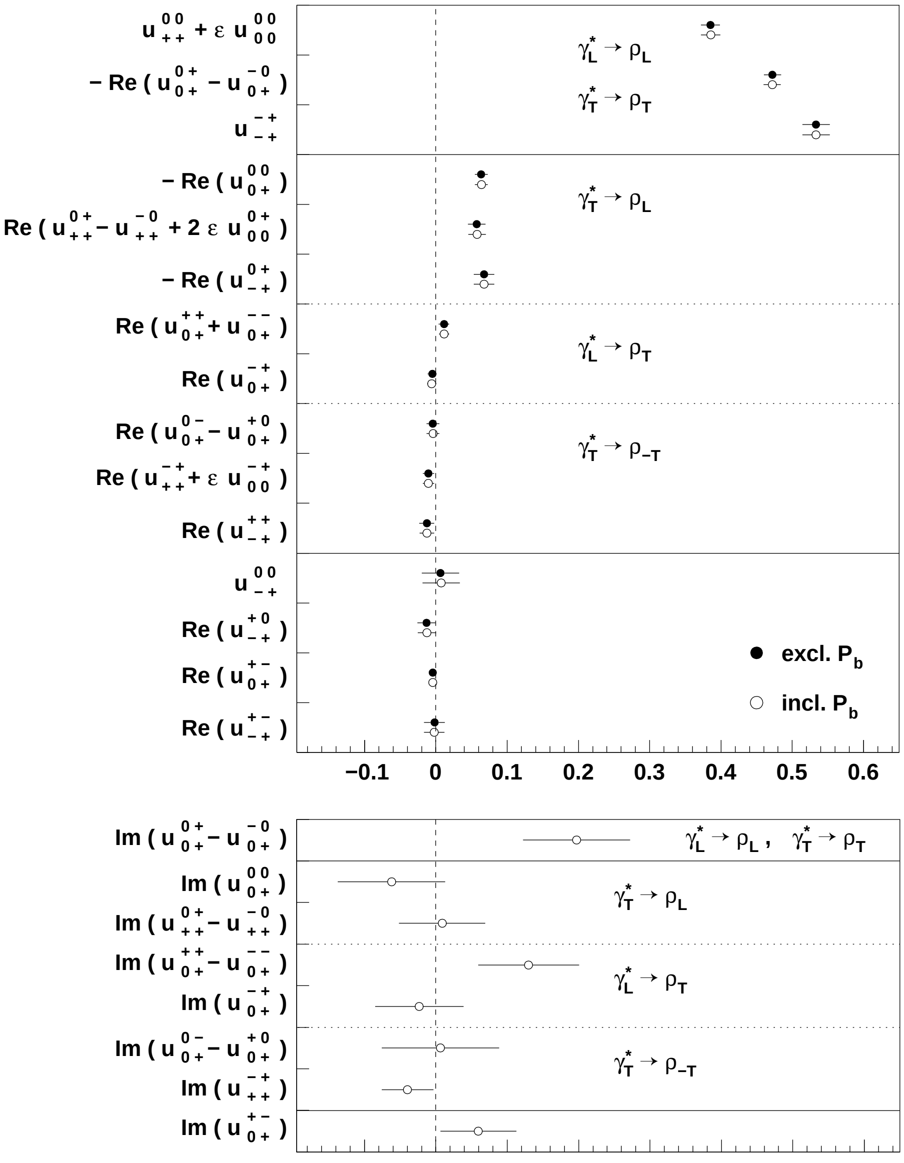

Figure 7.9: The results for the SDMEs for an unpolarized target obtained from a fit including the P_b dependence (open circles), and from a fit not including the P_b dependence (filled circles). The determined (combinations of) SDMEs corresponding to W_{UU} are shown in the upper panel and those corresponding to W_{LU} are shown in the lower panel.

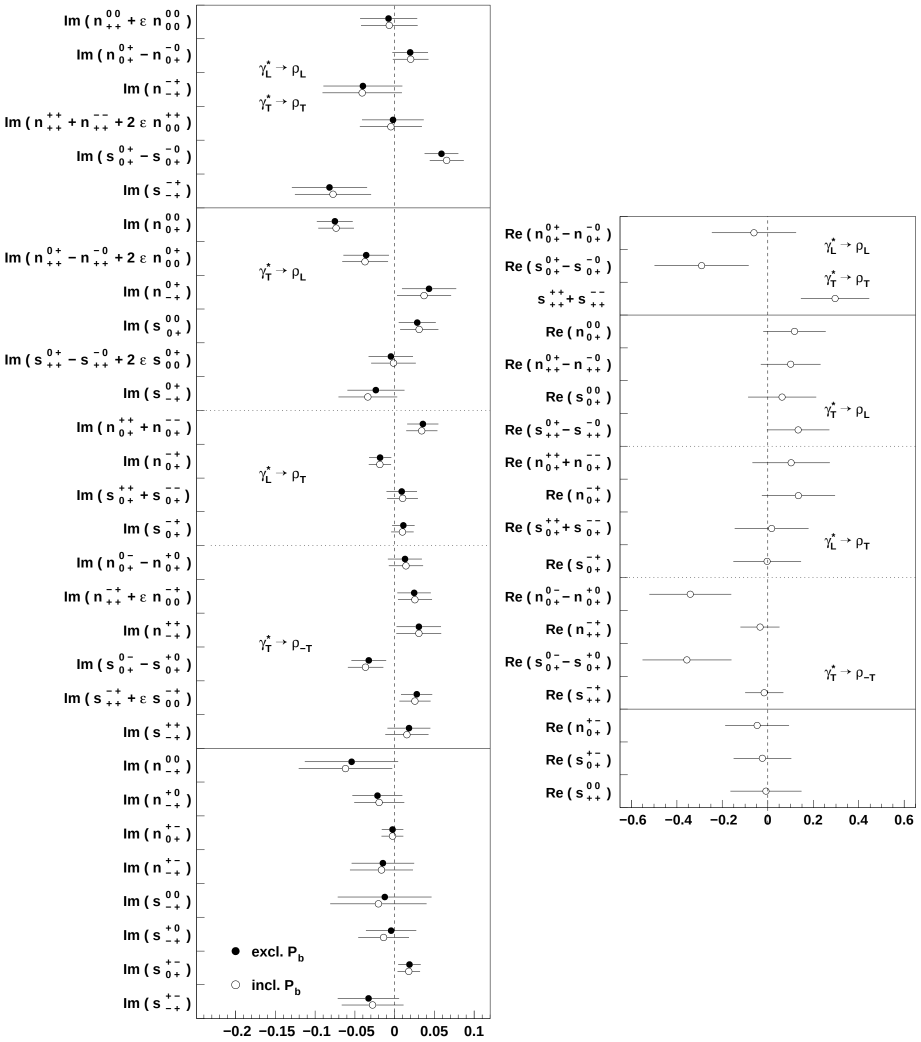

Figure 7.10: The results for the SDMEs corresponding to transverse target polarization obtained from a fit including the P_b dependence (open circles), and from a fit not including the P_b dependence (filled circles). The determined (combinations of) SDMEs corresponding to W_{UT} are shown in the left-hand panel and those corresponding to W_{LT} are shown in the right-hand panel.

Contributions due to admixture from longitudinal target polarization As the data were taken with a transverse target polarization P_T with respect to the direction of the lepton beam, a longitudinal component S_L of the target polarization was present with respect to the virtual-photon direction (see section 5.2.1). As a result, an admixture from the corresponding angular distribution W_{UL} is present, which is associated with 14 additional (combinations of) SDMEs denoted by $\mathrm{Im}\, l$ (see [11] and section 2.9.2). Due to the relatively small size of S_L, these SDMEs cannot be determined from the data taken with a transversely polarized target[4]. Therefore, a different approach was chosen to estimate to what extent the admixture from S_L has affected the SDMEs determined for a transversely polarized target.

In the extraction procedure that was used to extract SDMEs, the admixture from W_{UL} was ignored, and the angular distribution function of the cross section was approximated by

$$W^{\ell} = W_{UU} + S_T W_{UT}. \tag{7.9}$$

In order to estimate the systematic uncertainty mentioned above, the fit was repeated 20 times, with the admixture from W_{UL} included in the parameterization of the angular distribution function,

$$W^{\ell} = W_{UU} + S_T W_{UT} + S_L W_{UL}, \tag{7.10}$$

where the values of S_L and S_T were determined per event. Here S_T/P_T is very close to unity, whereas $|S_L/P_T|$ can reach values up to about 0.15 at most (see figure 5.2).

The 14 combinations of SDMEs $\mathrm{Im}\, l$ parameterizing the angular distribution W_{UL} were randomly inserted as fixed parameters of the fit by using equation 7.10. The ranges of the input values of $\mathrm{Im}\, l$ were based on the conditions[5]

$$\left(\mathrm{Im}\, l^{-+}_{-+}\right)^2 \leq \left(u^{++}_{++}\right)^2 - \left(u^{-+}_{-+}\right)^2, \tag{7.11}$$

$$\left(\mathrm{Im}\, l^{0+}_{0+}\right)^2 \leq u^{00}_{00}\, u^{++}_{++} - \left(\mathrm{Re}\, u^{0+}_{0+}\right)^2, \tag{7.12}$$

which follow directly from the positivity bounds given in [11]. From the results for the SDMEs u, in combination with equations 7.11 and 7.12, the upper bounds for $|\mathrm{Im}\, l^{-+}_{-+}|$ and $|\mathrm{Im}\, l^{0+}_{0+}|$ were found to be typically 0.3 and 0.2, respectively. The combinations of SDMEs associated with s-channel helicity changing amplitudes were assumed to satisfy comparable bounds. Hence, the input value for each of the 14 independent combinations of SDMEs $\mathrm{Im}\, l$ was randomly taken from the range $[-0.3, 0, 3]$. The quadratic mean of the differences between the new results and the original results is taken as an estimate of the systematic uncertainty. The obtained systematic uncertainties, which are listed in the last column of tables 7.3 and 7.5, are small compared to the statistical uncertainties.

---

[4] The SDMEs associated with W_{UL} can be extracted from the HERMES data taken with a longitudinally polarized target. However, such an analysis, which can be done using the HERMES data collected during the 1996-2000 periods, is a project that goes beyond the scope of this work.

[5] These conditions are not as strong as the conditions originally described in [11], since SDMEs associated with a longitudinally polarized beam are not considered here.

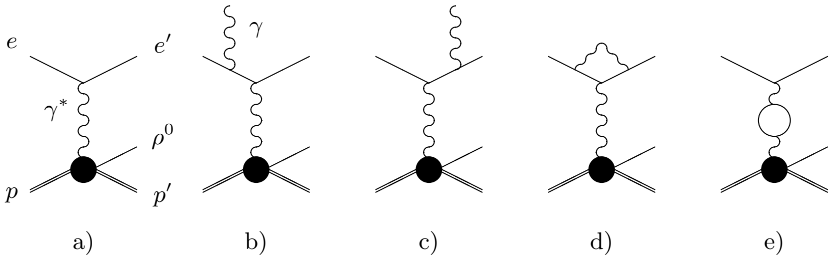

Figure 7.11: Feynman diagrams representing the Born amplitude (a) and the next order amplitudes contributing to ρ^0 meson electroproduction (b-e).

Radiative effects In addition to the Born process, higher-order processes in quantum electrodynamics (QED) contribute to the cross section of ρ^0 meson electroproduction [71]. These higher-order processes are referred to as radiative processes and the corresponding corrections to the cross section as radiative corrections. The amplitudes of the Born process and the lowest-order radiative processes are represented by the diagrams shown in figure 7.11. The radiative corrections arise from the emission of a real photon, vertex corrections (i.e., the exchange of an additional virtual photon), and loop corrections due to vacuum polarization (see figure 7.11b-e, respectively).

For the determination of spin-density matrix elements and azimuthal asymmetries it needs to be investigated to what extent radiative corrections affect the shape of the angular distributions. In [72] it was found that the reconstructed angular dependencies are mainly affected by hard photon emission. Due to the emission of an undetected photon the reconstructed kinematical variables and angles are different from the true variables. At the same time this causes a shift of the reconstructed value of ΔE to higher values. The selection requirement $\Delta E < 0.6$ GeV discards the majority of these events. For the events satisfying this requirement the energy of a possibly radiated photon is relatively low, which implies that the effect on the reconstruction of kinematic variables and angles is limited.

Various software programs are available for the calculation and simulation of radiative effects. The RADGEN generator [73] was used in combination with the PYTHIA generator to include radiative effects in the Monte Carlo simulation. The DIFFRAD code [71] calculates the radiative corrections by using a semi-analytical approach. The DIFFRAD code was used to study the effect of radiative corrections on the extraction of SDMEs for an unpolarized target. At HERMES kinematics the modulations of the shape of the ϕ dependence were found to be smaller than 2.5%. This effect was found to be negligible in the determination of the matrix elements [25, 26].

In general the dependence of radiative corrections on the orientation of the target polarization with respect to the virtual-photon direction is considered to be small. Radiative effects for the case of a transversely polarized target have been studied for semi-inclusive production of pions at HERMES in [57]. The radiative effects on the $\sin(\phi - \phi_s)$ and $\sin(\phi + \phi_s)$ amplitudes of the transverse target-spin asymmetry A_{UT} were found to be typically in the range of 0-5% in magnitude. For the determined azimuthal moments of the asymmetries in exclusive ρ^0 production, corrections of such a magnitude are small compared to the statistical uncertainties. For the present data the effects are expected to be even smaller due to the requirement on ΔE.

Since the studies of radiative effects in comparable analyses have only found effects that are small or negligible compared to the statistical uncertainties it was decided to neglect radiative corrections as well in the present analyses of the transverse target-spin asymmetry and the spin-density matrix elements.

	cent. val.	stat	syst	syst1	syst2	syst3
$A_{UT,\rho_L}^{\sin(\phi-\phi_s)}$	-5.07e-03	6.44e-02	1.58e-02	1.53e-04	6.66e-04	1.58e-02

Table 7.3: Extracted asymmetry $A_{UT,\rho_L}^{\sin(\phi-\phi_s)}$ (labelled as "cent. val.") and the statistical (stat) and systematic uncertainties. Shown are the total systematic uncertainty (syst), the systematic uncertainty due to the background fraction (syst1), the angular dependencies of the background (syst2) and the admixture from A_{UL} (syst3).

SDME	cent. val.	stat	syst	syst1	syst2
$u_{++}^{00} + \varepsilon u_{00}^{00}$	3.95e-01	1.30e-02	9.33e-03	2.44e-03	9.00e-03
$\mathrm{Re}\,(u_{0+}^{0+} - u_{0+}^{-0})$	-4.73e-01	1.15e-02	2.91e-02	6.31e-03	2.84e-02
u_{-+}^{-+}	5.25e-01	1.83e-02	6.02e-02	1.39e-02	5.86e-02
$\mathrm{Re}\,u_{0+}^{00}$	-7.28e-02	8.90e-03	1.10e-03	5.55e-04	9.46e-04
$\mathrm{Re}\,(u_{++}^{0+} - u_{++}^{-0}$ $+2\varepsilon u_{00}^{0+})$	6.08e-02	1.17e-02	2.32e-03	4.82e-04	2.27e-03
$\mathrm{Re}\,u_{-+}^{0+}$	-7.84e-02	1.39e-02	5.13e-03	1.59e-03	4.87e-03
$\mathrm{Re}\,(u_{0+}^{++} + u_{0+}^{--})$	1.30e-02	6.99e-03	1.53e-02	3.45e-03	1.49e-02
$\mathrm{Re}\,u_{0+}^{-+}$	-3.92e-03	6.16e-03	8.92e-04	5.17e-04	7.27e-04
$\mathrm{Re}\,(u_{0+}^{0-} - u_{0+}^{+0})$	5.15e-04	8.63e-03	8.86e-04	4.48e-04	7.64e-04
$\mathrm{Re}\,(u_{++}^{-+} + \varepsilon u_{00}^{-+})$	-1.31e-02	7.58e-03	2.63e-04	1.53e-04	2.15e-04
$\mathrm{Re}\,u_{-+}^{++}$	-1.75e-02	1.00e-02	4.51e-03	1.21e-03	4.34e-03
u_{-+}^{00}	-1.41e-02	2.52e-02	1.89e-03	1.70e-03	8.30e-04
$\mathrm{Re}\,u_{-+}^{+0}$	-1.43e-02	1.23e-02	3.17e-03	8.18e-04	3.06e-03
$\mathrm{Re}\,u_{0+}^{+-}$	-5.52e-03	4.69e-03	6.38e-04	2.41e-04	5.91e-04
u_{-+}^{+-}	7.94e-03	1.39e-02	4.02e-03	8.86e-04	3.92e-03

Table 7.4: Extracted SDMEs associated with W_{UU} (labelled as "cent. val.") and the statistical (stat) and systematic uncertainties. Shown are the total systematic uncertainty (syst), the systematic uncertainty due to the background fraction (syst1) and the angular dependencies of the background (syst2).

SDME	cent. val.	stat	syst	syst1	syst2	syst3
$\mathrm{Im}\,(n^{0\,0}_{++} + \varepsilon n^{0\,0}_{0\,0})$	-2.00e-03	2.54e-02	6.15e-03	5.20e-05	2.23e-04	6.14e-03
$\mathrm{Im}\,(n^{0\,+}_{0\,+} - n^{-\,0}_{0\,+})$	1.40e-02	1.52e-02	5.28e-03	3.56e-04	1.57e-03	5.03e-03
$\mathrm{Im}\,n^{-+}_{-+}$	-1.28e-02	3.37e-02	1.40e-02	3.27e-04	1.44e-03	1.40e-02
$\mathrm{Im}\,(n^{++}_{++} + n^{--}_{++}$ $+2\varepsilon n^{++}_{0\,0})$	1.26e-02	2.66e-02	7.83e-03	3.22e-04	1.41e-03	7.70e-03
$\mathrm{Im}\,(s^{0\,+}_{0\,+} - s^{-\,0}_{0\,+})$	4.58e-02	1.47e-02	1.01e-02	1.17e-03	5.13e-03	8.57e-03
$\mathrm{Im}\,s^{-+}_{-+}$	-5.48e-02	3.25e-02	1.10e-02	1.40e-03	6.15e-03	9.01e-03
$\mathrm{Im}\,n^{0\,0}_{0\,+}$	-5.36e-02	1.59e-02	7.95e-03	1.37e-03	6.00e-03	5.03e-03
$\mathrm{Im}\,(n^{0\,+}_{++} - n^{-\,0}_{++}$ $+2\varepsilon n^{0\,+}_{0\,0})$	-1.75e-02	1.99e-02	5.79e-03	4.47e-04	1.96e-03	5.43e-03
$\mathrm{Im}\,n^{0\,+}_{-+}$	1.59e-02	2.33e-02	9.46e-03	4.05e-04	1.78e-03	9.28e-03
$\mathrm{Im}\,s^{0\,0}_{0\,+}$	1.39e-02	1.63e-02	6.94e-03	3.54e-04	1.56e-03	6.75e-03
$\mathrm{Im}\,(s^{0\,+}_{++} - s^{-\,0}_{++}$ $+2\varepsilon s^{0\,+}_{0\,0})$	9.21e-03	1.91e-02	6.26e-03	2.35e-04	1.03e-03	6.17e-03
$\mathrm{Im}\,s^{0\,+}_{-+}$	-8.92e-03	2.50e-02	8.73e-03	2.28e-04	9.99e-04	8.67e-03
$\mathrm{Im}\,(n^{++}_{0\,+} + n^{--}_{0\,+})$	2.40e-02	1.36e-02	5.32e-03	6.11e-04	2.68e-03	4.55e-03
$\mathrm{Im}\,n^{-+}_{0\,+}$	-9.81e-03	9.67e-03	3.26e-03	2.50e-04	1.10e-03	3.06e-03
$\mathrm{Im}\,(s^{++}_{0\,+} + s^{--}_{0\,+})$	1.03e-02	1.31e-02	4.23e-03	2.62e-04	1.15e-03	4.06e-03
$\mathrm{Im}\,s^{-+}_{0\,+}$	8.23e-03	9.74e-03	2.88e-03	2.10e-04	9.23e-04	2.72e-03
$\mathrm{Im}\,(n^{0\,-}_{0\,+} - n^{+\,0}_{0\,+})$	1.61e-02	1.49e-02	8.67e-03	4.12e-04	1.81e-03	8.47e-03
$\mathrm{Im}\,(n^{-+}_{++} + \varepsilon n^{-+}_{0\,0})$	2.35e-02	1.45e-02	6.50e-03	5.98e-04	2.63e-03	5.91e-03
$\mathrm{Im}\,n^{++}_{-+}$	2.10e-02	1.92e-02	8.13e-03	5.35e-04	2.35e-03	7.76e-03
$\mathrm{Im}\,(s^{0\,-}_{0\,+} - s^{+\,0}_{0\,+})$	-2.45e-02	1.52e-02	6.84e-03	6.23e-04	2.74e-03	6.23e-03
$\mathrm{Im}\,(s^{-+}_{++} + \varepsilon s^{-+}_{0\,0})$	1.87e-02	1.35e-02	3.99e-03	4.75e-04	2.09e-03	3.36e-03
$\mathrm{Im}\,s^{++}_{-+}$	1.14e-02	1.88e-02	4.87e-03	2.91e-04	1.27e-03	4.69e-03
$\mathrm{Im}\,n^{0\,0}_{-+}$	-4.25e-02	4.16e-02	1.29e-02	1.08e-03	4.76e-03	1.20e-02
$\mathrm{Im}\,n^{+\,0}_{-+}$	-1.49e-02	2.18e-02	5.90e-03	3.79e-04	1.67e-03	5.65e-03
$\mathrm{Im}\,n^{+-}_{0\,+}$	7.07e-04	9.35e-03	3.90e-03	1.77e-05	7.87e-05	3.90e-03
$\mathrm{Im}\,n^{+-}_{-+}$	-7.75e-03	2.69e-02	8.63e-03	1.98e-04	8.70e-04	8.58e-03
$\mathrm{Im}\,s^{0\,0}_{-+}$	3.35e-04	4.11e-02	1.36e-02	8.90e-06	3.64e-05	1.36e-02
$\mathrm{Im}\,s^{+\,0}_{-+}$	-3.30e-03	2.16e-02	7.80e-03	8.44e-05	3.70e-04	7.79e-03
$\mathrm{Im}\,s^{+-}_{0\,+}$	1.45e-02	9.68e-03	4.90e-03	3.69e-04	1.62e-03	4.61e-03
$\mathrm{Im}\,s^{+-}_{-+}$	-1.07e-02	2.66e-02	1.14e-02	2.74e-04	1.20e-03	1.13e-02

Table 7.5: Extracted SDMEs associated with W_{UT} (labelled as "cent. val.") and the statistical (stat) and systematic uncertainties. Shown are the total systematic uncertainty (syst), the systematic uncertainty due to the background fraction (syst1), the angular dependencies of the background (syst2) and the admixture from W_{UL} (syst3).

7.5 Comparison with GPD-model calculations

As discussed in section 2.10, various GPD-model calculations of the transverse target-spin asymmetry A_{UT} for longitudinally polarized ρ^0 mesons produced by longitudinally polarized virtual photons are available. Within the available GPD models, the generalized parton distributions H^u, H^d, and H^g have been extrapolated from the available information on parton distribution functions and elastic form factors. Different approaches have been used for the modelling of the nucleon spin-flip GPDs E^u, E^d, and E^g, which cannot be obtained from inclusive deep-inelastic scattering data.

In the GPD models presented in [10, 28] J^u and J^d enter directly as free parameters in the parameterization of the GPDs E^q. Comparison of these calculations to the experimental data for the asymmetry can be used to provide a model dependent constraint for J^u. In [29, 30] another approach is proposed. In this case the descriptions of the GPDs E^u and E^d have been obtained from fits of the electromagnetic Pauli form factors of the proton and the neutron. Within these models the transverse target-spin asymmetry and the total angular momentum carried by quarks are fixed by these fits. The calculated asymmetry can be compared with the experimentally obtained asymmetry in order to investigate whether it is consistent with the data. Both approaches are discussed in section 7.5.2. First, however, in section 7.5.1 the uncertainties of the model calculations are summarized.

7.5.1 Model uncertainties

When comparing the calculations for A_{UT} to the measured asymmetries, one should bear in mind that model assumptions and approximations have been made, which result in uncertainties on the calculations that affect the reliability of the interpretation of the measured asymmetry. Apart from uncertainties related to the assumptions used in the parameterization of GPDs and uncertainties on the used models for parton density functions and form factors, other uncertainties are present, which are discussed in [10, 28, 29, 30]. Below, a short overview of the various model uncertainties is presented.

Violation of s-channel helicity conservation A direct comparison of GPD-model calculations with the extracted asymmetry

$$A_{UT,\rho_L}^{\sin(\phi-\phi_s)} = \frac{\mathrm{Im}\left(n_{++}^{0\,0} + \varepsilon n_{0\,0}^{0\,0}\right)}{u_{++}^{0\,0} + \varepsilon u_{0\,0}^{0\,0}}, \tag{7.13}$$

requires the assumption of SCHC under which the contributions from the higher-twist SDMEs $u_{++}^{0\,0}$ and $\mathrm{Im}\, n_{++}^{0\,0}$ are equal to zero. From the extracted values for the SDMEs u it follows that non-zero amplitudes for the helicity changing transition $\gamma_T^* \rightarrow \rho_L^0$ are present, although such amplitudes are small in comparison to the amplitudes of helicity-conserving transitions. The possible impact of such violations of SCHC on both the numerator and the denominator of equation 7.13 are ignored in the present comparisons.

Power corrections Most of the available GPD-model calculations have been performed at leading twist. The leading-twist calculations were performed for the case where the virtual-photon momentum and the average nucleon momentum are collinear and in opposite direction. The transverse momenta of the partons entering the hard-scattering subprocesses were assumed to be negligible in comparison to the longitudinal momenta, which is a good approximation only in case Q^2 is large enough. Power corrections (i.e., higher-twist corrections) due to the parton's transverse momenta were found to be sizeable for the cross section up to Q^2 values of a few GeV^2 [10, 75]. In [30] effects from the transverse momenta of partons are included in the calculation of A_{UT}. The difference between the full result and the leading twist results was found to be in the range 10-25% for $3 \lesssim Q^2 \lesssim 4$ GeV (at $W = 5$ GeV) and was found to decrease with increasing Q^2 values. Hence, in the Q^2 range covered by the present data, the neglect of power corrections may have an effect larger than 25%. However, these uncertainties are most likely still smaller than those on the data.

The contribution from gluons In the description of exclusive vector-meson production the contribution from gluons enters at the same order in α_s as the contribution from quarks. Previous data on the ratio of ϕ to ρ^0 electroproduction cross sections indicate that there is a substantial contribution from gluons to the cross section for ρ^0 production at HERMES kinematics [32]. A complete model description therefore requires the inclusion of gluonic GPDs. In the original calculations of [10] the gluonic GPDs were not included. In [28, 29, 30] parameterizations for the gluonic GPD H^g are included by means of extrapolations of existing information on regular parton distribution functions. The contribution from H^g, which increases for decreasing x, results in an increase of the denominator of the asymmetry A_{UT} and therefore causes the asymmetry to be smaller [28].

No direct phenomenological information is available for the modelling of the gluonic spin-flip GPD E^g. However, since a prominent role of the GPD E^g is considered to be unlikely [28, 29, 30], it is usually assumed that at HERMES kinematics the GPD E is dominated by (valence) quarks. An unexpectedly large measured asymmetry A_{UT} could imply that the gluonic GPD E^g is larger than expected [28]. This possibility is not considered any further in the present work.

The contribution from sea quarks to proton spin-flip GPDs No direct experimental information is available on the contribution of sea quarks to the proton spin-flip GPDs E^u and E^d, which play an important role in the calculations of the asymmetry A_{UT}. This contribution is assumed to increase with decreasing x. However, the relative contribution is considered to be small for the spin-flip GPDs in comparison with proton spin-conserving GPDs [29]. In [28, 29] various scenarios for the contribution of sea quarks were studied. The differences found for A_{UT} and the associated total angular momentum J^u are small in each of the scenarios considered.

Next-to-leading order corrections in α_s Most of the available GPD-model calculations have been performed to leading order (LO) in α_s. In the studies in [29] also the next-to-leading order (NLO) corrections are analyzed. For A_{UT} the NLO corrections were found to be substantial over a wide range of kinematics. The corrections were found to increase with decreasing x. At $Q^2 = 4$ GeV^2, $-t = 0.4$ GeV^2, and $x \geq 0.05$, which is on the edge of the kinematic range of the present data, the NLO corrections on the asymmetry were found to be at most between 0.025 and 0.08 (at $x = 0.05$). Such corrections are comparable to, or larger than, the LO value of A_{UT} in various models. In comparison to the statistical uncertainty of the measured asymmetries these NLO corrections are at most of the same order of magnitude, but in general smaller.

In summary, various uncertainties on the GPD-model calculations of the asymmetry A_{UT} were estimated to be in magnitude smaller than or comparable to the present experimental uncertainties. The comparison of GPD-model calculations to possible more precise future data requires that many of the corrections mentioned above are included in the calculations.

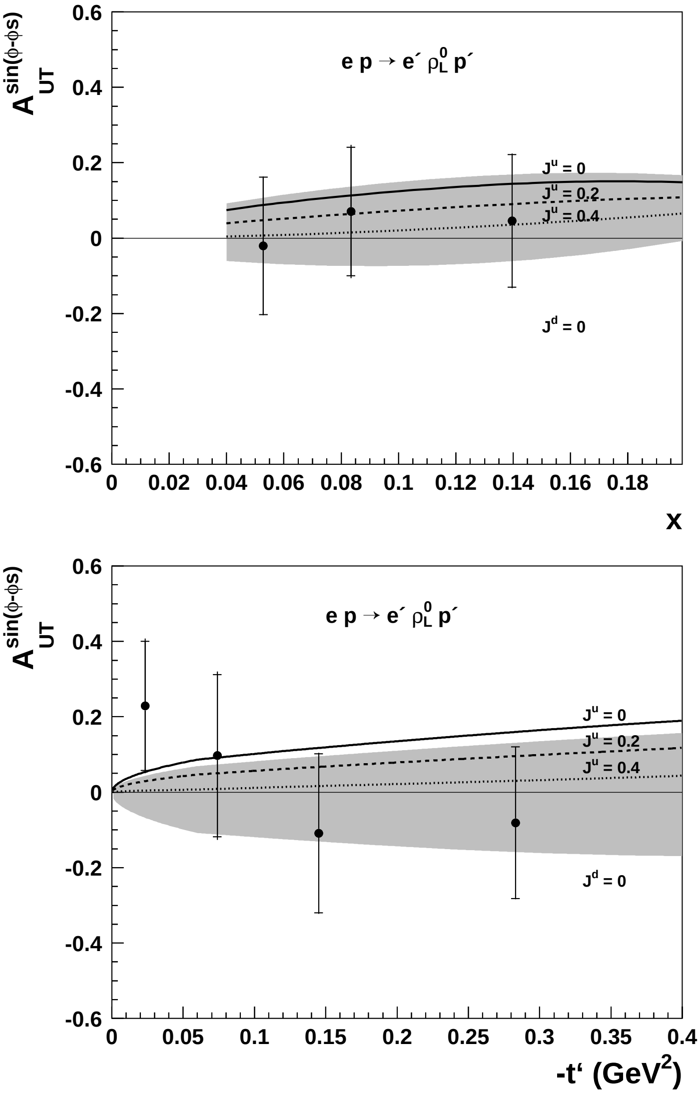

Figure 7.12: The extracted azimuthal moment $A_{UT}^{\sin(\phi-\phi_s)}$ for longitudinally polarized ρ^0 mesons binned in x (upper plot) and $-t'$ (lower plot). The curves represent GPD based calculations [28] assuming different values for the angular momentum carried by quarks inside the proton ($J^u = 0, 0.2, 0.4$ and $J^d = 0$). The grey bands represent the 1σ uncertainty intervals for the azimuthal moment estimated by fits of interpolations of the GPD based calculations with J^u as free fit parameter.

7.5.2 Comparison to GPD-models

In this section GPD-model calculations are compared to the experimental results for the $\sin(\phi-\phi_s)$ moment of the asymmetry A^{ℓ}_{UT} in electroproduction of longitudinally polarized ρ^0 mesons. These comparisons are done with the results extracted with the 36-parameter fit presented in section 7.2.2. Although the GPD-model calculations are subject to the various uncertainties discussed in section 7.5.1, these comparisons are justified, since the model uncertainties were estimated to be less than or comparable to the uncertainties on the data. A precise determination of the model uncertainties and a discussion of their impact on the comparison between the calculations and the data is beyond the scope of this work.

The calculations of the azimuthal moment from [28] are shown together with the experimentally determined values binned in x and $-t'$ in figure 7.12. The calculation of the moment has been performed as a function of x or $-t'$ with the other kinematic variables fixed at values representative for the experimental data: $\langle Q^2\rangle = 2$ GeV^2 and $\langle -t'\rangle = 0.14$ GeV^2 or $\langle x\rangle = 0.085$, respectively. Several assumptions for the quark angular momentum were used: $J^u = 0$, 0.2, 0.4 and $J^d = 0$. For each of the values taken for J^u the calculated azimuthal moment is consistent with the experimentally obtained results.

We have used the calculations of the azimuthal moment for the various values of J^u to obtain parameterizations of the moment in terms of J^u. The parameterizations were obtained from interpolations of the calculations with a second order polynomial in J^u. From the various interpolations, each performed for a specific value of x and of $-t'$, we obtained parameterizations of the x and $-t'$ dependencies of the azimuthal moment. These parameterizations were fit to the values of the azimuthal moment determined in the various x and $-t'$ bins to obtain two results for J^u. These results are given by $J^u = 0.33 \pm 0.43$ and $J^u = 0.53 \pm 0.44$, respectively. In figure 7.12 the results of the fits are represented by the grey bands, which denote the 1σ uncertainty intervals.

As the two fit functions describe the dependence of the azimuthal moment on different kinematic variables while assuming constant values for the other variables, the fit functions represent two different approximations. Hence, the results from the two fits may be different. However, since both approximations are justified at the present precision of the data (see section 6.8) the average value of the two results for J^u has been taken as our best estimate of J^u, whereas for the uncertainty on this estimate the average value of the uncertainties on both results is taken. The resulting estimate is then equal to $J^u = 0.43 \pm 0.43$. Despite the relatively large uncertainty the data seem to prefer a positive value of J^u. The favored range for J^u agrees with the model-dependent constraint of $0.2 < J^u < 0.6$ at $J^d = 0$ that was obtained from the results from deeply virtual Compton scattering measurements [76, 77].

The data are compared as well to the GPD-model calculations of [30], for which the GPDs E^u and E^d and the corresponding values of J^u and J^d were constrained by form-factor data. These calculations are available for the average kinematics of the data in the highest Q^2 bin: $\langle Q^2\rangle = 3.07$ GeV^2 and $\langle W\rangle = 5$ GeV. The calculated asymmetry of 0.02 ± 0.01 is consistent with the experimental value of the asymmetry of 0.11 ± 0.14 determined in this bin. This calculation is also in good agreement with the value of the asymmetry of 0.03 ± 0.10 determined from the entire kinematic range of the data. From the GPD model used in these calculations the value of J^u was estimated to be between 0.211 and 0.241 and the value of J^d between -0.02 and 0.02, considering only valence quarks [79]. Comparable values were obtained from the GPD models discussed in [29].

7.5.3 Orbital angular momentum

From the estimate $J^u = 0.43 \pm 0.43$ obtained under the assumption $J^d = 0$ one can obtain an estimate of the total angular momentum carried by the quarks inside the proton, by using the approximation $J_q = J^u + J^d$, where the contributions from sea quarks are assumed to be negligible. The estimate obtained in this way is given by $J_q = 0.43 \pm 0.43$. From this estimate one can obtain an estimate of the orbital angular momentum L_q of quarks inside the proton by using

$$J_q = \frac{1}{2}\Delta\Sigma + L_q, \tag{7.14}$$

where $\Delta\Sigma$ represents the quark-spin contribution to the nucleon spin. In order to obtain such an estimate the result $\Delta\Sigma = 0.330 \pm 0.039$ from [6] was used (where the uncertainty represents the total uncertainty). The resulting estimate for L_q is thus given by $L_q = 0.27 \pm 0.43$.

From the information on J^u one can also obtain an estimate of the orbital angular momentum L^u of up-quarks by using

$$J^f = \frac{1}{2}\Delta f + L^f, \tag{7.15}$$

where f represents the quark flavor and Δf represents the corresponding quark helicity distribution $\Delta f(x)$ integrated over x. Semi-inclusive DIS measurements at HERMES have yielded the results $\Delta u = 0.601 \pm 0.063$ and $\Delta d = -0.226 \pm 0.063$ [7], where the total uncertainties are given[6]. By using the result for Δu in combination with equation 7.15 the estimate $L^u = 0.13 \pm 0.43$ is obtained.

As a result of the large uncertainty on the estimate of the quark orbital angular momentum, no distinction can be made between relatively small or relatively large positive values of L_q. However, it can be concluded that large negative values of L_q are less likely. Future results for the transverse target-spin asymmetry in exclusive ρ^0 production and for deeply virtual Compton scattering are needed to provide a more precise estimate of the contribution of quark orbital angular momentum to the spin of the nucleon.

---

[6] It is noted that the results used from [7] imply that $\Delta\Sigma = 0.347 \pm 0.070$, which is consistent with the value for $\Delta\Sigma$ from [6] that was used to estimate L_q.

Chapter 8

Summary and outlook

Summary At present the total angular momentum J_q carried by the quarks in the nucleon is unknown. One can investigate the angular momentum carried by the quarks by using the recently developed framework of generalized parton distributions (GPDs). Within the GPD framework, it has been shown that specific observables in exclusive production processes, such as deeply virtual Compton scattering and hard exclusive meson production, are sensitive to J_q. By measuring these observables, one can obtain a model-dependent estimate of J_q. From the estimated value of J_q, in combination with the available data on the quark-spin contribution $\Delta\Sigma$ to the nucleon spin, information on the unknown orbital angular momentum L_q of quarks inside the nucleon can be obtained.

More in particular, the $\sin(\phi - \phi_s)$ component of the transverse target-spin asymmetry A_{UT} for exclusive ρ^0 production from a transversely polarized nucleon has been predicted to be sensitive to J_q. Here, ϕ and ϕ_s are the azimuthal angles of the produced ρ^0 meson and the transverse component of the nucleon spin, respectively, around the direction of the exchanged virtual photon. The GPD description of exclusive meson production only applies if both the exchanged virtual photon and the produced meson are longitudinally polarized. Hence, in order to compare GPD-based calculations of A_{UT} with measurements, the asymmetry has to be determined for this specific case.

This thesis reports the first measurements of the asymmetry A_{UT} in exclusive ρ^0 electroproduction from a transversely polarized proton. The asymmetry was extracted from data taken by the HERMES experiment at DESY with a polarized internal hydrogen gas target and the 27.6 GeV electron (positron) beam of HERA. These data were collected during the 2002-2005 running periods of HERMES. The exclusive ρ^0 production events were reconstructed from the measured information on the scattered lepton and the ρ^0 decay products. The recoil protons could not be detected by the HERMES spectrometer. Requirements on the invariant mass of the detected hadron pairs were used to select pions resulting from ρ^0 decay events. Additional requirements on the missing energy enabled the selection of exclusive events. A Monte Carlo simulation provided an estimate of the non-exclusive background contributions coming from semi-inclusive deep-inelastic scattering events. The background contribution from exclusive non-resonant events was estimated from a fit of the reconstructed invariant mass distribution for exclusive hadron pairs, but was found to be negligible.

The transverse target-spin asymmetry A_{UT} was determined as a function of ϕ and ϕ_s by fits of the angular distribution of events measured with two opposite transverse orientations of the target polarization. Since A_{UT} needed to be determined separately for longitudinally and transversely polarized ρ^0 mesons, also the dependence of the yields on the decay angle $\theta_{\pi\pi}$ was accounted for in the extraction procedure. Two different approaches were used to take this additional dependence into account. In one approach a combination of the Diehl-Sapeta [13] and Wolf-Schilling [14] formalisms was used. In this case the relevant angular distributions were effectively integrated over the ρ^0 decay angle $\phi_{\pi\pi}$. In the other approach the more recently developed Diehl formalism [11] for vector-meson production on a polarized target was used. In this case the dependence on the decay angle $\phi_{\pi\pi}$ was taken into account in the description of the angular distribution.

In both approaches so-called spin density-matrix elements (SDMEs) for exclusive ρ^0 production were used to represent the information contained in the angular distribution. The SDMEs parameterize the sensitivities of the angular distribution to the polarization states of the exchanged virtual photon and the produced ρ^0 meson. The SDMEs representing ρ^0 production on an unpolarized target and on a transversely polarized target were extracted in the Diehl formalism. This extraction is the first experimental determination of the SDMEs for a transversely polarized target. The results that were obtained for an unpolarized target were converted to the Wolf-Schilling formalism and compared with the results of an earlier analysis based on that formalism, which made use of the HERMES data taken with an unpolarized target during the 1996-2000 data taking period. The results from both analyses were found to be consistent.

From the extracted SDMEs it can be concluded that, for an unpolarized target, the amplitudes for s-channel helicity conserving transitions (where the helicity of the virtual photon is transferred to the produced ρ^0 meson) are significantly larger than those for the helicity changing transitions. However, the results indicate that also the amplitudes for the helicity changing transitions $\gamma^*_T \to \rho_L$ from transverse virtual-photon helicity to longitudinal ρ^0 helicity deviate significantly from zero. Considering the SDMEs for transverse target polarization, the most significant deviation was found for the SDME Im $n^{\,0\,0}_{\,0+}$, suggesting additional violation of s-channel helicity conservation (SCHC) through the transition $\gamma^*_T \to \rho_L$. This SDME was found to be comparable in magnitude with the observed SCHC-violating SDMEs for an unpolarized target. Overall, the extracted values of the SDMEs for transverse target polarization are within their statistical uncertainties consistent with zero.

The extracted $\sin(\phi - \phi_s)$ component of the asymmetry A_{UT} for longitudinally polarized ρ^0 mesons was compared with available GPD-model calculations [28, 79] assuming SCHC. The calculations were found to be consistent with the data. The calculations of [28] were used to obtain a model-dependent estimate of J^u under the assumption $J^d = 0$. The resulting estimate $J^u = 0.43 \pm 0.43$ is consistent with the constraints on J^u and J^d provided by DVCS measurements [76, 77, 78] and GPD-model fits on form factor data [29, 74]. By using the available estimate $\Delta\Sigma = 0.330 \pm 0.039$ from [6] in combination with the obtained estimate of $J_q \approx J^u + J^d = 0.43 \pm 0.43$ an estimate $L_q = 0.27 \pm 0.43$ of the orbital momentum carried by the quarks inside the proton was obtained.

Outlook New data for the exclusive leptoproduction of ρ^0 mesons from a polarized proton are needed to increase the amount of statistics available for the asymmetry A_{UT}, so that the relatively large uncertainties on the available estimates on J_q and L_q can be reduced. Such data are foreseen to be collected by the COMPASS experiment at CERN [80] and the CLAS experiment at JLab [81]. After the 12 GeV upgrade at JLab the CLAS experiment will be able to measure A_{UT} in the x-range $0.3 \lesssim x \lesssim 0.5$. In this kinematic range GPD-model calculations [10] predict relatively large magnitudes of the $\sin(\phi - \phi_s)$ component of A_{UT} assuming $J^d = 0$ and $0.1 \leq J^u \leq 0.4$ (It should be noted, however, that the calculations of [10] did not yet take into account the contribution from gluons, which may cause a dilution of the asymmetry). At COMPASS first results already exist for the asymmetry for exclusive ρ^0 production on a transversely polarized deuteron target [80]. New data on the asymmetry are expected for a transversely polarized proton target. At COMPASS the x-range covered reaches down to $x \approx 0.01$ and higher values of Q^2 are reached, up to 10 GeV^2, although most of the data will be taken at $Q^2 < 5$ GeV^2. Together, the expected COMPASS and CLAS data will have the potential to increase the kinematic coverage and the statistical precision of the data on A_{UT} substantially. As a result these data will enable a more precise model-dependent determination of the total and the orbital angular momentum carried by quarks in the nucleon.

Appendix A

The density matrix

For a given quantum mechanical state Ψ the information needed to calculate the outcome of a measurement of an observable is contained in its density matrix [22]. The density matrix ρ for Ψ is defined through the expression of the corresponding expectation value $\langle A\rangle$ of an operator A:

$$\langle A\rangle = \mathrm{Tr}(A\rho), \tag{A.1}$$

where the trace Tr is taken of the matrix product $A\rho$. In general Ψ is mixture, i.e., an incoherent superposition of pure states Φ^i (with $i = 1, 2, \ldots$). Explicitly, $\langle A\rangle$ can be expressed as the weigthed sum of the expectation values of these pure states:

$$\langle A\rangle \equiv \langle\Psi|A|\Psi\rangle = \sum_i p^i \langle\Phi^i|A|\Phi^i\rangle, \tag{A.2}$$

where the statistical weights are given by p^i. One can express the pure states relative to a set of basis states $|e^i_m\rangle$ as $\Phi^i = \sum_m c^i_m |e^i_m\rangle$, where c^i_m $(m = 1, 2, \ldots)$ represent the corresponding coefficients. Relative to this basis $\langle A\rangle$ is expressed as

$$\begin{aligned}\langle A\rangle &= \sum_i p^i \sum_{mn} \langle\Phi^i|e^i_m\rangle\langle e^i_m|A|e^i_n\rangle\langle e^i_n|\Phi^i\rangle \\ &= \sum_{mn} a_{mn}\rho_{nm} = \mathrm{Tr}(A\rho),\end{aligned} \tag{A.3}$$

where a_{mn} are the elements of the matrix of the observable A. From this equation it follows that the density matrix ρ_{nm} of Ψ is given by

$$\rho_{nm} = \sum_i \langle e^i_n|\Phi^i\rangle p_i \langle\Phi^i|e^i_m\rangle = \sum_i p^i (c^i_n c^{i*}_m). \tag{A.4}$$

Alternatively, one can use the property that each operator can be expanded in terms of a set of orthogonal operators T_j, with one of the operators being a multiple of the unit operator I. The density matrix is represented by

$$\rho = \sum_j \mathrm{Tr}(\rho T_j^\dagger) T_j = \sum_j t_j^* T_j, \tag{A.5}$$

where t_j are the mean values of the operators T_j and the number of operators equals the number of independent parameters in the ρ matrix.

The spin density matrix

The mean spin orientation of an ensemble of particles is specified by the polarization vector $\boldsymbol{P}$. From equation A.2 it follows that $\boldsymbol{P}$ is given by

$$\boldsymbol{P} = \langle \boldsymbol{P_{op}} \rangle = \mathrm{Tr}(\rho \boldsymbol{P_{op}}), \tag{A.6}$$

with $\boldsymbol{P_{op}}$ being the polarization operator. Within this context ρ is referred to as the spin density matrix, since it contains the information regarding the spin orientation. In general, for an ensemble of particles with spin j, ρ is a $(2j+1) \times (2j+1)$ matrix.

For a spin $\frac{1}{2}$ particle the polarization operator is represented by $\boldsymbol{\sigma} = (\sigma_x, \sigma_y, \sigma_z)$, with σ_i the Pauli matrices for the spin directions $i = x, y, z$. These are 2×2 matrices operating on two-component spinors, e.g. $\chi_{\pm\frac{1}{2}}$ representing the spin-up and spin-down states with respect to the z-direction:

$$\chi_{+\frac{1}{2}} = \begin{pmatrix} 1 \\ 0 \end{pmatrix}, \qquad \chi_{-\frac{1}{2}} = \begin{pmatrix} 0 \\ 1 \end{pmatrix}. \tag{A.7}$$

The polarization is given by the mean of $\boldsymbol{\sigma}$: $\boldsymbol{P} = \langle \boldsymbol{\sigma} \rangle$ and the corresponding spin density matrix can be expressed in terms of $\boldsymbol{P}$ by using equation A.5

$$\rho = \frac{1}{2}(I + \boldsymbol{P} \cdot \boldsymbol{\sigma}). \tag{A.8}$$

By inserting this expression in equation A.6 it can be shown that equation A.8 indeed satisfies the definition of the spin density matrix: $\boldsymbol{P} = \langle \boldsymbol{\sigma} \rangle = \mathrm{Tr}(\rho\, \boldsymbol{\sigma})$.

Appendix B

SDME formalism for an unpolarized target

In this appendix the spin density-matrix elements (SDMEs) for ρ^0 production on an unpolarized target are introduced within the Wolf-Schilling formalism [14]. The SDMEs are related to the amplitudes $T_{\alpha\sigma,\,m\,i}$ of the process $\gamma^*(m)\;p(i) \to p(\sigma)\;\rho^0(\alpha)$, where the helicities $i, \sigma = \pm\frac{1}{2}$ and $m, \alpha = -1, 0, 1$ of the involved particles are specified between the brackets. First the matrix elements $\rho'^{mn}_{\alpha\beta}$ are introduced, which are given by

$$\rho'^{mn}_{\alpha\beta} = (2N')^{-1} \sum_{i\,\sigma} T'_{\alpha\sigma,m\,i} \left(T'_{\beta\sigma,n\,i}\right)^*, \tag{B.1}$$

where N' is the normalization factor. Equation B.1 is similar to equation 2.62 for the matrix elements given within the Diehl formalism [11], despite the fact that different conventions are used for the phase of the virtual photon and for the notation of the transition amplitudes and SDMEs[1]. The exact relation between the matrix elements in equations B.1 and 2.62 is given in [11]. Within the Wolf-Schilling formalism, the spin density matrix is decomposed in terms of hermitian matrices ρ'' for specific polarization states of the virtual photon:

$$\rho''^{a}_{\alpha\beta} = \sum_{mn} \Sigma^a_{mn} \rho'^{mn}_{\alpha\beta}, \tag{B.2}$$

where the matrices Σ^a_{mn} form an orthogonal set of independent hermitian matrices, which are given explicitly in [14]. The superscript $a = 0, \ldots, 8$ indicates the virtual-photon polarization states, with $a = 0, 1, 2, 3$ indicating transverse polarization, $a = 4$ longitudinal polarization and $a = 5, 6, 7, 8$ the interference between longitudinal and transverse polarization states. In [14] the SDMEs are initially

---

[1] Note that the upper and lower indices of the matrix ρ' have changed their positions compared to the convention used in equation 2.62.

given for the case where different polarization states of the virtual photon can be separated. For this reason the normalization factor N'_a is different for different virtual-photon polarization states:

$$N'_a = N'_T = \sum_{i,\alpha,\sigma} \left| T'_{\alpha\sigma,\,+\,i} \right|^2 , \qquad a = 0, \ldots, 3\,, \tag{B.3}$$

$$N'_a = N'_L = \sum_{i,\alpha,\sigma} \left| T'_{\alpha\sigma,\,0\,i} \right|^2 , \qquad a = 4\,, \tag{B.4}$$

$$N'_a = \sqrt{N'_T N'_L}, \qquad a = 5, \ldots, 8\,. \tag{B.5}$$

In case longitudinal and transverse virtual-photon polarization states cannot be separated experimentally, it is more convenient to use the same normalization factor for all polarization states of the virtual photon, as is done in equation 2.62. The SDMEs $r^{a}_{\alpha\beta}$ and $r^{04}_{\alpha\beta}$ for that case can be obtained from the SDMEs $\rho''^{a}_{\alpha\beta}$ by using [14]

$$r^{04}_{\alpha\beta} = \frac{\rho''^{0}_{\alpha\beta} + \varepsilon R\, \rho''^{4}_{\alpha\beta}}{1 + \varepsilon R}\,; \tag{B.6}$$

$$r^{a}_{\alpha\beta} = \frac{\rho''^{a}_{\alpha\beta}}{1 + \varepsilon R}, \qquad a = 1, \ldots, 3\,; \tag{B.7}$$

$$r^{a}_{\alpha\beta} = \frac{\sqrt{N}\rho''^{a}_{\alpha\beta}}{1 + \varepsilon R}, \qquad a = 5, \ldots, 8\,, \tag{B.8}$$

where $R = \sigma_L/\sigma_T$ is the ratio of the cross sections σ_L and σ_T for longitudinally and transversely polarized virtual photons, respectively. In equation B.6 matrix elements $\rho''^{0}_{\alpha\beta}$ and $\rho''^{4}_{\alpha\beta}$ corresponding to the same term of the angular distribution function are combined.

Appendix C

Extraction methods

Moments method

In the so-called moments method the $\sin(\phi - \phi_s)$ moment of the asymmetry A_{UT} is extracted as a normalized $\sin(\phi - \phi_s)$ moment of the measured yields by using

$$A_{UT}^{\sin(\phi-\phi_S)} = \frac{2\int d\phi\, d\phi_s\, \sin(\phi-\phi_s) \left[N^{\uparrow}(\phi,\phi_s)/\mathcal{L}^{\uparrow} - N^{\downarrow}(\phi,\phi_s)/\mathcal{L}^{\downarrow} \right]}{\int d\phi\, d\phi_s\, \left[N^{\uparrow}(\phi,\phi_s)/\mathcal{L}^{\uparrow} + N^{\downarrow}(\phi,\phi_s)/\mathcal{L}^{\downarrow} \right]}, \tag{C.1}$$

where $\mathcal{L}^{\uparrow}$ and $\mathcal{L}^{\downarrow}$ are the luminosities corresponding to the yields $N^{\uparrow}$ and $N^{\downarrow}$, respectively. The integrals in equation C.1 are numerically computed as weighted sums over the events for positive and negative target polarization, which are indicated here by, respectively $i = 1, 2, \ldots N^{\uparrow}$ and $j = 1, 2, \ldots N^{\downarrow}$. The resulting moment of the asymmetry and its statistical error estimate are given by

$$A_{UT}^{\sin(\phi-\phi_S)} = 2\,\frac{\mathcal{L}^{\downarrow} \sum_i^{N^{\uparrow}} \sin(\phi_i - \phi_{S,i}) - \mathcal{L}^{\uparrow} \sum_j^{N^{\downarrow}} \sin(\phi_j - \phi_{S,j})}{\mathcal{L}^{\downarrow} N^{\uparrow} + \mathcal{L}^{\uparrow} N^{\downarrow}} \tag{C.2}$$

and

$$\Delta A_{UT}^{\sin(\phi-\phi_S)} = 2\,\frac{\sqrt{(\mathcal{L}^{\downarrow})^2 \sum_i^{N^{\uparrow}} \sin^2(\phi_i - \phi_{S,i}) + (\mathcal{L}^{\uparrow})^2 \sum_j^{N^{\downarrow}} \sin^2(\phi_j - \phi_{S,j})}}{\mathcal{L}^{\downarrow} N^{\uparrow} + \mathcal{L}^{\uparrow} N^{\downarrow}}. \tag{C.3}$$

Note that in equation C.1 effects from the non-uniform acceptance efficiency ϵ on the extracted value of the azimuthal moment of the asymmetry are neglected.

Least-χ^2 fit method

A conventional approach to determine the azimuthal Fourier moments of the transverse target-spin asymmetry A_{UT} is to use the least-χ^2 fit method. In this method the value of the asymmetry is first determined in bins of the angles ϕ and ϕ_s, or alternatively in bins of the angles $\phi - \phi_s$ and $\phi + \phi_s$.

In each bin, labelled here with i, the asymmetry can be determined from the yields $N_i^{\uparrow(\downarrow)}$ normalized by their corresponding luminosities by using

$$A_{UT,i} = \frac{1}{|P_T|} \frac{N_i^{\uparrow}/\mathcal{L}^{\uparrow} - N_i^{\downarrow}/\mathcal{L}^{\downarrow}}{N_i^{\uparrow}/\mathcal{L}^{\uparrow} + N_i^{\downarrow}/\mathcal{L}^{\downarrow}}. \tag{C.4}$$

The uncertainty on the value of the asymmetry in each bin can be estimated by using equation C.4 and propagation of the estimated uncertainty on the measured yields, $\Delta N_i^{\uparrow(\downarrow)} \approx \sqrt{N_i^{\uparrow(\downarrow)}}$, which results into

$$\begin{aligned} \Delta A_{UT,i}^{\text{data}} &= \left(\left(\frac{\partial A_{UT,i}^{\text{data}}}{\partial N_i^{\uparrow}} \Delta N_i^{\uparrow} \right)^2 + \left(\frac{\partial A_{UT,i}^{\text{data}}}{\partial N_i^{\downarrow}} \Delta N_i^{\downarrow} \right)^2 \right)^{\frac{1}{2}} & \text{(C.5)} \\ &= \frac{2\sqrt{N_i^{\uparrow} N_i^{\downarrow} (N_i^{\uparrow} + N_i^{\downarrow})}}{\langle |P_T| \rangle (N_i^{\uparrow} + N_i^{\downarrow})^2}, & \text{(C.6)} \end{aligned}$$

where the approximation $\mathcal{L}^{\downarrow} = \mathcal{L}^{\uparrow}$ is used for reason of brevity.

The moments of the asymmetry can then be obtained by fitting the binned azimuthal dependence of the asymmetry with a function A_{UT}^{fit} describing the asymmetry in terms of the moments, which are the free parameters of the fit. This is done by minimizing the χ^2, which is given by

$$\chi^2 = \sum_i \left(\frac{A_{UT,i}^{\text{fit}} - A_{UT,i}^{\text{data}}}{\Delta A_{UT,i}^{\text{data}}} \right)^2 . \tag{C.7}$$

As was mentioned before, different choices are possible for the binning. A two-dimensional binning is required for a fit with the function

$$A_{UT}^{\text{fit}}(\phi, \phi_s) = A_{UT}^{\sin(\phi-\phi_s)} \sin(\phi - \phi_s) + A_{UT}^{\sin(\phi+\phi_s)} \sin(\phi + \phi_s) \tag{C.8}$$

including both the moments $A_{UT}^{\sin(\phi-\phi_s)}$ and $A_{UT}^{\sin(\phi+\phi_s)}$ as free parameters. Separate fits of these azimuthal moments can also be performed by using one-dimensional binnings in the angles $\phi - \phi_s$ and $\phi + \phi_s$, respectively.

Appendix D

Conversion between SDME formalisms

$$\begin{aligned}
r^{04}_{00} &= u^{00}_{++} + \varepsilon u^{00}_{00} && \text{(D.1)}\\
\mathrm{Re}\, r^{04}_{10} &= \frac{1}{2}\left(u^{0+}_{++} - u^{-0}_{++} + 2\varepsilon u^{0+}_{00}\right) && \text{(D.2)}\\
r^{04}_{1-1} &= \mathrm{Re}\left(u^{-+}_{++} + \varepsilon u^{-+}_{00}\right) && \text{(D.3)}\\
r^{1}_{11} &= \mathrm{Re}\, u^{++}_{-+} && \text{(D.4)}\\
r^{1}_{00} &= u^{00}_{-+} && \text{(D.5)}\\
\mathrm{Re}\, r^{1}_{10} &= \frac{1}{2}\mathrm{Re}\left(u^{+0}_{-+} + u^{0+}_{-+}\right) && \text{(D.6)}\\
r^{1}_{1-1} &= \frac{1}{2}\left(u^{+-}_{-+} + u^{-+}_{-+}\right) && \text{(D.7)}\\
\mathrm{Im}\, r^{2}_{10} &= \frac{1}{2}\mathrm{Re}\left(u^{+0}_{-+} - u^{0+}_{-+}\right) && \text{(D.8)}\\
\mathrm{Im}\, r^{2}_{1-1} &= \frac{1}{2}\left(u^{+-}_{-+} - u^{-+}_{-+}\right) && \text{(D.9)}\\
r^{5}_{11} &= -\frac{\sqrt{2}}{2}\mathrm{Re}\left(u^{++}_{0+} + u^{--}_{0+}\right) && \text{(D.10)}\\
r^{5}_{00} &= -\sqrt{2}\mathrm{Re}\, u^{00}_{0+} && \text{(D.11)}\\
\mathrm{Re}\, r^{5}_{10} &= \frac{\sqrt{2}}{4}\mathrm{Re}\left((u^{0-}_{0+} - u^{+0}_{0+}) - (u^{0+}_{0+} - u^{-0}_{0+})\right) && \text{(D.12)}\\
r^{5}_{1-1} &= -\frac{\sqrt{2}}{2}\mathrm{Re}\left(u^{-+}_{0+} + u^{+-}_{0+}\right) && \text{(D.13)}\\
\mathrm{Im}\, r^{6}_{10} &= \frac{\sqrt{2}}{4}\mathrm{Re}\left((u^{0-}_{0+} - u^{+0}_{0+}) + (u^{0+}_{0+} - u^{-0}_{0+})\right) && \text{(D.14)}\\
\mathrm{Im}\, r^{6}_{1-1} &= -\frac{\sqrt{2}}{2}\mathrm{Re}\left(u^{-+}_{0+} - u^{+-}_{0+}\right) && \text{(D.15)}
\end{aligned}$$

Appendix E

SDMEs for an unpolarized target

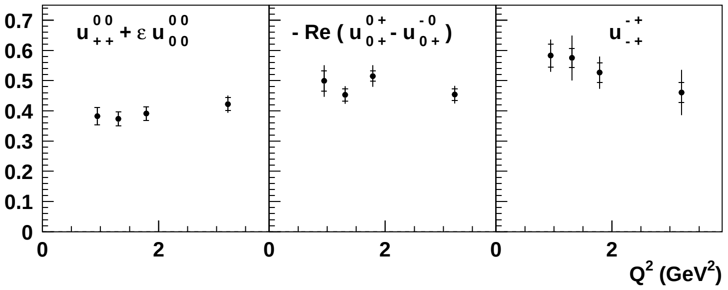

Figure E.1: Combinations of SDMEs for an unpolarized target and an unpolarized beam binned in Q^2. Each combination contains an s-channel helicity-conserving SDME.

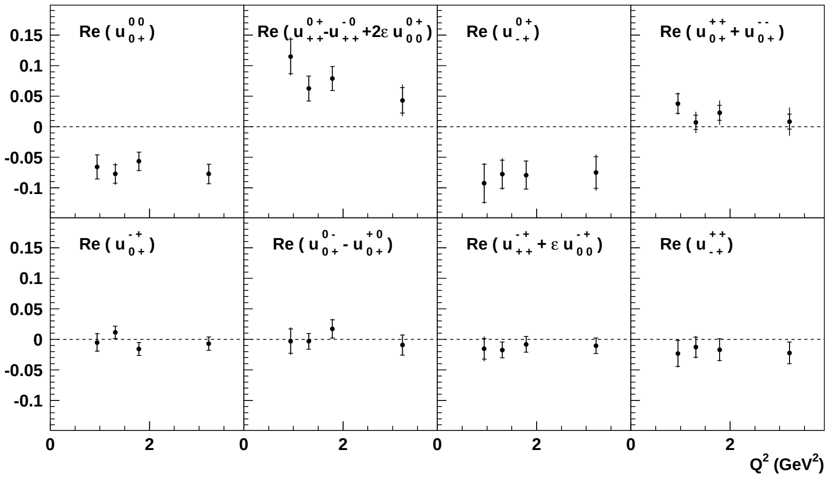

Figure E.2: Combinations of SDMEs for an unpolarized target and an unpolarized beam binned in Q^2. Each combination contains an SDME associated with the interference between helicity-conserving and helicity-changing amplitudes.

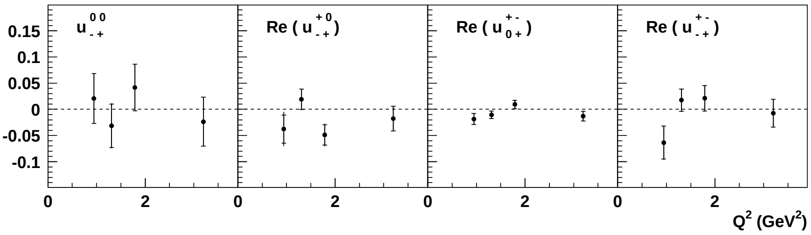

Figure E.3: SDMEs for an unpolarized target and an unpolarized beam binned in Q^2. Each SDME is associated with the interference between different helicity-changing amplitudes.

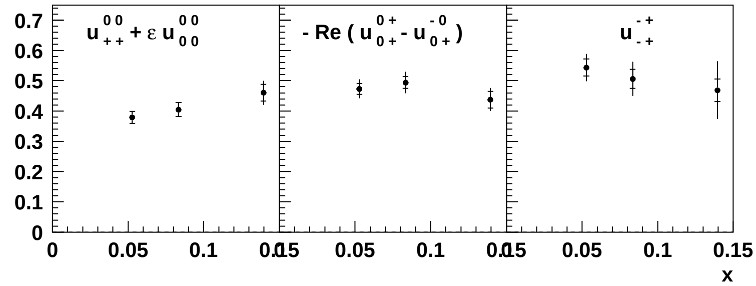

Figure E.4: Combinations of SDMEs for an unpolarized target and an unpolarized beam binned in x. Each combination contains an s-channel helicity-conserving SDME.

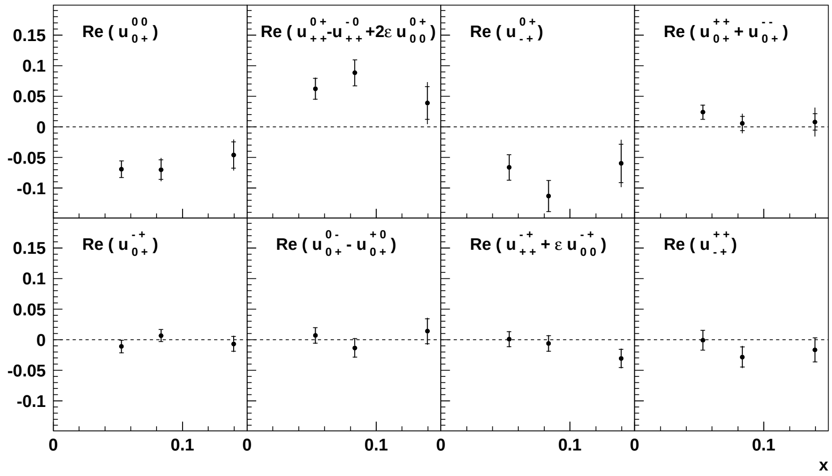

Figure E.5: Combinations of SDMEs for an unpolarized target and an unpolarized beam binned in x. Each combination contains an SDME associated with the interference between helicity-conserving and helicity-changing amplitudes.

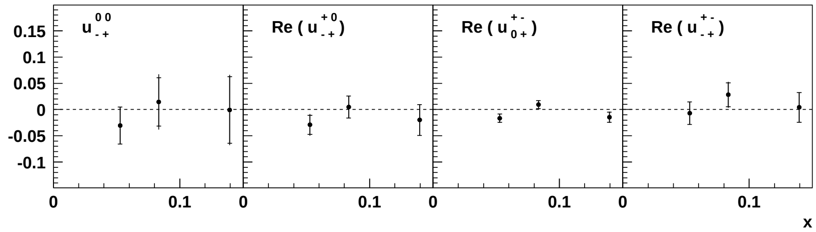

Figure E.6: SDMEs for an unpolarized target and an unpolarized beam binned in x. Each SDME is associated with the interference between different helicity-changing amplitudes.

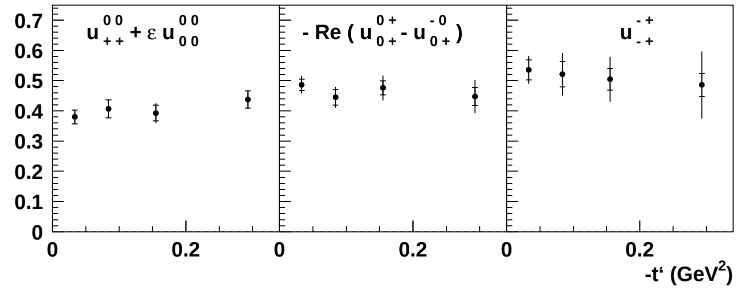

Figure E.7: Combinations of SDMEs for an unpolarized target and an unpolarized beam binned in $-t'$. Each combination contains an s-channel helicity-conserving SDME.

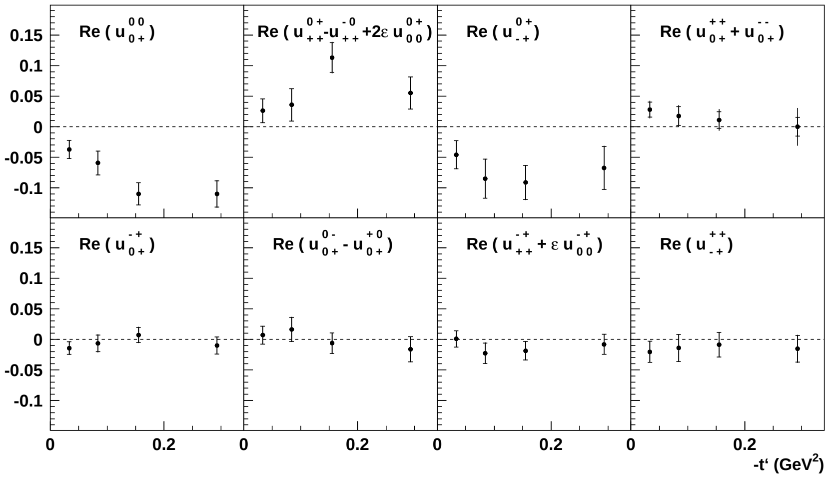

Figure E.8: Combinations of SDMEs for an unpolarized target and an unpolarized beam binned in $-t'$. Each combination contains an SDME associated with the interference between helicity-conserving and helicity-changing amplitudes.

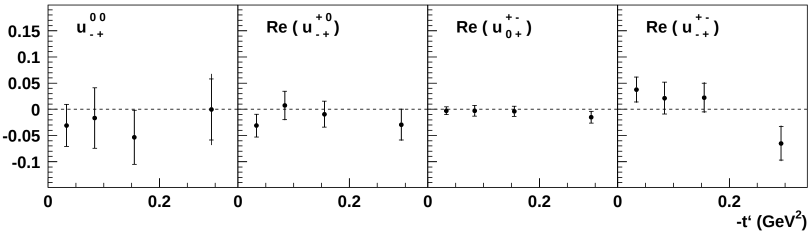

Figure E.9: SDMEs for an unpolarized target and an unpolarized beam binned in $-t'$. Each SDME is associated with the interference between different helicity-changing amplitudes.

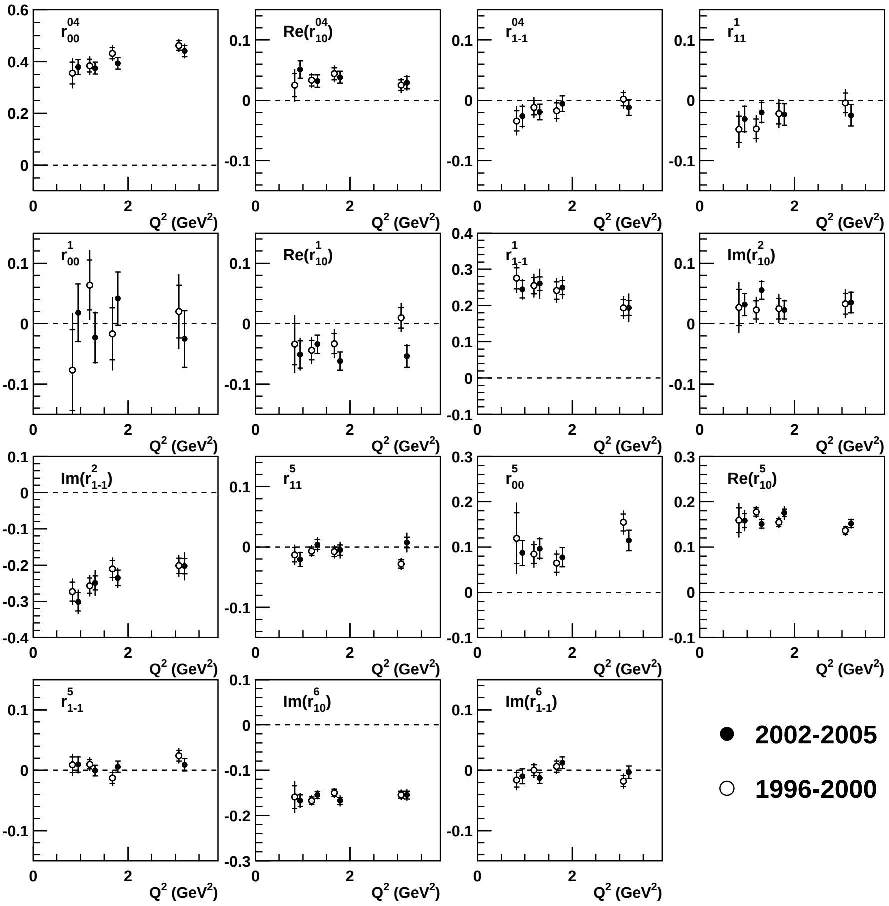

Figure E.10: The SDMEs for an unpolarized target and an unpolarized beam extracted in different Q^2 bins. The SDMEs are represented within the Wolf-Schilling formalism [14]. The results from this analysis obtained from the HERMES 2002-2005 data for a transversely polarized target are compared with the results from an other analysis obtained from the HERMES 1996-2000 data for an unpolarized hydrogen target [26].

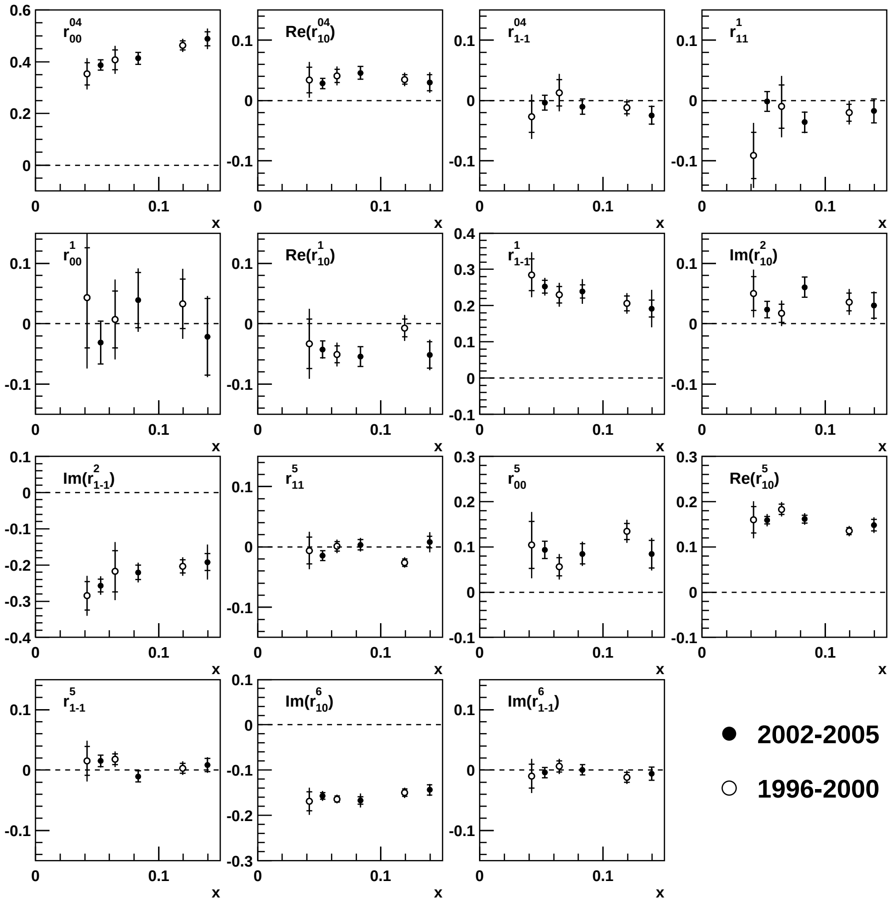

Figure E.11: The SDMEs for an unpolarized target and an unpolarized beam extracted in different x bins. The SDMEs are represented within the Wolf-Schilling formalism [14]. The results from this analysis obtained from the HERMES 2002-2005 data for a transversely polarized target are compared with the results from an other analysis obtained from the HERMES 1996-2000 data for an unpolarized hydrogen target [26].

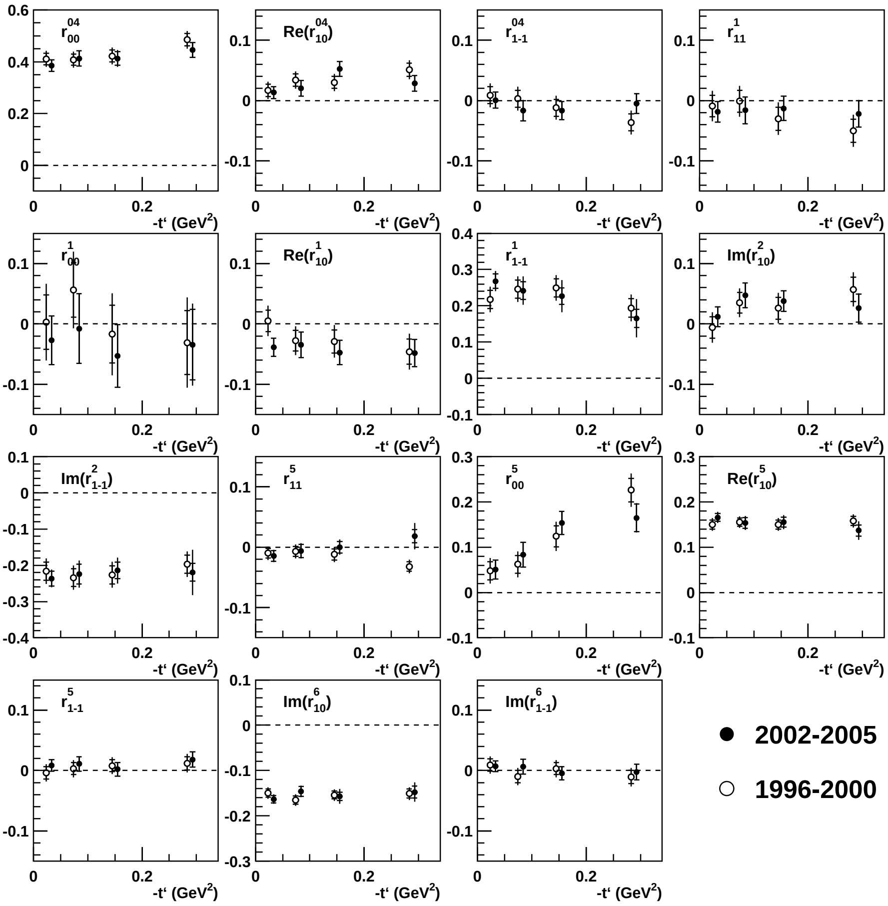

Figure E.12: The SDMEs for an unpolarized target and an unpolarized beam extracted in different $-t'$ bins. The SDMEs are represented within the Wolf-Schilling formalism [14]. The results from this analysis obtained from the HERMES 2002-2005 data for a transversely polarized target are compared with the results from an other analysis obtained from the HERMES 1996-2000 data for an unpolarized hydrogen target [26].

Appendix F

SDMEs for a transversely polarized target

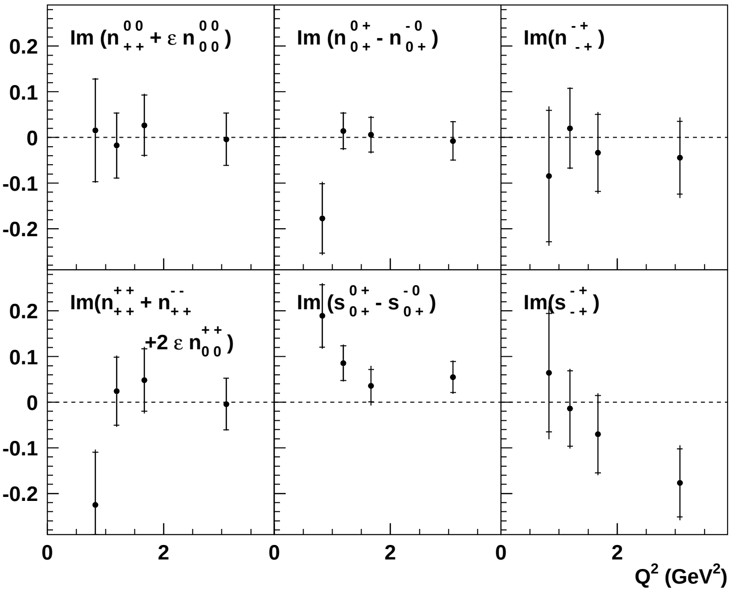

Figure F.1: Combinations of SDMEs for a transversely polarized target and an unpolarized beam binned in Q^2. Each combination contains an s-channel helicity-conserving SDME.

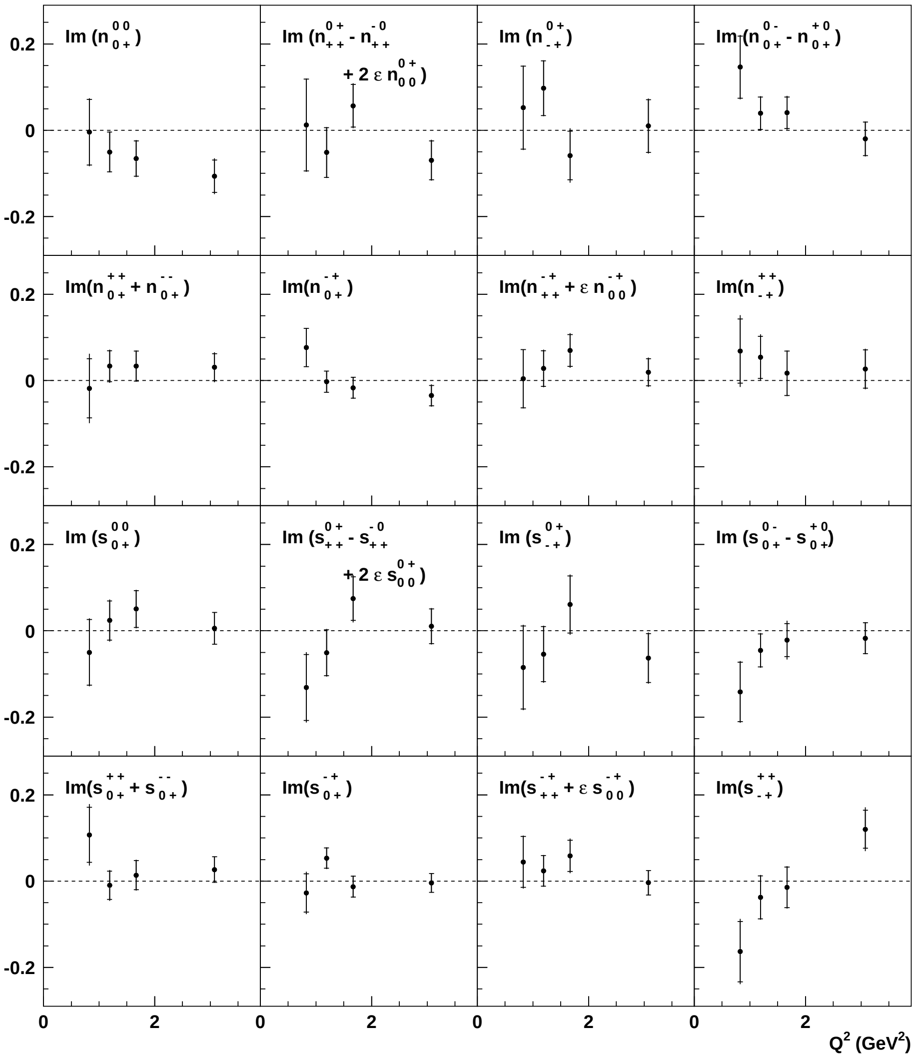

Figure F.2: Combinations of SDMEs for a transversely polarized and an unpolarized beam binned in Q^2. Each combination contains an SDME associated with the interference between helicity-conserving and helicity-changing amplitudes.

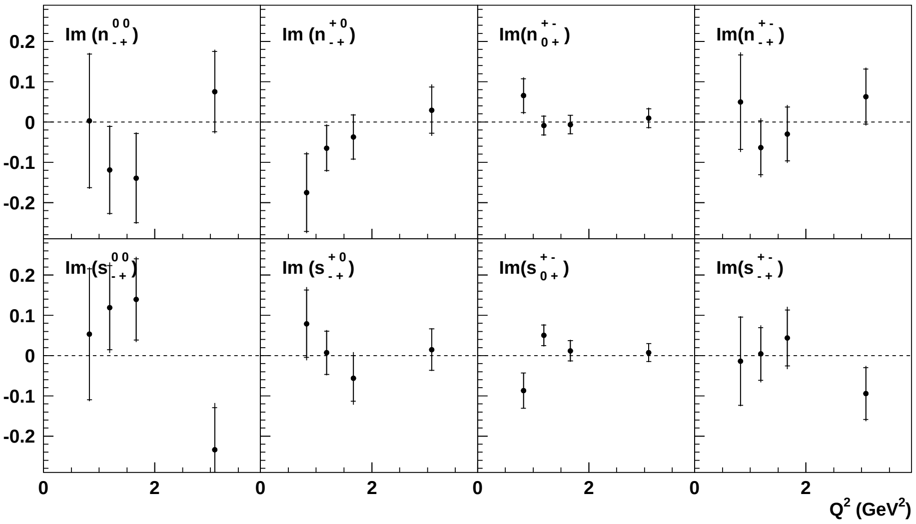

Figure F.3: SDMEs for a transversely polarized target and an unpolarized beam binned in Q^2. Each SDME is associated with the interference between different helicity-changing amplitudes.

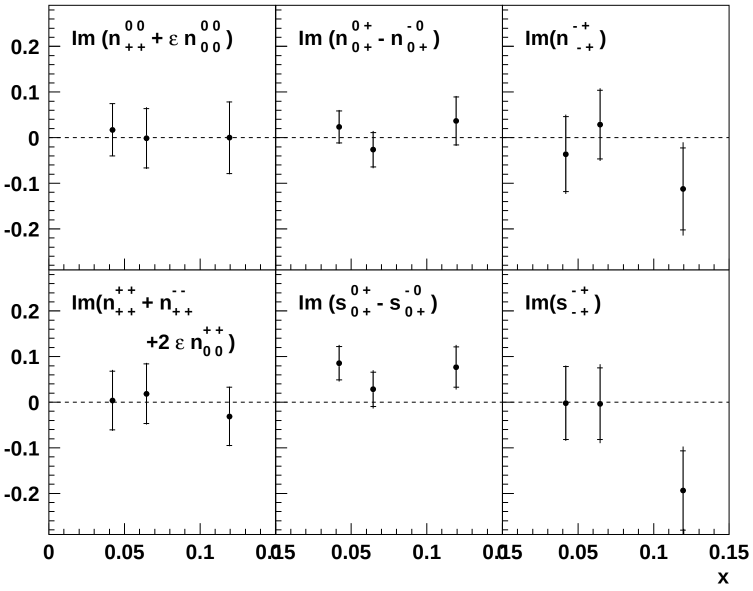

Figure F.4: Combinations of SDMEs for a transversely polarized target and an unpolarized beam binned in x. Each combination contains an s-channel helicity-conserving SDME.

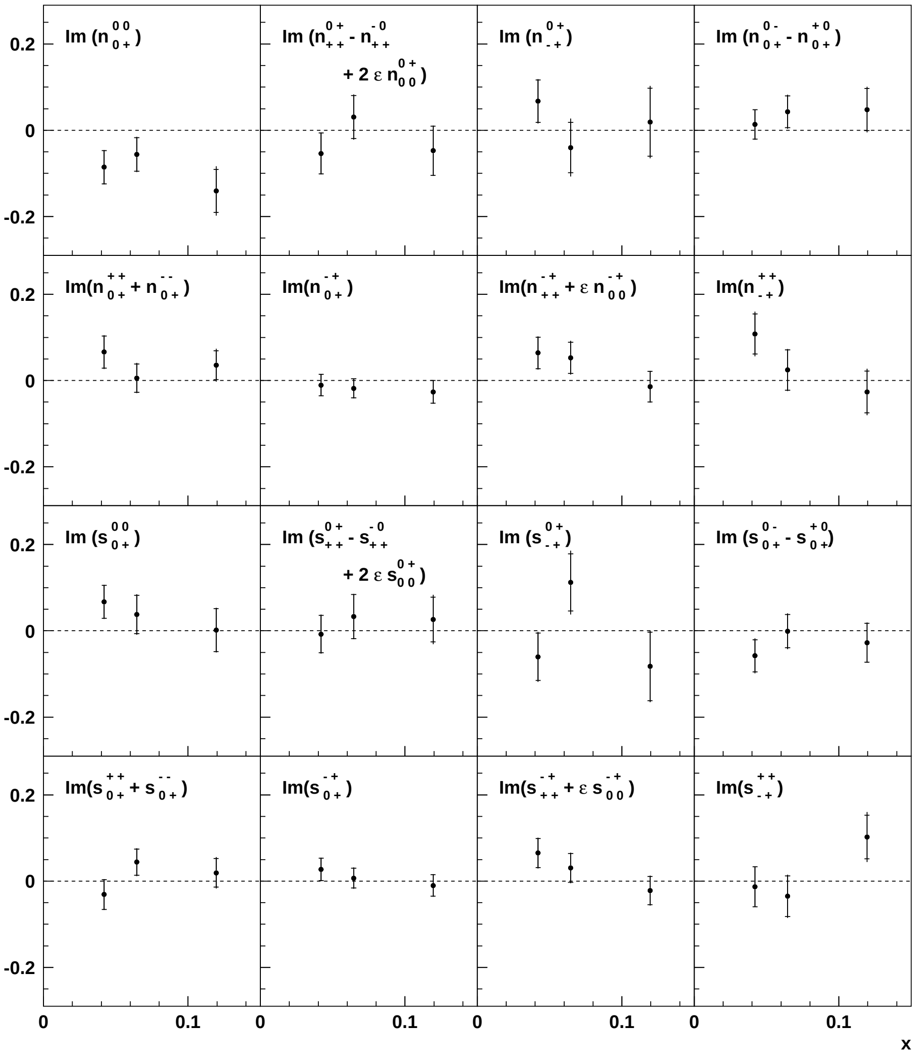

Figure F.5: Combinations of SDMEs for a transversely polarized and an unpolarized beam binned in x. Each combination contains an SDME associated with the interference between helicity-conserving and helicity-changing amplitudes.

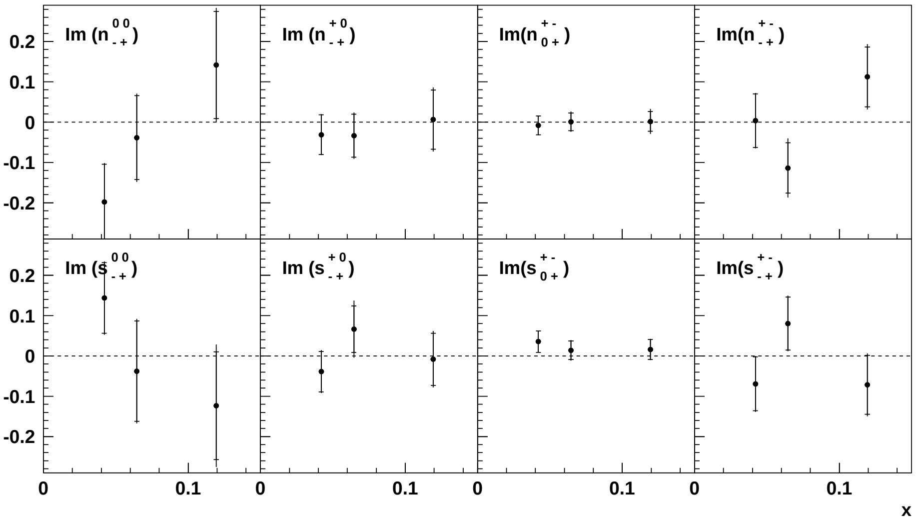

Figure F.6: SDMEs for a transversely polarized target and an unpolarized beam binned in x. Each SDME is associated with the interference between different helicity-changing amplitudes.

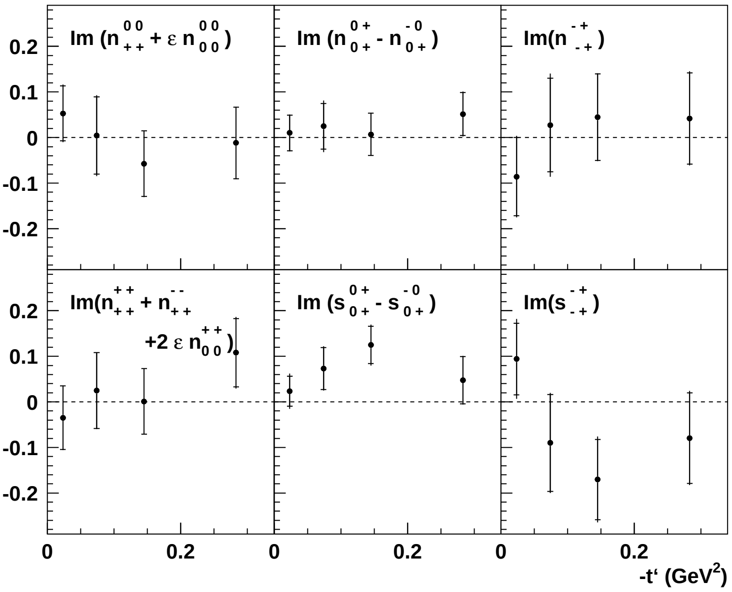

Figure F.7: Combinations of SDMEs for a transversely polarized target and an unpolarized beam binned in $-t'$. Each combination contains an s-channel helicity-conserving SDME.

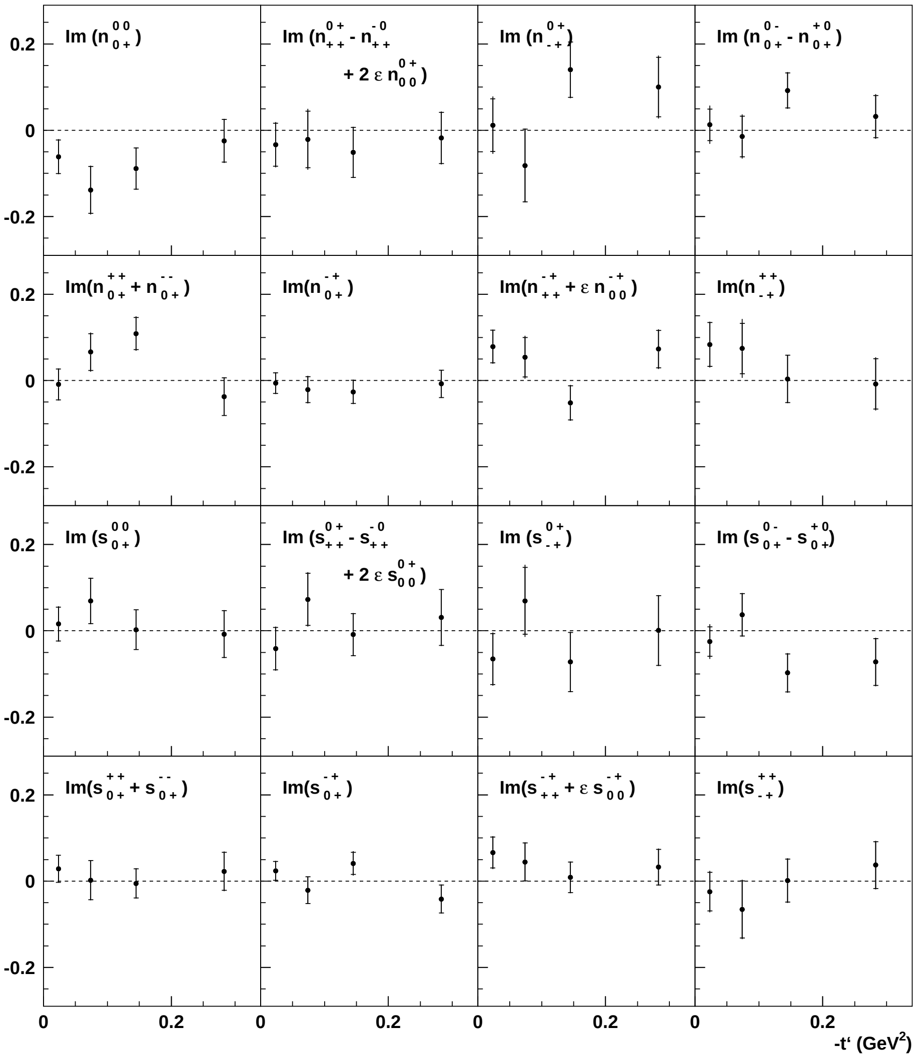

Figure F.8: Combinations of SDMEs for a transversely polarized and an unpolarized beam binned in $-t'$. Each combination contains an SDME associated with the interference between helicity-conserving and helicity-changing amplitudes.

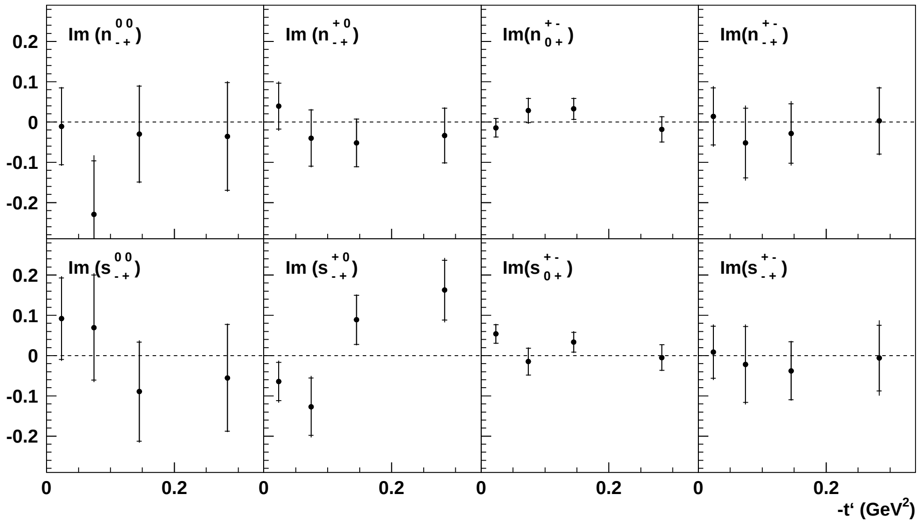

Figure F.9: SDMEs for a transversely polarized target and an unpolarized beam binned in x. Each SDME is associated with the interference between different helicity-changing amplitudes.

Bibliography

[1] F. Halzen and A. D. Martin, *Quarks and Leptons: An introductory course in modern particle physics*, Wiley (1984).

[2] I. Estermann, O. C. Simpson and O. Stern, *The Magnetic Moment of the Proton*, Phys. Rev. **52** (1937) 535 - 545.

[3] R. Hofstadter and R. W. McAllister, *Electron Scattering from the Proton*, Phys. Rev. **98** (1955) 217 - 218.

[4] E. D. Bloom et al., *High-Energy Inelastic e-p Scattering at 6° and 10°*, Phys. Rev. Lett. **23** (1969) 930 - 934.

M. Breidenbach et al., *Observed Behavior of Highly Inelastic Electron-Proton Scattering*, Phys. Rev. Lett. **23** (1969) 935 - 939.

[5] J. Ashman et al. (European Muon Collaboration), *A measurement of the spin asymmetry and determination of the structure function g_1 in deep inelastic muon-proton scattering*, Phys. Lett. **B206** (1988), 364-370.

[6] A. Airapetian et al. (The HERMES Collaboration), *Precise determination of the spin structure function g_1 of the proton, deuteron and neutron*, Phys. Rev. **D75** (2007) 012007, arXiv:hep-ex/0609039, DESY 06-142.

[7] A. Airapetian et al. (The HERMES Collaboration), *Quark helicity distributions in the nucleon for up, down, and strange quarks from semi-inclusive deep-inelastic scattering*, Phys. Rev **D71** (2005) 012003, arXiv:hep-ex/0407032, DESY-04-107.

[8] R. L. Jaffe and A. Manohar, *The g_1 problem: deep inelastic electron scattering and the spin of the proton*, Nucl. Phys. **B337** (1990) 509-546.

[9] X. Ji, *Gauge-Invariant Decomposition of Nucleon Spin*, Phys. Rev. Lett **78** (1997) 610.

[10] K. Goeke, M. V. Polyakov, M. Vanderhaeghen, *Hard Exclusive Reactions and the Structure of Hadrons*, Prog. Part. Nucl. Phys. **47** (2001) 401.

[11] M. Diehl, *Vector meson production from a polarized nucleon*, arXiv:0704.1565 [hep-ph]. DESY-07-049.

[12] J. Collins, L. Frankfurt, M. Strikman, *Factorization for hard exclusive electroproduction of mesons in QCD*, Phys. Rev. **D56** (1997) 2982.

[13] M. Diehl, S. Sapeta, *On the analysis of lepton scattering on longitudinally or transversely polarized protons*, Eur. Phys. J. **C41** (2005) 515.

[14] K. Schilling and G. Wolf, *How to analyse vector-meson production in inelastic scattering*, Nucl. Phys. **B61** (1973) 381.

[15] W.-M. Yao et al., *The Review of Particle Physics*, Journal of Physics **G33** (2006) 1.

[16] R. L. Jaffe, *Spin, twist and hadron structure in deep inelastic processes*, Talk given at Ettore Majorana International School of Nucleon Structure, 1st Course: the Spin structure of the Nucleon, Erice, Italy, 3-10 August 1995, arXiv:hep-ph/9602236.

[17] P. J. Mulders, *Polarized structure functions*, Prog. Part. Nucl. Phys. **55** (2005) 243-269.

[18] A. Airapetian et al. (The HERMES Collaboration), *Subleading-twist effects in single-spin asymmetries in semi-inclusive deep-inelastic scattering on a longitudinally polarized hydrogen target*, Phys. Lett. **B622** (2005) 14-22, arXiv:hep-ex/0505042, DESY-05-072.

[19] P. B. van der Nat,*Transversity in two-hadron fragmentation*, PhD thesis, Vrije Universiteit Amsterdam, Sept. 2007.

[20] A. Bacchetta, U. D'Alesio, M. Diehl, C. A. Miller, *Single-spin asymmetries: The Trento conventions*, Phys. Rev. **D70** (2004) 117504.

[21] P. Joos et al., *Rho production by virtual photons*, Nucl. Phys. **B113** (1976) 53.

[22] A. D. Martin, T. D. Spearman, *Elementary Particle Theory*, North-Holland Pub. Co (1970).

[23] M. Kolstein, *Exclusive ρ^0-Meson Electroproduction at HERMES*, PhD Thesis, Vrije Universiteit Amsterdam, Netherlands, 1998.

[24] K. Ackerstaff et al. (The HERMES Collaboration), *Measurement of Angular Distributions and $R = \sigma_L/\sigma_T$ in Diffractive Electroproduction of ρ^0 Mesons*, Eur. Phys. J. **C18** (2000) 303-316, DESY-99-199, arXiv:hep-ex/0002016.

[25] M. Tytgat, *Diffractive Production of ρ^0 and ω Vector Mesons at HERMES*, PhD Thesis, Universiteit Gent, March 2001.

[26] The HERMES Collaboration, *Spin Density Matrix Elements in Exclusive Diffractive ρ^0 Production on Proton and Deuteron at Intermediate Energies*, DRAFT v7.4.

[27] C. Adloff et al. (H1), Eur. Phys. J. **C13** (2000) 371;
J. Breitweg et al. (ZEUS), Eur. Phys. J. **C12** (2000) 393;
V. Eckardt et al. (DESY 1), Nucl. Phys. **B55** (1973) 45;
P. Joos et al. (DESY 2), Nucl. Phys. **B113** (1976) 53;
D. G. Cassel et al. (CORNELL), Phys. Rev. **D24** (1981) 2787;
C. del. Papa et al. (SLAC 1), Phys. Rev. **D19** (1979) 1303;
J. T. Dakin et al. (SLAC 2), Phys. Rev. **D8** (1973) 687;
J. Ballam et al. (SLAC 3), Phys. Rev. **D10** (1974) 765;
M. R. Adams et. al. (E665), Z. Phys. **C74** (1997) 237;
M. Arneodo et al. (NMC), Nucl. Phys. **B429** (1994) 503;
J. J. Aubert et al. (EMC), Phys. Lett. **B161** (1985) 203;
W. D. Shrambroom et al. (CHIO), Phys. Rev. **D26** (1982) 1.

[28] F. Ellinghaus, W.-D. Nowak, A. V. Vinnikov, Z. Ye, *Can the total angular momentum of u-quarks in the nucleon be accessed at HERMES?*, Eur. Phys. J. **C46** (2006) 729-739, arXiv:hep-ph/0506264.

[29] M. Diehl, W. Kugler, *Next-to-leading order corrections in exclusive meson production*, arXiv:0708.1121v1 [hep-ph], DESY 07-117.

[30] S. V. Goloskokov, P. Kroll, *The role of the quark and gluon GPDs in hard vector-meson electroproduction*, arXiv:0708.3569v2 [hep-ph].

[31] A. Airapetian, et al. (The HERMES Collaboration), *Exclusive Leptoproduction of ρ^0 Mesons from Hydrogen at Intermediate Virtual Photon Energies*, Eur. Phys. J. **C17** (2000) 389-398, DESY-00-058, arXiv:hep-ex/0004023.

[32] M. Diehl, A. V. Vinnikov, *Quarks vs. gluons in exclusive ρ electroproduction*, Phys. Lett. **B609** (2005) 286-290, arXiv:hep-ph/0412162.

[33] The HERMES Collaboration, *Technical Design Report*, Technical Report DESY-PRC 93/06, DESY, (1993).

[34] K. Ackerstaff et al., *The HERMES spectrometer*, Nucl. Instr. & Meth. **A417** (1998) 230, arXiv:hep-ex/9806008.

[35] A. Sokolov and I.M. Ternov, *On polarization and spin effects in the theory of synchotron radiation*, Sov. Phys. Doklady (1964) 1203.

[36] M. Beckmann et al., *The longitudinal polarimeter at HERA*, Nucl. Instum. Meth. **A479** (2002) 334-348, arXiv:physics/0009047.

[37] D. P. Barber et al., *The HERA polarimeter and the first observation of electron spin polarization at HERA*, Nucl. Instrum. Meth. **A329** (1993) 79-111.

[38] A. Nass et al., *The HERMES polarized atomic beam source*, Nucl. Instum. Meth. **A505** (2003) 633-644.

[39] C. Baumgarten et al., *An atomic beam polarimeter to measure the nuclear polarization in the HERMES gaseous polarized and deuterium target* (2001). DESY-01-078.

[40] W. Wander, *Reconstruction of High Energy Scattering Events in the HERMES Experiment.* PhD Thesis, Friedrich-Alexander-Univ. Erlangen-Nuernberg, (1997). DESY-HERMES 97/031.

[41] M. G. van Beuzenkom, E. Garutti, D. Heesbeen, J. J. M. Steijger and J. Visser, *First experience with the HERMES silicon detector*, Nucl. Instrum. Meth. **A461** (2001) 247-250.

[42] J. J. M. Steijger, *The lambda wheels, a silicon vertex detector for HERMES*, Nucl. Instrum. Meth. **A453** (2000) 98-102.

[43] M. Demey, *The polarization of* Λ^0 *hyperons in quasi-real photoproduction*, PhD thesis, Universiteit van Amsterdam, The Netherlands (2007).

[44] D. Ryckbosch, *The HERMES RICH detector*, Nucl. Instrum. Meth. **A433**, 98 (1999).

[45] N. Akopov et al., *The HERMES dual ring imaging Cerenkov detector*, Nucl. Instum. Meth. **A479** (2002) 511-530, arXiv:physics/0104033.

[46] H. Avakian et al., *Performance of the electromagnetic calorimeter of the HERMES experiment*, Nucl. Instum. Meth. **A417** (1998) 69, arXiv:hep-ex/9810004.

[47] J. Wendland, *Particle Identification for HERMES Run I*, HERMES internal report 01-067.

[48] HERMES Data Quality website,
http://www-hermes.desy.de/groups/daqlgrp/ .

[49] H. Tanaka et al., *A gain monitoring system with a Nd:YAG laser for the photomultipliers of the HERMES experiment*, Nucl. Instrum. Meth. **A515** (2003) 725.

[50] D. Aston et al., *Photoproduction of* ρ^0 *and* ω *on hydrogen at photon energies of 20 to 70 GeV*, Nucl. Phys. **B209** (1982) 56.

[51] J. Park et al., *The reaction* $\gamma p \rightarrow \rho^0 p$ *at 5.5 to 18 GeV*, Nucl. Phys. **B36** (1972) 404.

[52] F. Bulos et al., *Photoproduction of Rho Mesons from Complex Nuclei at 9 BeV*, Phys. Rev. Lett. **22** (1969) 490.

[53] M. Ross, L. Stodolsky, *Photon Dissociation Model for Vector-Meson Photoproduction*, Phys. Rev. **149** (1966) 1172.

[54] J. D. Jackson, *Phenomenological analysis of resonances*, Nuovo Cimento **34** (1964) 1644.

[55] W. D. Shambroom et al., *Diffractive production of vector mesons in muon-proton scattering at 150 and 100 GeV*, Phys. Rev. **D26** (1982) 1.

[56] C. A. Miller, *Extracting azimuthal Fourier moments from sparse data, Presentation*, HERMES Transversity Week, June 2006.

[57] U. Elschenbroich, *Transverse Spin Structure of the Proton Studied in Semi-inclusive DIS*, PhD Thesis, Universiteit Gent, 2006.

[58] J. Dreschler, A. Rostomyan, *Target spin asymmetry in exclusive electroproduction of ρ^0 mesons on a transversely polarized target*, HERMES release report, 2007.

[59] J. Dreschler (The HERMES Collaboration), *Exclusive meson production at HERMES*, presentation at the Pan-Pacific Symposium on High Energy Spin Physics, Vancouver 2007.

[60] A. Rostomyan, J. Dreschler (The HERMES Collaboration), Proceedings of *DIS 2007*, World Scientific (2007), arXiv:0707.2486 [hep-ex].

[61] T. Sjöstrand et al., *High-energy-physics event generation with PYTHIA 6.1*, Comput. Phys. Commun. **135** (2001) 238-259, arXiv:hep-ph/0010017.

[62] T. Sjöstrand, L. Lonnblad, and S. Mrenna, *PYTHIA 6.2: Physics and manual*, arXiv:hep-ph/0108264.

[63] C. Friberg and T. Sjöstrand, *Total cross sections and event properties from real to virtual photons*, JHEP **09** (2000) 010, arXiv:hep-ph/0007314.

[64] T. H. Bauer, R. D. Spital, and D. R. Yennie, *The hadronic properties of the photon in high-energy interactions*, Rev. Mod. Phys. **50** (1978) 261.

[65] P. Liebing, *Can the Gluon Polarization in the Nucleon be Extracted from HERMES Data on Single High-p_T Hadrons?*, PhD thesis, Universität Hamburg (2004).

[66] A. Hillenbrand, *Measurement and Simulation of the Fragmentation Process at HERMES*, PhD thesis, Friedrich-Alexander Universität, Erlangen-Nürnberg, 2005.

[67] CERN, CERN Program Library, http://wwwasd.web.cern.ch/wwwasd/geant.

[68] C. A. Miller, *Extracting azimuthal Fourier moments from sparse data*, Presentation, HERMES collaboration meeting, October 2005.

[69] P. B. van der Nat, H. Blok, *(Another) correction in binned fitting of asymmetries*, HERMES internal report 05-027.

[70] S. Manayenkov, *Natural an unnatural parity exchange amplitudes of* ρ^0 *meson production*, Presentation, HERMES vector-meson week, November 2006, Hamburg.

A. Borissov, S. Manayenkov, B. Marianski, *Helicity amplitudes of exclusive* ρ^0*-meson electoproduction in DIS*, Presentation, HERMES collaboration meeting, December 2007, Hamburg.

[71] I. Akushevich, *Radiative Effects in Processes of Diffractive Vector Meson Electroproduction*, Eur. Phys. J. **C8** (1999), arXiv:hep-ph/9808309.

[72] I. Akushevich, P. Kuzhir, *QED radiative correction to spin-density matrix elements in exclusive vector meson production*, Phys. Lett. **B474** (2000) 411-415, arXiv:hep-ph/9911346.

[73] I. Akushevich, H. Böttcher, D. Ryckbosch, *RADGEN 1.0 Monte Carlo Generator for Radiative Events in DIS on Polarized and Unpolarized Targets*, arXiv:hep-ph/9906408.

[74] M. Diehl, Th. Feldmann, R. Jakob, P. Kroll, *Generalized parton distributions from nucleon form factor data*, Eur. Phys. J. **C39** (2005) 1-39, arXiv:hep-ph/0408173.

[75] S.V. Goloskokov, P. Kroll, *The longitudinal cross section of vector meson electroproduction*, arXiv:hep-ph/0611290v1.

[76] Z. Ye (The HERMES Collaboration), *Transverse target-spin asymmetry associated with DVCS on the proton and a resulting model-dependent constraint on the total angular momentum of quarks in the nucleon*, arXiv:hep-ex/0606061.

[77] JLab Hall A, M. Mazouz, et al., *Deeply Virtual Compton Scattering off the neutron*, Phys. Rev. Lett. **99** (2007) 242501, arXiv:0709.0450v2 [nucl-ex].

[78] T. Keri (The HERMES Collaboration), Proceedings of *HADRON07*, Frascati Physics Series, Volume XLVI (2007)

[79] P. Kroll, private communication.

[80] C. Schill (COMPASS), *Transversity Measurements at COMPASS*, arXiv:0709.4625v1 [hep-ex].

[81] A. Bruell, *The JLab 12 GeV Upgrade*, Presentation, PACSPIN 2007, Vancouver, Canada.

Samenvatting

Inleiding

Protonen en neutronen zijn de bouwstenen van alle in de natuur waargenomen atoomkernen. In het onderzoek naar de structuur van nucleonen, de verzamelnaam van protonen en neutronen, is de oorsprong van hun spin een belangrijk onderwerp. Spin, ook wel het intrinsieke impulsmoment genoemd, is een fundamentele kwantummechanische eigenschap van deeltjes. Deeltjes kunnen op basis van hun spin worden ingedeeld in twee categorieën, bosonen, die een heeltallige spin van $0, 1, 2, \ldots$ (uitgedrukt in eenheden van de gereduceerde Planck constante $\hbar$) dragen, of fermionen, die een halftallige spin van $1/2, 3/2, 5/2, \ldots$ dragen. Het is bekend dat nucleonen een spin dragen van $1/2$. Van nucleonen weten we dat het geen elementaire deeltjes zijn, maar samengestelde systemen van elementaire deeltjes die bij elkaar worden gehouden door één van de fundamentele krachten in de natuur, namelijk de sterke wisselwerking [1]. De individuele eigenschappen van deze elementaire deeltjes, waaronder hun spin, zijn tot in detail bekend. Maar, op welke manier deze deeltjes gezamenlijk zorg dragen voor de halftallige spin van het nucleon, is één van de onopgeloste vraagstukken in de fysica van de sterke wisselwerking.

Onderzoek naar de structuur van nucleonen Het eerste bewijs dat nucleonen samengestelde deeltjes zijn werd geleverd door metingen van het magnetische moment van het proton in 1932-33 door Estermann, Frisch en Stern in Hamburg [2]. Het gemeten magnetische moment week duidelijk af van de waarde die het zou aannemen als het proton een elementair deeltje zou zijn. Hieruit kon men concluderen dat het proton een interne structuur heeft.

Sindsdien zijn er veel experimenten uitgevoerd om de interne structuur van nucleonen te onderzoeken. In veel van deze experimenten werden leptonen (elektronen, positronen, muonen of neutrino's) verstrooid aan protonen of deuteronen. Men heeft waargenomen dat bij het elastische verstrooiingsproces $ep \rightarrow ep$, waar e het lepton aanduidt en p het proton, het verstrooiingspatroon afwijkt van de verwachting voor verstrooiing aan een puntdeeltje, een elementair deeltje zonder ruimtelijke uitgebreidheid. Dit is voor het eerst waargenomen in 1955 door Hofstadter en medewerkers [3] in metingen van elastische elektronverstrooiing aan protonen in Stanford. Een goede beschrijving van de elastische verstrooiing kon worden gegeven met behulp van modellen, waarin wordt aangenomen dat nucleonen een ruimtelijke verdeling hebben van lading en magnetisatie, die in rekening wordt gebracht door de zogenaamde elektromagnetische vormfactoren. Uit de gemeten elektromagnetische vormfactoren heeft men bepaald dat het proton een ladingsstraal van ongeveer 0.8 fm heeft.

Onderzoek van zogenaamde diep-inelastische verstrooiing (DIS) biedt de mogelijkheid om de samenstelling van het nucleon in meer detail te bepalen. In dit verstrooiingsproces vindt een wisselwerking plaats tussen een inkomend lepton en één van de individuele deeltjes waaruit het nucleon is opgebouwd. Als gevolg van deze wisselwerking breekt het nucleon op in verscheidene zware samengestelde deeltjes (hadronen), die collectief worden aangeduid met X. De eerste metingen van het DIS-proces $ep \rightarrow eX$ werden uitgevoerd in Stanford aan het einde van de zestiger jaren van de vorige eeuw [4]. Op basis van deze metingen kwamen Feynman en Bjorken tot de interpretatie van het DIS-proces als zijnde verstrooiing aan individuele elementaire deeltjes in het binnenste van het nucleon. Deze elementaire deeltjes werden partonen genoemd.

In het partonmodel wordt een nucleon beschreven als een verzameling van partonen, elektrisch geladen spin-1/2 deeltjes die later (anti)quarks genoemd werden. De wisselwerking tussen quarks wordt beschreven als de uitwisseling van elektrisch neutrale spin-1 partonen, gluonen genaamd. Men kan verder onderscheid maken tussen valentiequarks en een 'zee' van quark-antiquark paren die ontstaan vanuit gluonen door kwantumfluctuaties. Nucleonen bevatten elk drie valentiequarks die verantwoordelijk zijn voor de belangrijkste statische eigenschappen van nucleonen, zoals de isospin (het kwantumgetal dat bepaalt of een nucleon een proton of een neutron is), de elektrische lading en de spin.

De werkzame doorsnede van het DIS-proces voor een bepaalde polarisatietoestand van het inkomende lepton en het nucleon wordt uitgedrukt in termen van zogenaamde structuurfuncties. Binnen het partonmodel wordt een fenomenologische beschrijving gegeven van de DIS-structuurfuncties in termen van zogenaamde partonverdelingsfuncties. Deze verdelingsfuncties relateren de structuurfuncties aan de impulsverdelingen van partonen in het nucleon.

De spinafhankelijke structuurfunctie g_1 kan worden gemeten in DIS met een longitudinaal gepolariseerde leptonbundel en een longitudinaal gepolariseerd nucleon ten opzichte van de bundelrichting. Deze structuurfunctie is gerelateerd aan de heliciteitsverdeling van quarks in het nucleon, waarbij de heliciteit aangeeft of de spinrichting van quarks parallel of antiparallel aan de bundelrichting staat. Vanuit deze verdelingsfunctie kan men de relatieve bijdrage $\Delta\Sigma$ van de quarkspins aan de spin van het nucleon bepalen. In 1988 bracht het EMC-experiment te CERN verslag uit van de eerste metingen van $\Delta\Sigma$. De resultaten van het EMC-experiment leidden tot de verrassende ontdekking dat quarkspins slechts voor een klein deel bleken bij te dragen aan de spin van het proton. Op basis van de resultaten van verschillende vergelijkbare experimenten aan de instituten CERN, SLAC en DESY, is bepaald dat de bijdrage $\Delta\Sigma$ van de spin van quarks tot de spin van het nucleon ongeveer 20-30% is. De vraag rijst dus wat de oorsprong is van het resterende en grootste gedeelte van de spin van nucleonen.

Het baanimpulsmoment van quarks, 'generalized parton distributions' en exclusieve processen Zoals hierboven is beschreven, levert de spin van quarks slechts een relatief kleine bijdrage aan de spin van het nucleon. Er moeten derhalve ook andere bijdragen zijn. De verschillende bijdragen aan de nucleonspin worden gespecificeerd in de volgende vergelijking [8]

$$\frac{1}{2} = \frac{1}{2}\Delta\Sigma + L_q + \Delta G + L_g,$$

waar L_q staat voor het baanimpulsmoment van quarks in het nucleon en waar respectievelijk ΔG en L_g de bijdragen van de intrinsieke spin en het baanimpulsmoment van gluonen voorstellen. Het totale impulsmoment J_q van quarks in het nucleon kan worden geschreven als

$$J_q = \frac{1}{2}\Delta\Sigma + L_q.$$

Aangezien voor $\Delta\Sigma$ reeds metingen beschikbaar zijn, kan men informatie verkrijgen over het, tot dusver onbekende, baanimpulsmoment L_q van quarks, als men de waarde van het totale impulsmoment J_q kan bepalen.

Het is mogelijk om experimenteel informatie te verkrijgen over het totale impulsmoment J_q door gebruik te maken van het theoretische kader van zogenaamde 'generalized parton distributions' (GPDs). GPDs zijn generalisaties van de gebruikelijke partonverdelingsfuncties en vormfactoren. GPDs geven een beschrijving van exclusieve productieprocessen. Dit zijn processen waarbij het nucleon intact blijft en waarbij men alle eindtoestanden expliciet kan identificeren, zoals bij diep-virtuele Comptonverstooiing (DVCS) $e\,p \to e\,p\,\gamma$ en exclusieve mesonproductie $e\,p \to e\,p\,M$, waar γ en M, respectievelijk, een reëel foton en een meson vertegenwoordigen. Hierbij moet worden opgemerkt dat, in het geval van exclusieve mesonproductie, de GPD-beschrijving alleen van toepassing is als zowel het uitgewisselde virtuele foton als het geproduceerde meson longitudinaal gepolariseerd zijn.

Zoals voor het eerst is aangetoond in [9], zijn specifieke GPDs gerelateerd aan het totale impulsmoment van quarks in het nucleon. Omdat GPDs niet direct kunnen worden gemeten, zijn er modellen ontwikkeld voor GPDs op basis van de beschikbare informatie over partonverdelingsfuncties en vormfactoren. Met de extra informatie die het onderzoek naar exclusieve processen oplevert, kunnen de GPD-modellen verder verfijnd worden. Dit zal resulteren in meer gedetailleerde kennis van de structuur van het nucleon. In het bijzonder, zoals is beschreven in [10], kan met behulp van metingen van specifieke observabelen in exclusieve meson productie een modelafhankelijke schatting gemaakt worden van het totale impulsmoment J_q van quarks in het nucleon. Op deze manier kan dus ook een schatting gemaakt worden van het baanimpulsmoment L_q van quarks. Dat is van belang, omdat er tot op heden geen nauwkeurige experimentele informatie beschikbaar is over het baanimpulsmoment van quarks en gluonen in het nucleon.

De meting

GPD-modelberekeningen zijn beschikbaar voor de zogenaamde 'transverse target-spin asymmetry' A_{UT} in exclusieve ρ^0-leptoproductie. Dit is een asymmetrie van de werkzame doorsnede van dit proces bij een transversaal gepolariseerd nucleon en een ongepolariseerde leptonbundel. Het gaat hier om de asymmetrie onder het draaien van de oriëntatie van de nucleonpolarisatie met een hoek van 180 graden. De asymmetrie is afhankelijk van de azimuthale hoeken ϕ en ϕ_S van het geproduceerde ρ^0-meson en de nucleon-polarisatievector, respectievelijk, rondom de richting van het uitgewisselde virtuele foton. Uit de berekeningen volgt dat de asymmetrie A_{UT} een $\sin(\phi - \phi_s)$ component heeft, die afhankelijk is van de waarde van J_q. Door deze hoekafhankelijkheid van de asymmetrie te meten en deze vervolgens te vergelijken met beschikbare berekeningen, kan men dus een schatting van J_q verkrijgen. Hierbij moet men in acht nemen dat de berekeningen alleen van toepassing zijn in het geval dat zowel het uitgewisselde virtuele foton als het geproduceerde ρ^0-meson longitudinaal gepolariseerd is. Experimenteel moet de asymmetrie dus ook voor dit specifieke geval worden bepaald.

De gebruikelijke manier om de werkzame doorsnede voor longitudinaal en transversaal gepolariseerde virtuele fotonen te scheiden is de Rosenbluth methode. Deze methode vereist echter dat metingen worden gedaan bij verschillende bundelenergieën. Indien metingen gedaan zijn bij één bundelenergie moet een andere benadering gebruikt worden. Onder de aanname van 's-channel helicity conservation' (SCHC) wordt de heliciteit van het virtuele foton overgenomen door het geproduceerde ρ^0-meson. In het geval dat SCHC geldig is, kan men dus volstaan met het meten van de asymmetrie voor een longitudinaal gepolariseerd ρ^0-meson. Experimenteel is dit mogelijk, door gebruik te maken van het feit dat het ρ^0-meson vrijwel direct na de productie vervalt in twee pionen met een tegengestelde lading. Het ρ^0-meson is net zoals het virtuele photon een spin-1 deeltje. Omdat de intrinsieke spin van een pion gelijk aan nul is, wordt de spin van ρ^0-meson volledig overgedragen op het baanimpulsmoment van het pionpaar en daarmee op de hoekverdeling van het pionpaar.

Door deze vervalshoekverdeling tegelijkertijd te bepalen, kan de werkzame doorsnede, en dus ook tot de asymmetrie A_{UT}, voor zowel longitudinaal als transversaal gepolariseerde ρ^0-mesonen geëxtraheerd worden. De bijdragen van de verschillende polarisatietoestanden van het virtuele foton en het ρ^0-meson kunnen worden uitgedrukt in termen van zogenaamde 'spin density-matrix elements' (SDMEs). De (combinaties van) SDMEs voor een specifieke polarisatietoestand van het geproduceerde ρ^0-meson kunnen bepaald worden uit de hoekverdelingen van het ρ^0-meson en de bijbehorende vervalspionen. Beschikbare resultaten voor SDMEs impliceren dat SCHC een redelijke aanname is voor een ongepolariseerd nucleon. Recentelijk is een nieuw SDME formalisme ontwikkeld voor vector-mesonproductie op een gepolariseerd nucleon [11]. Met behulp van dit formalisme is het mogelijk om de asymmetrie A_{UT} gescheiden voor longitudinaal en transversaal gepolariseerde ρ^0-mesonen te bepalen.

Indeling proefschrift

Dit proefschrift behandelt de eerste bepaling van de asymmetrie A_{UT} in exclusieve ρ^0-elektroproductie op het proton. In hoofdstuk 2 wordt het theoretische kader, in het bijzonder voor A_{UT}, SDMEs en GPDs, behandeld. De asymmetrie is bepaald op basis van metingen verricht in de periode 2002-2005 met het HERMES-experiment bij het instituut DESY in Hamburg, Duitsland. Het HERMES-experiment maakte gebruik van de 27.6 GeV elektron (of positron) bundel van de HERA-versneller. De leptonbundel werd verstrooid aan een gas van waterstofatomen met een transversaal gepolariseerde kern. De hierbij verstrooide leptonen en geproduceerde deeltjes werden gedetecteerd door de HERMES-spectrometer. In hoofdstuk 3 kan men een meer gedetaileerde beschrijving van de experimentele opstelling vinden.

De selectie van data voor exclusieve ρ^0-productie is beschreven in hoofdstuk 4. De informatie over exclusief geproduceerde ρ^0-mesonen werd gereconstrueerd vanuit de verkregen informatie over het verstrooide lepton en de vervalsproducten van het geproduceerde ρ^0-meson. Pionparen afkomstig van het verval van ρ^0-mesonen werden geselecteerd door grenzen te stellen aan de invariante massa van gedetecteerde hadronparen met tegengestelde ladingen. Het teruggestoten proton kon niet worden gedetecteerd door de HERMES-spectrometer. Desondanks konden exclusieve processen worden geselecteerd door een bovengrens te stellen aan de zogenaamde ontbrekende energie. Bij de dataselectie is getracht de relatieve bijdrage van achtergrondprocessen te minimaliseren. Een Monte Carlo-simulatie werd gebruikt om een schatting te geven van de bijdrage van de niet-exclusieve achtergrond afkomstig van semi-inclusieve diep-inelastische verstrooiingsprocessen. De achtergrondbijdrage van exclusieve, niet-resonante processen, waarbij de gedetecteerde hadronparen niet afkomstig zijn van ρ^0-verval, is geschat aan de hand van een fit van de invariante massa verdeling van exclusieve hadronparen. Volgens deze schatting is deze achtergrondbijdrage verwaarloosbaar klein.

De procedures die zijn gebruikt voor de bepaling van de asymmetrie A_{UT} en de SDMEs voor ρ^0-productie zijn beschreven in hoofdstuk 5. De asymmetrie is bepaald als functie van de hoeken ϕ en ϕ_S door middel van fits van de hoekverdelingen van ρ^0-mesonen gemeten met twee tegengestelde oriëntaties van de transversale protonpolarisatie. Hierbij werd gebruikt gemaakt van de 'unbinned maximum likelihood fit' methode. Zoals eerder is uitgelegd was het onze doelstelling om A_{UT} afzonderlijk te bepalen voor verschillende polarisatietoestanden van het ρ^0-meson. Om dit te bewerkstelligen is de afhankelijkheid van de vervalshoek $\theta_{\pi\pi}$ van het ρ^0-meson in rekening genomen in de extractieprocedure.

Het modelleren van de extra hoekafhankelijkheid is op twee verschillende manieren aangepakt. In de ene aanpak is gebruik gemaakt van een combinatie van de Diehl-Sapeta [13] en Wolf-Schilling [14] formalismen. Hierin is de hoekverdeling geïntegreerd over de vervalshoek $\phi_{\pi\pi}$ van het ρ^0-meson. In de andere aanpak is gebruik gemaakt van het meer recentelijk ontwikkelde Diehl formalisme [11] voor vector-mesonproductie vanaf een gepolariseerd nucleon. In dat geval is de vervalshoek $\phi_{\pi\pi}$ wel in rekening gebracht. In beide benaderingen zijn SDMEs gebruikt om de informatie besloten in de verschillende hoekverdelingen te vertegenwoordigen.

Hoofdstuk 7 is gewijd aan de verkregen resultaten voor SDMEs en voor de asymmetrie A_{UT}. Op basis van de resultaten voor de SDMEs verkregen in het Diehl formalisme, kan worden geconcludeerd dat voor een ongepolariseerd proton SCHC een redelijke, maar niet exacte benadering is. De resultaten voor een ongepolariseerd proton zijn omgezet naar het Wolf-Schilling formalisme en vergeleken met de resultaten van een eerdere analyse, gedaan in dit formalisme, van HERMES-data voor een ongepolariseerd proton uit de periode 1996-2000. Uit deze vergelijking volgt dat de resultaten van beide analyses consistent zijn.

Gebruik makend van de nieuwe resultaten voor SDMEs voor een ongepolariseerd proton is de asymmetrie A_{UT} afzonderlijk bepaald voor longitudinaal en transversaal gepolariseerde ρ^0-mesonen. De verschillen tussen de resultaten verkregen met de twee hierboven genoemde procedures voor de bepaling van de asymmetrie zijn klein ten opzichte van de experimentele onzekerheden.

Het is de eerste keer dat de SDMEs ook zijn bepaald voor een transversaal gepolariseerd proton. De meeste van deze 30 (combinaties van) SDMEs zijn, binnen de experimentele onzekerheid, consistent met nul. De resultaten geven aan dat de amplitudo's voor het productieproces waarin de oriëntatie van de protonspin verandert in het algemeen kleiner zijn dan die voor het proces waarin de oriëntatie van de protonspin gelijk blijft. Een afwijking van nul is echter waargenomen voor de SDME Im $n^{0\,0}_{0+}$, wat een extra schending van SCHC suggereert voor de overgang van een transversaal gepolariseerd foton naar een longitudinaal gepolariseerd ρ^0-meson voor een transversaal gepolariseerd proton.

Het resultaat voor de $\sin(\phi-\phi_s)$-component van de asymmetrie A_{UT} voor longitudinaal gepolariseerde ρ^0-mesonen is vergeleken met beschikbare GPD-modelberekeningen [28, 79] onder de aanname van SCHC. Uit deze vergelijking volgt dat de berekeningen consistent zijn met de data. De berekening van [28] zijn gebruikt om een modelafhankelijke schatting te verkrijgen van J^u onder de aanname $J^d = 0$. De resulterende schatting $J^u = 0.43 \pm 0.43$ is consistent met andere schattingen op basis van DVCS-metingen [76, 77, 78] en GPD-model fits van vormfactor data [29, 74]. De grote onzekerheid in de bepaling van J^u wordt gedomineerd door de statistische onzekerheid. Door gebruik te maken van de eerdere bepaling van $\Delta\Sigma = 0.330 \pm 0.039$ [6] in combinatie met de schatting $J_q \approx J^u + J^d = 0.43 \pm 0.43$ is een schatting verkregen van het baanimpulsmoment L_q van quarks in het proton. Deze schatting leverde een waarde op van $L_q = 0.27 \pm 0.43$.

Acknowledgements

Many people have earned my gratitude for their support, ideas, cooperation, inspiration, or entertainment in the course of the process that led to the completion of this thesis. Especially, I would like to thank my promotor Gerard van der Steenhoven and my copromotor Henk Blok for keeping a close eye on this process and for sharing their experience, ideas, and time. In this respect I am also grateful for the support of Jos Steijger, group leader of HERMES at NIKHEF. Moreover, I sincerely appreciate the reading committee for reviewing this thesis.

I would like to collectively thank the HERMES collaboration. The HERMES data would not have been available without the efforts of all of us. I thank those members who have made a more than average contribution to collecting the data and making it suitable for physics analyses. While working on my analysis I had a pleasant cooperation with many HERMES members, in particular with Delia Hash, Armine Rostomyan, and Cynthia Hadjidakis. The exchange of ideas during the many meetings has helped and inspired me a lot. Furthermore, I would like to thank Andy Miller, Alexander Borissov, Avetik Hayrapetyan, the vector-meson group, Gunar Schnell, and Naomi Makins. Special gratitude goes to Markus Diehl. I am thankful for the helpful discussions we have had and for his theoretical work that has provided an important contribution to the physics analysis presented in this thesis.

During my stay in Hamburg, working on the commissioning and maintenance of hardware, I had a good cooperation with the onsite group, the St. Petersburg group, and the NIKHEF technicians. I would like to thank everybody for their support. Special thanks also go to Jos, Elke Aschenauer, Jim Stewart, and Beni Zihlmann. Many people have contributed to a pleasant working environment at DESY, in particular the guys at 55a and the various other people that accompanied me for lunch and other breaks. I enjoyed the interesting and entertaining conversations.

It was great to meet you also outside of DESY. Thanks Caro and Larry, for choosing the many nice locations of our famous offsite meetings! Special thanks also go to the group I regularly went climbing with in Eimsbüttel, in particular to those with the courage to secure me while climbing. Not to forget, for a great deal my impression of Hamburg has also been shaped by people I met over the years, who did not have a direct connection with HERMES or DESY. I would like to thank you all for sharing the good times, for showing me around, providing me

a place to stay, helping me to improve my German, or for being there as a friend, sparring partner, or Mannschaftskamerad.

Moreover, I am grateful to have met and got to know so many colleagues and friends over the years at my home base in Amsterdam. It was nice to meet people from various groups at the many coffee breaks, or at the topical lectures at NIKHEF. I enjoyed meeting many of you also outside work. To my direct colleagues of the HERMES group in Amsterdam I owe my gratitude for their contributions to a good cooperation and a pleasant working atmosphere. It was great to be located at the same corridor as the people from the NNV and the NTvN and to have lunch together. I enjoyed the meetings with my friends from the Vrije Universiteit, which focused mainly on discussing a wide range of topics while having some good food and/or drinks, or on watching some good movie. I would like to thank all friends who's company has enabled me to refresh my mind and to look at my work from different perspectives.

Finally, I would like thank my parents, brother and sister, and my girlfriend for being there, showing interest, motivating and supporting me throughout the years. Evelyn, thank you for being such great company!